EPSC Abstracts
Vol. 10, EPSC2015-16, 2015
European Planetary Science Congress 2015

The thick early atmosphere of Mars

A. Pilchin
Universal Geoscience & Environmental Consulting, North York, Ontario, Canada (arkadypilchin@yahoo.ca)

Abstract

Analysis of available data on Mars shows that it had a thick early atmosphere composed mainly of H_2O, CO, CO_2, SO_2 and SO_3. Its minimum pressure was between 3 and 11 MPa (most likely > 5 MPa). The atmosphere was stratified by density with water, sulfur, and carbon based layers formed above the Martian magma-ocean. The water layer was at the top and initially had no contact with the surface.

1. Introduction

Available data on Mars shows that: after accretion it passed a magma-ocean stage [1, 2]; its crust is mostly basaltic; its atmosphere composed mostly of CO_2 (~0.6 kPa), containing no SO_2; its average surface temperature is ~210 K; its polar caps have ice and dry ice; its regionally extensive sedimentary layers are up to ~5 km thick [3]; it contains vast river valleys, lake basins and signs of ocean; it contains olivine-rich units, huge amounts of Noachian phyllosilicates (including Noachian serpentine [4], local carbonate deposits (likely of Noachian age) [5] and great amounts of sulfates (Late Noachian-Hesperian) including a variety of evaporite minerals [3, 6]; sulfuric acid alteration of basaltic rocks and minerals is well established on the Martian surface [6]; at some point Mars contained a thicker atmosphere rich in H_2O and CO_2 [1, 2]. For analysis of content, composition and thermodynamic conditions within the early Martian atmosphere, methods used for similar analysis for the early Earth [7, 8] were employed. Since Mars' crust is basaltic, its magma-ocean surface temperature was at least ~1273-1473 K and therefore decomposition of typical carbonates, sulfides, sulfates and hydrated minerals on Mars was quicker and more efficient than it was on Earth [7, 8], and nearly the entire inventory of C, S and H_2O was within Mars' early atmosphere. Since the temperature of formation for a compound is always less than that of its stability [7, 8], CO and SO_2 would not have been re-distributed from the atmosphere above the magma-ocean until it solidified and the surface temperature dropped.

2. Distribution of Main Components of Early Mars' Atmosphere

Different estimates of H_2O content on Mars give: a global equivalent layer of water (GEL) of 500 m or 300-1030 m [9] (exerting a pressure of ~1.87 MPa and 1.12-3.85 MPa); 600–2700 m GEL [10] (~2.24-10.07 MPa); 540-2430 m GEL [11] (~2.01-9.06 Pa); and >2000 m GEL [12] (>7.46 MPa). The maximum content of water on Mars could have been as great as 7.2×10^{21} kg [13] (~185.5 MPa) or 1.4×10^{22} kg [1] (~360.64 MPa) and the absolute minimum (present surface content of H_2O) is 137 m GEL [12] (~0.51 MPa). Estimates of the SO_2 content in the sedimentary reservoir on Mars gave 2.3×10^{19} kg [6] (~0.59 MPa). Estimates of partial pressure of the CO_2 content on Mars came to 0.2-1.0 MPa [14]. Partial pressure was estimated for bulk abundances of C and S within Mars from [15] at 0.99-179.61 MPa for CO_2, 0.63-114.03 MPa for CO, and 22.0-734.0 MPa for SO_2. Depending on thickness of the magma-ocean and concentration of volatiles, the amount of outgassed H_2O and CO_2 was estimated [2] to be ~5.2–25.7 MPa and ~1.1–5.4 MPa, respectively.

3. Summary and Conclusions

The analysis shows that: there is strong evidence of presence of vast amounts of water, CO and SO_2 on Mars at the time of the magma-ocean; the minimal pressure within early Mars' atmosphere above the magma-ocean was ~3-11 MPa (most likely > 5 MPa), but actual pressure may have been much greater; the maximal atmospheric pressure could have been very high (100s of MPa); at temperature 1273 K and pressure 10 MPa, measured densities of H_2O and CO_2 are 17.1 and 40.7 kg/m^3, respectively, and calculated densities of SO_2 and CO are ~71.5 and 89.9 kg/m^3, respectively, which would result in an atmosphere stratified by density forming sulfur,

carbon, and water based layers (with H_2O above the other major layers, having no contact with the surface); the atmosphere contained mostly CO above- and CO_2 below- ~947 K [7, 8] among carbonate compounds, and mostly SO_2 above ~900 K, SO_3 between ~900 K and ~600 K, and H_2SO_4 below ~600 K among sulfur compounds [7, 8]; the main compounds of the atmosphere (H_2O, SO_2, SO_3, CO and CO_2) were in critical conditions under temperature and some in supercritical conditions if pressure was greater than 9-10 MPa; at 10 MPa water becomes denser than CO_2 and CO below ~600 K, and it is denser than SO_2 between ~600 K and 400 K; the magma-ocean on Mars solidified quickly, because of its basic composition at the top; surface formation of the water-ocean first was inevitable, because water could not penetrate the still very hot rocks at shallow depths (mostly plastic crust and low relief), and so covered the entire surface of Mars; the water-ocean was formed quite early in Noachian when surface temperatures dropped below 500-540 K; sulfuric acid was formed at some point with surface temperatures below ~630-670 K (similar to its formation on Earth [7, 8]), and it was in direct contact with the surface; since the formation of serpentine requires temperatures >473 K [7, 8] and formation of carbonates needs temperatures <473 K [7, 8] the presence of these rocks indicate variable temperatures in the Noachian; formation of phyllosilicates in Noachian and sulfates by ~3.5 Ga shows that ocean or sea water existed on Mars prior to ~3.5 Ga, but fresh water in rivers and lakes may have existed longer; presence of significant content of olivine indicates that for most of the Noachian the temperature was below ~473 K, which prevented serpentinization; SO_2 is the second most abundant compound in basalt volatiles [7, 8], and its absence in the atmosphere of Mars means that magmatic activity on the planet ended a long time ago; since Mars had limited energy collected during its accretion, radioactive decay and core differentiation, it is unlikely that it lost most of its atmosphere to space; presence of significant amount of CO_2 on Mars shows that it was not completely re-distributed by the formation of carbonates; liquid water most likely penetrated to great depths of the cold planet through a system of fractures and faults and sealed from above by subsurface permafrost of the entire planet.

References

[1] Elkins-Tanton, L.T.: Linked magma ocean solidification and atmospheric growth for Earth and Mars Earth and Planetary Science Letters, Vol. 271, pp. 181–191, 2008.

[2] N.V. Erkaev, H. Lammer, L.T. Elkins-Tanton, et al.: Escape of the martian protoatmosphere and initial water inventory. Planet. Space Sci., Vol. 98, 106–119, 2014.

[3] Grotzinger, J. P. & Milliken, R. E., 2012. The sedimentary rock record of Mars: Distribution, origins, and global stratigraphy. Sedimentary Geology of Mars, SEPM Special Publication No. 102, pp. 1-48.

[4] Ehlmann, B. L., Mustard, J. F. and Murchie S. L.: Geologic setting of serpentine deposits on Mars, Geophysical Research Letters, Vol. 37, L06201, 2010.

[5] Morris, RV, Ruff, SW, Gellert, R, et al.: Identification of carbonate-rich outcrops on Mars by the Spirit rover. Science, Vol. 329, pp. 421–424, 2010.

[6] McLennan, S. M. and Grotzinger, J. P.: Sulfur and the sulfur cycle on Mars. 40th Lunar and Planetary Science Conference, March 23-27, 2009, Woodlands, Texas, USA, abstract 2152, 2009.

[7] Pilchin, A. and Eppelbaum, L.: The Early Earth Formation and Evolution of the Lithosphere in the Hadean - Middle Archean. In: (Sato, F. and Nakamura, Sh., Eds.), Encyclopedia of Earth Science Research, Vol. 1, 1-93. Nova, 2012.

[8] Eppelbaum, L., Kutasov, I. and Pilchin, A.: Applied Geothermics. Springer, 2014.

[9] Chassefière, E, Langlais, B, Quesnel, Y, et al.: The Fate of Early Mars' Lost Water: The Role of Serpentinization. Journal of Geophysical Research: Planets, Vol. 118, pp. 1123–1134, 2013.

[10] Lunine, J. I., Chambers, J., Morbidelli, A. et al.: The origin of water on Mars. Icarus, 165, pp. 1-8, 2003.

[11] Carr, M.H., and Head, J.W.: Oceans on Mars: An assessment of the observational evidence and possible fate: Journal of Geophysical Research, Vol. 108, E5, 5042, 2003.

[12] Villanueva, G. L., Mumma, M. J., Novak, R. E. et al.: Strong water isotopic anomalies in the martian atmosphere: Probing current and ancient reservoirs. Science DOI:10.1126/science.aaa3630, 2015.

[13] Pommier, A., Grove, T.L. and Charlier B.: Water storage and early hydrous melting of the Martian mantle. Earth and Planetary Science Letters, Vol. 333-334, pp. 272–281, 2012.

[14] Pollack J.B, Kasting J.F, Richardson S.M., et al.: The case for a wet, warm climate on early Mars. Icarus, Vol. 71, pp. 203–224, 1987.

[15] Lodders K. and Fegley, B.: An oxygen isotope model for the composition of Mars. Icarus, Vol. 126, pp. 373–394, 1997

EPSC Abstracts
Vol. 10, EPSC2015-41, 2015
European Planetary Science Congress 2015

Production of liquid water on Mars by basal melting of ice sheets: a glacial interpretation of the 3 Ga old Thumbprint Terrain in Isidis Planitia

O. Bourgeois (1), O. Souček (2), S. Pochat (1) and T. Guidat (1)

(1) LPG, CNRS, Université de Nantes, Nantes, France (olivier.bourgeois@univ-nantes.fr), (2) Charles University in Prague, Faculty of Mathematics and Physics, Mathematical Institute, Prague, Czech Republic (soucek@karel.troja.mff.cuni.cz)

Isidis Planitia is a 1350 km wide impact crater located close to the martian equator. Its floor exhibits a 2.8 to 3.4 Ga old landform assemblage, nicknamed Thumbprint Terrain, made of Arcuate Ridges, Aligned Cones, Isolated Cones, Cone Fields, associated with a peripheral network of Sinuous Ridges, Linear Depressions, and Mounds (Fig. 1). The spatial organization of these landforms is consistent with the hypothesis that they form a glacial landsystem inherited from the former presence of a polythermal ice sheet over the entire basin [1].

To explore the dynamics and thermal regime of this ice sheet, we perform a simulation with a thermomechanically coupled numerical model [2]. As model inputs, we use surface temperatures and ice accumulation patterns predicted by a General Circulation Model based on the present-day atmospheric characteristics, and values of the geothermal heat flux provided by a global model of planetary thermal evolution. We find that, under favorable orbital conditions, an ice sheet covering the entire basin can develop in 2 to 5 Ma, with a maximal thickness of 4.9 km (Figs. 2 and 4).

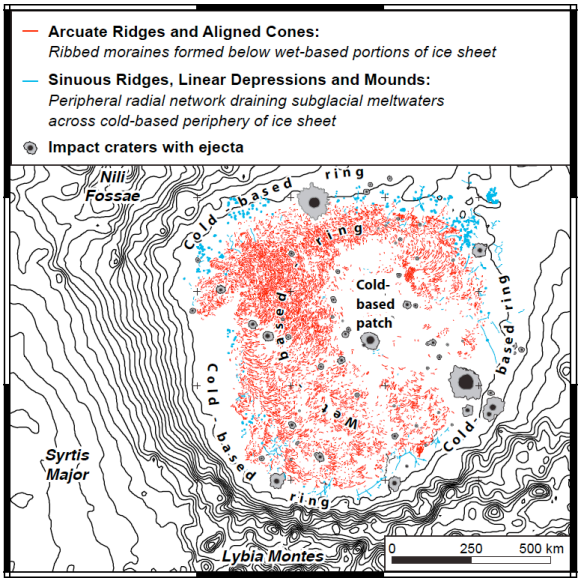

Figure 1: Map of the landform assemblage in Isidis Planitia (Mars), with interpretation in terms of a polythermal glacial landsystem [1].

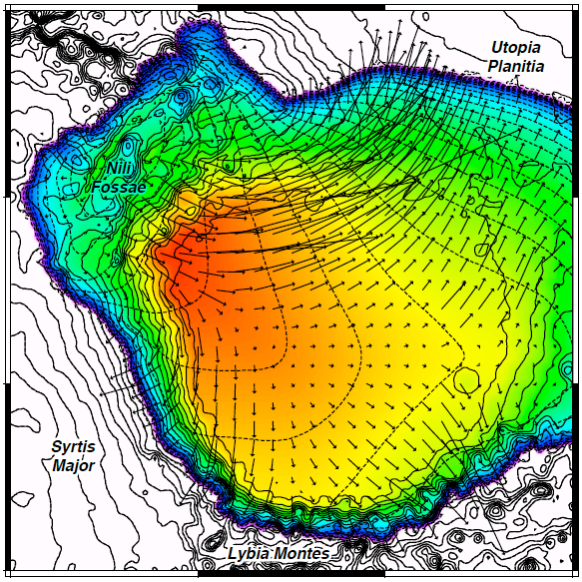

Figure 2: Thickness and surface flow lines of the modeled ice sheet at 5 Ma [2].

The modeled ice sheet is polythermal and its flow is controlled by its basal thermal regime. The pressure melting point is reached in a circular region, where Arcuate Ridges and Aligned Cones are present (Fig. 3). By contrast, the modeled ice sheet is permanently cold-based at the basin periphery and, due to a negative heat-flux anomaly, also in the basin center, where only Isolated Cones and Cones Fields are present.

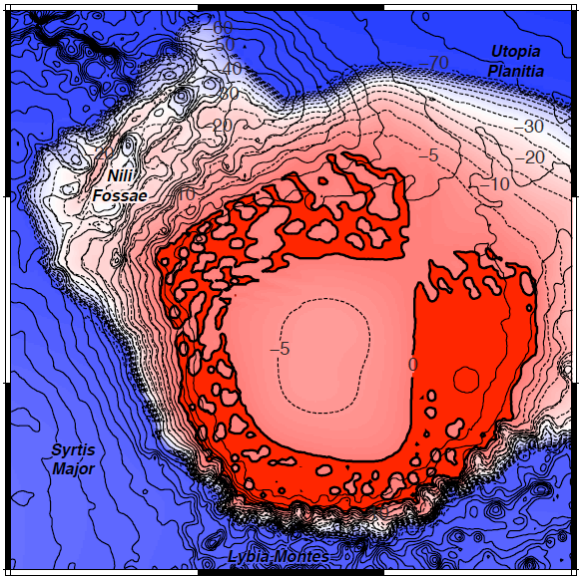

Figure 3: Basal temperature of the modeled ice sheet at 5 Ma. Red regions correspond to wet-based areas, where liquid water is produced by basal melting [2].

These results are consistent with the interpretation that the Thumbprint Terrain in Isidis Planitia is a martian equivalent of terrestrial fields of ribbed moraines and has formed below wet-based ice. They support also the interpretation that Sinuous Ridges, Linear Depressions and Mounds observed at the basin periphery are parts of a subglacial network of eskers, tunnel valleys and subglacial lakes that drained the glacial meltwater outwards, across the cold-based periphery of the ice sheet.

This work strengthens the hypothesis that glaciers as thick as a few km may have existed on Mars in the past and that glacial basal melting may have contributed to the production and flow of surface liquid water at that time, under an atmosphere no thicker than the present-day one [3].

References

[1] Guidat, T., Pochat, S., Bourgeois, O., and Souček, O.: Landform assemblage in Isidis Planitia, Mars: Evidence for a 3 Ga old polythermal ice sheet. Earth Planet. Sci. Lett. Vol 411, pp. 253-267, 2015.

[2] Souček, O., Bourgeois, O., Pochat, S., and Guidat, T.: A 3 Ga old polythermal ice sheet in Isidis Planitia, Mars: dynamics and thermal regime inferred from numerical modeling. Earth Planet. Sci. Lett., submitted.

[3] Carr, M.H., and Head, J.W.: Basal melting of snow on early Mars: a possible origin of some valley networks. Geophys. Res. Lett. Vol 30, 2245.

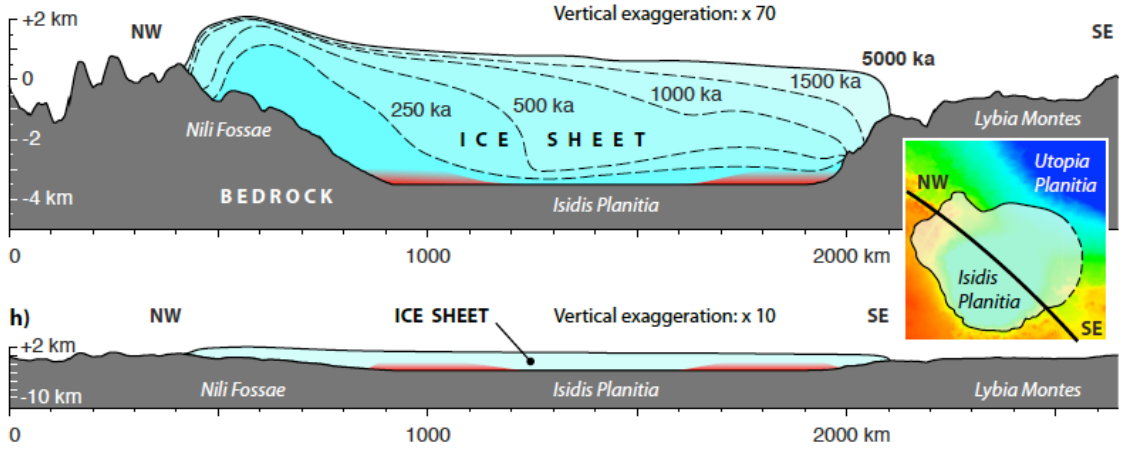

Figure 4: Topographic profiles of the modeled ice sheet at different time steps. Wet-based regions at 5 Ma indicated by red lines at base of ice sheet. Location of profiles indicated by black line in inset map [2].

EPSC Abstracts
Vol. 10, EPSC2015-52, 2015
European Planetary Science Congress 2015

Mars Atmospheric Characterization Using Advanced 2-μm Orbiting Lidar

U. Singh, W. Engelund, T. Refaat, M. Kavaya, J. Yu and M. Petros.
NASA Langley Research Center, Virginia, USA, (upendra.n.singh@nasa.gov)

Abstract

Mars atmospheric characterization is critical for exploring the planet. Future Mars missions require landing massive payloads to the surface with high accuracy. The accuracy of entry, descent and landing (EDL) of a payload is a major technical challenge for future Mars missions. Mars EDL depends on atmospheric conditions such as density, wind and dust as well as surface topography. A Mars orbiting 2-μm lidar system is presented in this paper. This advanced lidar is capable of measuring atmospheric pressure and temperature profiles using the most abundant atmospheric carbon dioxide (CO_2) on Mars. In addition Martian winds and surface altimetry can be mapped, independent of background radiation or geographical location. This orbiting lidar is a valuable tool for developing EDL models for future Mars missions.

1. Introduction

Characterization of Mars atmosphere is an important challenge for future exploration of the planet. The ability to land large payloads on surface depends upon EDL strategy, which relies on atmospheric and surface conditions to reduce uncertainties and risks for future Mars missions. Landing spacecraft on Mars is known to be hazardous. However, EDL operation risk can be reduced by improved knowledge of atmospheric conditions, surface range and approach velocity, while continuously mapping the approaching terrain for potential hazards. Atmospheric and surface investigations from orbit are the highest priority objectives for EDL of large systems. Laser remote sensing techniques are strong candidates to meet such objectives. For example, orbiting lidar instrument capabilities would include surface mapping, planetary atmospheric profiling, and 3-D imaging for hazard avoidance, motion sensing and docking activities [1]. To address these challenges, a Mars orbiting pulsed 2-μm lidar instrument is presented in this paper. This instrument has the capability to characterize critical parameters of Martian atmosphere. Orbiting 2-μm lidar would target CO_2, the most abundant atmospheric gas on Mars, for temperature, pressure and density profiling. Using the backscatter lidar signal, range-resolved profiles of wind, aerosols and dust could be obtained. Ranging, a byproduct of the pulsed operation, is useful for surface studies. Measurements are obtained with resolutions that are difficult to achieve by other means.

2. Technical Approach

NASA Langley Research Center (LaRC) has been developing lidar enabling technologies for atmospheric wind and CO_2 measurements for Earth science [2-4]. This includes state-of-the-art 2-μm single or multi-pulsed laser transmitters for various lidar applications [2, 5]. Single-pulse 2-μm lasers based on LuLiF technology is compatible with the CO_2 R32 absorption line. Using this technology Doppler lidar and coherent DIAL are used for airborne 3D-wind and CO_2 measurements, respectively [2-3]. Multi-pulse 2-μm laser based on YLF technology, targeting the CO_2 R30 line, demonstrated accurate airborne sensing of CO_2 using the IPDA technique [4-5]. Key advantages of these systems include multi-pulsed operation, using single pump-pulse, and wavelength tuning, switching and locking for each pulse. Other capabilities include high repetition rate, which is preferable for space platform, space qualified packaging, rigid system design with low power consumption and small size.

Adopting this 2-μm lidar technology from a Martian orbiter, figures 1 and 2 compare near-surface CO_2 absorption cross section spectra for Earth and Mars environments. The profiles are driven from HITRAN.

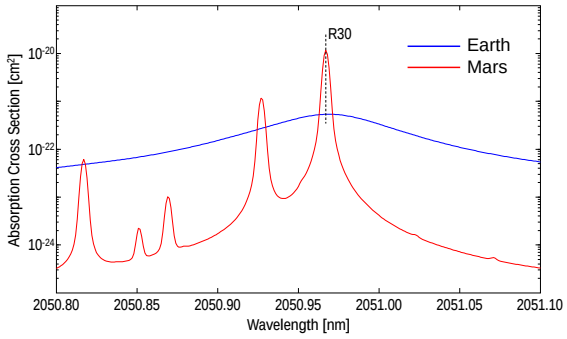

Figure 1: CO_2 absorption spectra around R30 line, achievable by Ho:Tm:YLF laser transmitter, for both Earth and Mars surfaces.

For Earth, standard atmospheric conditions and 400 ppm CO_2 dry-air mixing ratio are considered. For Mars, mean surface pressure and temperature of 600 Pascal and -60°C, respectively and 100% CO_2 abundance are assumed. Operating from a Martian orbiter, while implementing multi-pulsed operation, would generate enough information to solve for pressure, temperature and density profiles. For example, wavelength tuning and locking capabilities could target temperature insensitive lines, to solve for pressure and density. Backscatter return signal would include aerosol and dust profiling. Using coherent-detection, wind velocity could be achieved. Altimetry is directly obtained through time-delay measurement of the pulsed nature of the transmitter. This exhibits the multi-pulsed 2-µm orbiting lidar as a valuable tool for developing EDL models for future Mars missions.

3. Summary and Conclusions

NASA LaRC has been developing advanced wind and CO_2 airborne enabling 2-µm pulsed lidar technologies for Earth science. Continuing efforts are focused to extend such technology to space. Key capabilities of the 2-µm lidar include multi-pulse generation, with wavelength tuning, switching and locking. Based on LuLiF and YLF technologies, the transmitter can target the R32 and R30 CO_2 lines, respectively. CO_2 is the most abundant atmospheric gas on Mars. Targeting precise wavelengths, temperature, pressure and number density profiles could be obtained from a Martian orbiter. Winds, aerosol, dust and altimetry are other products of this lidar system. Measurements from this orbiting lidar are valuable for developing EDL models for future Mars missions.

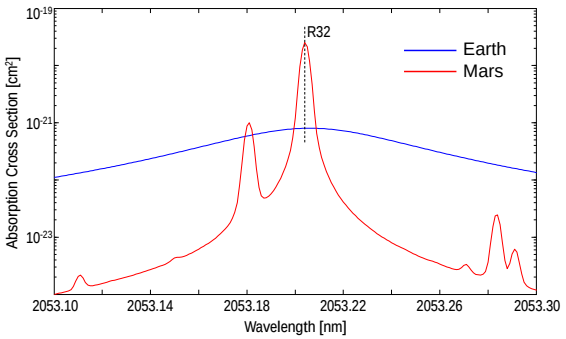

Figure 2: CO_2 absorption spectra around R32 line, achievable by Ho:Tm:LuLiF laser transmitter, for both Earth and Mars surfaces.

References

[1] Singh, U., Emmitt, G., Levine, J., Engelund, W., Yu, Yu., Koch, G., and Kavaya, K.: A Mars-orbiting 2-micron lidar system to monitor the density, winds and dust of the atmosphere of Mars, 4th International Workshop on the Mars Atmosphere: Modeling and Observations, Paris, France, 2011.

[2] Singh, U., Walsh, B., Yu, J., Petros, M., Kavaya, M., Refaat, T., and Barnes, N.: Twenty years of Tm:Ho:YLF and LuLiF laser development for global wind and carbon dioxide active remote sensing, Optical Material Express, Vol. 5, pp. 827-837, 2015.

[3] Kavaya, M., Beyon, J., Koch, G., Petros, M., Petzar, P., Singh, U., Trieu, B., and Yu, J.: The Doppler aerosol wind (DAWN) airborne, wind-profiling, coherent-detection lidar system: overview and preliminary flight results, Journal of Atmospheric and Oceanic Technology, Vol. 31, pp. 826-842, 2014.

[4] Singh, U., Yu, J., Petros, M., Refaat, T., Remus, R., Fay, J., and Reithmaier, K.: Airborne 2-µm double-pulsed integrated path differential absorption lidar for column CO_2 measurement, Proceeding of SPIE, Vol. 9246, 924602, 2014.

[5] Refaat, T., Singh, U., Yu, J., Petros, M., Ismail, S., Kavaya, M., and Davis, K.: Evaluation of an airborne triple-pulsed 2-µm IPDA lidar for simultaneous and independent atmospheric water vapor and carbon dioxide measurements, Applied Optics, Vol. 54, pp. 1387-1398, 2015.

EPSC Abstracts
Vol. 10, EPSC2015-103, 2015
European Planetary Science Congress 2015

Meteorological Circulations at Gale Environment Through Rover Environmental Monitoring Station (REMS) Observations and Mesoscale Modeling (MRAMS)

Jorge Pla-García[1,2], Scot C.R. Rafkin[1] and the REMS and MSL Science teams

[1]Southwest Research Institute, Boulder CO 80302, USA
[2] Departamento de Astrofísica y CC. de la Atmósfera, Universidad Complutense de Madrid, E-28040 Madrid, Spain

Abstract

Gale Crater, in which the Mars Science Laboratory (MSL) landed in August 2012, is the most topographically complex area visited to date on Mars. The meteorology within the crater may also be one of the most dynamically complex meteorological environments, because topography is thought to strongly drive the near-surface atmospheric circulations. The Rover Environmental Monitoring Station (REMS) [5] has provided some clues on the nature of the local meteorology strongly influenced by the complex topography, as predicted by numerous previous studies. The types of perturbations of pressure, air and ground temperature and wind measured by REMS have never been observed at other locations and these data provide a great opportunity to test the models at the most meteorological interesting area measured to date. In an effort to better understand the atmospheric circulations of the Gale Crater, the Mars Regional Atmospheric Modeling System (MRAMS) [6] was applied to the landing site region using nested grids with a spacing of 330 meters on the innermost grid that is centered over the landing site. We provide a comparison of MRAMS predictions for pressure, air temperature, winds and ground temperature, to the REMS data available at the location of the Rover for sols 51-55 (L_s=180), sols 195-199 (L_s=270), sols 348-352 (L_s=0) and sols 541-545 (L_s=90), in order to provide a baseline of model performance. Pressure and ground temperature provide the most robust parameters with which to test the model predictions (Figures 2 and 3).

2. Circulations at Gale

Simulations with MRAMS indicate thermal and wind thermal signatures associated with slope flows, katabatic winds, and nocturnal mixing events that are consistent with the rover environment monitored by REMS. Some pressure structures are shown both in model and observations during L_s=270 at night, and could be related to strong downslope winds (Figure 3). Potential temperature studies allows thermal comparison of air at different altitudes, showing evidence for two distinct air masses—one in the bottom of the crater (a relatively cold dense air mass) and one on the plateau, that produces minimal interaction with one another during L_s=0, 90 and 180. Warm air from south overrides the crater and gravity waves are formed in the north rim (Figure 5). An exceptional case is season L_s=270, when colder air from north plateau (downslope winds) can flush out crater air mass and northern hemisphere air make it into the bottom crater in a massive push of cold air (Figures 4 and 5). If there are indeed two distinct air masses, there are strong implications for dust, water vapor and chemical (including methane) cycles within Gale Crater. The air within Gale should be drier and less dusty due to more limited mixing with the environment and limited dust lifting due to dust devils during L_s=0, 90 and 180. There are strong indications that there is a complex interplay between circulations over a large range of spatial and temporal scales. In particular, the modeling will demonstrate that global (Hadley cell), regional (Mars dichotomy) and local (Gale crater) circulations must all be considered in order to explain the observational data. Complex crater circulations result from adding all scales of motion (Figure 6).

3. Figures

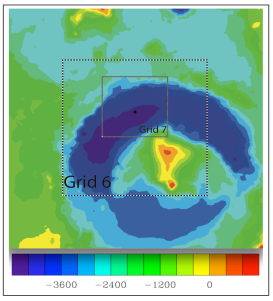

Figure 1: Horizontal Grid Spacing applied to landing site. The black dot is Curiosity landing site location.

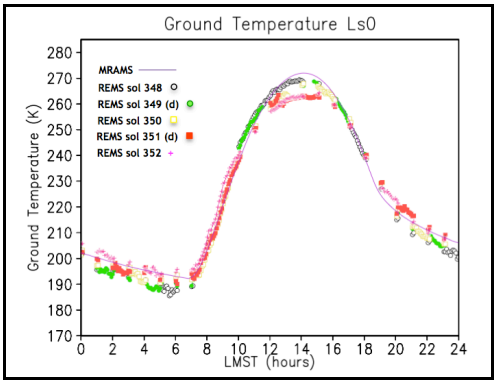

Figure 2: Comparison of MRAMS predictions to Gale diurnal temperature cycle measured by REMS in sols 348-352 (Ls=0). "d" are rover driving sols.

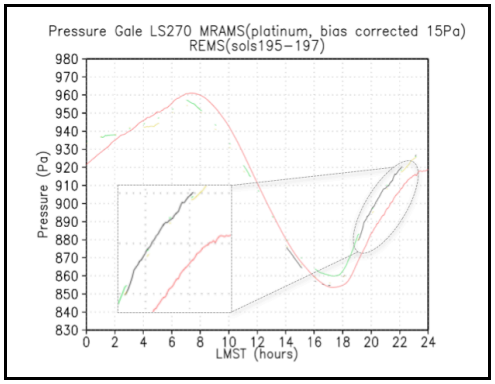

Figure 3: Comparison of MRAMS predictions to the diurnal pressure cycle measured by REMS in sols 195-197 (L_s=270).

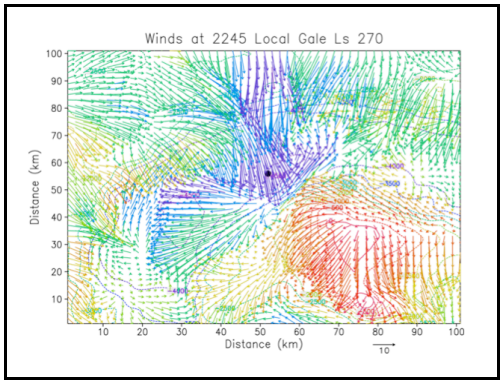

Figure 4: MRAMS model predictions of night winds (katabatic) colored by potential temperature for sol 197 (Ls=270). The black dot is the Curiosity location.

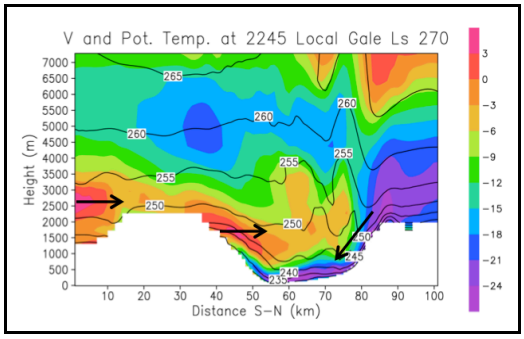

Figure 5: Winds colored by potential temperature in cross section. Strong downslope (katabatic) winds at Ls=270 along north rim during the night.

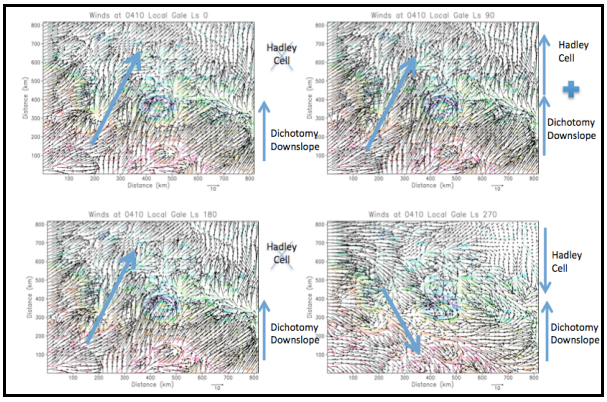

Figure 6: Multiscale scenario. Air flowing into crater originates from Southern Hemisphere for all seasons except Ls=270 where global winds (northern) are fighting against regional dichotomy (downslope) winds during the night.

References

[1] Rafkin, S. C. R., and T. I. Michaels (2003), J. Geophys. Res., 108(E12), 8091. [2] Michaels, T. I., and S. C. R. Rafkin (2008), J. Geophys. Res.-Planets, 113. [3] Toigo, A. D., and M. I. Richardson (2003), J. Geophys. Res., 108(E12), 8092. [4] Tyler, D., J. R. Barnes, and E. D. Skyllingstad (2008), J. Geophys. Res.-Planets, 113(E8). [5] Gómez-Elvira, J., et al. (2012), Space Science Reviews, 170(1-4), 583-640. [6] Rafkin, S. C. R., R. M. Haberle, and T. I. Michaels (2001), Icarus, 151, 228–256. [7] Rafkin, S. C. R., M. R. V. Sta. Maria, and T. I. Michaels (2002), Nature, 419, 697–699. [8] Haberle, R.M., Murphy, J.R., Schaeffer, J., 2003. Icarus 161, 66–89.

EPSC Abstracts
Vol. 10, EPSC2015-110, 2015
European Planetary Science Congress 2015

A map of D/H on Mars using high-resolution spectroscopy with EXES aboard SOFIA

T. Encrenaz (1), M. Richter (2), C. DeWitt (2), T. Greathouse (3), T. Fouchet (1), F. Montmessin (4), F. Lefèvre (4), B. Bézard (1), S. Atreya (5), M. Case (2), N. Ryde (6)
(1) LESIA, Paris Observatory, 92195 Meudon, France, (2) University of California Davis, CA 95616, USA, (3) SwRI, San Antonio, TX 78228, USA, (4) LATMOS, IPSL, 75252 Paris, France, (5) University of Michigan, Ann Arbor, MI 48109-2143, USA, (6) Lund Observatory, 221 00 Lund, Sweden (therese.encrenaz@obspm.fr / Fax: +33-1-45072806)

Abstract

We have obtained a map of D/H on Mars on April 8, 2014, when the planet was close to opposition (15.3" in diameter) and close to northern summer solstice (Ls = 113°). Data were recorded with the EXES (Echelon Cross Echelle Spectrograph) imaging spectrometer aboard the Stratospheric Observatory for Infrared Astronomy (SOFIA). A preliminary reduction indicates an increase of the D/H ratio from south to north, with a disk-integrated value of about 6.5 times the terrestrial value.

1. Introduction

The D/H ratio on Mars is a key tracer of the atmospheric evolution of the planet, both at global and regional scales. As an effect of differential escape rates of HDO and H_2O (HDO being slightly heavier than H_2O), a measurement of the present D/H, integrated over the planet, is an indicator of the global loss of water over the history of the planet. At a local scale, a measurement of D/H over the Martian disk, and its evolution with latitude, altitude and season, is an indicator of the water cycle and its exchange with surface reservoirs, through fractionation processes associated with differential condensation mechanisms.

The first measurement of D/H on Mars was achieved by Owen et al. (1988)[1] who inferred a disk-integrated D/H enrichment of 6 (+/- 3) with respect to the terrestrial Standard Mean Ocean Water (SMOW) value. This was the first indication of the loss of water from Mars over geologic time, implying that Mars must have been wetter and warmer than today. The previous results for the present day Mars atmosphere have been confirmed by subsequent measurements on a global and local scale [2, 3]. Maps of D/H were also recorded for different seasons [4, 5]. In particular, Villanueva et al. (2015) [5] found a D/H enrichment higher than previously thought, and stronger local variations than expected in the theoretical model [6].

2. Observations

EXES (Echelon Cross-Echelle Spectrograph) is an imaging spectrometer that operates at high, medium or low resolution in the medium infrared range (4.5 – 28.3 μm). It is mounted on the 2.5-m telescope of SOFIA (Stratospheric Observatory for Infrared Astronomy), operating at altitudes of 12 – 14 km and allowing the simultaneous observations of H_2O and HDO lines. Our observations took place on April 8, 2014 between 5:00 and 5:30 UT. The planet was very close to opposition with a diameter of 15.3". The areocentric longitude Ls was 113°, just after northern summer solstice.

Data were recorded between 1383 and 1390 cm^{-1} (7.19 – 7.23 μm), with a spectral resolving power of 5 10^4 ($\Delta\nu$ = 0.028 cm^{-1}). As Mars was close to opposition, the Doppler shift (0.011 cm^{-1}) was about three times smaller than our spectral resolution.

3. Data analysis

Figure 1 shows a portion of the EXES spectrum between 1387.8 and 1390 cm^{-1}, which includes weak transitions of CO_2, H_2O, and HDO. As a first analysis of our data, we have used the line depth ratios of H_2O/CO_2 and HDO/CO_2 to retrieve mixing ratios of H_2O and HDO, respectively, and then to infer the D/H ratio on Mars using the relation D/H = 0.5 x $[HDO]/[H_2O]$. This method has the advantage of removing, to first order, the effects associated with the thermal structure and the geometry of the

observations; it has been successfully applied to study the seasonal variations of H_2O_2 and HDO on Mars [7, 8].

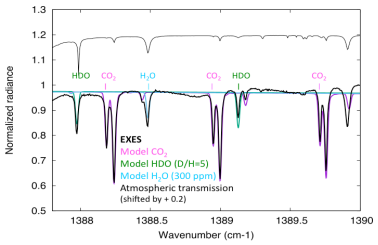

Figure 1: The disk-integrated spectrum of Mars recorded by EXES between 1387.8 and 1390 cm^{-1} (thick black line). Models including absorptions by CO_2, H_2O and HDO are shown for comparison, with a model of the atmospheric transmission.

5. Results

Figure 2 shows the map of D/H on Mars inferred from the line depth ratios of HDO (at 1389.13 cm^{-1}) and H_2O (at 1388.47 cm^{-1}). The contribution of the terrestrial absorption at these two frequencies was inferred from both the atmospheric model (Figure 1) and the measurement of the sky, recorded simultaneously with our Mars spectrum. We derive a disk-integrated D/H value of about 6.5 times the terrestrial value, with variations ranging, from south to north, from 5.5 times to 8 times the terrestrial value.

6. Conclusions

Our results are in good agreement with previous estimates [1-5], in particular with the maps obtained by Villanueva et al. (2015) for Ls = 80° [5]. They illustrate that the latitudinal variation of D/H, although consistent with the trend expected from a fractionation process dominated by condensation, are stronger than predicted in the theoretical model [6]. In the future, we plan to refine this analysis by modeling the entire EXES spectrum to get a more accurate estimate of the uncertainty associated with our measurement.

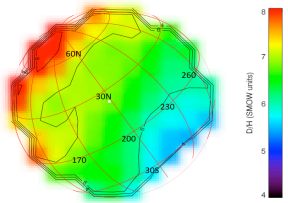

Figure 2: The map of D/H on Mars inferred from the EXES data. Mars was close to opposition, and the season was just after northern summer solstice (Ls = 113°).

Acknowledgements

We are grateful to the SOFIA and EXES staff for their help in the observations. TE and BB acknowledge support from CNRS. TG acknowledges support of NASA grant NNX14AG34G. TF acknowledges support from UPMC.

References

[1] Owen, T. et al. Deuterium on Mars – The abundance of HDO and the value of D/H. Science 240, 1767-1770, 1988.

[2] Krasnopolsky, V. A. et al. High-resolution spectroscopy of Mars at 3.7 and 8 μm: A sensitive search for H_2O_2, H_2CO, HCl and CH_4, and detection of HDO. J. Geophys. Res. 102, 6525-6534, 1997.

[3] Webster, C. R. et al. Isotope ratios of H, C and O in CO_2 and H_2O of the Martian atmosphere. Science 341, 260-263, 2013.

[4] Novak, R. E. et al. Measurement of the isotopic signatures of water on Mars; Implications for studying methane. Plan. Space Sci. 59, 163-168, 2011.

[5] Villanueva G. L. et al. Strong water isotopic anomalies in the martian atmosphere: Probing current and ancient reservoirs. Science 248, 218-221, 2015.

[6] Montmessin, F. et al. Modeling the annual cycle of HDO in the Martian atmosphere. J. Geophys. Res. 110, E03006, 2005.

[7] Encrenaz, T. et al. Hydrogen peroxide on Mars: Observation, interpretation and future plans. Plan. Space Sci. 68, 3-17, 2012.

[8] Encrenaz, T. et al. Seasonal variations of hydrogen peroxide and water vapor on Mars: Further indications of heterogeneous chemistry. Astron.Astrophys. In press, 2015.

EPSC Abstracts
Vol. 10, EPSC2015-111, 2015
European Planetary Science Congress 2015

Thermal cracking of CO_2 slab ice as the main driving force for albedo increase of the martian seasonal polar caps

S. Philippe, B. Schmitt, P. Beck and O. Brissaud
Institut de Planétologie et d'Astrophysique de Grenoble, France, Université Grenoble-Alpes
sylvain.philippe@obs.ujf-grenoble.fr

Introduction

Understanding the microphysical processes occuring on the Martian seasonal cap is critical since their radiative properties can affect the martian climate. A well documented phenomenom is the albedo increase of the Martian seasonal caps during spring, Fig.1. There are a lot of hypotheses that have been proposed as an explanation for this observation : the decrease of the CO_2 grain size [2], a cleaning process of the CO_2 slab that would imply either the sinking or the ejection of the dust contained in its volume ([1], [2], [5]), a water-layer accumulation on the top of the slab [5], the role played by aerosols [2] etc ... So far, no experimental simulations have been realized to discriminate between these processes. We designed an experiment to investigate the hypothesis of CO_2 ice grain size decrease through thermal cracking as well as that of dust segregation as the possible reasons for albedo increase.

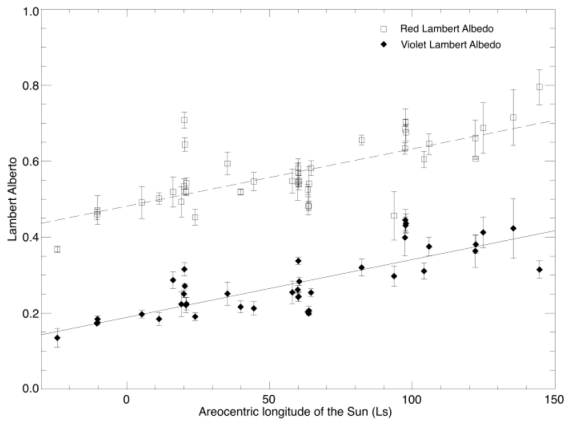

Figure 1: Albedo increase of the Northern seasonal cap seen by Hubble [1]

Experiment

Protocol

To reproduce Martian seasonal deposits, an homogenous mix of CO_2 ice with dust was produced and introduced into the Carbo-NIR cell, which is a chamber developed at IPAG to simulate Martian environment. CO_2 ice is obtained in a granular form which is then 'slabised' (transformed into polycrystalline ice) in the cell using CO_2 gas injection. The entire experiment has been conducted at a temperature of -126^{o}C and a pressure of 6.5 mbar, characteristic of the martian environment during winter. The dust used in this experiment is a volcanic tuf that has been characterised in reflectance spectroscopy ([3], [4]) and which is used as an analog for martian dust in this experiment.

Reflectance spectra were acquired with the Spectrogonio-radiometer at IPAG laboratory. Our measurements span the range 0.5-4 μm with an acquisition step of 20 nm between 0.5 and 1 μm and 10 nm between 1 and 4 μm. Spectral resolution varies along the spectrum : from 19 nm between 0.5–3 μm to 39 nm between 3–4 μm. All the spectra were acquired with an incidence angle of 0°and emergence angle of 15°, azimuth of 0°.

Ice cracking could be potentially produced by 2 types of stresses induced by thermal gradient : the temperature gradient inside the slab could either be produced by the absorption of solar energy or, in atmospheric depression condition, by the rapid cooling of the surface due to CO_2 high sublimation enthalpy. Both hypotheses were tested with several experiments, including: illumination with stable pressure, decrease of pressure, illumination with pressure increase. The first situation represent a full martian analogy since we pumped into the volume limited cell to keep a stable CO_2 gas pressure all along the experiment to simulate the stable atmosphere. In the second case of decreasing pressure, we investigated typical ΔP experienced in Mars' atmosphere with baroclinic waves ac-

tivity (typically 0.5-1 mbar). In our simulations, illumination is realized with an hallogen lamp and the flux brought to the sample is equal to the flux received by seasonal deposits in early spring (around 200 W.m^{-2}).

Results

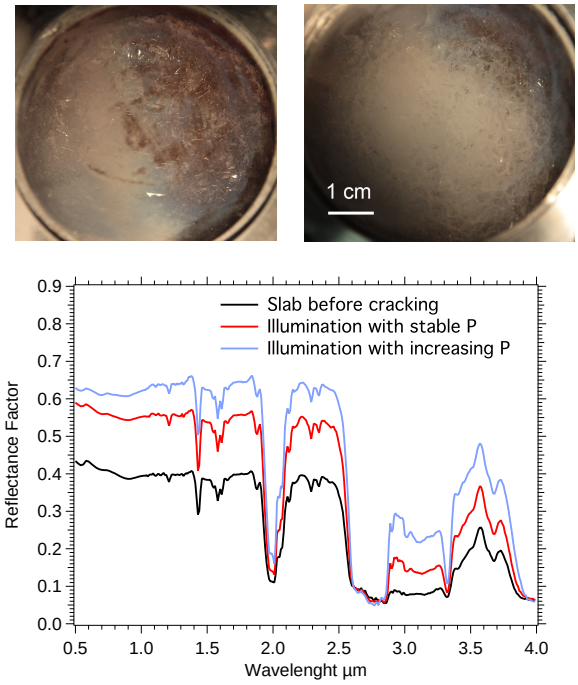

Figure 2: Bidirectional reflectance spectra of the CO_2 slab initial state (black), after thermal cracking (red) and after cracking only due to thermal stress (blue).

Fig.2 presents bidirectional reflectance spectra of the sample during the experiments. The black one is a typical slab spectrum as we can obtain it in our cell with deep CO_2 bands and a low reflectance. The blue and red spectra are obtained after thermal cracking of the slab ice with 2 different protocols : thermal cracking for the red spectrum was produced using illumination + pumping (stable P and surface T) while thermal cracking for the blue spectrum is realized with illumination only (i.e. the pressure increased inside the cell as the sample warmed up). Results associated with pumping only (ΔP = 1 mbar) are not displayed since we didn't observed any ice fracturing using this method.

At 1 μm, the reflectance is increased by 41% on the red spectrum and 58% on the blue spectrum. The difference of albedo increase between both cases is simply due to a longer illumination time for the second case (2h instead of 1h). This albedo increase can be compared to the one observed on Mars (see Fig.1).

The dust grain evolution into the slab was harder to get from these experiments. We can already say that dust contained into slab ice don't accumulate on the surface and would rather 'sink' into the slab since dust would preferably absorb light compared to CO_2 ice, warm and sublimate the ice around and sink with the same phenomenom that we observe on terrestrial glaciers.

Conclusions

This preliminary study showed that thermal cracking of CO_2 slab ice can produce a strong increase of the reflectance (as high as 60%) and mimic the Martian CO_2 photometric behaviour during spring. This value is consistent with the increase observed on Mars. We are currently developping a way to get a more quantitative estimation of the grain size variation of the polycristalline ice during sublimation with optical techniques and radiative transfer modeling. Furthermore, the evolution of dust into the slab will be reinvestigated.

References

[1] Cantor, B.A., Wolff, M.J., James, P.B. and Higgs, E.: Regression of Martian North Polar Cap: 1990-1997 Hubble Space Telescope Observations, Icarus, Vol. 136, pp. 175-191, 1998.

[2] Langevin, Y., Bibring, J.P., and Montmessin, F., Forget, F., Vincendon, M., Douté, S., Poulet, F. and Gondet, B.: Observations of the south seasonal cap of Mars during recession in 2004–2006 by the OMEGA visible/near-infrared imaging spectrometer on board Mars Express, JGR, Vol. 112, E08S12, 2007.

[3] Pommerol, A. and Schmitt, B.: Strength of the H2O near-infrared absorption bands in hydrated minerals: Effects of particle size and correlation with albedo, JGR, Vol. 113, pp., 2008.

[4] Pommerol, A. and Schmitt, B.: Strength of the H2O near-infrared absorption bands in hydrated minerals: Effects of measurement geometry, JGR, Vol. 113, pp., 2008.

[5] Portyankina, G., Markiewicz, W., and Thomas, N., Hansen, C.J., Milazzo, M.: HiRISE observations of gas sublimation-driven activity in Mars' southern polar regions: III. Models of processes involving translucent ice, Icarus, Vol. 205, pp. 311-320, 2010.

EPSC Abstracts
Vol. 10, EPSC2015-146, 2015
European Planetary Science Congress 2015

Mars' "Magnetospheric" Response to Interplanetary Field Orientation: Inferences from Models for MAVEN Investigation

J.G. Luhmann (1), C. Dong (2), Y-J. Ma (3), S.M. Curry (1), K. Alvarez (1), T. Hara (1), J. Halekas (4), D.A. Brain (5), S. Bougher (2), J. Espley (6), (1) Space Sciences Laboratory, University of California, Berkeley, CA, USA, (2) AOSS Dept., University of Michigan, Ann Arbor, MI, USA, (3) IGPP UCLA, Los Angeles, CA, USA, (4) Department of Physics and Astronomy, University of Iowa, Iowa City, IA, USA, (5) LASP, Boulder, CO, USA, (6) NASA Goddard Space Flight Center, Greenbelt, MD, USA (jgluhman@ssl.berkeley.edu)

Abstract

Planetary space weather at Mars has attracted much interest, but the focus is usually on the response to solar activity and its related disturbances in the solar wind. While this aspect is important and may be key to understanding Mars' atmosphere evolution, an additional consideration is based on the sensitivity of Earth's magnetospheric solar wind interaction to southward interplanetary magnetic fields. The study described here investigates whether Mars has its own specific interplanetary field orientation sensitivities that might be identified in the MAVEN data analyses.

1.Introduction

At Earth, the coupling of solar wind energy into geospace is extremely sensitive to the occurrence of southward interplanetary magnetic fields. This sensitivity is a consequence of the antiparallel orientation of the Earth's dipole field and the external field at the magnetopause. Under southward IMF circumstances, the magnetosphere has its maximum magnetic connection to the interplanetary field, and thus to convection electric fields in the solar wind that map down into large areas in the polar regions. The consequence for Earth is geomagnetic activity and its related atmospheric and ionospheric effects- including significant heating and momentum transfer.

Mars' more complex crustal magnetic fields at its solar wind obstacle boundary similarly allow reconnection with the draped external fields. However in this case the result is varying degrees of open field connection depending on both crustal field and interplanetary field orientations. Larger open field areas can presumably create stronger coupling.

2. Approach

We use BATS-R-US MHD simulations of the solar wind interaction with Mars [1] to explore some interplanetary field orientation effects on the solar wind coupling. To isolate these, a nominal solar wind density and velocity is assumed for all cases, while the orientation of the strong crustal fields of Mars and the interplanetary field are varied. We compare the areas and locations of open magnetic fields (those connecting Mars to interplanetary space) and the model ionospheric characteristics (e.g. velocities) for cases with the strongest Mars crustal fields at noon, dusk, midnight and dawn, and for interplanetary fields that are at nominal toward (Eastward) and away (Westward) Parker spiral orientations, or atypically northward or southward (relative to the Mars orbit plane). The results suggest coupling to the solar wind should be particularly strong for Southward interplanetary fields when the strong crustal fields are at dawn. While the IMF 'coupling function' at Mars is not as extreme as for Earth, the open field area in the ionosphere is 3-4X greater for that condition than for the other combinations.

MAVEN's comprehensive solar wind interaction and aeronomy measurements allow a search for times when the interplanetary conditions and crustal fields correspond to these 'best connected' conditions. However, major challenges come with this search. For one, strongly northward or southward interplanetary fields are rare and usually found in interplanetary coronal mass ejections (ICMEs)- that also include enhanced solar wind pressures and magnetic field strengths affecting solar wind

response. For another, the crustal field location at dawn must coincide with the ICME passage, which typically lasts 1-2 days. While these requirements are restrictive at this relatively early stage of the mission, the current solar activity level continues to produce coronal mass ejections and thus opportunities.

References

[1] Ma, Y. et al. (2004), *JGR, 109, doi:10.1029/2003JA010367*.

EPSC Abstracts
Vol. 10, EPSC2015-148, 2015
European Planetary Science Congress 2015

Study of the cold oxygen corona with IUVS/MAVEN

J-Y. Chaufray (1), J. Deighan (2), M. Chaffin (2), N. Schneider (2), B. McClintock (2), I. Stewart (2), G. Holsclaw (2), J. Clarke (3), and B. Jakosky (2)
(1) LATMOS-IPSL, CNRS, Guyancourt, France, (2) LASP, Boulder, CO, USA, (3), Boston University, Boston, MA, USA

Abstract

The Mars Atmosphere and Volatile Evolution Mission (MAVEN) has observed the Martian upper atmosphere for several months. The Imaging Ultraviolet Spectrograph (IUVS) is able to measure the resonance line of the atomic oxygen at 130.4 nm. From this emission we are able to derive information of the oxygen content in the Martian upper atmosphere and its variability. Atomic oxygen is a key species to better understand the chemistry, heating, dynamics and escape of the Martian upper atmosphere.

1. Introduction

The Mars Atmosphere and Volatile Evolution mission (MAVEN) has been recently inserted around Mars (3). This mission is motivated by the study of the Mars atmospheric erosion rates along its history. Most of the atmospheric erosion rates occur in the upper atmosphere and therefore the understanding of the energetics, chemistry and dynamics of the Martian upper atmosphere is crucial to constrain the contribution of the different escape channels to the Martian atmospheric erosion (2, 5).

The atomic oxygen, produced by photodissociation of the atmospheric carbon dioxide, becomes the main neutral species in the upper thermosphere and low exosphere of Mars.

2. IUVS observations

Examples of spectra measured by IUVS (4) during one orbit are displayed in Fig. 1. The two dominant lines above 150 km are the hydrogen resonance line at 121.6 nm and the oxygen resonant line at 130.4 nm.

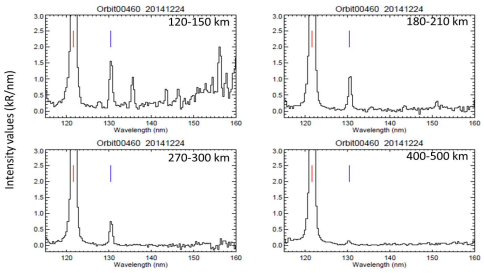

Figure 1: Examples of spectra obtained by IUVS at different altitudes.

Based on the radiative transfer model used to interpret Mars Express data (1), we have developed a fast and full inversion code to automatically derive the oxygen density and temperature at the exobase (Fig. 2)

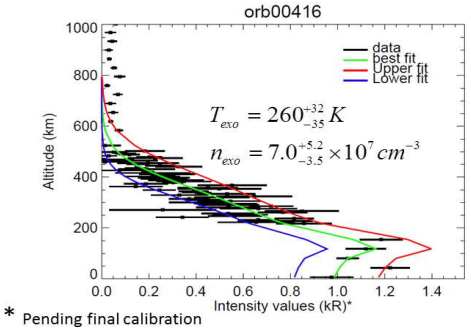

Fig. 2 Brightness profile of the O I 130.4 nm line and best fit derived The parameters of the fit are indicated on the figure.

The current absolute calibration of IUVS is still under investigation and because the O 130.4 nm is

optically thick, the derived parameters vary non-linearly with the brightness. Example of the sensitivity of the derived oxygen density and temperature is given in Fig.3.

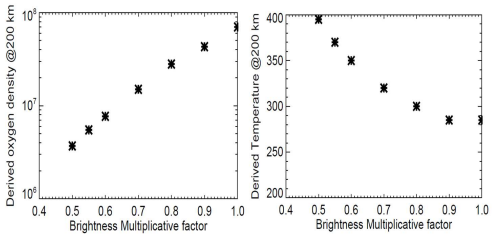

Fig. 3 Sensitivity of the oxygen density and temperature at the exobase to the absolute calibration of the instrument.

In this presentation, results obtained at several SZA will be presented as well as comparison with previous observations (Mariner, Mars Express, HST).

3. Summary and Conclusions

The first observations of IUVS/MAVEN of the Martian cold oxygen corona have been performed and first quantitative estimate of the oxygen density derived. The emission is systematically observed for SZA < 100° and several hundreds of profiles have been done during the first months of the mission. The comparison with previous observations show a larger brightness derived by IUVS/MAVEN compared to other instruments. These differences could be due to absolute calibration of these instruments or to change in the oxygen density in the Martian upper atmosphere.

Acknowledgements

MAVEN is a space mission from NASA. We wish to express our gratitude to all NASA members who participate in this mission. JYC wishes to thank CNES for funding this work in France.

References

[1] Chaufray, J-Y et al., Martian oxygen density at the exobase deduced from O I 130.4 nm observations by SPICAM on Mars Express, J. Geophys. Res., 114, E02006, 2009

[2] Gonzalez-Galindo, F. et al., A ground to exosphere Martian circulation model : 1 seasonal, diurnal and solar cycle variations of thermospheric temperatures, J. Geophys. Res., 114, E04001, 2009

[3] Jakosky, B. et al., The Mars Atmosphere and Volatile Evolution (MAVEN) Mission. Space Science Reviews, 2015, (in press).

[4] McClintock, B. et al., The Imaging Ultraviolet Spectrograph (IUVS) for the MAVEN Mission, Space Sci. Rev., doi 10.1007/s11214-014-0098-7, 2014.

[5] Valeille, A. et al., Three dimensional study of Mars upper thermosphere/ionosphere and hot oxygen corona, 1: General description and results at equinox for solar low conditions, J. Geophys. Res., 114, E11005, 2009

EPSC Abstracts
Vol. 10, EPSC2015-174, 2015
European Planetary Science Congress 2015

Precipitation of energetic neutral atoms on the Martian upper atmosphere: hybrid simulation

X.-D. Wang (1), E. Kallio (2), M. Alho (2), R. Jarvinen (3), S. Barabash (1), and Y. Futaana (1)
(1) Swedish Institute of Space Physics, Kiruna, Sweden, (2) Aalto University, Espoo, Finland, (3) Finnish Meteorological Institute, Helsinki, Finland (wang@irf.se)

Abstract

We explore the precipitation of energetic neutral atoms (ENAs) on the Martian upper atmosphere using a hybrid plasma model and a spherically symmetric exosphere model. ENAs are generated via charge-exchange reaction between the ions in the Martian plasma environment and the neutrals in the exosphere. ENAs do not feel the electromagnetic field, and their birth places are collisionless. Therefore ENAs moving towards the planet can precipitate to the exobase. We study the spatial distribution and spectral characteristics of these precipitating ENAs, and investigate the consequences caused to the upper atmosphere of Mars.

1. Introduction

Martian space environment is an active ENA source. Most of the ENAs are generated in the dayside hemisphere of Mars, via the charge exchange reaction between the solar wind protons (both upstream and shocked) with the highly extended Martian exosphere. These ENAs are not affected by the electromagnetic field in the interplanetary space, in the magnetosheath, or in the induced magnetosphere. In these regions, the particle mean free path is comparable to the altitude to the exobase, therefore ENAs can directly reach the exobase and precipitate to the upper atmosphere. The ENA precipitation can cause several consequences: 1) it is a source of hydrogen in the Martian atmosphere, 2) it transfer momentum from the super- and sub-sonic solar wind to the Martian atmosphere, and 3) it is an extra heating source for the Martian upper atmosphere.

In this work we focus on the spatial and energy distribution of ENAs that precipitate to the exobase, using a well-established hybrid plasma model and a well-received exosphere model.

2. Models

We use the HYB_MARS hybrid model [5] to get a self-consistent description of the fields and particles in the solar wind interaction with Mars. The model treats ions as particles and electrons as massless neutralizing fluid, and includes the electron pressure term, a fluid background ionosphere, and charge exchange processes. The latter allows for tracking of ENAs. The model was launched with the nominal solar wind parameters at Mars. The coordinate system is set such that the interplanetary magnetic field is in the xy plane, and the convective electric field (Ec) is in the xz plane, x being the vector from the center of Mars to the Sun.

The exosphere model was adopted from a community-wide model challenge project [1]. It includes both cold and hot components for hydrogen and oxygen exospheres, respectively. In the production of ENAs, the hydrogen exosphere is dominant due to its large scale height and the relatively large resonant charge exchange cross section with protons. The model is spherically symmetric, for the nightside of Mars is not within the scope of this study.

3. ENA precipitation map

We collect the birthplaces and velocity vectors for all ENAs produced in the model. Then we only select those penetrating the exobase, a spherical surface at 200 km altitude above the surface of Mars. We calculate the penetration position of each ENA particle on the exobase, expressed in longitude and latitude in the Mars-centered spherical coordinate system. The resultant precipitation map is achieved by binning the precipitating ENAs according to the penetration location into 6°×6° grid. **Figure 1** is such a map for the ENAs generated in the dayside magnetosheath. We will also plot a similar precipitation map for the ENAs generated upstream of the bow shock.

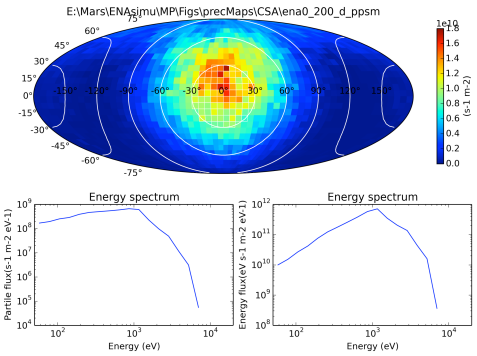

Figure 1: (Top) Particle precipitation map on the exobase of ENAs produced in the magnetosheath. Black numbers are the longitude (horizontally distributed in the middle) and latitude (on the left of the map). White curves are the iso-SZA (solar zenith angle) lines on the exobase. (Bottom) Energy spectrum of (left) precipitating ENAs and (right) precipitating energy within the SZA<30° region (white gridded region in the top panel).

Following aspects will be explored:

1. The role of magnetosheath ENAs. In previous models [3, 4], the ENAs from upstream solar wind is dominant. This is because the plasma model used in these studies did not account for the spread of proton velocity direction in the subsolar point, which was important for the production of ENAs in the magnetosheath. In our model the precipitating flux and energy due to magnetosheath ENAs are comparable to that of the upstream ENAs. Moreover, as shown in **Figure 1**, the precipitation pattern of magnetosheath ENAs is deviated to the +Ec direction

2. The variability of energy deposition rate due to the variability of the hydrogen exosphere. The exobase temperature for atomic hydrogen is the most important controlling factor of the ENA production rate [3]. The exobase temperature affects the scale height and eventually the column density of the hydrogen, and it is highly variable [2]. Particularly, a ~50% difference in the Sun-Mars distance can cause a factor of ~8 difference in the exospheric density of hydrogen. Therefore one may expect that ENA precipitation during the perihelion period would be of more importance compared to the total energy deposition due to solar EUV radiation, which scales with the square of Sun-Mars distance.

References

[1] Brain, D. et al., A comparison of global models for the solar wind interaction with Mars, Icarus, Vol. 206(1), pp. 139-151, 2010.

[2] Chaufray, J.-Y. et al., Variability of the hydrogen in the Martian upper atmosphere as simulated by a 3D atmosphere-exosphere coupling, Icarus, Vol. 245(2015), pp. 282-294, 2015.

[3] Holmström, M., Barabash, S. and Kallio, E., Energetic neutral atoms at Mars 1. Imaging of solar wind protons, J. Geophys. Res., Vol. 107(A10), 10.1029/2001JA000325, 2002.

[4] Kallio, E. and Barabash, S., Atmospheric effects of precipitating energetic hydrogen atoms on the Martian atmosphere, J. Geophys. Res., Vol. 106(A1), pp. 165-177, 10.1029/2000JA002003, 2001.

[5] Kallio, E. et al., Oxygen ion escape at Mars in a hybrid model: High energy and low energy ions, Icarus, Vol. 206(1), pp. 152-163, 2010.

EPSC Abstracts
Vol. 10, EPSC2015-183, 2015
European Planetary Science Congress 2015

Grid Mapping of Hellas Planitia – Preliminary Results from the Northern Impact Rim

M. Voelker (1), E. Hauber (1) S. van Gasselt (2) and R. Jaumann (1,2)
(1) German Aerospace Center (DLR), Rutherfordstr. 2, 12489 Berlin, Germany (martin.voelker@dlr.de); (2) Institute for Planetary Sciences, Freie Universität Berlin, Malteserstr. 74 – 100, 12449 Berlin, Germany

1. Introduction

The Hellas impact basin, located in the southern highlands of Mars, is one of the largest basins and the deepest impact structure on the planet. With a diameter of 2,300 km and a depth of more than 8,000 m it is a melting pot of several diverse geomorphic systems. Today, the basin is enriched with volatiles and ice-cemented materials [1], and its central parts show a scarcity of craters, smooth surfaces, and a high albedo, supporting the assertion of a recently modified and/or active surface. It is likely that the low elevation once accommodated more favorable conditions for volatiles and freeze–thaw cycles than most other areas on the planet. Glacial and fluvial landforms, glacier-like features [2, 3], polygons [4] and fluvial channels [5, 6] have been reported throughout the whole basin. All of them require at least temporary water and/or melting conditions.

2. Methods and Data

We examined the geomorphologic setting of northern Hellas using the planetary grid mapping method developed by [7]. The study area encompasses the entire Hellas floor below an approximate elevation of 5,500 m below the Martian datum. As Hellas is a circular formation located in the mid-latitudes we used a stereographic projection centered at λ=69°, φ=-49°. To be able to compare our results with other grid-mapped regions [7] we use the same grid size of 20 × 20 km and a CTX-based (Context camera [8]) dataset. For creating an exact grid the tool *Repeating Shapes* [9] has been applied. Due to the vast size of the study area, however, we will only analyze every second grid cell in a checkered pattern. This sampling density already produces a representative dataset for preliminary results for some of the mapped landforms. Mapping scale is 1:30,000 and is carried out in an *ArcGIS 10.3* environment. The total number of grid cells being mapped is approx. 10,200. Mapped landforms are: latitude-dependent mantle (LDM), concentric crater fills (CCF), layered sediments, glacier-like features, viscous valley flows, banded terrain, honeycomb terrain, polygons, scalloped terrain, texture, chaos', channels, gullies, fans, fluvial sheet deposits, shorelines, bedrock, and dunes. The presented results are based on 1,500 already analyzed grids, located along the northern margin of the Hellas basin floor.

3. Results

The most important results using grid mapping concern the geospatial distribution of each mapped landform. The majority of the mapped landforms are not very prominent at the northern rim; so there are no representative results available for them by now. However, some relevant inferences can be already made for LDM, CCF, and layered sediments (Fig. 1).

LDM is distributed all over the northern rim and the floor of the basin, although in different roughness (i.e. degradation state) and thickness. The LDM is less prominent on the rim than on the basin floor. Moreover, its thickness decreases towards northeast on both the rim and the basin floor. This observation is consistent with the roughness map of [10], as their map postulates a rougher surface in that area, and thus, a possibly thinner LDM layer. LDM is also a little less dominant along the base of Coronae Scopulus (Fig. 1). The spatial distribution of **CCF** is similar to LDM. It is also less prominent in the NE part of Hellas, and disappears completely in small craters there (<3 km). There are also some small areas to the east and west of Coronae Scopulus lacking CCF's. The third type of major landforms in northern Hellas is represented by (often bright or light-toned) **layered sediments**. These are located along the northern rim and display an elevation range of around -6,400 to -4,500 meters. They occur more often along the NE part of the rim, and at some

scattered places on the NW part. There are also a few outcrops on the floor of the basin, albeit less distinctive. Other less prominent features in northern Hellas are channels (which are mainly located on the rim, and only in very few places on the basin floor), a few gullies, and reticulate terrain (in very small and isolated patches). It is also remarkable that despite of the high atmospheric pressure no large dune fields have been observed.

4. Discussion

Based on visual inspection, the preliminary results for the distribution of LDM show a relatively good correlation with both the dust cover index [11] and roughness map [10], as both of them indicate a lower abundance of dust with a relatively rough (possibly degraded) surface in the NE. While the LDM is very dominant in the SW of the mapped area, it is absent or less distinctive in the east. Moreover, our map shows that the LDM extends further north than predicted by [1, 10]. The reason may be found in different generations of LDM. Madeleine et al. [1] find that the mantling unit in Hellas extends from 40°S poleward, and the roughness map shows a more rugged landscape north of 30°S. Our CTX examinations have shown, however, that the mesoscale surface smoothening caused by LDM extends at least up to 27°S to the north outside of the Hellas basin. A comparison to our preliminary low-resolution mapping of the whole Hellas area has shown, that the LDM surface appears to be significantly rougher in the northern part of Hellas. This roughness could be caused by a higher age or a higher rate of degradation of the LDM in this area; as the more southern LDM (south of 30°S) has been covered by more recent LDM layers (within the last 2 Ma [1]), the rougher LDM (north of 30°S) may originate from an atmospheric dust and ice deposition older than 2 Ma, and could thus have been degraded over a longer time period, without having been covered by a younger LDM again. The thinner and missing LDM cover in the NE of Hellas does not show any sharp margins, so we can exclude a superposition of this unit by other materials. Hence we hypothesize that the rougher LDM in that area is possibly caused by the atmospheric circulation pattern within the basin. As wind currents rotate clockwise in the basin [12], the areas in NE Hellas receive the warmest winds coming from the most northern parts of the basin. This may cause a drier atmosphere and/or a faster sublimation of ice on the ground. This could also explain the lack of CCF's in this part of Hellas.

The spatial distribution of layered sediments seems to depend on the topography, as they are located on the inner slopes of the rim. Their similar elevation may indicate that they could have been formed in the same standing body of water. Future work will show how continuous a possible ring of layered sediments around Hellas is. They are best visible in the NE quadrant where the LDM thickness is low or absent. If they originate from the same body of water, Hellas Planitia must have contained a sea with a depth of up to 4,000 m and a diameter of around 2,700 km.

References

[1] Madeleine J.-B. et al. (2014) GRL 41(14), 4873–4879. [2] van Gasselt S. (2007) Cold-Climate Landforms on Mars, 264 p. [3] Hubbard B. et al. (2011) Icarus 211, 330–346. [4] Diot X. (2014) Planetary and Space Science 101, 118–134. [5] Kostama V.-P. et al. (2008) LPSC 39, #2018. [6] Kostama V.-P. et al. (2010) Earth Planet. Sci. Lett. 294, 321–331. [7] Ramsdale J.D. et al. (2015) LPSC 46, #1339. [8] Malin M.C. et al. (2007) JGR 112, E05S04. [9] Jenness J. (2012) Repeating shapes for ArcGIS. Jenness Enterprises. [10] Kreslavsky M.A. & Head J.W. (2002) GRL 29(15), 1719 pp. [11] Ruff S.W. & Christensen P.R. (2002) JGR 107(E12), 5127. [12] Howard A.D. et al. (2012) LPSC 43, #1105.

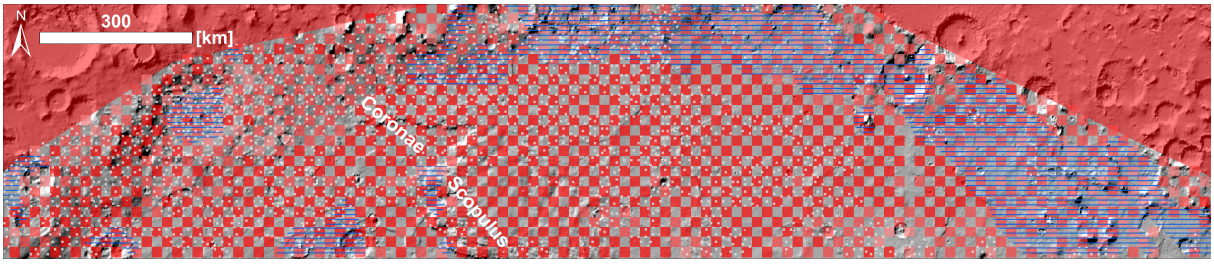

Figure 1: Map showing the northern rim of Hellas. Red squares = LDM (The darker the signature the more distinctive it is); blue crosshatches = layered sediments; grey dots = CCF; solid red areas = not mapped.

EPSC Abstracts
Vol. 10, EPSC2015-188, 2015
European Planetary Science Congress 2015

Dynamics of dust in Dust Devils in the atmospheres of Mars and Earth

Yu.N. Izvekova, S.I Popel
Space Research Institute, Russian Academy of Sciences, Moscow, Russia (e-mail: besedina_yn@mail.ru)
Moscow Institute of Physics and Technology (State University), Dolgoprudnyi, Moscow region, Russia

Abstract

Dust particle dynamics is modeled in the so-called Dust Devils (DDs). We develop methods for the description of dust particle charging in DDs, discuss the ionization processes in DDs, and model charged dust particle motion. Our conclusions are consistent with the fact that DD can lift a big amount of dust from the surface of a planet into its atmosphere.

1. Introduction

DDs are a widespread event in Earth's and Martian atmospheres. DD is a strong, well-formed, and relatively long-lived whirlwind, ranging from small (half a meter wide and a few meters tall) to large (more than 100 meters wide and more than 1000 meters tall) in Earth's atmosphere. Martian DDs can be up to fifty times as wide and ten times as high as terrestrial dust devils. DDs, even small ones, can produce radio noise and electric fields greater than 10^4 V/m. DD picks up small dust particles. As the particles whirl around, they bump and scrape into each other and become electrically charged. Particles of a small size acquire negative charge and large particles become charged positively [1]. In upward flow this leads to spatial charge separation and electric dipole emergence. The whirling charged particles also create a magnetic field. The electric fields assist the vortices in lifting materials off the ground and into the atmosphere. Instability characterizing the DD's generation is described by equations analogous to those for internal gravity waves [2]. Mathematically dynamics of DDs is close to that of toroidal plasmas. Correspondingly, methods developed in magnetic fusion research can be used for modeling the DDs. Strong local vortices are more efficient in lifting dust from the surface into the atmosphere than horizontal winds. Therefore dust devils are supposed to be the main mechanism for dust uplift on Mars [3]. Here, we study dynamics of dust in DDs.

2. Model

DDs are usually observed over the arid regions with a good insolation. Solar heating of the surface results in the formation of unstable stratification, i.e. the layers where the temperature decreases with altitude. In [2] the generation of DDs is shown to be a result of the convective instability of internal gravity waves. The first step is generation of vortex motion in vertical plane. Then toroidal vorticity appears which corresponds to horizontal velocities. Equations describing dynamics of nonlinear vortex structure are as follows [2]

$$\frac{\partial}{\partial t}\left(\tilde{\Delta}\psi+\frac{d\ln\rho_0}{dz}\frac{d\psi}{dz}\right)+\frac{1}{r}J\left\{\psi,\tilde{\Delta}\psi\right\}= =-r\frac{d\chi}{dr}+\frac{r}{\rho_0^2}J\left\{\tilde{\rho},\tilde{p}\right\} \quad (1)$$

$$r\frac{\partial\chi}{\partial t}-\omega_g^2\frac{\partial\psi}{\partial r}+J\left\{\psi,\chi\right\}=0 \quad (2)$$

$$\frac{\partial\omega_z}{\partial t}+u_r\frac{\partial\omega_z}{\partial r}=\omega_z\frac{\partial u_z}{\partial z}, \quad (3)$$

where

$$\tilde{\Delta}=r\frac{\partial}{\partial r}\frac{1}{r}\frac{\partial}{\partial r}+\frac{\partial^2}{\partial z^2}$$

is the Grad-Shafranov operator, ψ is the stream function of poloidal motion, ω_g is the buoyancy frequency, g is the gravity, $J\left\{A,B\right\}$ is Jacobian. The density and the pressure are $\rho=\rho_0+\tilde{\rho}$,

$p = p_0 + \tilde{p}$, correspondingly; the density and pressure disturbances are small $|\tilde{\rho}| << \rho_0$, $|\tilde{p}| << p_0$; $\chi = g\,\tilde{\rho}/\rho_0$ is the normalized density perturbation; ω_z is the toroidal vorticity. The poloidal components of the velocity u_r and u_z are determined by the stream function

$$u_r = -\frac{1}{r}\frac{\partial \psi}{\partial z},\ u_z = \frac{1}{r}\frac{\partial \psi}{\partial r}.$$

Eqs. (1) and (2) describe poloidal motion while Eq. (3) characterizes toroidal motion. Figure 1 shows poloidal stream lines and the dependence of toroidal velocity u_θ on the distance from the vortex axis.

3. Dust dynamics

We have calculated dynamics of dust particles in a modeled DD with taking into account forces of different nature. Figure 2 shows an example of trajectories of dust particle with diameter 50 μm in a vortex with a core radius r_0=10 m and maximum velocity u_{max}=30 m/s.

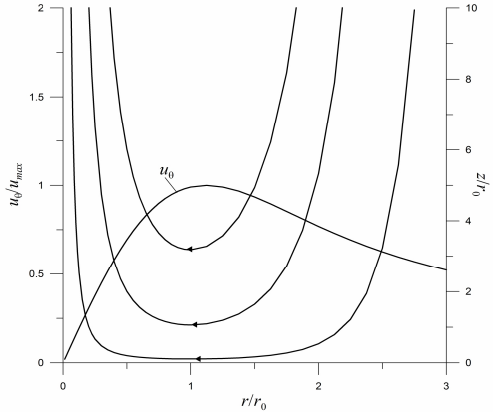

Figure 1: Poloidal stream lines and the dependence of toroidal velocity u_θ on the distance from the vortex axis.

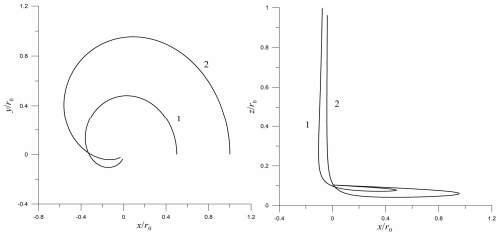

Figure 2: Example of trajectories of dust particle with diameter 50 μm in a typical vortex in Earth's atmosphere.

4. Summary

A model for the description of dust behavior in DDs has been developed. On the basis of the model we have performed calculations and shown that DDs are important mechanism for dust uplift in the atmospheres of Earth and Mars.

Acknowledgements

This work was supported by the Russian Federation Presidential Program for State Support of Young Scientists (project no. MK-6935.2015.2), the Russian Foundation for Basic Research (project no. 14-05-31410 мол_а), and was carried out as part of the Russian Academy of Sciences Presidium program no. 9 "Experimental and Theoretical Research of Objects of the Solar System and Planetary Systems of Stars".

References

[1] Lacks, D. J. and A. Levandowsky, Effect of particle size distribution on the polarity of triboelectric charging in granular insulator systems, J. Electrostatics, 65, 107–112 (2007), doi:10:1016/j.elsat.2006.07.010.

[2] O.G. Onishchenko, W. Horton, O.A. Pokhotelov, L. Stenflo, Dust devil generation, Physica Scripta, 89 (7), 075606, 2014.

[3] Ferri, Francesca, et al. "Dust devils as observed by Mars Pathfinder." Journal of Geophysical Research: Planets (1991–2012) 108.E12 (2003).

EPSC Abstracts
Vol. 10, EPSC2015-200, 2015
European Planetary Science Congress 2015

Small impact craters in crater counting: Examples from the Harmakhis Vallis channel, Mars.

S. Kukkonen and V.-P. Kostama
Astronomy and Space Physics, P. O. Box 3000, FI-90014 University of Oulu, Finland (soile.kukkonen@oulu.fi).

Abstract

Small impact craters are a useful tool for studying recent, short-time or small-scale geologic processes of the surface. Especially in age determination, the role of small impact craters is significant as they may often be the only way to measure the age of the surface. In this work, we compare our crater count results obtained from the Harmakhis Vallis channel floor of Mars based on the CTX and HiRISE images and discuss the benefits and limitations of small (< 1 km in diameter) craters in age determinations.

1. Introduction

The usability of small (diameter < 500 m) impact craters in crater counting has been under discussion since high-resolution images made it possible to extend the crater size-frequency distributions to smaller craters [1–5]. Originally the established method was, however, to leave out the small impact craters from the crater counts due to the uncertainty of their origin (primary or secondary crater). Afterwards, the new crater production studies (e.g. [1, 4–5]) have also made it possible to utilize small craters in age determination if obvious secondary craters and clusters are excluded and the areas showing signs of recent large impact craters are avoided. This has made it possible to expand the crater counts to the small and young units, too.

In this work we present some results of our crater counts performed on Harmakhis Vallis (see also our previous works [6–8]), one of the large outflow channels on the north-eastern Hellas rim region of Mars, based on MRO's CTX and HiRISE datasets. In addition to the evolution studies of the Harmakhis channel, we compare the crater count results based on the different data and thus reveal information on the benefits and limitations of very high-resolution imagery used in age determinations.

2. Data and methods

The age determinations of the Harmakhis Vallis flow units were performed by using established crater count methods (e.g. [9–12]) and the Mars Reconnaissance Orbiter's CTX and HiRISE datasets. The CTX images cover the entire channel system with a resolution of ~ 5 m/pixel whereas the availability of HiRISE imagery is more limited – on the Harmakhis Vallis channel there are only 14 HiRISE image pairs with a resolution of ~ 0.3 – 0.5 m/pixel and many of them focus on the walls of the channels only.

All the image data were imported onto a GIS environment, where the floor units of the Harmakhis channel were mapped and dated. The crater model ages were measured using the Craterstats software.

3. Results and discussion

Mapping on Harmakhis Vallis shows that the channel is almost entirely covered by the flows, the varying texture of which indicates that they are ice-facilitated (see [8]). Because the craters superposed to the flows are relatively small (i.e. the flows are relatively young) and the areas of the units are relatively small, it is necessary to use very high-resolution images for successful dating. In addition, it is acceptable to use very high-resolution images and small craters for dating on Harmakhis Vallis because if the flow units are relatively young, their formation and modification have to mainly postdate the latest secondary-forming impacts. Thus, the superposed craters on the floor units are mainly primaries.

The crater count results, based on the CTX data, show that the oldest measurable cratering model age of the Harmakhis flow units varies from ~ 0.1 Ga to ~ 1 Ga, which may be, however, the youngest limits for the oldest measurable age due to the possible ice-facilitated nature of the flows. In addition, the CTX images show that all the flow units also have 1–3 resurfacing ages. The results of the HiRISE data

instead indicate that although several channel-scale resurfacing processes may have occurred on the channel, their intensity and duration may have varied locally or at least in the HiRISE scale. Figure 1 shows an example of the crater count results from a flow unit at the beginning of the Harmakhis Vallis main channel. A CTX mosaic (Area A in Fig. 1) gives three ages for the unit; a formation age of 75.8 Ma and resurfacing ages of 17 Ma and 6 Ma. Additionally, the first of the two HiRISE images, which also cover parts of the unit, gives three ages for the unit (Area B, Fig. 1) which correlate well with the CTX results (oldest age of 86.9 Ma and resurfacing ages of 10.6 Ma and 5.82 Ma). However, the second HiRISE image (Area C, Fig. 1) shows only two ages which correlate well with the resurfacing ages: 16.3 Ma and 6.57 Ma. We found several possible reasons for this. First, the flow unit, which seems to be homogenous in the CTX scale, may actually consist of several units in the HiRISE scale. On the other hand, the flow unit may be so thin in places that the largest crater populations of older underlying units can be detected. It is also possible that there have been local differences in resurfacing intensities and durations (in this case mainly erosion by wind or sublimation, or the unit down-slope flowing), which have caused the large crater population to be erased in places (in this case the craters with a diameter > ~ 100 m on Area C, but not on Area A or B). A detailed HiRISE scale mapping, the morphology of the large craters and crater distribution studies reveal that the differences in the intensity and duration of the resurfacing events occurred on the region might be the main reason for the differences in the HiRISE results.

4. Conclusions

Small (< 500 m) impact craters are very useful and often also the only way to study the short-time, small-scale or young geologic processes on surfaces. Although the crater count data of the HiRISE images usually correlate quite well with the data of the lower-resolution CTX images, it is good to be careful when only single HiRISE images are used in age determination of larger units. All the results obtained from a specific counting area always represent primarily the results of that area – not the whole unit. Instead, together with the CTX images, the HiRISE images are a very valuable tool for providing unique information about the local surface processes.

Acknowledgements

S.K. is sincerely grateful to Jenny and Antti Wihuri Foundation for funding this study.

References: [1] McEwen A. S. et al., Icarus, 176, 351–381, 2005. [2] Hartmann W. K., Icarus 174, 294–320, 2005. [3] Hartmann W. K., Icarus, 189, 274–278, 2007. [4] Werner S. C. et al., Icarus, 200, pp. 406–417, 2009. [5] Hartmann W. K. and Werner S. C., Earth and Planetary Science Letters, 294, 230-237, 2010. [6] Kukkonen S. et al., LPS XLIV, abstract #2140, 2013. [7] Kukkonen S. et al., EPSC2013, #743, 2013. [8] Kukkonen S. et al., LPI Contrib. 1791, abstract #1218, 2014. [9] CATWG, Icarus, 37, 467-474, 1979. [10] Ivanov B., Space Sci. Rev. 96, 87-104, 2001. [11] Hartmann W. K. and Neukum G., Space Sci. Rev. 96, 165-194, 2001. [12] Michael G. and Neukum G., EPSL, 294, p. 223-229, 2010.

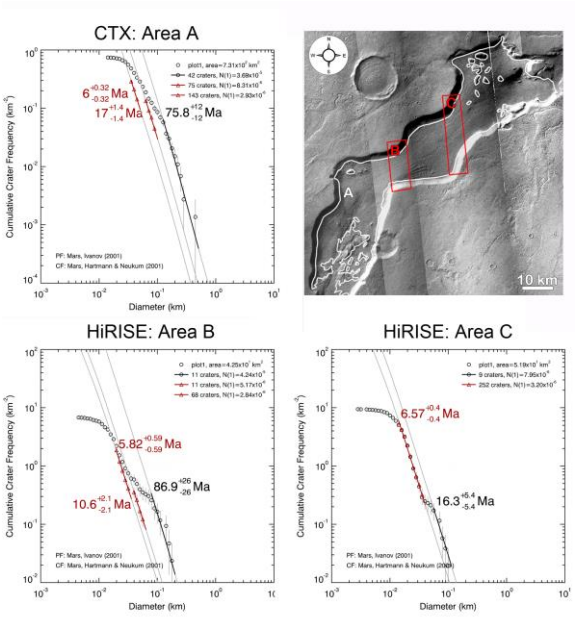

Figure 1: An example of the crater count results of a flow unit from Harmakhis Vallis based on the CTX (area A, outlined by white) and HiRISE images (areas B and C, outlined by red). The crater size-frequency distributions of Area A and B show that the unit has resurfaced twice after the oldest measurable age. The crater size-frequency distribution of Area C, however, shows only these resurfacing ages. The main reason for the lack of a large crater population on Area C might be the differences in the intensity and duration of the resurfacing events compared to the other crater count regions.

EPSC Abstracts
Vol. 10, EPSC2015-210, 2015
European Planetary Science Congress 2015

Photogeologic map of the Hellas basin floor, Mars: Nature, origin, and sequence of major infill units

H. Bernhardt (1), H. Hiesinger (1), M. Ivanov (2), G. Erkeling (1), O. Ruesch (1), D. Reiss (1)
(1) Institut für Planetologie, Westfälische Wilhelms-Universität, Wilhelm-Klemm-Str. 10, 48149 Münster, Germany (h.bernhardt@uni-muenster.de), (2) Vernadsky Institute, Russian Academy of Sciences, Kosygin St. 19, 119991 Moscow, Russia.

Abstract

Based on all state-of-the-art datasets and USGS-mapping guidelines [1,2], we produced a comprehensive photogeological map of the Hellas basin floor and its immediate surroundings (scale 1:2,000,000; Fig. 1). We compiled a self-consistent geologic history of the area, incorporating absolute and relative dating of identified units, as well as insights gained by previous investigations in and around the Hellas basin [e.g., 3-5]. Based on their ages, derived approximate volumes, as well as other characteristics, we suggest potential circum-Hellas source regions for specific basin floor units. Large deposits and erosional units in the basin show ages very similar to those of volcanic units in and around Hellas (~3.7 Ga), which is in agreement with certain volcanic outgassing models enabling liquid water runoff during that time.

1. Wrinkle-ridged plains

Wrinkle-ridged plains (units $Npwr_{1/r}$ and $Hpwr_2$) are exposed on a third of the Hellas basin floor and embay and partially superpose layered sequences along the basin rim. Morphometric analyses of the wrinkle ridges imply an average thickness D of the "wrinkled" layer of ~2 km (D ≈ 0.3 ridge width [6]), and, thus, a combined volume of ~1.7 x 10^6 km³ (~4 x Deccan traps, Earth).

The lower wrinkle-ridged plains ($Npwr_1$) show a crater-size frequency distribution-based apparent model age (AMA) of 3.78-3.82 Ga. Gamma Ray Spectrometer (GRS) data shows higher average K, Th, and Si concentrations than $Hpwr_2$ indicating a formation by "lesser evolved" basalts (i.e., from a not well differentiated mantle relatively rich in incompatible elements [7]). Plausible sources are Malea and Tyrrhena Paterae, which both have AMAs [8-10] and Th-abundances similar to $Npwr_1$. Although Thyrrena Patera is located ~1,500 km away, ancient lava flows have been shown to reach the Hellas basin floor [11].

The upper wrinkle-ridged plains ($Hpwr_2$) have an AMA of 3.63-3.74 Ga. Their spatial extent correlates well with a low-K / low to mid-Th /low to mid-Si area in GRS data indicative of "evolved" basalts derived from an already well-differentiated mantle depleted in incompatible elements [7]. Plausible sources are Hadriaca and Amphitrites Paterae, which both show very similar ages [8,9] and elemental abundances.

2. Interior formation ("Alpheus plateau")

Approximately one fifth of the entire basin floor is covered by highly degraded, hummocky material (mainly units Hih and Hik) superposing the wrinkle ridged plains amongst others. Hih's AMA of 3.67-3.74 Ga overlaps that of the underlying $Hpwr_2$ as well as of other dissected rim units (Hd_M and Hd_P). Numerous, up to ~300 m thick buttes and pedestal crates, likely composed of Hih-material, indicate a once complete coverage of the basin floor, implying a volume of ~1.1 x 10^6 km³. The volume of material removed from Hesperia Planum and the area between it and Hellas Planitia has been suggested to be on the order of 0.5- 1.5 x 10^6 km³ [12], thus being a plausible main source for Hih. Large-scale lava-ice interactions on Hesperia Planum around the AMA of Hih have been suggested as the source of huge amounts of meltwater [13], and might account for the erosion and transport of such a large volume of material. An interpretation of the interior formation containing mafic materials transported from the adjacent volcanic provinces into the Hellas basin by fluvial activity, is also in agreement with the detection of low-Ca pyroxene by OMEGA (southwestern Hih) as well as hydrous minerals by CRISM (northeastern Hih) [7,9,14,15,16].

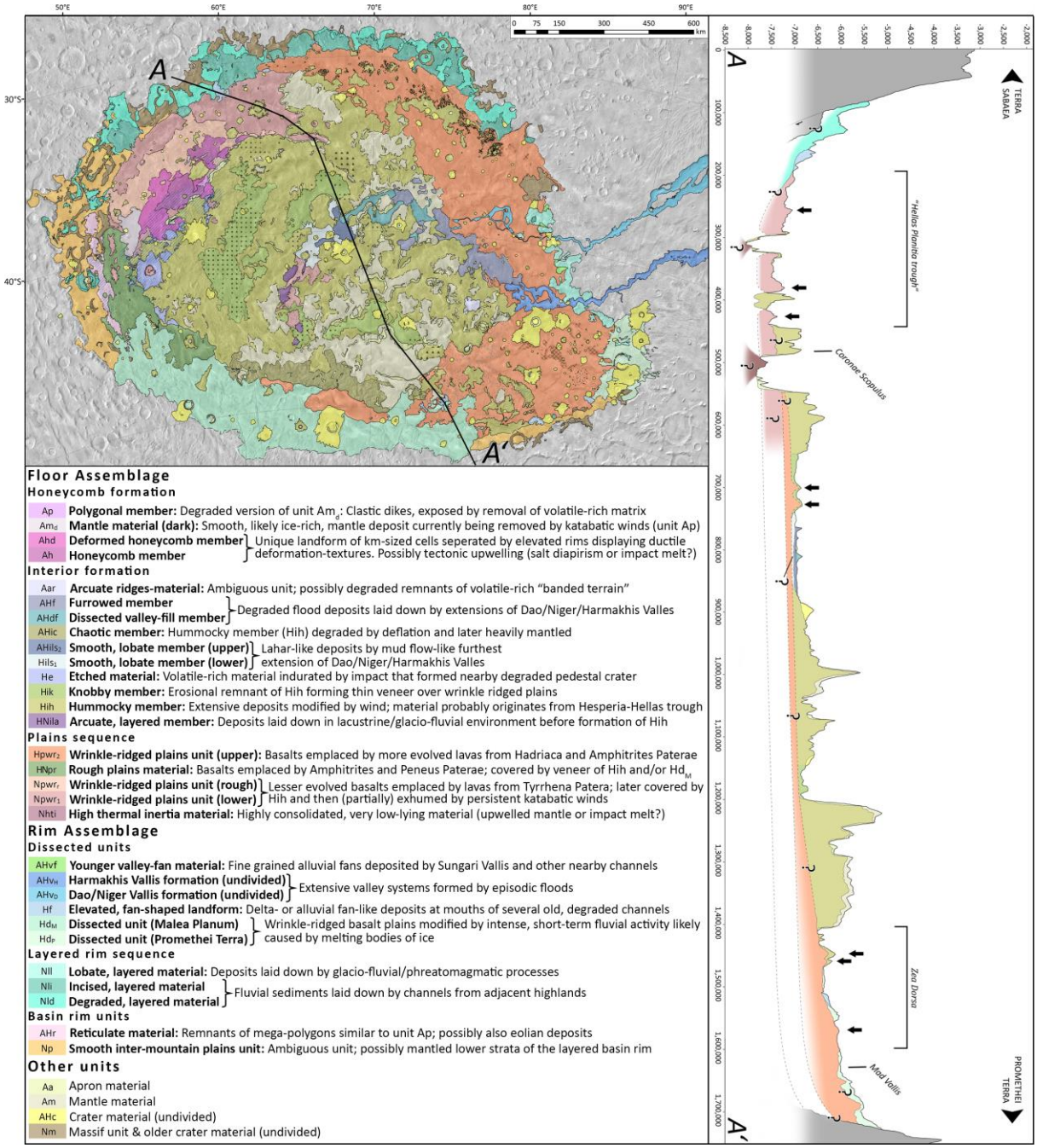

Figure 1: Simplified version of our photogeologic map of the Hellas basin floor (orthographic projection centered at 43°S, 69°E; background: THEMIS-IR Daytime 100 m Global Mosaic version 11.6) with highly condensed interpretations of all units. On the right is a MOLA DTM-based profile illustrating our stratigraphic model of the basin floor (path shown in (A)). Black arrows mark wrinkle ridges. Period extents for units labels based on [17].

References:

[1] Wilhelms, D. E. (1990) Geologic Mapping. In Planetary Mapping (p. 312). [2] Tanaka, K. L. et al. (2009) PSS, 57(5-6), 510–532. [3] Leonard, G. L., & Tanaka, K. L. (2001) *USGS Investigations*, 2694, 80225. [4] Moore, J. M., & Wilhelms, D. E. (2007), *USGS Investigations*, 2953, 80225. [5] Bleamaster, L. F., & Crown, D. A. (2010) *USGS Investigations*, 3096, 80225. [6] N. Mangold et al (1998), *PSS*, 246, 345-356. [7] Engel, A. E. J. et al. (1965) *GSA*, *76*(7), 719. [8] Williams, D. A. et al. (2009) *PSS*, 57(8-9), 895–916. [9] Williams, D. A. et al. (2010) *EPSL*, 294(3-4), 451–465. [10] Williams, D. A. et al. (2010) *EPSL*, 294(3-4), 492–505. [11] Crown, D. A., & Mest, S. C. (2015), *LPSC*, 2122. [12] Ivanov, M. A., et al. (2005), *JGR*, 110(E12), E12S21. [13] Head, J. W., & Cassanelli, J. (2015), *LPSC*, 2250. [14] Bassett, W. A. (1961), *Clays and Clay Minerals*, 10(1), 61–69. [15] Wilson, M. J. (1999), *Clay Minerals*, 34(1), 7–7. [16] Carter, J. et al. (2013), *JGR: Planets*, 118(April), 831–858. [17] Ivanov, B. A. (2001). Sp. Sc. Rev., 96(1-4), 87–104.

EPSC Abstracts
Vol. 10, EPSC2015-213, 2015
European Planetary Science Congress 2015

Science objectives and Expected performances of NOMAD, an ExoMars TGO instrument

Séverine Robert (1), Ann Carine Vandaele (1), Ian Thomas (1), Frank Daerden (1), Cédric Depiesse (1), Rachel Drummond (1), Lori Neary (1), Yannick Willame (1), José Juan Lopez-Moreno (2), Julio Rodriguez-Gomez (2), Manish R. Patel (3), Giancarlo Bellucci (4), and the NOMAD Team
(1) Belgian Institute for Space Aeronomy, Brussels, Belgium (severine.robert@aeronomie.be), (2) Instituto de Astrofisica de Andalucia CSIC, Granada, Spain, (3) Open University, Milton Keynes, UK, (4) Institute for Space Astrophysics and Planetology, Roma, Italy

Abstract

NOMAD, the "Nadir and Occultation for MArs Discovery" spectrometer suite is part of the payload of the 2016 ExoMars Trace Gas Orbiter Mission. This instrument suite will probe the atmosphere of Mars in the infrared, visible and ultraviolet regions covering 0.2 - 0.65 and 2.2 - 4.3 μm. Thanks to its very high spectral resolution and multiple channels and observational modes, NOMAD will be able to detect a wide range of atmospheric trace gases, many of which are important markers of geophysical and/or biogenic activity.

We will present the instrument, its science objectives and the performances we expect based on simulations we have done so far.

1. Introduction

NOMAD is one of four instruments on board the ExoMars Trace Gas Orbiter, scheduled for launch in January 2016 and to begin nominal science mission around Mars in late 2017. It consists of a suite of three high-resolution spectrometers which will generate a huge dataset of Martian atmospheric observations during the mission, across a wide spectral range.

The instrument will be delivered for spacecraft integration during the course of 2015. It is however important to already prepare the planning activities that will begin as soon as the Science Phase starts (expected in November 2017). One important issue is to determine the levels of detection for the different possible targets, and to derive optimal observation parameters (specific spectral interval, integration times, accumulations, etc.). Radiometric models have been developed for the three channels in order to obtain the expected Signal-to-Noise (SNR) ratios.

Detection limits for key species were obtained according to a simple methodology. The best spectral ranges (both in the UV and IR) were studied for each molecule and each observation mode.

2. The NOMAD instrument

NOMAD [2] is composed of 3 channels: a solar occultation only channel (SO) operating in the infrared wavelength domain, a second infrared channel capable of doing nadir, but also solar occultation and limb observations (LNO), and an ultraviolet/visible channel (UVIS) that can work in all observation modes. The spectral resolution of SO and LNO surpasses previous surveys in the infrared by more than one order of magnitude. It offers an integrated instrument combination of a flight-proven concept (SO is a copy of SOIR on Venus Express), and innovations based on existing and proven instrumentation (LNO is also based on SOIR on board Venus Express (VEx) and UVIS has heritage from the ExoMars lander), that will provide mapping and vertical profile information at high spatio-temporal resolution.

3. Science Objectives

An order-of-magnitude increase in spectral resolution over previous instruments will allow NOMAD to map previously unresolvable gas species, such as important trace gases and isotopes. CO, CO_2, H_2O, C_2H_2, C_2H_4, C_2H_6, H_2CO, CH_4, SO_2, H_2S, HCl, O_3 and several isotopologues of methane and water will be detectable, providing crucial measurements of the Martian D/H ratios. It will also be possible to map the sources and sinks of these gases, such as regions of surface volcanism/outgassing and atmospheric pro-

duction, over the course of an entire Martian year, to further constrain atmospheric dynamics and climatology. NOMAD will also continue to monitor the Martian water, carbon, ozone and dust cycles, extending existing datasets made by successive space missions in the past decades, and to derive surface UV radiation levels. Using SO and LNO in combination with UVIS, aerosol properties such as optical depth, composition and size distribution can be derived for atmospheric particles and for distinguishing dust from ice aerosols.

4. Expected Performances

ASIMUT-ALVL, a line-by-line radiative transfer code developed at IASB-BIRA [5], is used to simulate spectra in the 0.7 - 4.5 μm range as would be measured by the instrument and under various atmospheric conditions obtained from the IASB-BIRA GCM, GEM-Mars [1]. Random noise has then been added to the simulated spectra to match the real instrument characteristics of each channel: SNRs have been derived using a model that simulates the real instrument (e.g. transmission properties of optical components, expected in-flight instrument temperatures, detector responsivities, etc.) in [6] for the UV channel and in [4] for the IR channel.

Although the treatment is different for solar occultation and nadir observations, the philosophy to determine the detection limits is the same: simulate a series of spectra with known abundances of the target species, add noise, apply a retrieval method to fit the abundances, compare with the input values. We will detail the procedure for both solar occultation and nadir observations, and for all 3 channels.

5. Summary and Conclusions

We will show that NOMAD will be capable of measuring a long suite of species that are or could be present in the atmosphere of Mars. The solar occultation technique is a very powerful observational method allowing for the retrieval of high spatial vertical profiles of the target molecules from the upper layers of the atmosphere down to the surface or near-surface depending on the loading in dust and particles. The nadir observations will provide maps of a series of constituents that will permit the determination of sources and sinks, as well as put constraints on some surface processes.

The detection limits obtained will be presented at EPSC and published in [3].

Acknowledgements

The NOMAD instrument has been developed under the responsibility of a Belgian principal investigator team (IASB-BIRA, Brussels), assisted by Co-PI teams from Spain (IAA-CSIC, Granada) and the United Kingdom (OU, Milton-Keynes). Associated teams contributing to the design and development of NOMAD were CSL (Liège, Belgium), IAPS (Rome, Italy) and IDR-UPM (Madrid, Spain). We thank all engineering and supporting personnel in these teams for the hard and solid work. Several industrial partners were associated to the abovementioned teams. The industrial efforts were coordinated by a Belgian prime contractor (OIP, Oudenaarde). The UVIS channel has been developed at Lambda-X (Nivelles, Belgium).

NOMAD has been made possible thanks to funding by the Belgian Science Policy Office (BELSPO) and financial and contractual coordination by the ESA Prodex Office. The research was performed as part of the "Interuniversity Attraction Poles" programme financed by the Belgian government (Planet TOPERS).

References

[1] Daerden et al., Geophys. Res. Lett. (submitted), 2015.

[2] E. Neefs, et al. : NOMAD. An Integrated Suite of Three High-Resolution Spectrometers for the Infrared, Visible and Ultraviolet Domain for ESA's ExoMars Mission - Design, Manufacturing and Testing of the Infrared Channels, Applied Optics (submitted), 2015.

[3] S. Robert, et al. : Expected performances of the NOMAD/ExoMars instrument, (in preparation), 2015.

[4] I. Thomas, et al. : Optical and radiometric models of the NOMAD instrument – Part II: The IR channels, SO and LNO, (in preparation), 2015.

[5] A.C. Vandaele, M. Kruglanski and M. De Mazière : Modeling and retrieval of Atmospheric spectra using ASIMUT, Proc. of the First 'Atmospheric Science Conference, ESRIN, Frascati, Italy, 2006.

[6] A.C. Vandaele, et al. : Optical and radiometric models of the NOMAD instrument – Part I: The UVIS channel, (in preparation), 2015.

EPSC Abstracts
Vol. 10, EPSC2015-215, 2015
European Planetary Science Congress 2015

A high resolution study of the Martian water cycle with a global climate model

A. Pottier (1), F. Montmessin (1), F. Forget (2), T. Navarro (2), E. Millour (2), J.-B. Madeleine (2), A. Spiga (2), (1) Laboratoire Atmosphères, Milieux, Observations Spatiales, Guyancourt, France (2) Laboratoire de Météorologie Dynamique, Université Pierre et Marie Curie, Paris, France (alizee.pottier@latmos.ipsl.fr)

Abstract

The martian water cycle's main source is the northern polar cap. Running high resolution models, up to 360° per 180°, help better resolve this ice cap, and better mimic the gradual retreat of the seasonal cap. Atmospheric circulation is also better resolved. Water vapor advection and the subsequent formation of clouds quite differ when we compare these brand new high resolution simulations and the usual lower resolution ones at 64 per 48 grid points.

1. Introduction

On Mars, there is no liquid water in present time, even if geological evidence of it exists. The planet is a cold, dry desert. Yet, there is still a water cycle. Its main source is the northern polar ice cap : the perennial one is indeed mainly composed of water ice which is exposed in summer and fuels the water cycle. Water ice frost was observed during the retreat of the seasonal cap[1] below the dry ice and mixed with it. While a significant part of the atmosphere condenses in winter at the poles, it traps water vapor that can be released in the subsequent warmer season.

The martian global climate model (GCM) used in this study was developed in the LMD laboratory over the course of many years. Radiatively active water ice clouds were recently included, that make the temperature profiles agree more with observations[2]. There is a new microphysical scheme of growth of clouds over dust particles[4]. The model is now able to simulate the observed supersaturation[3]. The northern polar hood now vanishes in summer[5].

2. High resolution model

A set of models was run to unravel new phenomena to be seen with this increased resolution. Standard models are run on a 64 per 48 grid. The new, higher resolution grid is made up of 360 per 180 points. The height levels are the same, 29 ranging from the ground to around 100 km. Runs with and without clouds that are radiatively active were computed, to be able to understand better the physical origin of the observed effects on climate and the water cycle.

3. Results

The advection of the water vapor sublimated from the northern seasonal cap in summer when the polar hood disappears is visibly changed, as can be seen on figure 1.

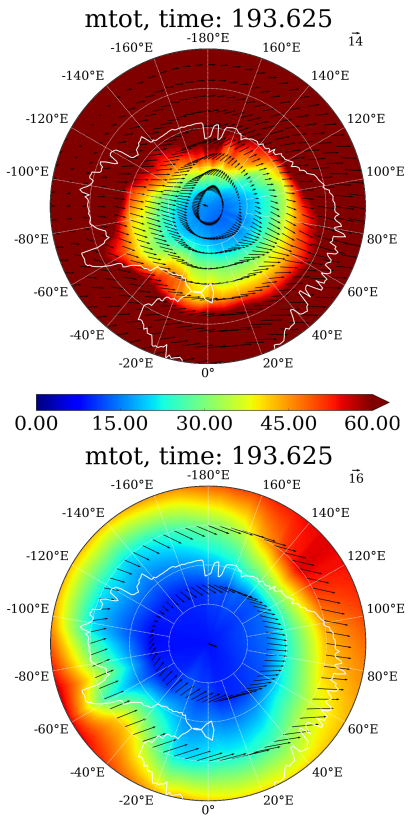

Figure 1: Total vapor column and a sample of wind vectors at 8 km over the north polar cap, summer solstice. Up: high resolution, down: low resolution.

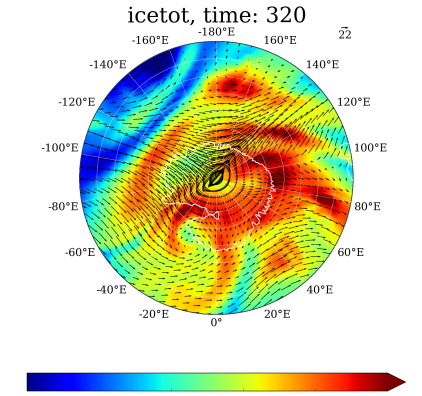

Figure 2: Spiralling clouds, L_s=150°

There are also significant differences in waves in the high resolution runs. The active clouds seem to be one of the triggers of these waves. The study is ongoing.

One effect of the better resolution is interesting spiralling clouds during the dust storm season, or earlier, like on figure 2 which shows cloud column and a sample of the wind vectors for clarity.

4. Validation of a new parametrisation

High resolution model runs can also help validate new parametrisations. An example is the inclusion of a subgrid scale temperature distribution, which allows to compute partial cloudiness in the model.

Rebinning high resolution runs, a cloudiness diagnosis may be made to compare with new parametrisation models. On figure 3, the aphelion cloud belt of clouds at low latitudes (between -10° and 30°) is visible, and partially cloudy at its edge.

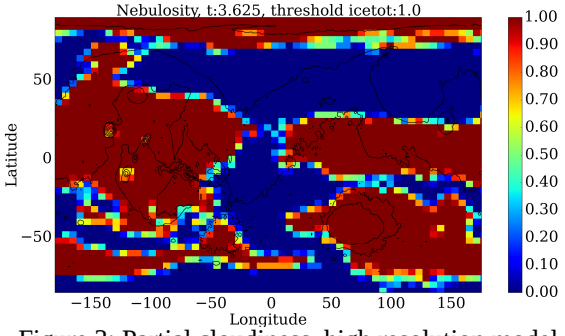

Figure 3: Partial cloudiness, high resolution model, threshold on ice cloud column: 1 pr. µm, L_s=90°

5. Conclusions and perspectives

The study of these high resolution simulations with the LMD GCM helps uncover new dynamical phenomena. These are linked to interesting cloud patterns and even some spiralling clouds. New insights into the fascinating water cycle of the red, desert planet will be allowed. Watching the clouds and advected vapor swirling in high resolution is very interesting and opens new opportunities of study.

The next step will be the improvement of the regolith water adsorption scheme and the frost representation. Combined with the power of high resolution modelling, they might help understand the water cycle of Mars even better.

Acknowledgements

Thanks to René Ernenwein and Jérémy Foulon who provided advice to optimise the model runs on the Mesu supercomputer.

References

[1] Langevin, Y., Poulet, F., Bibring, J.-P., Schmitt B., Douté, S., and Gondet, B.: Summer evolution of the north polar cap of Mars as observed by OMEGA/Mars Express, Science, vol. 307(5715), pp. 1581-4, 2005.

[2] Madeleine, J.-B, Forget, F., Millour, E., Navarro, T., and Spiga, A.: The influence of radiatively active water ice clouds on the Martian climate, *Geophys. Res. Lett.*, *39*, 2012.

[3] Maltagliati, L., Montmessin, F., Fedorova, A., Korablev, O., Forget, F., and Bertaux, J.-L.: Evidence of Water Vapor in Excess of Saturation in the Atmosphere of Mars, Science, 333, 1868-1870, 2011.

[4] Montmessin, F., Rannou, P., and Cabane, M.: New insights into Martian dust distribution and water-ice cloud microphysics, JGR., 107, 2002.

[5] Navarro, T., Madeleine, J.-B., Forget, F., Spiga, A., Millour, E., Montmessin, F., and Määttänen, A.: Global climate modeling of the Martian water cycle with improved microphysics and radiatively active water ice clouds, JGR : Planets, 119, 2014.

EPSC Abstracts
Vol. 10, EPSC2015-216, 2015
European Planetary Science Congress 2015

Ionosphere of Mars as seen by Mars Express. Effect of crustal fields

E. Dubinin (1), M. Fraenz (1), D. Andrews (2), O. Witasse (3) and S. Barabash (4)
(1) Max-Planck-Institute for Solar System Research, Goettingen, Germany (dubinin@mps.mpg.de / Fax: +49-551-384 979 240), (2) Swedish Institute of Space Physics, Uppsala, Sweden, (3) ESA, ESTEC, Nordwijk, Netherlands,(4) Swedish Institute of Space Physics, Kiruna, Sweden.

Abstract

The Martian ionosphere is studied using the local electron number densities and total electron content (TEC) derived from the observations onboard Mars Express. The data are complemented by the ASPERA-3 observations which provide us with the information about upward/downward velocity of the low-energy ions and electron precipitation. We consider 5 years of Mars Express observations at different solar cycle intervals. Different factors which influence the ionosphere dynamics are analyzed. The focus is made on a role of the crustal magnetic field on the Martian ionosphere.

EPSC Abstracts
Vol. 10, EPSC2015-229, 2015
European Planetary Science Congress 2015

Landform assemblage in Isidis Planitia, Mars: Evidence for a 3 Ga old polythermal ice sheet.

Thomas Guidat [a,b], **Stéphane Pochat** [a,b*], Olivier Bourgeois [a,b], Ondřej Souček [c]

[a] Université de Nantes, LPG-Nantes, UMR 6112, 2 rue de la Houssinière, BP 92208, F-44322 Nantes, France

[b] CNRS, LPG-Nantes, UMR 6112, F-44322 Nantes, France

[c] Charles University in Prague, Faculty of Mathematics and Physics, Mathematical Institute, Sokolovská 83, Praha 8 -Karlín, CZ-186 75, Czech Republic

Numerous landforms on Mars suggest that glacial processes played a significant role in the surface evolution of the planet. While several landforms indicate ongoing cold-based glaciation within and beyond the limits of the present-day polar caps, other fossilized landforms suggest that the planet may have been glaciated over the major part of its history and that wet-based glaciers may have been present at some times.

Among the fossilized landforms that may be of glacial origin, a particularly remarkable feature is the so-called Thumbprint Terrain (TT). This distinctive landform assemblage consists of parallel sets of periodic ridges and cones, which exhibit summit depressions and resemble human fingerprints in their overall spatial organization. There is no general agreement on the geological interpretation of the TT however: the interpretations proposed so far include volcanism, mud volcanism and glaciation.

Most occurrences of the TT are located in the Hesperian Northern Lowlands, on the floor of mid-latitude topographic basins such as Utopia Planitia and Arcadia Planitia. However, the largest field of TT identified so far is located near the equator, on the Hesperian floor of Isidis Planitia (Figure 1). We perform a new, comprehensive, mapping initiative of landforms in this impact basin, from both local high-resolution data (CTX and HiRISE optical orbital images at 6 and 0.3 m/pixel respectively) and regional medium-resolution data (THEMIS infrared orbital image mosaics at 100 m/pixel, MOLA gridded elevation data at 300 m/pixel). We describe the individual geomorphic characteristics of the TT and associated landforms, their spatial organization and their mutual relationships.

We found that the T.T. floor of Isidis Planitia are in close association with a peripheral network of Sinuous Ridges, Linear Depressions, and Mounds. This association is equivalent to terrestrial analogues (ribbed moraines, dirt cones, kettle holes, eskers, tunnel valleys and moraine plateaux). We demonstrate that this distinctive assemblage is a glacial landsystem inherited from the presence of a massive polythermal ice sheet over the basin during the Hesperian. The flow of the ice sheet was controlled by its basal thermal regime. Wet-based conditions led to the formation of Arcuate Ridges and Aligned Cones in most parts of the basin, while a negative geothermal anomaly due to impact-related crustal thinning was responsible for cold-based conditions in its central part, where only Isolated Cones and Cones Fields are present (Figure 1). Sinuous Ridges, Linear Depressions and Mounds at the basin margins are interpreted as relicts of a radial network of subglacial channels, which drained the glacial meltwater produced within the interior of the ice sheet across its cold-based periphery (Figure 1).

Acknowledgements

This work benefited from financial support from the OSUNA, CNRS (INSU SYSTER and PICS), .project ERC-CZ Ministry of Education, Youth and Sports of the Czech Republic.

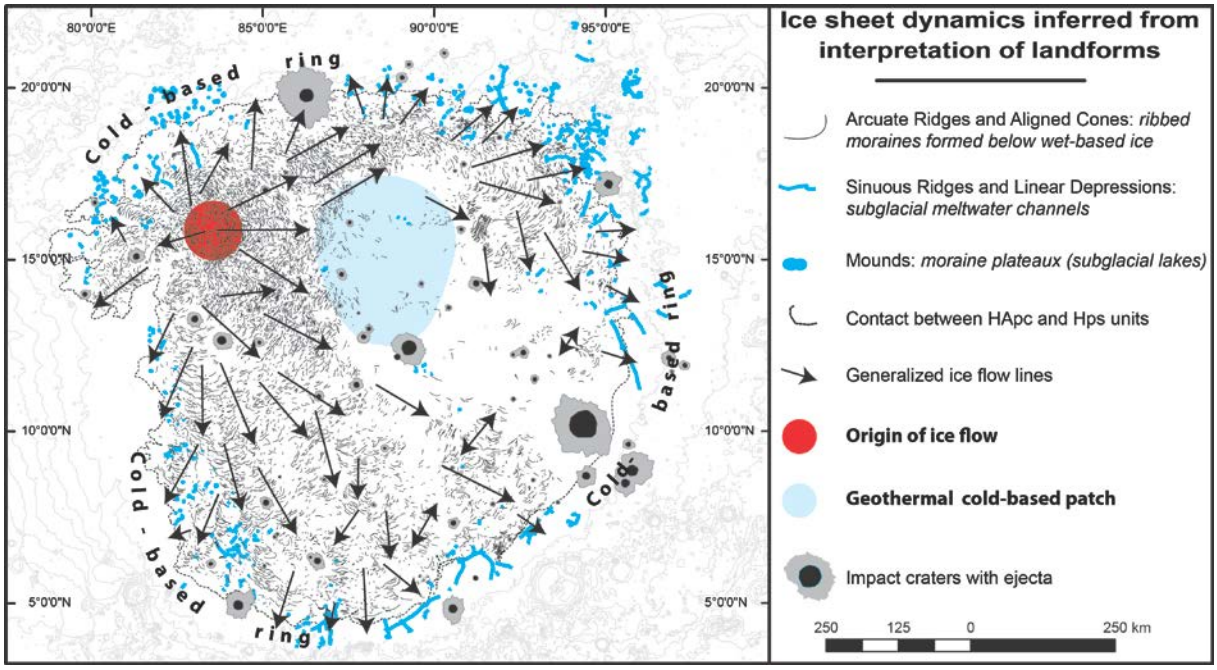

Figure 1: Landform assemblage in Isidis Planitia and reconstitution of ice sheet dynamics.

EPSC Abstracts
Vol. 10, EPSC2015-237, 2015
European Planetary Science Congress 2015

Mapping and formation timescales of Martian valley networks

G. Alemanno (1), V. Orofino (1), G. Di Achille (2), F. Mancarella (1)
(1) Dipartimento di Matematica e Fisica "Ennio De Giorgi", Università del Salento, Lecce, Italy (giulia.alemanno@le.infn.it).
(2) Istituto Nazionale di Astrofisica, Osservatorio Astronomico di Teramo, Italy.

Abstract

To understand the formation mechanisms of Martian fluvial systems we have mapped all the valleys longer than 20 km and for a sample extracted among them, containing the widest and more developed systems, we have also determined the formation time finding values typically in the range 10^5-10^8 years.

1. Introduction

Since the first observation of valley networks on Mars, these systems have aroused great interest [1] because their presence suggests that in the past the planet contained a significant amount of water at the liquid state, that today is totally absent. These valleys show features resulting from the formation due to water surface flow likely supported from rain or snow melting, phenomena now also absent on Mars. This suggests that early Mars could have been warmer and wetter than today with atmospheric pressure and surface temperature different from the present ones [2]. However, detailed geomorphic analysis of individual valley networks did not lead to a general consensus regarding their formation timescales. Therefore from a paleoclimatic point of view is interesting to map Martian valley networks and to determine their formation timescales.

2. Data and methods

In this work we have used QuantumGIS (QGIS), a Geographic Information Software as a tool to create a map of martian valleys and to calculate their area and volume, based on MOLA and THEMIS data. The THEMIS daytime IR imagery, with a resolution of 100 m/pixel, is the highest resolution global dataset for MARS. The MOLA data have a resolution of 463 m/pixel. In some cases we have also used CTX data with a resolution up to about 6 m/pixel.

2.1. Mapping

The valleys have been mapped manually using same criteria as those of Carr (1995) [3] and Hynek et al. (2010) [4]. We searched for sublinear, erosional channels that form branching networks, slightly increasing in size downstream and dividing into smaller branches upslope. The mapped valleys have also been divided into different groups: valley networks (systems highly developed with many tributaries); single valleys (systems with no tributaries or at most with one or two tributaries); longitudinal valleys (structures characterized by a long main branch and few tributaries); valleys on vulcanoes (valley networks and single valleys which are located on vulcanoes). Central coordinates and valleys' total length were included for each valley. The process of manual mapping is subjective and it can be influenced by albedo variations and image quality. Due to geological resurfacing events subsequent to the formation of valley networks, the observed geographic distribution is likely an underestimation of the original distribution and partly represents the overprinting effects of later geological history. For example, it is increasingly difficult to recognize valley networks drainage patterns at the higher latitudes of the southern hemisphere (south of 30°S) due to the effects of recent mantling and terrain softening [5], [6], [7].

2.2. Formation timescales

To understand the formation mechanisms of these fluvial systems and consequently make assumptions on the ancient climatic conditions of the planet, we have determined the formation time of a sample of Martian valleys, among them: Ma'adim Vallis, Warrego Valles and other important valley networks located in Arabia Terra, Meridiani Planum and Terra Sabea. To estimate the duration of water flow in these valleys we have used a method never used before for Martian valleys and based on the evaluation of erosion rate of the terrain. The latter is a key parameter for calculating the timescale of valleys formation and depends on a large

number of factors such as the size of the river, the nature of the load, the speed of the current, the gradient of the fluvial valley and finally the climatic and environmental conditions. In the present work the erosion rate has been evaluated using data obtained on Earth and extrapolated to the Martian case assuming different possible situations.

3. Results and discussion

More than 50% of Martian surface have been mapped. Thus far, the use of 100 m/pixel global mosaic allowed us to identify more developed valley systems with respect to previous studies based on the 200 m/pixel mosaic. Moreover, the obtained results for the formation timescales range from 10^5 to 10^8 years (depending on erosion rate) and are in good agreement with those reported in literature and obtained through more detailed models of sediment transport [8]. These results imply that Mars experienced at least short periods of clement conditions toward the end of the Noachian Era that supported a hydrologic cycle and potentially a biosphere.

References

[1] Masursky H.: 1973, Jou. Geophys. Res., **78**, 4009.

[2] CraddockR.A., Howard A.D.: 2002, Jou. Geophys. Res., **107**, doi:10.1029/2001JE001505.

[3] Carr M.H.: 1995, Jou. Geophys. Res., **100**, doi:10.1029/95JE00260.

[4] Hynek B.M., Hoke M.R.T., Beach M.: 2010, Jou. Geophys. Res., **115**, doi:10.1029/2009JE003548.

[5] Kreslavsky, M.A., Head, J.W.: 2000,Jou. Geophys. Res., **105**, 26695.

[6] Mustard, J.F., Cooper, C.D., Rifkin, M.K.: 2001, Nature, **412**, 4111.

[7] Squyres, S.W., Carr, M.H., 1986, Science, **231**, 249.

[8] Hoke M.R.T., Hynek B.M., Tucker G.E.: 2011, Earth Planet. Sci. Lett., **312**, doi:10.1016/j.eps1.2011.09.053.

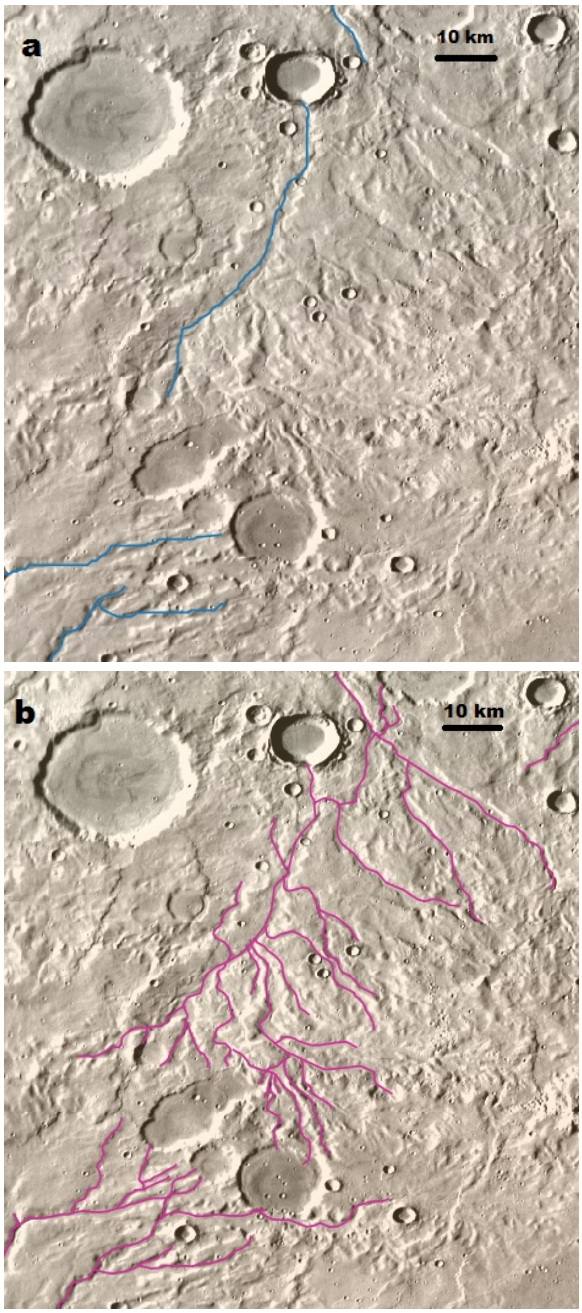

Figure 1: Comparison between valleys mapped by Hynek et al.(2010) [4] from THEMIS data with a resolution of 200 m/pixel (a) and those identifiable from THEMIS data at 100 m/pixel (b). The area is centered around 32 °S, 162°E.

EPSC Abstracts
Vol. 10, EPSC2015-247, 2015
European Planetary Science Congress 2015

Binding of methane to activated mineral surfaces – a methane sink on Mars?

S. J. Knak Jensen (1), J. Skibsted (1), H. J. Jakobsen (1), I. L. ten Kate (2), H. P. Gunnlaugsson (3), J. P. Merrison (4), K. Finster (5), Ebbe Bak (5), J. J. Iversen (4), J. C. Kondrup (1), **P. Nørnberg** (5)
(1) Instrument Center for Solid-State NMR Spectroscopy, Department of Chemistry, Center (iNANO), Aarhus University. Denmark, (2) Department of Earth Sciences, Utrecht University, The Netherlands. (3) CERN, PH Div, CH-1211 Geneve 23, Switzerland and KU-Leuven, Instituut voor Kern- en Stralingsfysica, Celestijnenlaan 200d, B-3001 Leuven, Belgium (4) Department of Physics and Aarhus University, Denmark. (5) Department of Bioscience, Aarhus University, Denmark.

Abstract

Tumbling experiments that simulate the wind erosion of quartz grains in an atmosphere of ^{13}C-enriched methane are reported. The eroded grains are analyzed by ^{13}C and ^{29}Si solid-state NMR techniques after several months of tumbling. The analysis shows that methane has reacted with the eroded surface to form covalent Si–CH_3 bonds, which stay intact for temperatures up to at least 250º C. These findings offer a model for a methane sink that might explain the fast disappearance of methane on Mars.

1. Introduction

Recently methane (CH_4) has been observed in the Martian atmosphere from a satellite orbiting the planet [1] as well as from Earth based telescopes [2]. A significant feature of methane concentrations is that they show a substantial time and spatial variation. Detailed snapshots measurements by MSL have shown that the concentration of methane is very low, i.e., 0.18 ± 0.67 ppbv and considered unlikely related to microbial activity [3]. However, the most recent results from Curiosity at Gale crater (7.2 ± 2.1 ppbv) indicate episodically methane production [4]. To reconcile these findings a fast destruction mechanism is required. Here we show, using solid-state ^{13}C and ^{29}Si magic-angle spinning NMR spectroscopies, that wind driven erosion produces highly reactive sites on mineral grain surfaces that sequester methane by forming covalent bonds with methyl groups and propose that this mechanism can be the hitherto undiscovered methane sink on Mars [5].

2. Materials and Methods

The wind driven erosion of surface material is simulated using the specially designed apparatus depicted in Fig. 1. Commercially available quartz (Merck, 1.07536) was chosen as an analogue for surface material because of its simple chemical composition. The quartz was placed in a borosilicate flask with ^{13}C-methane (Sigma-Aldrich, 490229, 99% enriched) to facilitate NMR investigations.

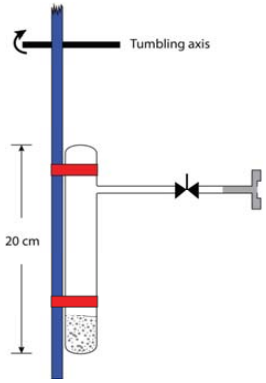

Figure 1: Schematic drawing of the tumbling apparatus.

3. Results and discussion

The reaction of ^{13}C-enriched methane with surface sites of highly active quartz particles is unambiguously demonstrated by the ^{13}C{^{1}H} CP/MAS and ^{29}Si{^{1}H} CP/MAS NMR spectra, of which the latter spectra are shown in Fig. 2. In these spectra the cross-polarization (CP) NMR technique transfers ^{1}H magnetization to either the ^{13}C or ^{29}Si spins via heteronuclear dipolar couplings and thereby acts as a filter for detecting only ^{13}C and ^{29}Si spin nuclei within a distance less than 3-5 Å to nearby ^{1}H nuclei. An un-tumbled quartz/methane flask was stored and used as a control for the activation effect.

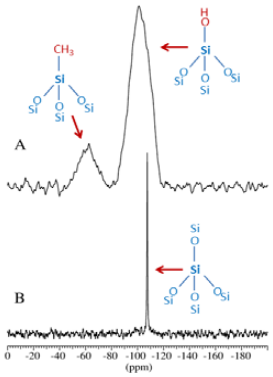

Figure 2: ^{29}Si MAS and CP/MAS NMR spectra

The standard one-pulse ^{29}Si MAS NMR spectrum of the methane-quartz sample in Fig. 2B exhibits a narrow resonance (FWHM = 0.11 ppm) at $\delta(^{29}Si) = -107.5$ ppm, i.e., the well-known ^{29}Si chemical shift for α-quartz [6] and [7], and thus is assigned to the bulk SiO_2 structure of the sample. More importantly, the ^{29}Si surface sites of the sample are selectively detected in the $^{29}Si\{^1H\}$ CP/MAS NMR spectrum (Fig. 2A), which reveals two broadened resonances at –61 and –101 ppm. The high-intensity resonance at –101 ppm originates from ^{29}Si sites associated with hydroxyl groups, following earlier ^{29}Si CP/MAS NMR studies of silica gels. More importantly, only this resonance at –101 ppm is observed in a similar spectrum of pure quartz exposed to tumbling in ambient air under the same conditions as used for the $SiO_2/^{13}CH_4$ sample. Most interestingly, from previous investigations of modified silica surfaces, HPLC materials, and heterogeneous catalysts [8] and [9] it is known that methyl groups directly bonded to a Si atom on a silica surface give ^{29}Si resonances in distinct regions of the ^{29}Si chemical shift scale according to the number of attached methyl groups. For example, for a $(CH_3)_2Si(OSi)_2$ species: $\delta(^{29}Si) = -14$ to -20 ppm, while for $CH_3Si(OSi)_3$ species: $\delta(^{29}Si) = -53$ to -65 ppm. Thus, the observed resonance at –61 ppm can be assigned to a $(SiO)_3Si–CH_3$ site. This result and the absence of the resonance at –61 ppm for the tumbled sample of pure quartz present an unambiguous and direct proof that agitation of quartz in a methane atmosphere results in a methyl group being directly bonded to a Si atom.

In addition to the $SiO_2/^{13}CH_4$ experiments we also tumbled a sample of olivine (from the Spanish island of Lanzarote) in ordinary CH_4 (with an isotope distribution of about $^{12}C = 99$ % and $^{13}C = 1$ %). The rate of pressure change for olivine is lower than that for quartz, but not more than a factor of two.

4. Summary and Conclusions

Our laboratory studies show that a wind mediated erosion process of ordinary quartz crystals can produce activated quartz grains, which sequester methane by forming covalent Si-C bonds. If this process is operational on Mars, which our recent preliminary studies on olivine indicate could be the case then it can explain the observed fast destruction of methane.

Acknowledgements

This research was supported by Villum Kann Rasmussen Foundation, the Danish National Research Council, the Danish Council for Independent Research, Natural Sciences and the Carlsberg Foundation. The authors wish to thank Dr. Morten Bo Madsen, University of Copenhagen, for useful discussions.

References

[1] Formisano, V. et al.: Science 2004, 306, 1758-1761.

[2] Krasnopolsky, V. et al.: Icarus 2004, 172, 537-547.

[3] Webster, C.R. et al.: Science 2013, 342, 355–356.

[4] Webster, C.R. et al.: Science 2015, 347, 415-417.

[5] Jensen, S.K.J. et al.: Icarus 2014, 236, 24-27.

[6] Lippmaa, E. et al.: J. Am. Chem. Soc. 1980, 102, 4889-4893.

[7] Smith, J.V. and Blackwell, C.S.: Nature 1983, 303, 223-225.

[8] Albert, K. and Bayer, E. J.: Chromatogr. 1991, 544, 345-370.

[9] Kellberg, L. et al.: J. Catal. 1993, 143, 45-51.

EPSC Abstracts
Vol. 10, EPSC2015-249, 2015
European Planetary Science Congress 2015

High altitude plumes at Mars morning terminator

A. Sánchez-Lavega (1,2), A. García Muñoz (3), E. García-Melendo (1,4), S. Pérez-Hoyos (1-2), J. M. Gómez-Forrellad (4), C. Pellier (5), M. Delcroix (5), M. A. López-Valverde (6,2), F. González-Galindo (2,6), W. Jaeschke (7), D. Parker (8)*, J. Phillips (9), and D. Peach (10).

(1) Departamento de Física Aplicada I, E.T.S. Ingeniería, Universidad del País Vasco, Alameda Urquijo s/n, 48013Bilbao, Spain. (agustin.sanchez@ehu.eus / Fax: +34-946014178)
(2) Unidad Asociada Grupo Ciencias Planetarias UPV/EHU- IAA (CSIC), Spain.
(3) European Space Agency, ESTEC, 2201 AZ Noordwijk, The Netherlands.
(4) Fundació Observatori Esteve Duran, Montseny 46, 08553 Seva (Barcelona), Spain.
(5) Commission des observations planétaires, Société Astronomique de France, France.
(6) Instituto de Astrofísica de Andalucía, CSIC, Granada, Spain.
(7) Association of Lunar and Planetary Observers, West Chester, Pennsylvania, USA.
(8) Association of Lunar and Planetary Observers, Cayo Largo, Florida, USA
* Deceased, 22 Feb. 2015.
(9) Association of Lunar and Planetary Observers, Charleston, SC 29401, USA.
(10) British Astronomical Association, Burlington House, Piccadilly, London W1J 0DU. UK.

Abstract

In March and April 2012 two extremely high altitude plumes were observed at the Martian terminator reaching 200 - 250 km or more above the surface [1]. They were located at about 195º West longitude and 45º South latitude (at Terra Cimmeria) and extended ~ 500 – 1,000 km in both North-South and East-West, and lasted for about 10 days. Both plumes exhibited day-to-day variability, and were seen at the morning terminator but not at the evening limb. Another large plume was captured on Hubble Space Telescope images in May 1997 at 99º West longitude and 3º South latitude, but its altitude cannot be precisely determined. Broad-band photometry was performed of both events in the spectral range 255 nm – 1052 nm. Based on the observed properties, we discuss different possible scenarios for the mechanism responsible for the formation of these plumes.

1. Mars terminator plumes

The Martian thin, cold and dusty atmosphere allows condensed clouds to form at ~ 100 km and surface dust to reach ~ 50 km altitudes [2, 3]. In 2012 a high altitude Martian plume was imaged for the first time on March 12 using telescopes with apertures 25-40 cm diameter and CCD cameras working in the "lucky imaging" mode [1]. Its emergence and evolution at terminator was tracked by 19 independent observers between 12 and 23 de March at Terra Cimmeria showing great variability (Figures 1 and 2). A second plume was observed between 6 and 16 April showing properties similar to the previous event. These events occurred in early winter in the southern hemisphere at a solar longitude Ls = 85-90º.

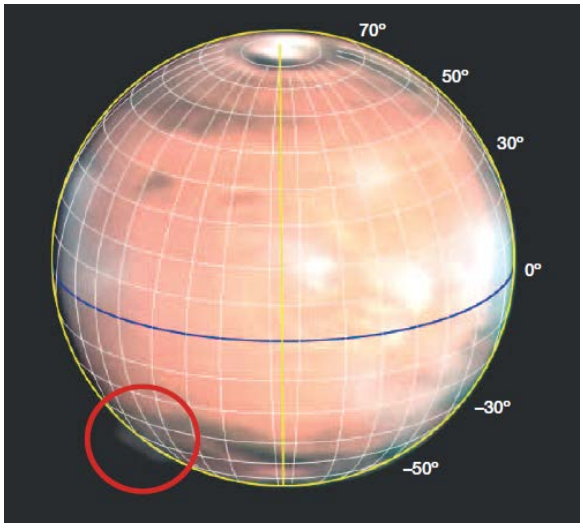

Figure 1: Mars plume location at terminator on 21 March 2012 (image by D. Parker).

The second limb protrusion we report here was observed in a single broad-band image series obtained Wide Field Planetary Camera onboard the Hubble Space Telescope at Ls = 119º (Figure 3). Its horizontal extent was similar to the 2012 events.

The 2012 March and April plumes were observed at different times rotating from the night side into view, allowing determination of its top altitude located between ~ 200 and 250 km from the surface, much higher than previously reported clouds [1].

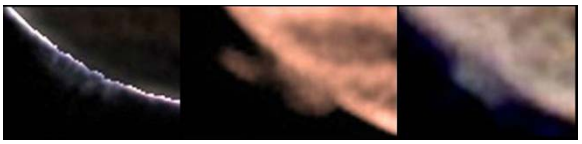

Figure 2: Morphology changes on the Martian plume on 21 March 2012 (from left to right images by W. Jaeschke, D. Parker, J. Phillips).

The 1997 event was above 50 km but its top altitude cannot be determined because of the lack of a rotating sequence.

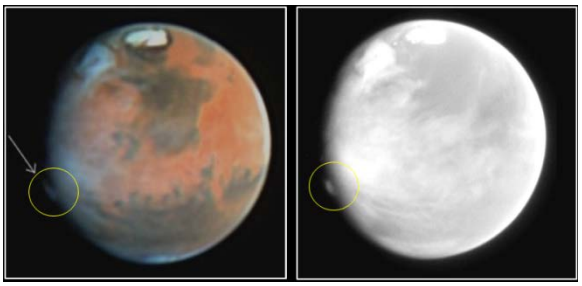

Figure 3: A Martian plume observed on 17 May 1997 using HST (left color composite, right ultraviolet filter).

2. Analysis and discussion

The measured plumes reflectivity curves for both 1997 and 2012 events have been used to perform a radiative transfer analysis of the solar reflected radiation at terminator by a volume a spherical particles. The model assumes three possible plume composition: icy condensates of CO_2 and H_2O, and Martian dust. Only for small icy condensates of 0.1 μm in radii and densities 0.01 particles per cm^3 the model fits the observations. Under such scenario and for the 2012 plumes, using the vertical temperature profiles provided by a GCM at Terra Cimmeria and for the epoch of the year [4,5], water icy condensation is favored [1]. In such a case, rapid particle transport by the intense winds predicted by the GCM should be involved.

Alternatively, since the Cimmeria region shows a crustal magnetic anomaly, the plume could be the result of an emission aurora phenomenon. However the observed emission intensity would be so high that this explanation is highly unlikely. We finally comment on other possible mechanisms .

Acknowledgements

This work has been supported by research grants AYA2012-36666, Grupos Gobierno Vasco IT765-13 y UPV/EHU UFI11/55. The IAA (CSIC) team was supported by MINECO with projects CONSOLIDER ASTROMOL CSD2009-00038 and AYA2011-30613-CO2-1. F.G.-G. acknowledges support by CSIC JAE-Doc. All grants supported with European FEDER funds.

References

[1] Sanchez-Lavega A. et al., An extremely high-altitude plume seen at Mars' morning terminator. *Nature* 518, 525-528 (2015).

[2] Mättänen, A. et al., A complete climatology of the aerosol vertical distribution on Mars from MEx/SPICAM UV solar occultations. *Icarus* 223, 892–941 (2013).

[3] Heavens, N. G. et al. The vertical distribution of dust in the Martian atmosphere during northern spring and summer: observations by the Mars Climate Sounder and analysis of zonal average vertical dust profiles. *J. Geophys. Res. Planets* 116, E04003 (2011).

[4] Gonzalez-Galindo F., Määttänen A., Forget F. & Spiga A. The Martian mesosphere as revealed by CO_2 cloud observations and General Circulation Modeling, *Icarus*, **216**, 10-22 (2011)

[5] González-Galindo F. *et al.* Three-dimensional Martian ionosphere model: I. The photochemical ionosphere below 180 km, *J. Geophys. Res.*, **118**, 2105-2123 (2013)

EPSC Abstracts
Vol. 10, EPSC2015-254, 2015
European Planetary Science Congress 2015

The role of sublimation and condensation on the development of ice sedimentation waves on the North Polar Cap of Mars

C. Herny (1), S. Carpy (1), O. Bourgeois (1), M. Massé (1), A. Spiga (2), S. Le Mouélic (1), L. Perret (3), I.B. Smith (4), S. Rodriguez (5)
(1) Laboratoire de Planétologie et de Géodynamique de Nantes, Nantes, France, (2) Laboratoire de Météorologie et de Dynamique, Paris, France, (3) Laboratoire de Recherche en Hydrodynamique, Energétique et Environnement Atmosphérique, Nantes, France, (4) Southwest Research Institute, Boulder, Colorado, USA, (5) CEA-Saclay, DSM/IRFU/Service d'Astrophysique, Gif/Yvette, France (clemence.herny@univ-nantes.fr)

Abstract

Mass and energy balance of ice sheets are driven by complex interactions between the atmosphere and the cryosphere. For instance, it has been demonstrated that feedbacks between katabatic winds and the cryosphere lead to the formation of sedimentation waves at the surface of Martian and terrestrial ice sheets [1, 2, 3 and 4]. Here we explore the role of sublimation and condensation of water vapor in the development of these sedimentation waves. We conduct this study by complementary observational and numerical investigations on the North Polar Cap of Mars.

1. Ice sedimentation waves on Mars

Spectacular fields of ice sedimentation waves occur on the Gemina Lingula lobe of the North Polar Cap of Mars. These waves are 10 km in wavelength and about 20 m in amplitude. Their downwind slopes are generally steeper than their upwind slopes and their crests develop at high angles to the katabatic wind streamlines. Investigations of complementary data sets reveal that these sedimentation waves grow and migrate upwind in response to the development of an asymmetric ice accumulation pattern [1 and 4]. Their shallow-dipping upwind sides, their tops and the intervening troughs are covered by young fine-grained ice and occasional longitudinal ridges, indicative of net accumulation. On the other hand, their steep-dipping downwind sides expose smooth surfaces of coarse-grained ice, indicative of reduced net accumulation associated with metamorphism.

2. Physical processes at the surface of the North Polar Cap of Mars

The Martian atmosphere is thin (7 mbar), cold (220 K) and dry (< 80 µm-pr) [5]. These extreme climatic conditions set up a water cycle that is controlled by change of state between ice and water vapor. The North Polar Cap of Mars experiences a permanent katabatic wind regime [6] and periods of accumulation by condensation (autumn and winter) alternate with periods of ablation by sublimation (spring and summer). Ice redistribution at the surface of the North Polar Cap is therefore driven by the interaction of winds and sublimation/condensation of water vapor [2, 3 and 4].

3. Model of mass transfer on a wavy surface

We designed a numerical model to explore the coupled interaction between the mass transfer of water vapor and a steady unidirectional flow on a wavy surface. The mass transfer of water vapor is computed by an equation of transport-diffusion and the flow by Navier-Stokes equations [7]. The model solves the water vapor content as a function of the Martian solar longitude and therefore as a function of surface and atmosphere temperatures. We set as input data a logarithmic boundary layer profile tuned with atmospheric models [6]. We impose at the ice surface the saturation pressure of water vapor and let evolve the water vapor profile in the resolution domain. The model was validated with different benchmarks and applied to flat and wavy surfaces on Mars.

4. Results

At the North Polar Cap temperatures, the rate of water vapor mass transfer increases with the wind speed. Above wavy surfaces, the maximum of water vapor flux coincides with the maximum shear stress, located on the upwind sides of the waves. On the downwind sides, mass transfer rates are smaller. These results are the same for sublimation (ablation) and condensation (accumulation). During a given simulation, the ice waves do not experience simultaneous accumulation and ablation as it would be the case, for instance, for aeolian sand dunes. These results mean that if the accumulation rate is greater than the ablation rate the waves will migrate upwind by redistribution of ice by sublimation and condensation of water vapor.

5. Conclusion

Our observations and simulations are in accordance with the hypothesis that the sedimentation waves could migrate upwind due to enhanced accumulation on their upwind sides and reduced accumulation on their downwind sides over a Martian year (Figure 1). Our model shows that the dynamics of these patterns result from the interaction between the fluid flow and the wavy icy surface trough mass transfer. The initiation of the sedimentation waves is probably due to oscillations in the lower atmosphere.

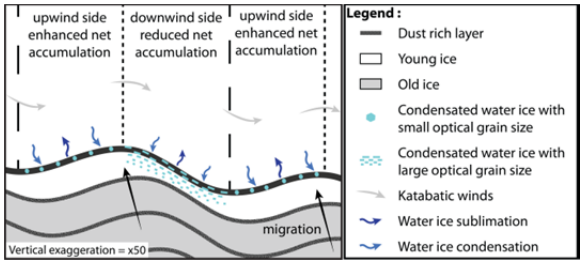

Figure 1: Interpretative cross-section of a part of Gemina Lingula, illustrating the surface topography, the internal stratigraphy and the physical processes involved in the dynamics of the ice sedimentation waves over a year.

Acknowledgements

This work benefited from financial supports from the Center National de la Recherche Scientifique (CNRS), Centre National d'Études Spatiales, Institut National des Sciences de l'Univers (INSU), Programme National de Planétologie (PNP), Agence Nationale de la Recherche (Project ANR-12-BS05-001 EXODUNES), ATLAB project from the European program RegPot and the Fundation for Polish Science project (FNP) TEAM/2011-7/9. C. Herny is supported by a Ph.D. research grant from the French government (Ministère de l'Enseignement Supérieur et de la Recherche).

References

[1] Frezzotti, M., Gandolfi, M., and Urbini, S.: Snow megadunes in Antarctica: sedimentary structure and genesis, Journal of Geophysical Research, 107 (D18), pp. 4344, 2000.

[2] Howard, A.D.: The role of eolian processes in forming surface features of the Martian Polar Layered Deposits, Icarus, 144 (2), pp. 267-288, 2000.

[3] Smith, I.B., Holt, J.W., Spiga, A., Howard, A.D., and Parker, G..: The spiral troughs of Mars as cyclic steps, Journal of Geophysical Research (Planets), 118 (9), pp. 1835-1857, 2013.

[4] Herny, C., Massé, M, Bourgeois, O, Carpy, S., LeMouélic, S., Appéré, T., Smith, I.B., Spiga, A., and Rodriguez, S.: Sedimentation waves on the Martian North Polar Cap: Analogy with megadunes in Antarctica, Earth and Planetary Sciences Letters, Vol 403, pp. 56-66, 2014.

[5] Pankine, A.A., Tamppari, L.K., and Smith, M.D.: MGS TES obersvation of water vapor above the seasonal and perennial cap during northern spring and summer, Icarus, 210 (1), pp. 5871, 2010.

[6] Spiga, A.: Elements of comparison between Martian and terrestrial mesoscale meteorological phenomena: katabatic winds and boundary layer convection. Planetary Space Science, 59 (10), pp. 915–922, 2011.

[7] Farahani, R., and Lange, C.F.: Method for calculating near surface water vapor flux under local winds on Mars, Planetary and Space Science, 73, pp. 271–282, 2012.

EPSC Abstracts
Vol. 10, EPSC2015-258, 2015
European Planetary Science Congress 2015

MARLI: MARs LIdar for global wind profiles from orbit

J. B. Abshire (1), M. D. Smith (1), H. Riris (1), X. Sun (1), B. M. Gentry (1), A. Yu (2), G. R. Allan (3)

NASA Goddard Space Flight Center, Greenbelt MD 20771 USA
James.B.Abshire@nasa.gov
(1) – Science and Exploration Directorate, (2) Lasers and Electro-Optics Branch,
(3) Sigma Space Corporation, Code 694, Greenbelt Md 20771 USA

Abstract

We are developing a multifunctional atmospheric lidar (MARLI) for Mars orbit. The lidar approach is to simultaneously measure atmospheric backscatter and depolarization profiles, wind profiles, and range from a near-polar circular orbit. These measurements address high priority needs for Mars as summarized in NASA's 2011 Planetary Decadal Survey.

1. Introduction

Although considerable progress has been made, knowledge of the present Mars atmosphere is limited by a lack of observations in several key areas including diurnal variations of aerosols and direct measurements of wind velocity. Both dust and water ice aerosols are pervasive in the Mars atmosphere. Dust interacts strongly with IR radiation causing large changes in the thermal structure and acting as a driver of atmospheric motions at all spatial scales. Water ice clouds play an important role in the water cycle altering the global transport of water vapor. The limited local time coverage of observations to date has shown large changes in the amount and vertical distribution of dust and ice aerosols and water vapor. However, existing observations do not allow the vertical distribution of the dust aerosols and ice to be characterized over the full diurnal cycle.

Winds on Mars play a fundamental role in climate and weather, yet basic questions still remain about the 3-D wind structure and how it changes with local time, location, and season. The winds transport water vapor, dust and ice aerosols, and mix all gaseous constituents. Winds are a primary player in all surface-atmosphere interactions. Wind velocities provide sensitive input and validation for Global Circulation Models (GCMs). Despite the importance of winds on Mars, presently there are only a few direct observations of them, and indirect inferences are often imprecise. Because the Mars atmospheric dust cycles and CO_2 cycles are coupled, and because they both partially drive the wind fields, it is important to measure the dust, wind and CO_2 column simultaneously. It is ideal to measure them with the same instrument operating continuously, day and night, from a polar orbit, which is the basis of the MARLI approach.

2. Lidar Measurement approach

Our new lidar measurement concept is shown in Figure 1. MARLI is designed for a nominally circular polar Mars orbit. It is pointed typically 30-45 degrees from nadir in the cross-track direction, and the lidar continuously measures the aerosol backscatter profiles, the cross polarized (ice) backscatter profiles, the Doppler (horizontal) wind profiles, the range to the surface from space. The lidar wavelength is near 1533 nm and is stabilized off, but near, a CO_2 absorption line. The MARLI measurement types are illustrated in Figure 2.

3. Lidar Description

The laser signal from the Mars atmosphere is weak and distributed, and its measurement requires a highly sensitive lidar approach. A key to allowing compatibility for an orbital planetary mission is using a direct detection approach with efficient lasers, and a low-mass large area telescope, and photon-sensitive detectors.

The baseline MARLI design uses a pulsed fiber laser. It is small, efficient and wavelength tunable and operates near a single CO_2 line in the 1533 nm CO_2 band. Its output is chopped into pulses and amplified by several fiber amplifier stages. The receiver uses a ~70 cm diameter receiver telescope, and splits the received signal into 3 paths in the receiver. Each path uses a photon sensitive detector element in a small array.

Our baseline approach builds on new lidar components developed for NASA and DoD, including laser power amplifier stages from Fibertek, and photon sensitive HgCdTe detectors from DRS-RSTA. The targeted lidar size is ~80 cm cube, a medium sized instrument similar to the Mars Orbiter Laser Altimeter (MOLA). Nominal payload

parameters are < 40 kg, < 65W, and ~ 50 Kbits/sec. The baseline transmitter uses an efficient and compact wavelength tunable laser that operates on and near a single CO_2 line in the 1533 nm CO_2 band. The receiver uses a ~70 cm diameter receiver telescope and new highly sensitive HgCdTe detectors. This approach leverages in technologies from our work measuring CO_2 in the Earth's atmosphere supported by the NASA ESTO Instrument Incubator (IIP) program. We are also investigating an alternative approach that uses a pulsed single frequency Nd:YAG laser operating at 1064 nm.

4. Performance Estimates

We have developed measurement models and calculated the expected performance. The estimates depend on vertical bin depth and averaging time. The summary in Table 1 is based on averaging into 2 km bins vertically and for 40 seconds along track (~2 deg in latitude). The plan for this work for is to evaluate the performance of key components in lab tests and demonstrate atmospheric measurements under conditions that simulate measurements from space. More details will be given in the presentation.

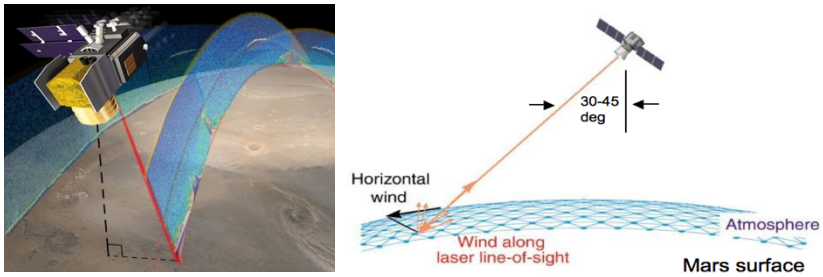

Figure 1. *(Left)* Mars Lidar measurement approach, which continuously measures the aerosol backscatter profiles, the cross polarized (ice) backscatter profiles, the Doppler (wind profiles), the column CO_2 absorption and the range to the scattering surface from orbit. *(Right)* Measurement orientation. Nominally the lidar is pointed cross-track at 30-45 deg off nadir, to measure the Doppler shift of the wind in the cross-track direction.

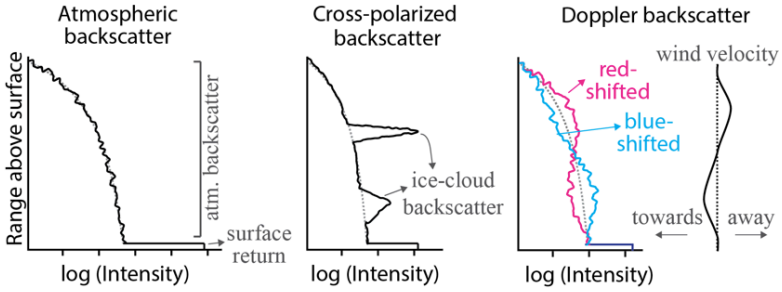

Figure 2. Illustrations of the MARLI measurements. *(Left)* Range (height) resolved aerosol backscatter profiles. The strong echo pulses reflected from the surface are used for the CO_2 column density measurements. *(Middle)* Profiles of cross-polarized backscatter, caused by clouds with ice-crystals. *(Right)* Height resolved Doppler (wind) backscatter profiles as seen by the two detectors after passing through the the double-edge filter. The horizontal wind profile *(Far Right)* is computed from the scaled ratio (difference/sum) from the detectors after the double-edge filter.

Table -1 Calculated MARLI performance

Parameter	*Surface*	*5 km*	*10 km*	*20 km*	*40 km*
Backscatter SNR	180	150	120	60	30
Wind horiz. velocity (m/sec)	1.2	1.4	1.8	3.5	~8
Range to surface (m)	<1	<1	<1	<1	<1

EPSC Abstracts
Vol. 10, EPSC2015-260, 2015
European Planetary Science Congress 2015

Ice flow in the deepest part of Mars: the banded terrain in Hellas basin.

X. Diot (1, 2), M. R. El Maarry (3), K.P. Norton (4), F. Schlunegger (1), N. Thomas (2, 3), L. Guallini (3), P.M.Grindrod (5, 6)
(1) Geologisches Institut, Universität Bern, Swtzerland, (2) Center for Space and Habitability, University of Bern, Switzerland, (3) Physis Institut, university of Bern, Switzerland, (4) School for Geography, Environment and Earth Science, Victoria University of Wellington, New Zealand, (5) Department of Earth and Planetary Sciences, Birkbeck, University of London, UK, (6) Centre for Planetary Sciences at UCL/Birkbeck, London, UK (corresponding author: xavier.diot@csh.unibe.ch)

Abstract

The morphometric, mapping, and high resolution 3D analyses performed in this study reveals that the banded terrain, which is located in the deepest part of Mars, may have formed through surface or sub-surface viscous flow. The presence of multiple periglacial landforms throughout the banded terrain suggests the presence of ice in the whole subsurface. The Viscous flow hypothesis is supported by a strong link to the topography and to the multiple interactions between the bands.

1. Introduction

The Hellas basin located in the southern hemisphere (centred at 40.8°S, 67.8°E) is one of the largest basins on Mars and the deepest region (depth > 7.5 km) as well. This basin contains multiple geologic units [1]. The NW part of Hellas hosts an enigmatic unit commonly named “banded terrain” [2, 3] (Figs. 1 and 2). The aim of this study is to characterize the particular flow structures of the banded terrain using morphometric and mapping analysis and gain insight into the formation mechanism through 3D views. We used images from the Mars Reconnaissance Orbiter Context Imager (CTX, resolution 6m/px) [4] and the High Resolution Imaging Science Experiment (HiRISE, 25–50 cm/px) [5] in addition to high resolution Digital Terrain Models (DTMs) generated from both datasets.

1.1 Architecture of the banded terrain and interactions with the landscape

Mapping and morphology of the banded terrain: The banded terrain is located in the lowest part of the interior of Hellas where deposition spans the Late Noachian to the Early Amazonian with the final deposition of the banded terrain approximately 3 Gyr ago, age determined by crater-size frequency analysis [2, 3]. The banded terrain itself covers a large (35–42°S, 51–60°E) in the NW of the Hellas basin. This terrain is made up of 3–15 km-long bands that are 90–1,000 m-wide with smooth changes in direction [2]. The bands display shapes that vary from linear to concentric forms (Fig. 1).

Morphometric analysis: Linear and lobate bands are located on the NW downslope of the Alpheus Colles plateau whereas the concentric bands are present in local depressions. MOLA slope and elevation profiles along given linear bands and perpendicular to lobate bands reveal that they are located on slopes of 7° on average. Interestingly, both linear and lobate bands terminate mainly on slopes ~ 2° (Fig. 1). Analogous profiles along the long and the short axes of the concentric bands clearly show their preferential location in depressions rimmed by a crest or a ridge (Fig. 1). Using HiRISE and CTX DTMs within Arcmap 10.1, a minimum thickness of 12 m has been determined from the bands.

2. Banded terrain: viscous flow of an ice-rich material

Multiple periglacial landforms: Many periglacial landforms (Fig. 3) are visible and laterally extensive in the banded terrain. These landforms include polygons with different sizes and elongated pits, scalloped depressions, isolated mounds and structures informally named an “collapse annuli”. Thermal contraction cracking combined with the sublimation of ice in the subsurface are known to form similar periglacial landforms on Mars [2].

Clear geomorphologic signs of viscous flow: 3D views (Fig. 2) obtained from CTX and HiRISE DTMs using ArcScene 10.1 reveal that the morphology of some of the linear and lobate bands is

strongly controlled by the surrounding topography. Multiple directional and morphologic changes of bands are linked to the interaction with the surrounding bands (Fig. 2).

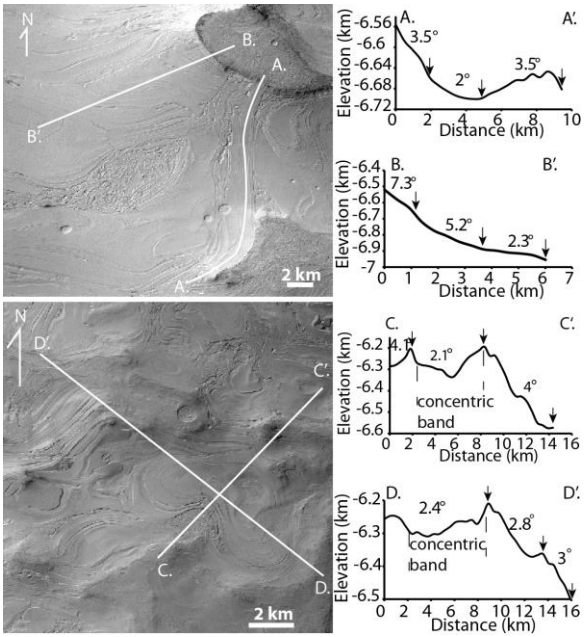

Fig. 1. (***Upper***) linear and lobate bands observed with the CTX camera (profiles AA'-BB'). (***Lower***) concentric bands observed with the CTX camera (profiles CC'-DD'). Image ID: (***Upper)*** P15_006924_1406, (***Lower***) P17_007557_1386.

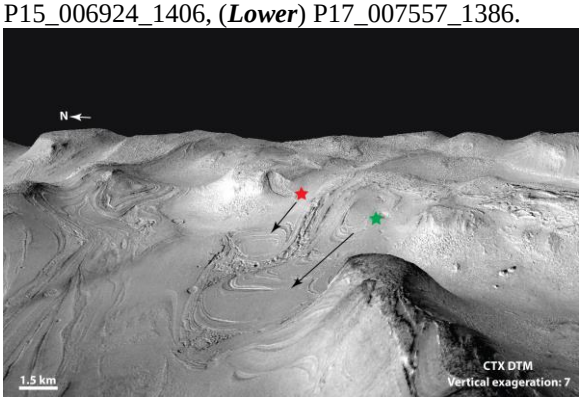

Fig. 2. 3D view from a CTX DTM (image pairs B18_016642_1371 – P18_007913_1371) presenting the competition, direct interaction between a lobate (green star) and a linear (red star) bands.

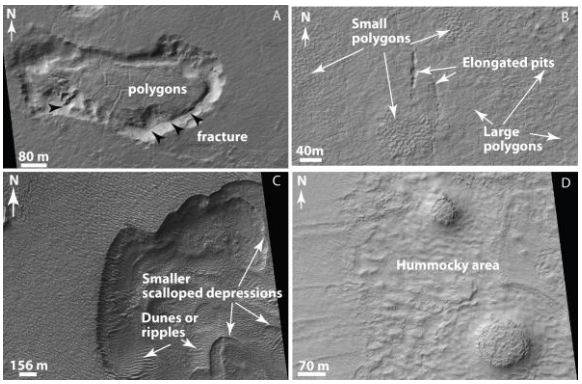

Fig. 3. High resolution images of periglacial landforms in the banded terrain. (A) Elongate rimless collapse annuli. (B) Small and large polygons with an N–S oriented chain of pits. (C) Example of scalloped depressions. (D) Fractured mounds. Image ID: (A) PSP_007781_1410, (B) PSP_007570_1415, (C) ESP_017565_1400, (D) PSP_006568_1415.

6. Summary and Conclusions

The banded terrain appears to be the youngest deposition of Hellas. Morphometric and 3D analyses suggest that the banded terrain may be the result of viscous flow controlled by the topography and the competition of the flow of the adjacent bands. The presence of periglacial landforms in the banded terrain suggests an ice-rich composition for this flow.

Acknowledgements

XD would like to thank the Center for Space and Habitability of the University of Bern for funding his PhD work. MR EM, NT, and FS are supported by funds from the Swiss National Science Foundation (SNSF).

References

[1] Tanaka, K. L., Leonard, G. J. JGR 100 (E3), 5407–5432, 1995.

[2] Diot, X., et al. PSS 101(0), 118–134, 2014.

[3] Diot, X., et al. Submitted to Icarus, 2015.

[4] Malin et al. JGR, 112, E002808, 2007.

[5] McEwen et al. JGR, 112, E05S02, 2007.

[6] Lefort, A., et al. Icarus 205(1), 259–268, 2010.

EPSC Abstracts
Vol. 10, EPSC2015-265, 2015
European Planetary Science Congress 2015

Outcrop of phyllosilicates near Huygens crater on Mars identified by MRO-CRISM

N. Jain and P. Chauhan
Planetary Sciences Division, Biological and Planetary Sciences and Applications Group, Space Applications Centre (SAC), Indian Space Research Organization (ISRO), Ahmedabad, Gujarat, India, 380 015 (nirmala@sac.isro.gov.in/ Fax-: +91-079-26915823)

Abstract

Aqueous minerals such as phyllosilicates have been identified near Huygens Crater on Mars with the help of Mars Reconnaissance Orbiter-Compact Reconnaissance Imaging Spectrometer for Mars (MRO-CRISM) hyperspectral data. The identified mineralogy in association with impact crater in the study area could have been formed by hydrothermal alteration and weathering processes due to surface and subsurface water activity. The present study shows that the minerals near Huygens crater are characterized by the presence of prominent spectral absorption features at 1.41 µm, 1.92 µm, 2.3 µm and 2.54 µm wavelength regions, indicating the existence of aqueous altered minerals, i.e., phyllosilicates. The study area also shows the spectral signatures of iron-bearing minerals at 1.16 µm with phyllosilicates. Phyllosilicates are products of chemical weathering of igneous rocks. Results of the study are important to understand the formation processes of aqueous mineral assemblages on Mars and evolutionary history of the planet.

1. Introduction

Huygens is well preserved impact crater on Mars located at 13.4°S, 55.4°E in the Noachian highlands above Hellas Basin (Figure. 1). It has with a diameter of ~450 km. In and around Huygens crater, large number of deposits of aqueously altered phyllosilicates and mafic minerals has been found in previous study [1, 2]. Spectroscopic study of phyllosilicates using Compact Reconnaissance Imaging Spectrometer for Mars (CRISM) gives information about past alteration history of the highlands crust around Huygens crater. Numbers of small impact craters have been found near Huygens crater. We are showing here the Spectral signature of phyllosilicates from these small craters.

2. Data sets and methodology

We utilize data from the Compact Reconnaissance Imaging Spectrometer for Mars (CRISM).

The CRISM instrument acquires visible and near infrared (0.36-3.9 µm) data which is important to collect the information of hydrated minerals like phyllosilicates. In the present study the mineralogy around Huygens crater was examined with the spectral range of 1.0 to 2.6 µm using the CRISM Analysis Tool (CAT) software (figure 2). Spectral signatures of altered minerals were obtained on a pixel-by-pixel basis. A ratio of mineral spectra with spectra of spectrally flat regions was done to remove the effect of atmospheric CO2 of Mars from the spectra signature and enhance the absorption features [3]. The spectral mineral matching was done in which the detected ratio spectra of unknown minerals on Mars were compared with the known spectra of minerals from the CRISM spectral library.

2. Results

Deposits of phyllosilicates were found in two smaller craters; one located away from the Huygens crater in its eastern part and second is present at the north western part of the Huygens crater at its rim (figure 1 and 3). These aqueously altered materials are localized floor and wall of these two smaller craters spectral matched process confirms the presence of mix deposits of kaolinite-serpentine. Absorption features of kaolinite-serpentine at 1.41 µm, 1.92 µm, 2.30 µm and 2.54 µm have been found in the present study. The presence of 1.16 µm could indicate the existence of ferrous iron-bearing mineral. Illite, a mineral of the phyllosilicate group mainly forms by the weathering or hydrothermal alteration of muscovite or feldspar on the Earth and their presence near Huygens crater shows the evidence of past aqueous activity in study area.

3. Figures

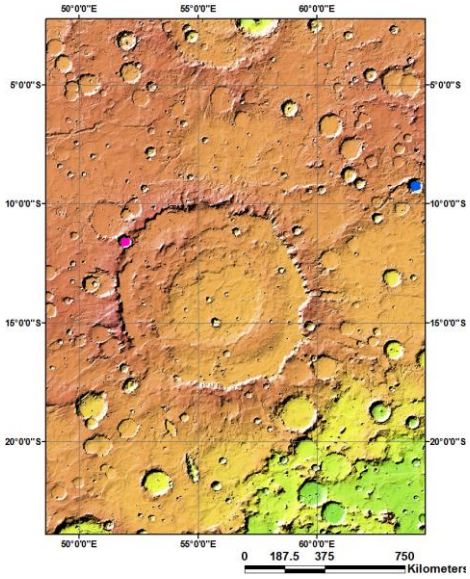

Figure 1: Regional view of Huygens crater on Mars Global Surveyor- Mars Orbiter Laser Altimeter (MGS-MOLA). Square boxes (pink and blue in color) show the locations of CRISM datasets for the study of phyllosilicates.

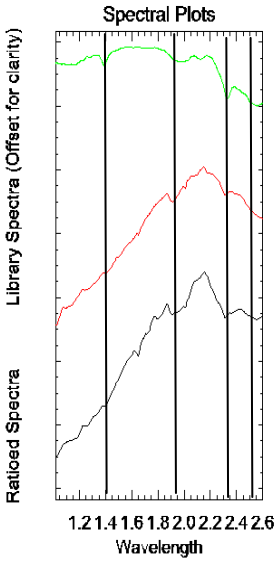

Figure 2: Spectral signature from FRT00012CD9 (red) and FRT000124B3 (black) of phyllosilicates (kaolinite-serpentine) from two small craters present near Huygens. Spectral signature of KAOLINITE-SERPENTINE SERP01 (green) is from CRISM spectral library

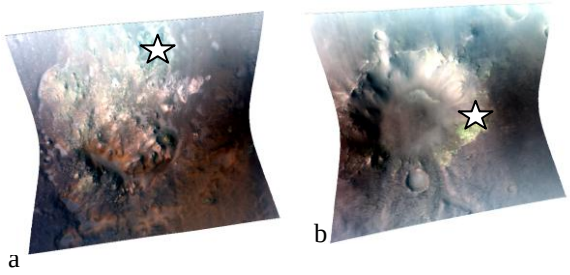

Figure 3: CRISM images were used for the study of phyllosilicates, a: FRT00012CD9 and b: FRT000124B3

6. Conclusions

Huygens crater is important region to study the past aqueous history of Mars. We have identified aqueously altered materials in smaller impact craters present near Huygens crater. These minerals play an evidence of past aqueous and hydrothermal processes in the study area.

Acknowledgements

We express our thanks to Shri Tapan Misra, Director, Space Applications Centre (SAC), of Indian Space Research Organistion (ISRO) for his constant support and encouragement for carrying out this study. We are also thankful to Dr. P. K. Pal, Deputy Director, EPSA, Space Applications Centre for their valuable guidance. We express our thanks to CRISM and MOLA team for providing free data sets. This research would not have been possible without team of PDS Geosciences Node of Washington University at St. Louis for providing planetary data.

References

[1] Bibring J. -P., et al.: Mars Surface Diversity as Revealed by the OMEGA/Mars Express Observations. Science 307, 1576-1581, 2005.

[2] Murchie S., et al.: Compact Reconnaissance Imaging Spectrometer for Mars (CRISM) on Mars Reconnaissance Orbiter (MRO), Journal of Geophysical Research, Vol. 112, E05S03, 2007.

[3] Mustard J. F., et al.: Hydrated silicate minerals on Mars observed by the Mars Reconnaissance Orbiter CRISM instrument, Nature Letters, 2008.

EPSC Abstracts
Vol. 10, EPSC2015-269, 2015
European Planetary Science Congress 2015

Application of factor analysis and target transformation to identify the spectral end-member from MRO-CRISM data

Banavath Suman (1), Ramdayal Singh (2), Nirmala Jain (2) and Prakash Chauhan (2)
(1) Indian Institute of Space Science and Technology, Thiruvananthapuram, Kerala.
(2) Planetary Sciences Division, Biological and Planetary Sciences and Applications Group,
Space Applications Centre, ISRO, Ahmedabad-380015 (ram@sac.isro.gov.in/Fax-:+91-079-26915823)

Abstract

Factor analysis and target transformation has been applied to near-infrared hyperspectral data collected by the Compact Reconnaissance Imaging Spectrometer for Mars (CRISM) onboard the Mars Reconnaissance Orbiter (MRO). We have confirmed the presence of Phyllosilicates (Nontronite, Serpentine) in Nili Fossae, and Sulphate (Gypsum) in Noctis Labyrinthus using factor analysis and target transformation methods. Identification of these minerals gives the knowledge about presence of past aqueous environment in study regions.

1. Introduction

In present study, we have used hyperspectral data MRO-CRISM in the range of 1.3-2.6 µm at Noctis Labyrinthus and 1.8-2.6 µm at Nili Fossae. There are two basic assumptions for factor analysis to apply on any dataset: (i) datasets are assumed as linear combination of individual spectral end-member, (ii) the obtained spectral end-members are added linearly. The selected spectral range contains diagnostic spectral features present in a variety of phases and is sufficient to accurately determine their presence. We have confirmed the presence of Gypsum detected by [1] and the presence of Phyllosilicates (Nontronite) detected by [2]. Determining the mineralogical composition of the Martian surface layer provides a means of understanding its origin and past evolutionary history. In turn, this knowledge is integral in understanding the climatic and geologic history of the planet.

2. Methodology

Datasets of mixed spectra selected from CRISM hyperspectral image was assumed to be a linear combination of spectral end-member. Factor analysis was applied on a set of mixed spectra. The covariance matrix has been used for deriving eigenvalues and orthogonal eigenvectors. Target transformation uses the least square fitting with the eigenvectors in the set of measured spectra which was derived from factor analysis and library spectra. If linear combination of eigenvectors closely matched with library spectra then that matched library spectra is a possible end-member over that region. The eigenvectors corresponding to higher eigenvalues are associated with the most significant information contained in the data. Smaller eigenvalues represents the noise. So eigenvectors corresponding to smaller eigenvalues are discarded to remove the noise from the dataset.

3. Results and discussion

CRISM image FRT00007E28 was selected for the study area from the Noctis Labyrinthus (Figure 1.1.a) region.

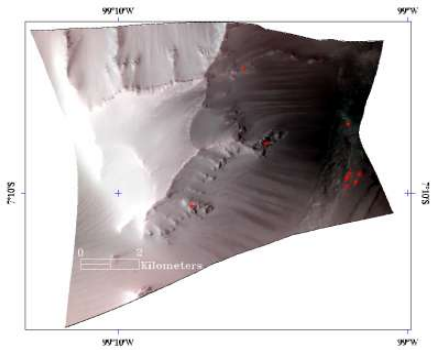

Figure 1.1: (**a**) The processed CRISM image with ID FRT00007E28 from Noctis Labyrinthus, 10 pixels selected for factor analysis which is shown in (red) stars.

For the confirmation of the presence of Gypsum using factor analysis and target transformation, we have selected ten spectra (red stars) from the CRISM FRT00007E28 image (figure 1.1.b) as dataset. Kaiser-Meyer-Olkin (KMO) measure of sampling values is 0.85 and Bartlett's test of sphericity has been conducted on CRISM dataset which confirms the factor analysis can produce the covariance matrix and can apply factor analysis for dataset. Factor analysis applied on selected dataset. Covariance matrix of selected dataset has been used for deriving eigenvalues. First eigenvalue explained 86.657%, second eigenvalue 10.156% and third eigenvalue 1.432% of variance. Cumulative of first three eigenvalues explains 98.813% of variance. So using scree plot slope change and percentage of variance we can say that three latent factor are sufficient to explain all spectral variations. Varimax rotation has been used for loadings. Three spectral end-members (figure 1.1.c) which are the linear combination of significant eigenvectors have been extracted from selected dataset. The derived spectral end-member is matching with the library spectra of Gypsum (figure 1.1.d). So Gypsum is

a possible end-member over this region. Factor analysis and target transformation has confirmed the presence of Gypsum in Noctis Labyrinthus.

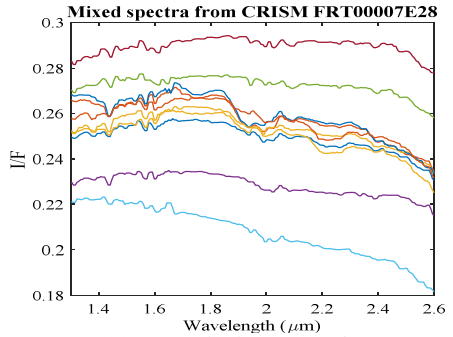

Figure 1.1: (**b**) 10 mixed spectra from CRISM FRT00007E28 to perform factor analysis.

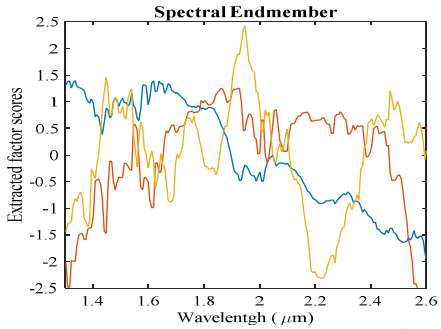

Figure 1.1: (**c**) Spectral end members extracted from factor analysis.

Similar analysis was done in Nili Fossae region. Same as above algorithm has been applied for Nili Fossae region for the confirmation of phyllosilicates (Nontronite). The CRISM FRT00005A3E data selected from the Nili Fossae. KMO sampling values is 0.879 for FRT 3A5E at Nili Fossae. First eigenvalue explained 90.438%, second eigenvalue 7.275% and third eigenvalue 1.84 % of variance. Cumulative of first three eigenvalues explains 99.516% of variance. Target transformation uses linear combination of eigenvector for least square fit which is matched with the library spectra of Nontronite (figure 2), so Nontronite is spectral end-member over Nili fossae region.

4. Summary and Conclusions

Factor scores are sensitive to small scale spectral variation. Selecting significant eigenvector and neglecting the smaller eigenvalue leads to both noise removal and dimensionality reduction of the dataset. We have confirmed the identified minerals such as Gypsum in Noctis Labyrinthus, Phyllosilicates in Nili Fossae using factor analysis and target transformation methodology. These minerals indicate that their formation in the study region probably occurred in past aqueous environment present in the study area.

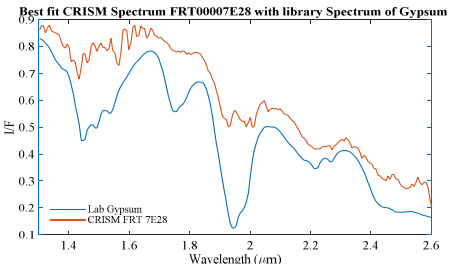

Figure 1.1: (**d**) Best fit of spectral end member derived from factor analysis with library spectrum of Gypsum.

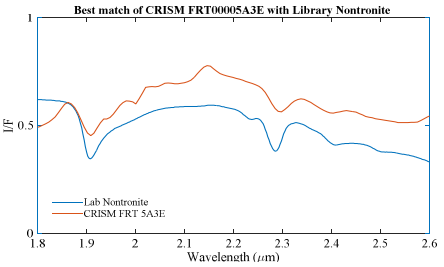

Figure 2: Best fit of spectral end member derived from factor analysis with library spectrum of Nontronite.

Acknowledgements

We express our thanks to Tapan Mishra, Director, Space Applications Centre, ISRO for his support and encouragement in this study. We are also thankful to Dr. P. K. Pal, DD, EPSA, Space Applications Centre, ISRO for his valuable guidance. We are grateful to the hard work of the entire team members of MRO-CRISM for data sets.

References

[1] Weitz, C.M., Bishop, J.L. and Grant, J.A., Gypsum, Opal, and Fluvial Channels within a Trough of Noctis Labyrinthus, Mars: Implications for Aqueous Activity during the Late Hesperian the Amazonian, Planet. Space Sci., V87, 130-145, 2013.

[2] Mustard J. F. et al., Hydrated silicate minerals on Mars observed by the Mars Reconnaissance Orbiter CRISM instrument, Nature Letters, doi: 10.1038/nature07097, 2008.

EPSC Abstracts
Vol. 10, EPSC2015-316, 2015
European Planetary Science Congress 2015

MHD Model Results of Solar Wind Plasma Interaction with Mars and Comparison with MAVEN Observations during Quiet Solar Wind Conditions

Y. J. Ma (1), C. T. Russell (1), A. F. Nagy (2), G. Toth (2), J. S. Halekas (3), J. E. P. Connerney (4), J. R. Espley (4), and P. R. Mahaffy (4), Mehdi Benna (4), James McFadden (5)
(1) Department of Earth and Space Sciences, UCLA, Los Angeles, CA, USA, (2) Department of Atmospheric, Oceanic and Space Sciences, University of Michigan, Ann Arbor, MI, USA, (3) Department of Physics and Astronomy, University of Iowa, Iowa City, IA, USA, (4) NASA Goddard Space Flight Center, Greenbelt, MD, USA (5) Space Sciences Laboratory, University of California, Berkeley, California, USA (yingjuan@ucla.edu)

Abstract

The Mars Atmosphere and Volatile Evolution mission (MAVEN), launched on November 18, 2013, is now in its primary science phase, orbiting Mars with a 4.5 hour period. In this presentation, we show detailed comparisons between the MHD model results and the relevant plasma observations from MAVEN during quiet solar wind conditions. Through comparison with relevant observation along MAVEN orbits, we find that in general, the time-dependent multi-species MHD model reproduces very well the plasma interaction process around Mars.

1. Introduction

The crustal remanent field on Mars rotates constantly with the planet, varying the magnetic field configuration interacting with the solar wind. It has been found that ion loss rates slowly vary with the sub-solar longitude, anti-correlating with the intensity of the dayside crustal field source, with some time delay, using a time-dependent multispecies MHD model [1]. In this study, we compare our model results with relevant MAVEN plasma observations along the spacecraft orbit during relative quiet solar wind conditions. During the selected time period, MAVEN orbits pass through all different plasma boundaries and regions. Such a comparison is essential in providing a baseline for the general performance of the model.

2. Methodology:

The time-dependent multi-species single-fluid MHD model [1] includes four continuity equations to track the mass densities of the proton and three major ions in Martian ionosphere: O_2^+, O^+ and CO_2^+. All ion species share the same velocity and temperature. The Mars-solar wind interaction is self-consistently calculated in the model by including the effects of the crustal magnetic field, ion-neutral collisions, and major chemical reactions.
We simulate one entire day of plasma interaction using solar wind conditions based on averaged SWIA (Solar Wind Ion Analyzer) observations in the solar wind on Dec 10, 2014 when the solar wind condition is relative steady. The rotation of the crustal field is included in the time-dependent simulation, and Mars rotation axis is set to match the real conditions.

3. Results

Figure 1 shows a three-dimensional view of one MAVEN orbit on Dec 10, from 16 UT to 20 UT. The color on the sphere corresponds to the crustal field magnitude at Dec. 10, 18 UT and the color on the orbit shows the altitude. MAVEN passed by the center of the plasma wake near 18 UT, 20 min before it flew by periapsis. Figure 2 shows trajectory information of MAVEN (latitude, SZA, altitude) and comparison of the density, velocity and magnetic field with relevant plasma observations along MAVEN orbits for Dec 10, 2014. During each orbit, MAVEN spent roughly half of the time in the solar wind. The good agreement of the plasma density, velocity and magnetic field demonstrates that the MHD model used here can reproduce the plasma interaction process around Mars very well.

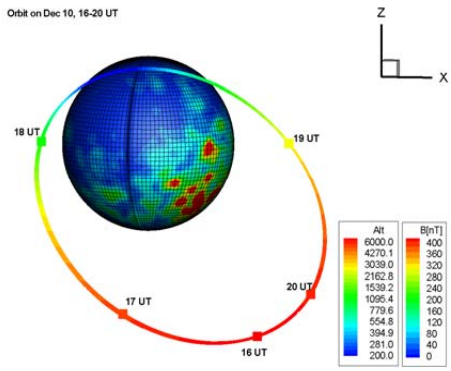

Figure 1: 3D view of MAVEN Trajectory from 16UT to 20UT on Dec 10, 2014.

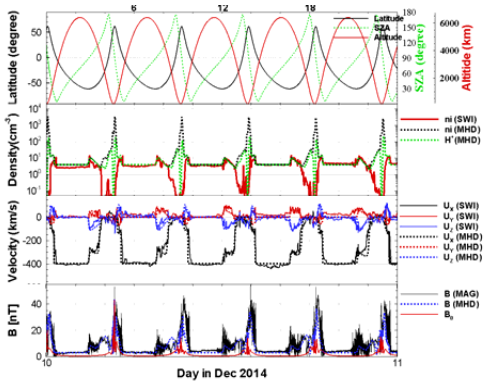

Figure 2: Trajectory information of MAVEN and comparison of the density, velocity and magnetic field with relevant plasma observations along MAVEN orbits for Dec 10, 2014. The solid lines are observations; the dashed lines are from model results.

4. Summary and Conclusions

Through comparison with relevant MAVEN plasma observations, we find that in general, the time-dependent multi-species MHD model reproduces quite well the plasma interaction process around Mars. The bow shock location and plasma conditions inside the magnetosheath region from the model results agree well with SWIA data. The density profiles predicted by the model agree well with both NGIMS and STATIC measurements. We also find that there are some discrepancies between the MHD and the observed magnetic field in the magnetic pile up region. To improve the fit, the model needs to update the neutral density profiles based on MAVEN observations, and photo-ionization rates from the modeled EUV spectrum.

References

[1] Ma, Y., X. Fang, C. T. Russell, A. F. Nagy, G. Toth, J. G. Luhmann, D. A. Brain, and C. Dong: Effects of crustal field rotation on the solar wind plasma interaction with Mars, Geophys. Res. Lett., 41, 6563–6569, doi:10.1002/2014GL060785, 2014

EPSC Abstracts
Vol. 10, EPSC2015-338, 2015
European Planetary Science Congress 2015

Martian surface microtexture from orbital observations

Fernando, J. (1,2,3), Schmidt, F. (1,2) and S. Douté (4)
(1) Univ. Paris-Sud, GEOPS, UMR 8148, 91405 Orsay, France (jennifer.fernando@u-psud.fr), (2) CNRS, 91405 Orsay, France, (3) Laboratoire de Géologie de Lyon, Terre, Planètes, Environnement (Université de Lyon-Université Claude Bernard Lyon 1-CNRS-ENS Lyon, ERC eMars Team, 69622 Villeurbanne Cedex, France, (4) Univ. Joseph Fourier/CNRS, IPAG, Grenoble, France.

Abstract

The information about the surface microtexture is useful to constrain the geological processes (e.g., transportation, deposition, weathering).

In this study, the grain microtexture is derived from the orbital CRISM/MRO multi-angular observations allowing to characterize the surface scattering behavior. The Hapke radiative transfer model is inverted to derive the photometric parameters which have physical meanings (e.g., grain size, roughness, shape, internal structure).

Eight sites having various geological contexts are selected. The results show a high diversity of grain microtexture. This result put forward that Mars have experimented various geological processes. The link between information about the grain microtexture and the geological processes will be presented at the conference.

1. Introduction

The Martian primary basaltic surface have been highly modified by exogenous (e.g., cosmic bombardments) and by interactions between the atmosphere, cryosphere, hydrosphere and surface (e.g., erosion, transportation, deposition, weathering).

The information about the surface microtexture (e.g., grain size, shape, roughness, internal structure) is helpful to identify and characterize the geological processes. For instance, information about the grain internal structures of volcanic materials can give constraints on the volatile content in the magma or on the cooling rate. The grain size and morphology can give on the grain transportation, erosion and deposition.

Direct in situ imagery can be used to characterize the grain microtexture and give constraints on the local geology but is limited to the rover landing site and along the rover path. Microtexture can also be indirectly estimated from remote photometric measurements by studying the manner in which the solar light is scattered by the surface materials). It has been experimented from in situ measurements from Panoramic Camera measurements on-board Mars Exploration Rover [1,2] and from orbital measurements from High Resolution Stereo Camera on-board Mars Express [3] and from Compact Reconnaissance Imaging Spectrometer for Mars (CRISM) on-board Mars Reconnaissance Orbiter [4,5,6].

2. Methodology

Taking into account the capability of CRISM on-board MRO to provide multi-angle images (eleven images with varied emission angles from 0-70°) [7], we estimate the surface bidirectional reflectance after aerosols correction using the Multi-angle Approach for Retrieval of Surface Reflectance from CRISM Observations technique (MARS-ReCO) [8].

Fernando et al. [5,6] proposed an approach to estimate the photometric parameters of the surface materials in terms of structural information by using the Hapke photometric model [9] in a Bayesian framework that considers: the single scattering albedo ω which depends on the grain size and the composition, the macroscopic roughness θ-*bar* which depends on the roughness from the particle to several centimeters and the particle phase function with a 2-term Henyey-Greenstein function that includes the asymmetry parameter b and the backscattering fraction c which qualitatively depends ont the grain morphology and its internal structures.. Maps of the surface photometric parameters are created and are estimated at 750 nm with a spatial resolution of ~200m/pixel.

3. Site selection and main results

The photometric parameters are estimated for eight sites (Figure 1) having various geological contexts, with favorable geometric and atmospheric conditions, avoiding the dust area [10] and with various mineralogy (alteration phases like phyllosilicates precipitation phases like sulfates and salts [e.g., 11, 12, 13, 14], and basaltic materials [e.g. 15]).

The phase function parameters are qualitatively related to the grain microtexture such as the grain shape, surface roughness and internal structure [16,17]. The results show a high diversity of surface photometric properties (e.g., forward and backward scattering behaviors) revealing a high diversity of grain microtexture, not observed on another planetary surface except the Earth. This diversity puts forward that Mars have experimented various geological processes which is still preserved. The results also showed that the processes are rather local than regional or global. The link between information about the grain microtexture and the geological processes will be presented in more details during the conference.

Part of the selected sites are landing site candidates for the next Exomars (ESA) and Mars2020 (Nasa) rover missions. Those results provide new constraints for the site selection procedure.

Acknowledgements

CNES and PNP support for this work. We thank Michael Wolff for making his aerosol optical thickness values available for this study and the CRISM team for providing the data. J. Fernando has received funding through the European Research Council under the European Union's Seventh Framework Program (FP7/2007-2013)/ERC Grant Agreement No. 280168.

References

[1] J. Johnson et al., J. Geophys. Res., 111, E02S14 (2006). [2] J. Johnson *et al.*, *J. Geoph. Res.* 111, E12S16 (2006). [3] A. Jehl *et al.*, *Icarus* 197, 403 (2008). [4] A. Shaw *al.*, *J. Geoph. Res.* 118 (2013). [5] J. Fernando *et al.*, *J. Geophys. Res.* 118, 514 (2013). [6] J. Fernando *et al.*, *Icarus* 253, 271 (2015). [7] S. Murchie *et al.*, *J. Geoph. Res.* 112, E05S03 (2007). [8] X. Ceamanos et al., *J. Geoph. Res.* 118, 540 (2013). [9] B. Hapke, *Cambridge Univ. Press.* (1993). [10] A. Ody *et al.*, *J. Geoph. Res.* 117, E00J14 (2012). [11] J.-P. Bibring *et al.*, *Science* 312, 400 (2006). [12] S. Murchie et al., *J. Geophys. Res.* 114, E00D06 (2009). [13] J. Carter *et al.*, *J. Geophys. Res.* 118, 831 (2013). [14] B. Ehlmann and C. Edwards, *Ann. Rev. Earth Planet Sci.* 42, 291 (2014). [15] A. Ody, *J. Geophys. Res.* 118, 234 (2013). [16] A. McGuire and B. Hapke, *Icarus* 113, 134. [17] A. Souchon *et al.*, *Icarus* 215, 313 (2011).

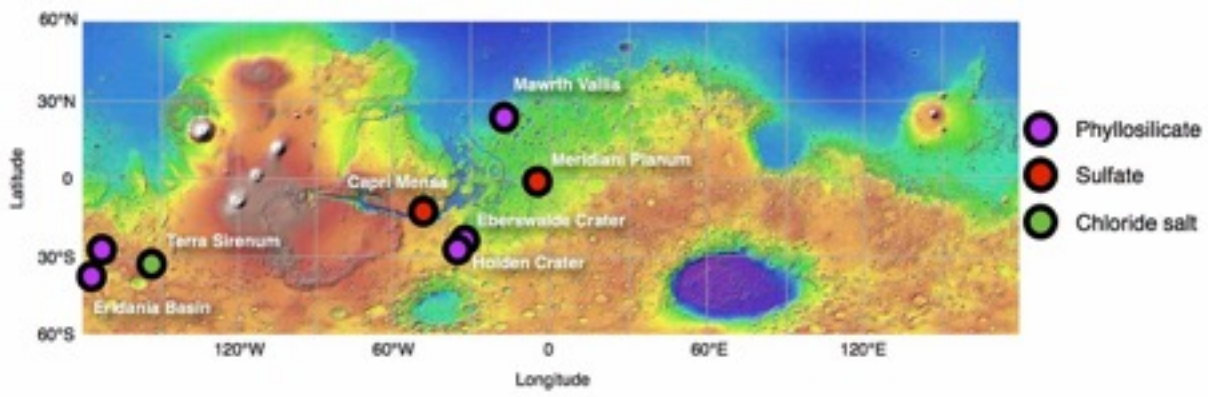

Figure 1: Site locations where hydrated silicates and salts have been detected by previous works [e.g., 11, 12, 13, 14] overlapped on the Mars Orbiter Laser Altimeter topographic map. The color of the filled circle indicates the dominant mineralogy.

EPSC Abstracts
Vol. 10, EPSC2015-341, 2015
European Planetary Science Congress 2015

Effects of the CO_2 defrosting cycle at martian mid-latitudes

Fernando, J. (1), Quantin-Nataf, C. (1), Pilorget, C. (2), Allemand, P. (1)
(1) Laboratoire de Géologie de Lyon, Terre, Planètes, Environnement (Université de Lyon-Université Claude Bernard Lyon 1-CNRS-ENS Lyon, ERC eMars Team, 69622 Villeurbanne Cedex, France, (2) Institut d'Astrophysique Spatiale, CNRS/ Université Paris Sud, UMR 8617, Orsay 91405, France.

Abstract

CO_2 seasonally condenses and defrosts at the surface of Mars which leads to the ejection of gas and materials leading to the formation of dark spots on top of the seasonal CO_2 layer. This process has been primarily described at the south polar regions where the process is more efficient. However, dark spots are also observed at lower latitudes, but little is known about the CO_2 defrosting process at those latitudes: is it the same process as those observed at the polar caps? what is the impact on the surface erosion? Are the defrosting features randomly distributed? We will present results at the global and local views in order to provide constraints on the effect of the current CO_2 defrosting cycle on the mid-latitude surface.

1. Introduction

A part of the atmospheric CO_2 alternately condenses in fall and winter forming the seasonal polar caps [1] and sublimates in spring when the insolation increases. The solar light penetrates the CO_2 slab and heats the regolith creating a basal sublimation. CO_2 gas and materials from the underlying regolith are then ejected leading to the formation of dark mineral dust spots and fans on top of the bright seasonal CO_2 layer [2, 3, 4]. The CO_2 defrosting process has a major impact on the surface erosion in polar regions, especially on the stratigraphic record [5] and the northern polar dunes [6, 7].

At lower latitudes, the CO_2 defrosting has been observed in many locations as for instance on dunes [6, 7, 8] and also on gully landforms [9, 10, 11, 12, 13] where basal sublimation may occur [14]. However, little is known on the current impact of the CO_2 defrosting process on the mid-latitude surface. Based on numerical modelings and combined with the observed temperature evolution, the dark material thickness on top of the CO_2 ice was estimated to range from a few hundreds of microns to a few millimeters at the polar regions [15]. Morphologic clues at the high spatial resolution scale should provide quantitative constraints on the surface evolution. This process may also has been an important process in the past Martian history when obliquity was higher allowing a seasonal CO_2 cap to extend up to 30° latitude.

2. Methodology and preliminary results

Thanks to the high resolution imaging science experiment (HiRISE) camera on-board Mars Reconnaissance Orbiter (MRO), high resolution images can be used to identify and to characterize the dark spots (e.g., size, morphology, density) but also the underlying materials (e.g., indurated or loose materials). This information is useful to evaluate the type of surfaces affected by CO_2 defrosting process.

Moreover, since 2006, the instrument has operated during 4 southern and 4 northern polar springs monitoring several sites on Mars which can be used to have constraints on the temporal evolution of these morphologies and the surface materials.

Previous detailed studies have already been conducted using monitoring and coupled HiRISE and compact reconnaissance imaging spectrometer for Mars (CRISM) observations at the south and north polar regions [e.g., 4, 16, 17, 18]. Those studies are used as supports for the characterization of the dark spots at lower latitudes in order to use same morphological classifications/terminologies and to evaluate the similarities and the differences in order to provide new constraints on the CO_2 defrosting process model [2, 3].

In this ongoing study, all the available HiRISE observations were studied to first localize regions driven by CO_2 defrosting by identifying potential dark spots which is considered as the result of the CO2 gas ejections. Our HiRISE survey gives an overview of the dark spot global occurrence at mid-latitudes. However, to due the narrow spatially and temporally covering of the HiRISE images, biases exist which do not imply that the process does not occur where HiRISE images are not acquired. Once

identified, each site where dark spots are observed was classified as a function of its context and as a function of type of surface (e.g., dune, crater slope, permafrost). For instance in the HiRISE scene displayed in Figure 1 which has been acquired at Ls=172.6°, dark spots are observed inside a crater over pre-existing gullies in the walls of the crater as well as over sand dunes that are lying down the floor of the crater. We noticed that the dark spots in and around gullies are less well-developed and less numerous.

In addition to the global survey, several sites were studied in details in order to quantify the temporal evolution of the surface materials and the dark spots. The results of this ongoing study results will be presented during the conference.

Acknowledgements

The research leading to these results has received funding through the European Research Council under the European Union's Seventh Framework Program (FP7/2007-2013)/ERC Grant Agreement No. 280168.

References

[1] James et al., *Univ. of Ariz. Press* (1992), [2] Piqueux et al., *J. Geophys. Res.* (2003), [3] Kieffer, *Geophys. Res.* (2007), [4] Portyankina et al., *Icarus*, (2010). [5] Piqueux and Christensen, *J. Geophys. Res.* (2008), [6] Hansen et al., *Science* (2011), [7] Hansen et al., *Icarus* (2013), [8] Gardin et al., *J. Geophys. Res.*, (2010), [9] Dundas et al. *GRL* (2010), [10] Reiss et al. *GRL* (2010), [11] Dundas et al. *Icarus* (2012), [12], Dundas et al. *Icarus* (2014) [13], [14] Pilorget et al., Icarus (2011), [15] Pilorget et al. *J. Geophys. Res.* (2013). [16] Hansen et al. *Icarus* (2010), [17] Thomas et al. *Icarus* (2010), [18] Pommerol et al. *J. Geophys. Res.* (2011).

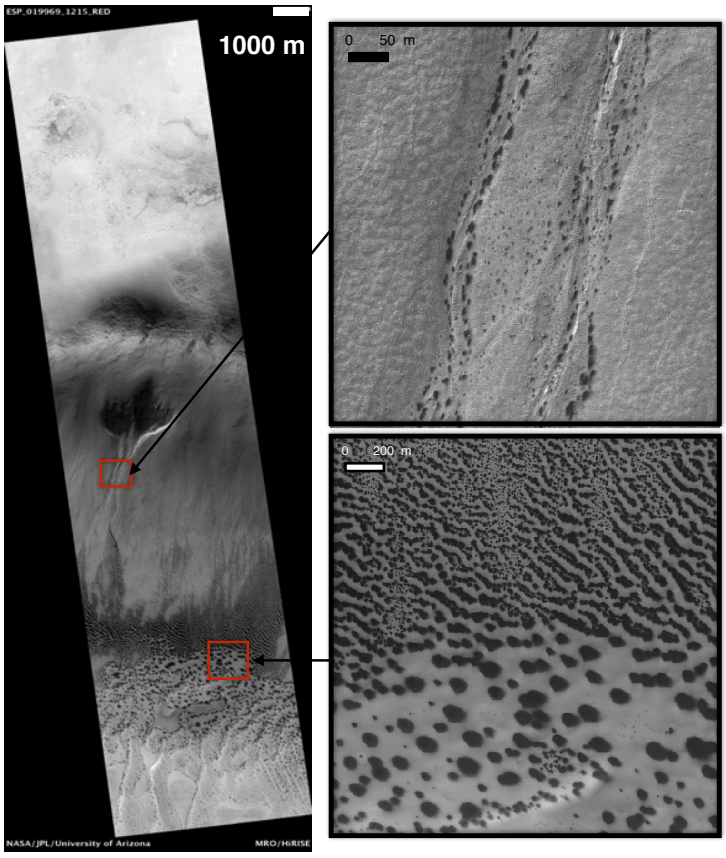

Figure 1: A HiRISE image (ESP_019969_1215_RED) and close-up located at lat. -50.378° and lon. 305.355° (Ls=172.6°, northern summer) showing dark spots in the crater slope associated with gullies and in granular sand dune inside the crater.

EPSC Abstracts
Vol. 10, EPSC2015-397, 2015
European Planetary Science Congress 2015

Hydrogen Coronae around Mars and Venus

H. Gröller (1), H. Lichtenegger (2), H. Lammer (2), and V. I. Shematovich (3)
(1) Lunar and Planetary Laboratory, University of Arizona, Tucson, AZ, USA, (2) Space Research Institute, Austrian Academy of Sciences, Graz, Austria (3) Institute of Astronomy, Russian Academy of Sciences, Moscow, Russia (hgr@lpl.arizona.edu)

Abstract

We present Monte-Carlo simulatios of the hydrogen corona around Mars and Venus for various possible photochemical sources of hot (energetic) hydrogen atoms. The aim of this study is to investigate those possible sources which may significantly contribute to the hydrogen corona and to compare the obtained densities with observations. The model includes the initial energy distribution of hot atoms, elastic, inelastic, and quenching collisions between the suprathermal atoms and the ambient cooler neutral atmosphere, and uses energy dependent total and differential cross sections for the determination of the collision probability and the scattering angles.

1. Monte-Carlo Modell

The simulations are based – if available – on the most recent data for both the atmospheric input and the collision cross sections. The model is limited by various circumstances: (a) the background atmosphere is represented by 1D ion and neutral density profiles, (b) the hot particles are treated as test particles, i.e. their influence on the background gas is neglected, (c) due to the lack of data, some types of collisions are simulated by using approximate values of the parameters.

The simulation of the hot particle corona is initiated by calculating for a specific reaction the corresponding velocity distribution of the products at discrete altitudes. The motion of these products through the thermosphere up to the exobase and beyond is followed by means of a Monte-Carlo model. On their way the hot particles can interact with the background neutral atmosphere via elastic, inelastic and quenching collisions and will loose on average part of their initial energy. For those particles which cross the exobase, the energy distribution function is determined which in turn serves as input for the exosphere density calculations. A more detailed description of the Monte-Carlo model can be found in [4], [2], and [3].

2. Hydrogen Simulation

Possible sources of hot hydrogen atoms due to dissociative and radiative recombination, photodissociation as well as charge exchange and chemical reactions are included in the model and listed in Table 1. In the course of this study other reactions may be considered. An additional task is to find proper cross sections for specific collisions. Currently only proper total and differential cross sections for H-H and O-H collisons, published by [6] and [7], respectively, are used in our model.

Table 1: Possible sources of hot hydrogen atoms due to dissociative and radiative recombination, photodissociation as well as chemical reactions.

Reactions
Dissociative recombination
$H_2^+ + e \longrightarrow H + H$
$OH^+ + e \longrightarrow H + O$
$HCO^+ + e \longrightarrow H + CO$
Radiative recombination
$H^+ + e \longrightarrow H + h\nu$
Photodissociation
$H_2 + h\nu \longrightarrow H + H$
Chemical reaction
$H_2 + O^+ \longrightarrow H + OH^+$
$H_2 + CO^+ \longrightarrow H + HCO^+$
$H_2^+ + O \longrightarrow H + OH^+$
$H_2^+ + CO \longrightarrow H + HCO^+$
$H_2 + CO_2^+ \longrightarrow H + HCO_2^+$
Charge transfer
$H^+ + O \longrightarrow H + O^+$
$H^+ + CO_2 \longrightarrow H + CO_2^+$

3. Results

Preliminary results of the hydrogen corona simulations at Venus are shown below for the reactions listed in Table 1. The obtained production rates for high and

low solar activity are shown in Figure 1. The prelim-

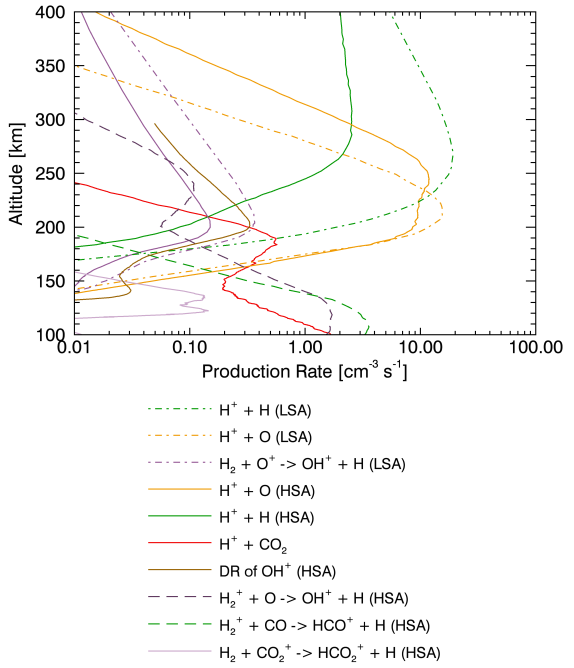

Figure 1: Production rates at Venus for high (solid lines) and low (dashed-dotted lines) solar activity of the reactions listed in Table 1.

inary number densities for high and low solar activity of reactions which show a significant contribution to the total density are illustrated in Figure 2. The black solid and dashed-dotted lines taken from [5] and [1], respectively, are in agreement with our preliminary results.

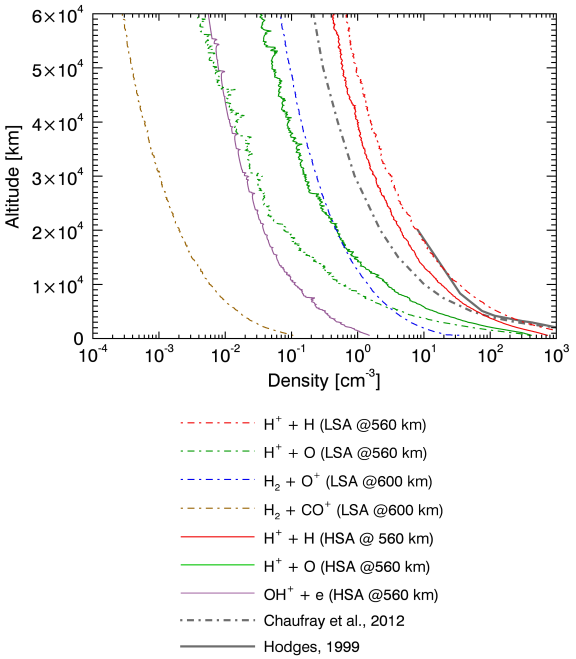

Figure 2: Calculated number densities at Venus for high (solid lines) and low (dashed-dotted lines) solar activity as well as the densities from [1] and [5].

Acknowledgements

H. Gröller and H. Lichtenegger acknowledges support by the Austrian Science Fund (FWF) under the project P24247-N16.

References

[1] Chaufray, J.-Y., Bertaux, J.-L., Quémerais, E., Villard, E., and Leblanc, F.: Hydrogen density in the dayside venusian exosphere derived from Lyman-α observations by SPICAV on Venus Express, Icarus, 217(2), 767, 2012.

[2] Gröller, H., Lammer, H., Lichtenegger, H. I. M., Pfleger, M., Dutuit, O., Shematovich, V. I., Kulikov, Y. N., and Biernat, H. K.: Hot oxygen atoms in the Venus nightside exosphere, Geophysical Research Letters, Vol. 39, L03202, 2012.

[3] Gröller H., Lichtenegger, H. I. M., Lammer, H., and Shematovich, V. I.: Hot oxygen and carbon escape from the martian atmosphere, Planetary Space Sciences, 98, 93, 2014.

[4] Gröller, H., Shematovich, V. I., Lichtenegger, H. I. M., Lammer, H., Pfleger, M., Kulikov, Y. N., Macher, W., Amerstorfer, U. V., and Biernat, H. K.: Venus' atomic hot oxygen environment, Journal of Geophysical Research, Vol. 115, E12017, 2010.

[5] Hodges, R. R., Jr.: An exospheric perspective of isotopic fractionation of hydrogen on Venus. Journal of Geophysical Research, 104(E4), 8463, 1999.

[6] Krstić, P. S., and Schultz, D. R.: Consistent definitions for, and relationships among, cross sections for elastic scattering of hydrogen ions, atoms, and molecules. Physical Review A, 60(3), 2118, 1999.

[7] Zhang, P., Kharchenko, V., Jamieson, M. J., and Dalgarno, A.: Energy relaxation in collisions of hydrogen and deuterium with oxygen atoms. Journal of Geophysical Research, 114(A7), A07101, 2009.

EPSC Abstracts
Vol. 10, EPSC2015-401, 2015
European Planetary Science Congress 2015

Martian CO_2 and O_2 abundances obtained from MAVEN/IUVS stellar occultations

H. Gröller (1), R. V. Yelle (1), F. Montmessin (2), G. Lacombe (2), N. M. Schneider (3), I. Stewart (3), J. Deighan (3), W. E. McClintock (3), J. T. Clarke (4), G. M. Holsclaw (3), B. M. Jakosky (3)
(1) Lunar and Planetary Laboratory, University of Arizona, Tucson, AZ, USA, (2) LATMOS, Université Versailles Saint-Quentin / CNRS, Guyancourt, France, (3) Laboratory for Atmospheric and Space Physics, University of Colorado, Boulder, CO, USA, (4) Astronomy Department, Boston University, Boston, MA, USA (hgr@lpl.arizona.edu)

Abstract

We present CO_2 and O_2 density profiles from stellar occultations by the IUVS instrument onboard MAVEN. The first occultation by MAVEN was of α Cru on February 8, 2015 and the first campaign of stellar occultations with 60 more observations of 11 different stars was executed from March 24, 2015 to March 26, 2015. To increase the longitudinal coverage, each star, except λ Sco, was observed 5 times; λ Sco was targeted 10 times. Density profiles from the first occultation are determined in the altitude range between 100 and 140 km. The derived O_2 mixing ratio in this region is 1.6×10^{-3}, in agreement with previous measurements.

1. Introduction

The stability of the Martian atmosphere is connected not only to the main constituent CO_2 but also to minor species like O_2 which are produced photochemically. A better understanding of the CO_2 and O_2 distribution is important for constraining models for the current state and the evolution of the Martian atmosphere.

UV occultations have proved to be a powerful technique for the study of upper atmospheric structure and composition. Sandel et al. (2015) recently presented CO_2 and O_2 abundance profiles in the Martian atmosphere obtained from UV stellar occultations observed by SPICAM onboard Mars Express [5]. The obtained O_2 mole fractions within 90 and 120 km vary from 1×10^{-3} to 5×10^{-3}. Seasonal variations of CO_2 densities and temperatures at various latitude and longitude over one Martian year was shown by Forget et al. (2009) using retrievals of 616 stellar occultations from SPICAM/MEX [1]. In the past, Viking mass spectrometer measurements were used to determine the CO_2 and O_2 densities and the corresponding O_2 mole fractions between 120 and 160 km [3].

The MAVEN IUVS instrument will measure numerous occultations through the course of the mission to increase the geographic and seasonal coverage and therefor the understanding of the CO_2 and O_2 abundance on Mars. Because they sample the region below MAVEN's periapse altitude, occultations provide a link between the middle and upper atmosphere. At the time of writing a single α Cru occultation observation and the first occultation campaign have been executed. The obtained CO_2 and O_2 number densities and their corresponding O_2 mole fractions are presented below.

2. IUVS Stellar Occultations

The FUV channel of the IUVS spectrograph onboard Maven covers the spectral range from 110 to 190 nm with an intrinsic spectral resolution of 0.6 nm [2]. For the α Cru occultation 3 spectral pixels and for the first occultation campaign 4 spectral pixels are binned resulting in spectral bin sizes of 0.24 and 0.33 nm, respectively.

The α Cru occultation observation begins below the limb and extends up to 500 km. With the cadence time of 2 s, including an integration time of 1.6 s, the resulting altitude resolution is around 5.5 km. Atmospheric absorption is evident below 150 km and occultation starlight is completely extinguished below 90 km.

Above 150 km the line of sight to the star is unattenuated and thus the unabsorbed reference spectrum from the star is measured. As the spacecraft moves along its trajectory the line of sight penetrates the atmosphere and the star spectrum attenuated by the atmosphere is measured. The transmission is obtained by dividing the attenuated spectrum by the unabsorbed spectrum. This method has the advantage that no absolute calibration of the spectograph is needed.

We fit the measured transmission spectra at each altitude assuming absorption by CO_2 and O_2 and us-

ing the Levenberg-Marquardt algorithm to retrieve the best fit column densities. We invert the column density profiles to obtain local densities by using the Tikhonov regularization method [4, 5].

3. Results and Discussions

The altitude dependence of the transmission spectra for this occultation is illustrated in Figure 1 for 7 different altitudes. The region between 200 and 500 km is

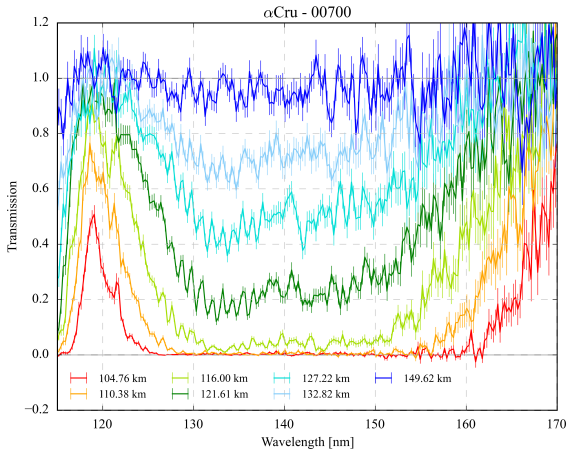

Figure 1: Transmission spectra of the α Cru occultation for 7 different altitudes including the 1σ-uncertainties.

used to characterized the unattenuated star spectrum.

The CO_2 and O_2 densities including the 1σ-uncertainties for the α Cru occultation are shown in Figure 2. The CO_2 and O_2 densities measured from Viking 1 and 2 as well as 6 different occultations from SPICAM on Mars Express for three stars (ζ Pup, β Cen, and γ Ori) with two different occultations each [5] are also shown. Both the CO_2 and O_2 densities inferred from the IUVS instrument are in good agreement with Viking and SPICAM/MEX occultations. The mean value of the mole fraction obtained from the MAVEN α Cru occultation is 1.6×10^{-3}. This value is in agreement with observations from SPICAM/MEX and Viking measurements.

Acknowledgements

This work was supported by NASA as part of the MAVEN Mission.

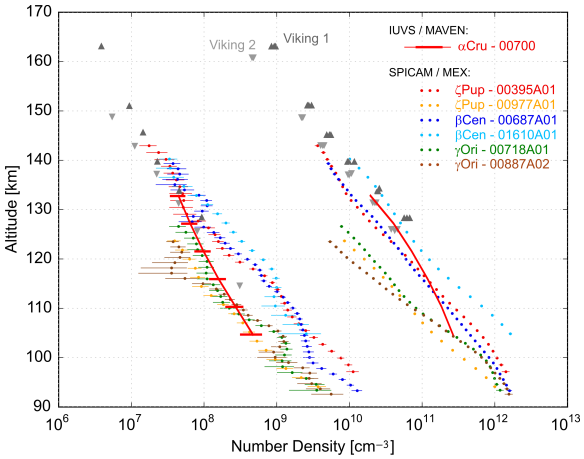

Figure 2: CO_2 and O_2 abundances including the 1σ-uncertainties for the α Cru occultation from the IUVS and for the SPICAM occultations of three different stars (ζ Pup, β Cen, and γ Ori) with two different occultations each (colored circles) as well as for the measurements from Viking 1 (gray upward pointing triangles) and Viking 2 (gray downward pointing triangles).

References

[1] Forget, F., F. Montmessin, J.-L. Bertaux, F. González-Galindo, S. Lebonnois, E. Quémerais, A. Reberac, E. Dimarellis, and M. A. López-Valverde: Density and temperatures of the upper Martian atmosphere measured by stellar occultations with Mars Express SPICAM, J. Geophys. Res., 114, E01004, 2009

[2] McClintock, W. E., N. M. Schneider, G. M. Holsclaw, J. T. Clarke, A. C. Hoskins, I. Stewart, F. Montmessin, R. V. Yelle, and J. Deighan: The Imaging Ultraviolet Spectrograph (IUVS) for the MAVEN Mission, Space Sci. Rev., 1–50, 2014

[3] Nier, A. O., and M. B. McElroy: Composition and structure of Mars' upper atmosphere - Results from the neutral mass spectrometers on Viking 1 and 2, J. Geophys. Res., 82, 4341–4349, 1977

[4] Quémerais E., J.-L. Bertaux, O. Korablev, E. Dimarellis, C. Cot, B. R. Sandel, and D. Fussen: Stellar occultations observed by SPICAM on Mars Express, J. Geophys. Res., 111, E09S04, 2006

[5] Sandel, B. R., H. Gröller, R. V. Yelle, T. Koskinen, N. K. Lewis, J.-L. Bertaux, F. Montmessin, and E. Quémerais, Altitude profiles of O_2 on Mars from SPICAM stellar occultations, Icarus, 252, 154–160, 2015

EPSC Abstracts
Vol. 10, EPSC2015-410, 2015
European Planetary Science Congress 2015

First Results From MAVEN's Imaging UV Spectrograph

N.M. Schneider (1), W.E. McClintock (1), A.I.F. Stewart (1), J.Deighan (1), J.T. Clarke (2), G.M. Holsclaw (1), F. Montmessin (3), F. Lefèvre (3), J.Y. Chaufray (3), S.K. Jain (1), A. Stiepen (1), M.S. Chaffin (1), M. Crismani (1), M. Matta (2), J.S. Evans (4), M.H. Stevens (5), R.V. Yelle (6) and B.M. Jakosky (1)

(1) Laboratory for Atmospheric and Space Physics, University of Colorado, 3665 Discovery Dr., Boulder, CO 80303, (2) Center for Space Physics, Boston University, Boston, MA, USA, (3) LATMOS/IPSL, Guyancourt, France, (4) Computational Physics, Inc., 8001 Braddock Road, Suite 210, Springfield, VA 22151, (5) Space Science Division, Naval Research Laboratory, 4555 Overlook Ave., SW, Washington, DC 20375, (6) Lunar & Planetary Laboratory, U. Arizona, Tucson, AZ 85721 (nick.schneider@lasp.colorado.edu)

Abstract

We report the first results from The Imaging Ultraviolet Spectrograph (IUVS) aboard the Mars Atmosphere and Volatile and EvolutioN (MAVEN) spacecraft orbiting Mars. The instrument is accomplishing its goals of characterizing the atmospheric composition and structure, enabling studies of atmospheric escape that will contribute to our understanding of Mars' atmospheric evolution. In addition, the instrument has made unexpected discoveries concerning meteor showers, aurora and nightglow on Mars.

1. Introduction

The Imaging Ultraviolet Spectrograph (IUVS) [1] is one of nine science instruments aboard the Mars Atmosphere and Volatile and EvolutioN (MAVEN) spacecraft which entered Mars orbit on 21 September 2014. IUVS is designed to explore the planet's upper atmosphere and ionosphere and examine their interaction with the solar wind and solar ultraviolet radiation. The instrument is one of the most powerful spectrographs sent to another planet, with several key capabilities: (1) separate Far-UV & Mid-UV channels for stray light control, (2) a high resolution echelle mode to resolve deuterium and hydrogen emission, (3) internal instrument pointing and scanning capabilities to allow complete mapping and nearly-continuous operation, and (4) optimization for airglow studies.

2. MAVEN Science Goals

IUVS, along with other MAVEN insturments, obtains a comprehensive picture of the current state of the Mars upper atmosphere and ionosphere and the processes that control atmospheric escape. Data returned by MAVEN will allow us to determine the role that loss of volatile species from the atmosphere to space has played in shaping the history of Mars climate, liquid water, and habitability. MAVEN is designed to answer three top-level science questions [2]:

- What is the current state of the upper atmosphere and ionosphere, and what processes control it?
- What are the rates of escape of atmospheric gases to space today and how do they relate to the underlying processes that control the upper atmosphere?
- What has been the total atmosphere loss to space through time?

3. IUVS Objectives

MAVEN's instrument complement answers these questions by combining observations of Mars' atmosphere and ionosphere with observations of the solar influences that control it. MAVEN has four instruments for atmospheric measurements that record atoms, molecules and ions through *in situ* measurements, probing conditions at the location of the spacecraft as it passes through the upper atmosphere. By contrast, IUVS derives atmospheric properties at a distance through spectroscopic measurements of UV emissions from atmospheric gases. IUVS makes quantitative measurements of the Mars atmosphere between altitudes of 30 and 4500 km, over all latitudes, longitudes and local times. Specifically, IUVS measures the composition and structure of the upper atmosphere by measuring:

- Thermosphere profiles of neutrals (H, C, O, N, CO, CO_2, N_2) and ions (C^+, CO_2^+) using limb scanning.

- Column abundance maps of H, C, O, CO_2, O_3 and dust in the upper atmosphere over the portion of the planetary disk that is illuminated and visible from high orbital altitudes using disk mapping.
- Coronal vertical profiles of hot species (H, D and O) using coronal scans.
- Mesosphere/thermosphere vertical profiles of CO_2 and O_3 using stellar occultations.

These observations offer three major contributions to MAVEN science: (1) making independent measurements of key properties also measured by *in situ* instruments for validation and redundancy; (2) providing the global context for *in situ* measurements taken along the spacecraft orbit, and (3) making unique measurements of atmospheric constituents and properties not possible with other instruments. Furthermore, thanks to instrument design and spacecraft accommodation, IUVS can observe Mars nearly continuously throughout the mission.

4. IUVS Initial Results

Each IUVS observational mode has successfully observed the spectral features and spatial distributions as intended, confirming and expanding our understanding of the Mars upper atmosphere as observed by the Mariner spacecraft, Viking and Mars Express. Initial results include:

- Observations of the aftermath of a meteor shower, in the form of intense emission from metal ions and neutrals from ablated Siding Spring meteors (Fig. 1);
- Diffuse auroral emissions of substantially greater nightside extent than seen by MEX/SPICAM, and frequent detections of nitric oxide nightglow;
- Significant persistent structures in the thermospheric dayglow emissions, dependent primarily on solar zenith angle, along with significant variability on daily timescales;
- Confirmation of N_2 emission in the VK band, as first reported by MEX/SPICAM;
- Spatially-resolved measurements of the D/H ratio in the upper atmosphere and its temporal evolution;
- The most complete maps and vertical profiles of H, C and O in the Mars corona (Fig. 2);
- The first global snapshot of the middle atmosphere obtained by a day-long stellar occultation campaign;
- Global ozone maps spanning six months of seasonal evolution.

5. Figures

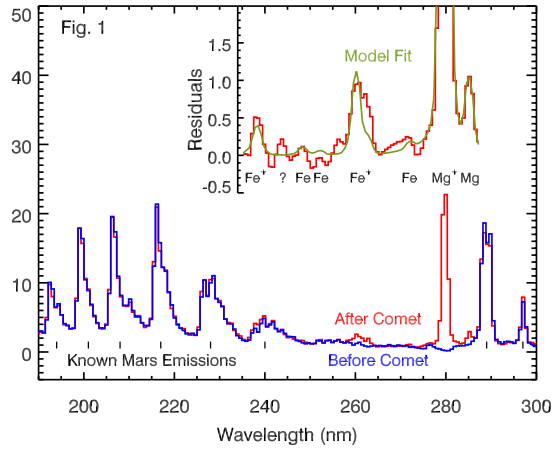

Figure 1: Spectra of Mars' atmosphere immediately before and after the closest approach of Comet Siding Spring. Spectra have been scaled and their backgrounds matched. The inset shows a smoothed difference spectrum, obtained by modeling and subtracting known Mars emissions and backgrounds. Numerous emissions from Mg^+, Mg, Fe^+, Fe, and other unidentified features are indicated.

.

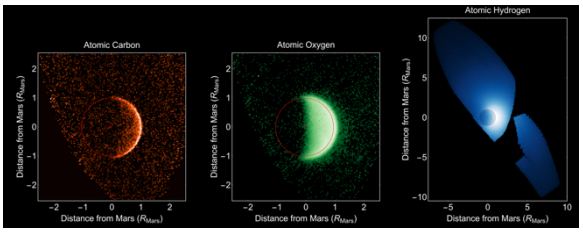

Figure 2. Three views of an escaping atmosphere, showing atomic carbon (166 nm), oxygen (130 nm) and hydrogen (122 nm). By observing all of the products of water and carbon dioxide breakdown, IUVS can characterize the processes that drive atmospheric loss on Mars.

References

[1] McClintock, W.E. *et al.* (2014), The Imaging Ultraviolet Spectrograph (IUVS) for the MAVEN Mission, *Space Sci. Rev.*, DOI 10.1007/s11214-014-0098-7.

[2] Jakosky, B., *et al.* (2014), The 2013 Mars Atmosphere and Volatile Evolution (MAVEN) mission to Mars. *Space Sci. Rev.*, doi: 10.1007/s11214-015-0139-x.

EPSC Abstracts
Vol. 10, EPSC2015-420, 2015
European Planetary Science Congress 2015

Coupling Photochemistry to the NASA Mars Climate Modeling Center 3D Mars Global Circulation Model (gcm2.1v24)

A. Brecht (1, 2), M. Kahre (2), R. Haberle (2), J. Hollingsworth(2), and F. Lefèvre(3)

(1) Bay Area Environmental Research Institute, Petaluma, CA, USA, (2) NASA Ames Research Center, Moffett Field, CA, USA, (3) LATMOS, Guyancourt, France (Amanda.s.brecht@nasa.gov / Fax: 650-604-6779)

Abstract

In the work to be presented, a photochemical model has been coupled to the NASA Mars Climate Modeling Center (MCMC) 3D Mars global circulation model (Mars GCM) (gcm2.1v24). This photochemistry coupling provides 3D chemical fields which interact spatially and temporally with the evolving temperature and winds fields. The addition of photochemistry is recognized to be critical in the effort in extending the Mars GCM to middle atmospheric levels and further to provide more constraints in understanding the Martian global atmospheric circulation.

1. Introduction

The NASA MCMC 3D Mars GCM (gcm2.1v24) has been extended to incorporate the middle atmosphere (~80 km to ~120 km). The model extension is important because it provides an integrated framework with a deeper domain to examine seasonal mean fields and large-scale wave activity with insight into circulation patterns in the middle atmosphere.

Temperatures from the Mars GCM with the extension (i.e. incorporation of Non-Local Thermodynamic Equilibrium (NLTE) heating and cooling) have been compared to observations, specifically observations from the ESA MEx SPICAM instrument. The comparison between SPICAM and Mars GCM are not in great agreement [2]. Results from the comparison show the simulation is very warm at lower pressures (<1E-3) compared to SPICAM profiles (see Fig. 1). The main reason for the extra warming is the underestimated fixed atomic oxygen profile used for the CO_2 15-µm cooling parameterization. [4] performed a study and found the fixed reference atomic oxygen profile used within the cooling parameterization (which is currently utilized within the Mars GCM) are below the actual abundance levels. Furthermore, it has been suggested that the CO_2 15-µm cooling is sensitive to the abundance of atomic oxygen ([1],[6]). The sensitivity to the atomic oxygen profile has been reproduced with test cases utilizing the Mars GCM (not shown). Therefore, this leads into incorporating calculated/updated chemistry (photochemical scheme) in the Mars GCM.

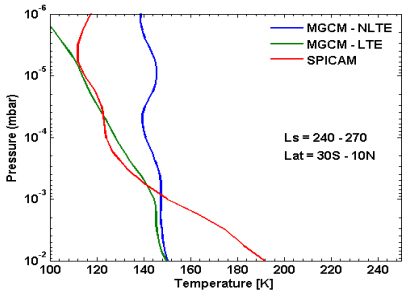

Figure 1: Comparison of zonally averaged temperature profiles from Mars GCM simulations (NLTE – blue solid line and LTE – green solid line) and SPICAM observations (red solid line).

2. Photochemistry within the Mars GCM

To properly simulate the middle atmosphere, specifically the temperatures, the Mars GCM needs updating chemistry for the CO_2 15-µm cooling scheme.

2.1 Photochemistry Scheme

The implemented photochemistry scheme within the Mars GCM is described in detail by [5]. The chemical package calculates oxygen, hydrogen, and CO. More specifically, the scheme accounts and transports 12 species (O, $O(^1D)$, O_2, O_3, H, OH, HO_2, H_2O_2, H_2, H_2O, CO, and CO_2). To save computational resources, the photolysis rates are calculated off-line using the [7] model adapted to Martian conditions. The rates are stored into a four-dimensional lookup table as a function of the overhead CO_2 column, the overhead O_3 column, the solar zenith angle, and the temperature. The model interpolates the table values to calculate the photolysis rate for the actual sunlight grid point. The Gas-phase reaction rate coefficients were mostly adopted from [8]. The rate coefficients of three-body reactions are increased by a factor of 2.5, to account for the higher efficiency of CO_2 as a third body in comparison with N_2 and O_2. Chemical families were adopted for O_x and HO_x species (O_x = O + O_3; HO_x = H + OH + HO_2) in order to reduce computational time. The chemical long-lived species (O_2, H_2, H_2O, CO, HO_x, O_x) are solved for by using the implicit method described by [9]. The short-lived species are assumed to be in photochemical equilibrium (O_3, $O(^1D)$, OH, HO_2).

2.2 Discussion

The important species for the NLTE CO_2 15-µm cooling scheme, besides CO_2, is atomic O. However, at this time measurements of atomic O are not possible. Therefore, ozone will be used as an initial study and constraint for atomic O.

Ozone is produced in two steps. The first step is photolysis of CO_2 and O_2; secondly, the recombination of the product of O and O_2. It is destroyed by two mechanisms: (1) photolysis and (2) the reaction with HO_x radicals (OH, HO_2). Because ozone is destroyed by HO_2, ozone is expected and predicted to be strongly anti-correlated with water vapor (e.g. [5]). Ozone has also been observed to vary seasonally and diurnally (e.g. [3]). The seasonal peak concentration has been observed in the Northern and Southern polar winters. The simulated results from the Mars GCM will be compared to observations and other published GCM results (i.e. LMD GCM). The anti-correlation, seasonal variation, and diurnal variation will be presented.

6. Summary and Conclusions

A photochemical package has been coupled to the NASA MCMC Mars GCM. One of the reasons for this coupling is to provide a more realistic atmosphere for the CO_2 15-µm parameterization, which is key to modeling the middle atmosphere temperatures. The initial testing of the photochemical package is to compare the simulated ozone to observations and other published GCM results, which will be presented. Furthermore, the current status of the NASA MCMC Mars MGCM vertical grid extension will be presented.

References

[1] Bougher, S. W., Hunten, D., and Roble, R.: CO_2 cooling in terrestrial planet thermospheres, J. Geophys. Res., 99(E7), pp. 14609-14622, 1994.

[2] Brecht, A., Hollingsworth, J., and Kahre, M.: Mars' Thermal Structure From the Lower to Middle Atmosphere: NASA Ames Mars General Circulation Simulations, Eighth International Conference on Mars, 14-18 July 2014, in Pasadena, CA, USA, 2014.

[3] Clancy, R. T., et al.: MARCI Global Daily Ozone Mapping and Comparison to LMD GCM Simulations: Polar Dynamics, Hellas Basin, and Heterogeneous Chemistry, The Fifth International Workshop on the Mars Atmosphere: Modelling and Observations, 13-16 January 2014, in Oxford U.K., 2014.

[4] Forget, F., et al..: Density and temperatures of the upper Martian atmosphere measured by stellar occultations with Mars Express SPICAM, J. Geophys.Res. (Planets), 114, 1004–+, 2009.

[5] Lefèvre, F., Lebonnois, S., Montmessin, F., and Forget, F.: Three-dimensional modelling of ozone on Mars, J. Geophys. Res., 109, E07004, 2004.

[6] M. López-Puertas and López-Valverde, M.: Radiative Energy Balance of CO_2 Non-LTE Infrared Emissions in the Martian Atmosphere, Icarus, Volume 114, Issue 1, pp. 113-129, 1995.

[7] Madronich, S. and Flocke, S.: The Role of Solar Radiation in Atmospheric Chemistry, pp. 1-26, Springer-Verlag, New York, 1998.

[8] Sander, S., et al.: Chemical kinetics and photochemical data for use in atmospheric studies, Evaluation number 14, JPL Publ. 02-25, Jet Propul. Lab., Pasadena, Calif., 2003.

[9] Shimazaki, T.: Minor Constituents in the Middle Atmosphere, Terra Sci, Tokyo, 1985.

EPSC Abstracts
Vol. 10, EPSC2015-421, 2015
European Planetary Science Congress 2015

CO_2-driven formation of gullies on Mars

C. Pilorget (1,2) and F. Forget (3)
(1) Division of Geological and Planetary Sciences, Caltech, Pasadena, CA 91125, USA, (2) Institut d'Astrophysique Spatiale, CNRS/Université Paris Sud, UMR8617, Orsay 91405, France, (3) Laboratoire de Météorologie Dynamique, IPSL, Paris, France (cedric.pilorget@ias.u-psud.fr)

Introduction and summary

Since their discovery by the Mars Observer Camera [1], Martian Gully landforms have attracted considerable attention because they resemble terrestrial debris flows formed by the action of liquid water [1,2]. They have thus been argued to be evidence for relatively recent potential liquid-water habitat on Mars. This interpretation is now questioned by the discovery of ongoing gully formation occurring in conditions much too cold for liquid water, but with seasonal CO_2 frost present and defrosting [3-5]. However, how a relatively thin seasonal dry ice cover could trigger the formation of decameter large debris flows exhibiting levees and sinuosities as if they were liquid-rich remained mysterious

Using a thermo-physical model of the Martian soil, we have found that, during the defrosting season, the pores below the ice layer can be filled with CO_2 ice, and subject to extreme pressure variations. The subsequent gas fluxes destabilize the soil and create gas-lubricated debris flows with the observed geomorphological characteristics of the Martian gullies. Moreover, such subsurface activities are precisely predicted at latitudes and slope orientations where gullies are observed. This shows that Martian gullies likely result from geological dry ice processes with no earthly analogs.

Modeling

We have developed a model able to compute the seasonal evolution of a column composed of an underlying regolith, a CO_2 ice layer, and the atmosphere above [6,7]. Below the surface, in the CO_2 ice layer (when present) and in the regolith, the model simultaneously solves the heat conduction and the radiative transfer through the ice [7] as well as the diffusion, condensation and sublimation of CO_2 and the related latent heat exchanges. A characteristic of the locations where CO_2 ice is predicted to condense (above 50° latitude on flat surface and down to ~30° latitude on pole-facing slope) is that a subsurface water ice table in equilibrium with the atmospheric water vapor is always expected to be present below a dry material layer of several centimeters to a few tens of centimeters [8]. We modeled the regolith accordingly, with a dry porous layer lying above an impermeable, ice-cemented, high thermal inertia soil.

Exemple on the Russell Crater megadune

Simulations were first performed to model the Russell crater megadune (54.5°S, 12.7°E), one of the key locations where recent gully formation has been observed [3,5]. While CO_2 condenses on the surface in late fall, it is observed that the albedo remains low [9], suggesting that the solid CO_2 forms a translucent slab of ice. In the model, as the daytime solar light penetrates into the CO_2 ice slab and heats the underlying regolith, the temperature at the base of the CO_2 ice slab increases. Some CO_2 sublimes and diffuses down to keep the porous layer sandwiched between the CO_2 ice and the impermeable permafrost in vapor pressure equilibrium with the CO_2 ice slab (Fig.1). The gas is trapped and the pressure can rise significantly. At the end of winter, the thickness of the CO_2 ice layer reaches 30 cm while the solar flux at midday increases. Around Ls=149°, the temperature in the regolith substrate increases from 153 K in the morning up to about 158 K in the afternoon. Accordingly the pressure rises daily from 1200 to 2300 Pa, well above the atmospheric pressure at 590 Pa. Two interesting phenomena then occur during daytime. First, the temperature within the regolith tends to be lower than at the top of the regolith where the solar flux is absorbed. As a consequence, CO_2 condenses in the coldest pores of the soil a few cm below the CO_2 ice slab base. Second, the pressure below the ice can overcome the cryostatic pressure exerted by the CO_2 ice layer and lift it. Eventually the slab should rupture to form jets of CO_2 gas [10] potentially carrying some regolith

material with it. The pressure within the pores then drops down to the atmospheric pressure, leading to a much lower condensation temperature than prior to the ejection (T_{cond} ~148 K). The CO_2 ice that is present within the pores and at the base of the slab sublimes rapidly.

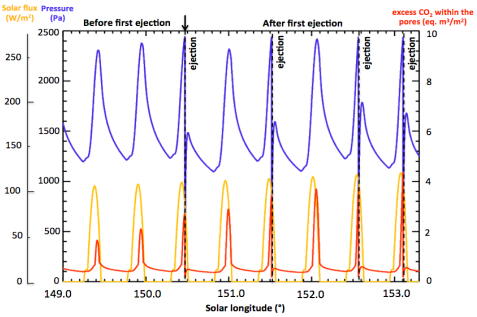

Figure 1: Evolution of the CO_2 gas pressure and total amount of CO_2 (pressurized gas and ice, converted to a volume at atmospheric pressure) in the porous soil below the seasonal CO_2 ice sheet simulated on the Russell crater megadune over an 8 sol period in late southern winter, at the time of the first CO_2 gas ejections and ice layer ruptures. This illustrates the large amount of gas in excess that must flow through the soil porous medium and which can destabilize and fluidize the subsequent debris flow.

When occurring on slopes, this process is likely to destabilize large amount of soil material. The volume of gas that has to flow up through the soil pores is considerable because it combines the depressurized excess gas (up to 1 m^3 per m^2 in our example) with the gas produced by the sublimation of the CO_2 ice present within the regolith and which becomes suddenly unstable (up to 3 m^3 per m^2). Furthermore, a large part of the gas will flow laterally through the porous medium to reach the location of the vent in the slab.

While this process has no exact analog on Earth, it can be related to terrestrial pyroclastic flows, which are gas-particle mixtures generated during volcanic eruptions. A wide range of pyroclastic flows exists, depending on the proportion of gases, and our case can be compared to the denser ones dominated by particle friction [11]. These have been found to exhibit levees [11] which are very similar in size to the ones observed on Mars [2]. The viscosity of typical flows in our simulations can be estimated to range from a few tens to a few thousands of Pa.s, similar to water triggered debris flows. In our simulation this process can repeat multiple times throughout the defrosting season. On the Russell crater's dune, CO_2 induced debris flows are thus predicted to occur between Ls=150° and Ls~205°, in agreement with the available observations [5]. However, each ejection will not generate a debris flow. As on Earth where debris flows triggered by melting snow are rare, stochastic events, it is likely that an uncommon combination of conditions are required to destabilize the slopes.

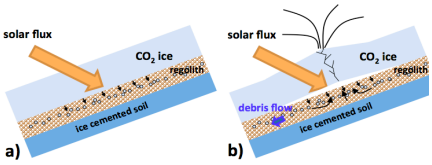

Figure 2: the sequence of events leading to the formation of CO_2-regolith viscous flows

Spatial distribution of gullies

We performed model calculations for a wide range of latitudes and slope orientations. These simulations reveal that high-pressure CO_2 gas trapping in the subsurface and the subsequent formation of ice within the regolith pores can occur where gullies are observed, and not elsewhere. In particular the model explains why gullies are only observed on pole facing slopes between 30° and 45° latitude, and with no orientation preference above 45° latitude [12].

Acknowledgements

C.P acknowledges support from NNX14AG54G and CNES.

References

[1] Malin et al. *Science* 288, 2330-2335 (2000) [2] Mangold et al. *JGR* 108, 5027 (2003). [3] Reiss et al. *GRL* 37, L06203 (2010) [4] Hansen et al., *Science* 331, 575- (2011) [5] Dundas et al. *Icarus* 220, 124-143 (2012). [6] Forget, *et al. JGR* 104, 24155-24176 (1999) [7] Pilorget et al. *Icarus* 213, 131-149 (2011) [8] Aharonson and Schorghofer *JGR.* 111, E11007 (2006). [9] Reiss et al. *GRL* 30, 1321 (2003). [10] Kieffer et al. *Nature* 442, 793-796 (2006) [11] Félix and Thomas *EPSL* 221, 197-213 (2004) [12] Balme et al. *JGR* 111, E05001 (2006).

EPSC Abstracts
Vol. 10, EPSC2015-436, 2015
European Planetary Science Congress 2015

3D Modelling of the impact of outflow channel events on Late Hesperian Mars climate.

M. Turbet (1,2), F. Forget (1), R. Wordsworth (3) and J.W. Head (4)
(1) Laboratoire de Météorologie Dynamique (LMD), Université Pierre et Marie Curie (UPMC), 4 place Jussieu, 75252 Paris, FRANCE (2) Ecole Normale Supérieure, Département de physique, 24 rue Lhomond, Paris, FRANCE (3) Harvard school of Engineering and Applied Sciences, Cambridge, MA, USA (4) Department Of Geological Sciences, Brown University, Providence, RI, USA. (mturbet@lmd.jussieu.fr)

1. Introduction

During late Hesperian, large outflow channels observed in the Chryse Planitia area [1] are thought to have been carved by catastrophic and sudden water floods [2,3]. It has been speculated that such events may have modified the climate, at least locally and episodically, and could have induced precipitations and even rain [4] that could explain the formation of Late Hesperian valley networks under a cold contemporaneous climate.

We present below 3D modeling of a sudden and extreme release of warm liquid water in the Chryse Planitia area on ancient Mars, assuming a faint young Sun and CO_2-dominated atmospheres thicker than today. 3D climate modeling under these conditions [5,6], and performed with a water cycle taking into account water vapor and clouds, have not been able yet to produce liquid water or at least significant precipitations by climatic processes anywhere on the planet, even when maximizing the greenhouse effect of CO_2 ice clouds.

2. Method

The study was lead thanks to the complete 3 Dimensions LMD Global Circulation Model, performed in a 64x64x15 resolution grid, that takes into account generalized radiative transfer and cloud physics. The model works with a water cycle that includes the formation of water clouds, ice clouds and CO_2 ice clouds. The version we use here is designed to work under CO_2 atmospheres presented in Forget et al. 2013 and Wordsworth et al. 2013 [5,6].

We started from a converging initial state with stabilized surface water ice reservoir [6] and assumed that a warm source of liquid water, modeled by a layer of fully mixed water above a multilayers cold martian regolith, suddenly fills the Chryse Planitia area. The largest estimations of outflow channel events [7] give an amount on the order of an equivalent of a several meters thick layer of water at few tens of degrees above the freezing point, over the whole planet. Thus, we explored the influence of warm (~300K) large amounts of water (~100 meters deep) discharged in area ranging from the Chryse Planitia area to the whole Northern plains, and under various atmospheric pressures.

3. Results and Discussion

The figure 1 presents the results of the total cumulative precipitations induced by the climatic impact of a 100m thick layer of 320K liquid water emplaced at the Chryse Planitia location (~2.10^{22}J event), under atmospheres of 40mbar and 1bar.

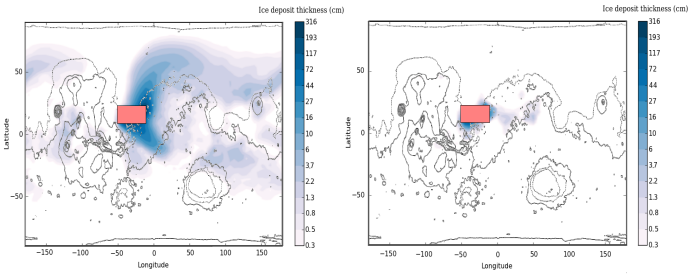

Figure 1: Total accumulation of surface ice (cm per m^2) induced by precipitations, 100 days after the outflow channel event, under a 40mbar atmosphere (left) and a 1bar atmosphere (right). The warm liquid water discharge area is displayed in pink.

We found that the climatic impact of the outflow channel, in spite of the fact that the intensity of the event was very high, is low. The precipitations – only snowfalls – stop after few tens of days whatever the atmospheric pressure is.

For the first few days, an intense local water cycle takes place. The atmosphere is warmed very quickly by the water vapor latent heat and by radiative transfer processes. But then, it takes only ~100 days (figure 2) for the initial energy reservoir to run out / for the liquid water to start to freeze and ~50 martian years to be completely frozen.

The thiner the atmosphere is, the shorter the relaxing timestep of the atmosphere will be. First, for the spread of a given initial reservoir amount of energy, a thin atmosphere will be warmer and will radiate more efficiently to space (figure 2). Second, because a thin atmosphere will inject (figure 3) more water but also create more water ice clouds which are responsible for a large solar absorption loss (figure 2).

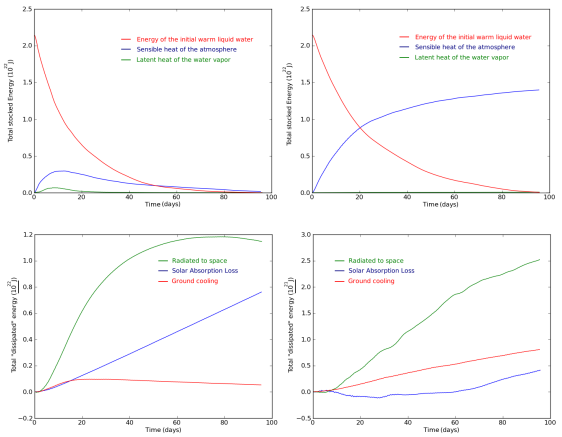

Figure 2: Evolution of energy reservoirs (top pannels) and energy cumulative loss (low pannels) with time, under a 40mbar atmosphere (left pannels) and a 1bar atmosphere (right pannels). These figures were drawn with respect to a control simulation.

We in fact found that the direct climatic impact is much higher for thiner atmospheres (figure 1). A thin atmosphere, because of its low volumetric heat capacity, will warm quickly and thus be able to transport much more water vapor. This will trigger the formation of a convective plume (figure 3) that is very efficient to transport water vapor and ice responsible for further global scale precipitations.

More results will be discussed at the EPSC about **1.** the conditions required for the outflow channel events to trigger a deep convection through the formation of a convective plume (figure 3) and **2.** the possible dumping of the warm liquid water from Chryse Planitia to Acidalia Planitia and even to the Northern Plains.

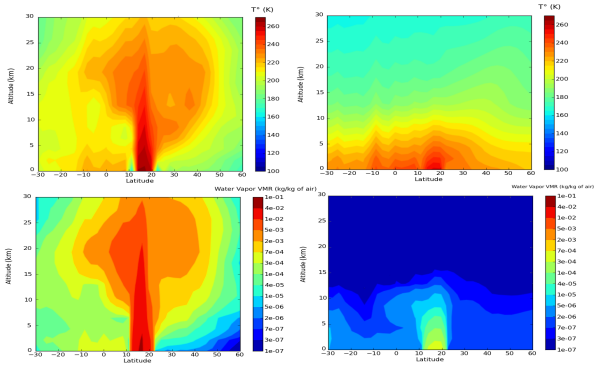

Figure 3: Temperature (top pannels) and Water Vapor Mixing Ratio (low pannels) distributions at the longitude of the liquid water discharge (40°W), 2 days after the outflow channel event, under a 40mbar atmosphere (left) and a 1bar atmosphere (right).

References

[1] Mangold, N. et al. 2004. Evidence for Precipitation on Mars from Dendritic Valleys in the Valles Marineris Area, Science, vol. 305.

[2] Baker, V.R. 1982. The channels of Mars, University of Texas Press, Austin.

[3] Carr M.H. et al. 1996, Water on Mars, Oxford University Press, Oxford.

[4] Kite E.S. et al. 2011, Localized precipitation and runoff on Mars, JGR, vol. 116, DOI:10.1029.

[5] Forget et al. 2013, 3D Modeling of the early martian climate under a denser CO_2 atmosphere : Temperatures and CO_2 ice clouds, Icarus 222 1-19.

[6] Wordsworth et al. 2013, Global Modeling of the early martian climate under a denser CO_2 atmosphere : Water cycle and ice evolution, Icarus 222 1-19.

[7] Kreslavsky M.A. & Head J.W. 2002, Fate of outflow channel effluents in the northern lowlands of Mars : The Vastitas Borealis Formation as a sublimation residue from frozen ponded bodies of water, JGR, vol. 107, NO. E12, 5121.

EPSC Abstracts
Vol. 10, EPSC2015-438, 2015
European Planetary Science Congress 2015

The Mars Climate Database (MCD version 5.2)

E. Millour(1), F. Forget(1), A. Spiga(1), T. Navarro(1), J.-B. Madeleine(1), L. Montabone(1,2), A. Pottier(1,3), F. Lefevre(3), F. Montmessin(3), J.-Y. Chaufray(3), M.A. Lopez-Valverde(4), F. Gonzalez-Galindo(4), S.R. Lewis(5), P.L. Read(6), J.-P. Huot(7), M.-C. Desjean(8) and the MCD/GCM development team.
(1) Laboratoire de Météorologie Dynamique, IPSL, Paris, France (millour@lmd.jussieu.fr), (2) Space Science Institute, Boulder, USA, (3) Laboratoire Atmosphères, Milieux, Observations Spatiales, IPSL, Paris, France, (4) Instituto de Astrofisica de Andalucia, Granada, Spain, (5) Department of Physics and Astronomy, The Open University, Milton Keynes, UK, (6) Atmospheric, Oceanic & Planetary Physics, University of Oxford, UK, (7) European Space Research and Technology Centre, European Space Agency, Noordwijk, Netherlands, (8) Centre National d'Etudes Spatiales, Toulouse, France

Abstract

The Mars Climate Database (MCD) is a database of meteorological fields derived from General Circulation Model (GCM) numerical simulations of the Martian atmosphere and validated using available observational data. The MCD includes complementary post-processing schemes such as high spatial resolution interpolation of environmental data and means of reconstructing the variability thereof. We have just completed (March 2015) the generation of a new version of the MCD, MCD version 5.2.

1. Introduction

The GCM that is used to create the MCD data is developed at Laboratoire de Météorologie Dynamique du CNRS (Paris, France) [1-3] in collaboration with the Open University (UK), the Oxford University (UK) and the Instituto de Astrofisica de Andalucia (Spain) with support from the European Space Agency (ESA) and the Centre National d'Etudes Spatiales (CNES).

The MCD is freely distributed and intended to be useful and used in the framework of engineering applications as well as in the context of scientific studies which require accurate knowledge of the state of the Martian atmosphere. Over the years, various versions of the MCD have been released and handed to more than 150 teams around the world. Current applications include entry descent and landing (EDL) studies for future missions (Insight, ExoMars), investigations of some specific Martian issues (via coupling of the MCD with homemade codes), analysis of observations (Earth-based as well as with various instruments onboard Mars Express and Mars Reconnaissance Orbiter),...

The MCD is freely available upon request (simply contact millour@lmd.jussieu.fr or forget@lmd.jussieu.fr); a simplified web interface for quick browsing at MCD outputs is available on http://www-mars.lmd.jussieu.fr .

2. Overview of MCD contents

The MCD provides mean values and statistics of the main meteorological variables (atmospheric temperature, density, pressure and winds) as well as atmospheric composition (including dust and water vapor and ice content), as the GCM from which the datasets are obtained includes water cycle [4,5], chemistry [6], and ionosphere [7,8] models.

The database extends up to and including the ther-mosphere [9,10] (~350km). Since the influence of Ex-treme Ultra Violet (EUV) input from the sun is signifi-cant in the latter, 3 EUV scenarios (solar minimum, average and maximum inputs) account for the impact of the various states of the solar cycle. MCD provides mean values and statistics of the main meteorological variables (atmospheric temperature, density, pressure and winds) as well as atmospheric composition (including dust and water vapor and ice content), as the GCM from which the datasets are obtained includes water cycle [4,5], chemistry [6], and ionosphere [7,8] models.

The database extends up to and including the thermosphere [9,10] (~350km). Since the influence

of Extreme Ultra Violet (EUV) input from the sun is significant in the latter, 3 EUV scenarios (solar minimum, average and maximum inputs) account for the impact of the various states of the solar cycle.

As the main driver of the Martian climate is the dust loading of the atmosphere, the MCD provides climatologies over a series of **dust scenarios** : **standard year** (a.k.a. **climatology**) , **cold** (i.e: low dust), **warm** (i.e: dusty atmosphere) and **dust storm**, These are derived from home-made, instrument-derived (TES, THEMIS, MCS, MERs), dust climatology of the last 8 Martian years [11]. In addition, we also provide additional "add-on" scenarios which focus on individual Martian Years (MY 24 to 31) for users more interested in specific climatologies than the MCD baseline scenarios designed to bracket reality.

The MCD provides users with:

- Mean values and statistics of main meteorological variables (atmospheric temperature, density, pressure and winds), as well as surface pressure and temperature, CO2 ice cover, thermal and solar radiative fluxes, dust column opacity and mixing ratio, [H20] vapour and ice concentrations, along with concentrations of many species: [CO], [O2], [O], [N2], [Ar], [H2], [O3], [H] ..., as well as electrons mixing ratios.
- Dust mass mixing ratio, along with estimated dust effective radius and dust deposition rate on the surface are also provided
- Following the recent improvements on the parametrization of physical processes in the Planetary Boundary Layer (PBL) [12], many related fundamental quantities such as PBL height, minimum and maximum vertical convective winds in the PBL, surface wind stress and sensible heat flux,... are available.
- A high resolution mode which combines high resolution (32 pixel/degree) MOLA topography records and Viking Lander 1 pressure records with raw lower resolution GCM results to yield, within the restriction of the procedure, high resolution values of atmospheric variables.
- The possibility to reconstruct realistic conditions by combining the provided climatology with additional large scale (derived from Empirical Orthogonal Functions extracted from the GCM runs) and small scale perturbations (gravity waves) schemes.

3. Validation of MCD version 5.2

At EPSC, we will show and discuss how MCDv5.2 compares with available measurements (as illustrated in Figure 1) from many available sources (e.g. landers and rovers, instruments onboard past and present orbiters).

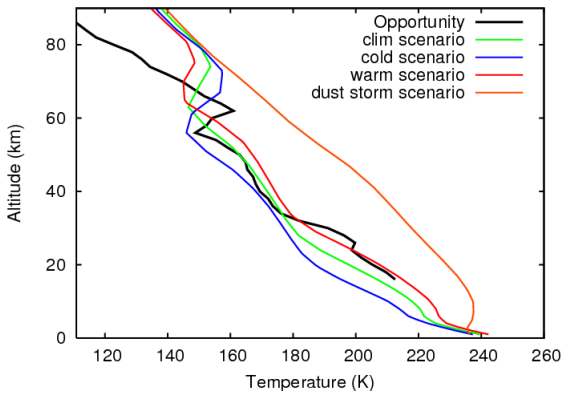

Figure 1: Illustration of the way the MCD dust scenarios bracket reality, in the present case with a comparison to the temperature profile (retrieved by P. Withers) from Opportunity entry, which occurred during a local dust storm.

References

[1] Forget F., et al. (1999) *JGR*, 104, E10. [2] Lewis S., et al. (1999) *JGR*, 104, E10. [3] Forget F., et al. (2014), *5th Int. Workshop on Mars Atmosphere Modeling and Observations.* [4] Madeleine J.-B., et al. (2012) *GRL*, 39:23202. [5] Navarro T., et al. (2014) *JGR (Planets).* [6] Lefevre F, et al. (2011), *4th Int. Workshop on Mars Atmosphere Modeling and Observations*. [7] Gonzalez-Galindo F., et al. (2013) *JGR (Planets)*, 118. [8] Chaufray J.-Y., et al. (2014), *5th Int. Workshop on Mars Atmosphere Modeling and Observations.* [9] Gonzalez-Galindo F., et al. (2009) *JGR*, 114. [10] Gonzalez-Galindo F., et al. (2014) , *5th Int. Workshop on Mars Atmosphere Modeling and Observations.* [11] Montabone L., et al. (2015) *Icarus*. [12] Colaitis A., et al. (2013) *JGR (Planets)*.

EPSC Abstracts
Vol. 10, EPSC2015-442, 2015
European Planetary Science Congress 2015

Long-Term evolution of the erosion rates during Early Mars

C. Quantin[1], R. A. Craddock[2], F. Dubuffet[1], L. Lozac'h[1], M. Martineau[1], [1] Laboratoire de Géologie de Lyon Terre, Planètes, Environnement (CNRS-ENSLyon-Université lyon1), ERC eMars Team, 2 rue Raphaël Dubois 69622 Villeurbanne Cedex, France, [2] Center for Earth and Planetary Studies, National Air and Space Museum, Smithsonian Institution, Washington,. District of Columbia, USA

Abstract

Many Geologic features attest to the fact that liquid water was once stable on the Martian surface. The erosional processes necessary to create these features must have been supported by a climate that is much different than today. However, the evolution of these primitives conditions toward the current dry and cold Martian climate where the erosion processes are 2-3 orders in magnitude lower represents a major gap in our understanding of the evolution of Mars history. Here we document the time-dependence of the erosion rates on Mars during early Mars, period during which the erosion rates have decreased of at least one order in magnitude.

1. Introduction

Despite recent observations about the processes that occurred on early Mars, we have yet to reconstruct the early climatic evolution of the red planet. Did Mars experience an early wet and warm climate as suggested by the presence of valley networks, modified crater or outflows channels ? If so, how long and intense (in term of erosion rates) was this wet period ?

Crater size distributions of a planetary surfaces, and especially old surfaces of Mars, record both the cratering rate and the geological history. Variations from a theoretical crater size distribution that would result from meteoritic bombardment is interpreted as erosional or depositional processes and is called the Opick effect [1,2]. From early as Mariner mission times, such processes have been suggested to explain the difference between Martian crater size distributions compared to the lunar ones [3, 4, 5]. In fact, noachian terrains on Mars display a typical S-shape crater size distribution that implies that processes have removed craters as large as 30 km in diameter from the cratering record. To date, no effort have been done to quantify these processes from crater statistics.

Here, we develop a numerical model to generate synthetic crater size distributions while applying a model of impact rate evolution as well as a model of obliteration rate evolution. Then, we used the model to inverse about 35 crater size distributions extracted from large Martian areas. First, we present the model and the inversion method. Then, we present the results that allow us to constrain the erosion rate evolution during early Mars.

2. Method

The model : To built the model of crater obliteration rate, we used the cratering rate model defined by [6] from the cratering analysis of the lunar surface and Apollo sample radiometric ages and applied to Mars [2]. The temporal resolution of the model is 1 My. Based on the crater diameter to depth ratio, we estimate the average crater depth of a crater size bin. Simultaneously, we apply an obliteration rate. The model produces a synthetic crater size distribution that integrates both impact cratering rate history and obliteration rate history. We use a simple biphasic models which corresponds to two successive periods during which the obliteration rate has been constant. This model reproduces the S-shape distribution typical of Ancient terrains on Mars.

Inversions: We used a variational approach for the inverse problem to determine the age of the terrain, the age of the change in erosion regime as well as the obliteration rate during the oldest period from crater size distribution. The starting age and as well as the age of the change of obliteration regime is directly inversed from the parts of the crater size distribution that follow the isochrones for several crater size bins. We fixed the obliteration rate of the recent period to the erosion rate estimated by the Martian rovers to return the obliteration rates of the oldest period.

Data set: We used the global crater data base from [7] that claims to be complete until 1 km of diameter and all global maps available under Geographic Information System (GIS) environment like the geological map. Then we mapped more than hundred of large area on the Martian surface mainly in noachian terrains but also in hesperian and amazonian terrains. The area have to be large enough to have good statistics for impact craters larger than 60 km while being in a coherent geological unit (from 10^5 to 10^6 km^2). Then using GIS techniques, crater size distributions of each area are extracted and used for inversion.

3. Results

About 35 sampled area of Mars returned a satisfactory fit. The starting ages of these 70 areas range from 4.2 Gy to 3.3 Gy covering the crucial period of early mars evolution. The ages of the change in the obliteration rate regime range from 3.7 Gy to 1 Gy. The values of erosion rates decrease from 6 m/My at 3.8 Gy to 0.6 m/My at 3.2 Gy. Our results indicate that the erosion rate decrease of at least one order in magnitude from at least the middle of Noachian until the end of Hesparian era. Consequently there was a decrease in the efficiency of water-related erosion over this period. These results can be compared to the morphology of the modified impact craters that is depending on the age of the crater [8].

4. Conclusion

We extract for the first time key information looked up in the crater size distributions of large Martian impact crater about the early evolution of Martian atmosphere. Indeed, we document the long term evolution of the erosion rate on Mars from Ancient times with erosion rate at least one order in magnitude larger than today to current low and limited erosion rates.

Acknowledgements: The research leading to these results has received funding from the European Research Council under the European Union's Seventh Framework Program (FP7/2007-2013)/ERC Grant agreement n° 280168.

References

[1] Hartmann W.K., 1966, Icarus, Vol. 5, pp. 565-576;

[2] Hartmann W.K. and Neukum G., 2001, Space Sci. Rev., Vol. 96, p.165-194;

[3] Jones, 1974, JGR, Vol 79, p3917-3931;

[4] Hartmann, 1971, Icarus, Vol15, p410;

[5] Chapman, Icarus, 1974;

[6] Neukum, G. et al., 2001, Space Sci. Rev., Vol. 96, p.55-86.

[7] Robbin and Hyneck, 2012, JGR, Vol 117;

[8] Mangold et al., 2012, JGR, Vol 117;

EPSC Abstracts
Vol. 10, EPSC2015-445, 2015
European Planetary Science Congress 2015

The Martian ionosphere: comparison of a global climate model with MARSIS data

F. González-Galindo (1), F. Němec (2), M.A. López-Valverde (1), J.-Y. Chaufray (3), F. Forget (4), D. D. Morgan (5), C. Diéval (5) and D. A. Gurnett (5)
(1) Instituto de Astrofísica de Andalucía, CSIC, Granada, Spain (ggalindo@iaa.es)
(2) Faculty of Mathematics and Physics, Charles University in Prague, Prague, Czech Republic
(3) Laboratoire Atmosphere, Milieux et Observations Spatiales (LATMOS), IPSL, CNRS, UVSQ, UPMC, Guyancourt, France
(4) Laboratoire de Météorologie Dynamique, IPSL, CNRS, Paris, France
(5) Department of Physics and Astronomy, University of Iowa, Iowa City, Iowa, USA

Abstract

We present here the comparison of the electron density profiles predicted by a 3D global climate model (GCM), the Mars GCM developed at the Laboratoire de Météorologie Dynamique (LMD-MGCM) [4], with the measurements from the instrument MARSIS on board Mars Express [5]. The observations were obtained during 5 Martian Years (MY), from MY27 to MY31 (mid 2005-end of 2013). The model was run using the observed day-to-day variability of the UV solar flux and of the dust load during that period. We focus the comparison on two parameters: the electron density at the main peak, and the altitude of the peak. Special attention will be paid to the variability of these two parameters with different geophysical parameters (latitude, SZA, ...), which can provide interesting information about the neutral upper atmosphere of Mars and its interaction with the UV solar radiation.

1. Model-data ionosphere comparison

The structure of the Martian ionosphere is strongly affected by the characteristics of the underlying neutral atmosphere [11]. So, the comparison of the electron density profiles predicted by a GCM with the observations provide an indirect validation of the predicted thermal and density structure in the mesosphere/lower thermosphere region.

The LMD-MGCM is a ground-to-exosphere GCM [2, 3] which self-consistently takes into account the couplings between different atmospheric regions and between different processes. Recently, the photochemical module used to simulate the chemistry of the upper atmosphere of the planet has been improved to simulate the Martian ionosphere [4]. A procedure to take into account the day-to-day variability of the UV solar flux has been included in the modelas well. The model is also able to simulate the dynamics of the ions [1], but we will limit this study to the photochemical region of the ionosphere, below about 180 km from the surface. The version of the model used for this study includes the radiative effects of water ice clouds, which have been shown to produce a significant effect over the mesospheric temperatures [6].

The Mars Advanced Radar for Subsurface and Ionosphere Sounding (MARSIS) instrument, on board Mars Express, has provided the largest dataset to date about the Martian ionosphere, with more than 140000 electron density profiles obtained during more than 5 Martian Years [12]. The main advantage of the MARSIS data when compared to radio-occultations is the large range of solar zenith angles and latitudes covered by the radar. MARSIS data have been used, among others, to characterise different aspects of the Martian ionosphere, such as the effects of the solar rotation [9], the effects of crustal magnetic fields [10] and the nightside ionosphere [8]

For this comparison, the LMD-MGCM has been run to simulate 5 MYs, from MY27 to MY31, the same period covered by MARSIS observations. The observed day-to-day variability of the UV solar flux is taken into account as described in [4]. The column dust optical depth is taken from [7]. The model results are interpolated to the location (in space and time) of each MARSIS observation, and the electron density at the main peak and the altitude of the peak are extracted, and compared to the observed ones.

Some preliminary conclusions can be already obtained from this comparison. Although the overall agreement is good, there are some differences that can provide interesting information about processes

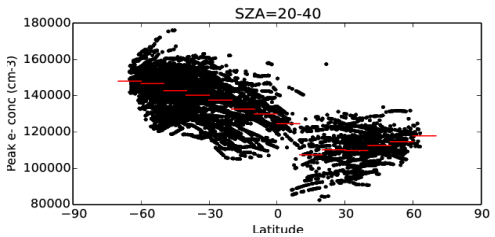

Figure 1: Latitudinal variation of the peak electron density predicted by the model at the location of MARSIS observations with SZA (solar zenith angle) between 20 and 40 degrees. The red lines indicate the median values.

not well represented or even missing in the model. The peak electron density is slightly underestimated by the model, as already found in a previous comparison with MGS radio-occultation data [4]. When the radiative effects of water ice clouds are not included in the LMD-MGCM, the simulated altitude of the peak is significantly underestimated. The peak electron densities predicted by the model show a significant latitudinal variability (Fig. 1), which is not the case in MARSIS observations. We will discuss the possible origin of these data-model discrepancies.

Acknowledgements

FGG was supported by a CSIC JAE-Doc fellowship financed by the European Social Fund. This work has received funding from the European Union's Horizon 2020 Programme (H2020-Compet-08-2014) under grant agreement UPWARDS-633127. CD, DAG and DDM are supported by contract 1224107 by the Jet Propulsion Laboratory. The MARSIS data are available on the Planetary Data System website.

References

[1] Chaufray, J.-Y., et al.: Three-dimensional Martian ionosphere model: II. Effect of transport processes due to pressure gradients, J. Geophys. Res., Vol. 119, pp. 1614-1636, 2014

[2] Forget, F., et al.: Improved general circulation models of the Martian atmosphere from the surface to above 80 km, J. Geophys. Res., Vol. 104, pp. 24,155–24,176, 1999

[3] González-Galindo, F., et al.: A ground-to-exosphere martian general circulation model: 1. seasonal, diurnal, and solar cycle variation of thermospheric temperatures, J. Geophys. Res., Vol. 114, pp. 4001–+, 2009

[4] González-Galindo, F., et al.: 3D martian ionosphere model: I. the photochemical ionosphere below 180 km, J. Geophys. Res., Vol. 118, pp. 2105–2123, 2013

[5] Gurnett, D.A., et al.: An overview of radar sounds of the Martian ionosphere from the Mars Express spacecraft, Adv. Space Res., vol. 41, pp. 1335-1346, 2008

[6] Madeleine, J.-B., et al.: The influence of radiatively active water ice clouds on the Martian climate, Geophys. Res. Lett., 39, pp. 23202-+, 2012

[7] Montabone, L., et al.: Eight-year climatology of dust optical depth on mars, Icarus, Vol. 251, pp. 65–95, 2015

[8] Nemec, F., et al.: Areas of enhanced ionization in the deep nightside ionosphere of Mars, J. Geophys. Res., Vol. 116, pp. E06006-+, 2011

[9] Nielsen, E., et al.: Observations of vertical reflections from the topside martian ionosphere. Space Sci. Rev., Vol. 126, pp. 373–388, 2006

[10] Nielsen, E., et al.: Local plasma processes and enhanced electron densities in the lower ionosphere in magnetic cusp regions on Mars. Planet. Space Sci., Vol. 55, pp. 2164–2172, 2007

[11] Withers, P.: A review of observed variability in the dayside ionosphere of Mars, Adv. Space Res., Vol. 44, pp. 277-307, 2009

[12] Withers, P., Morgan, D.D. and Gurnett, D.A.: Variations in peak electron densities in the ionosphere of Mars over a full solar cycle, Icarus, Vol. 251, pp. 5-11, 2015

EPSC Abstracts
Vol. 10, EPSC2015-460, 2015
European Planetary Science Congress 2015

The NOMAD Spectrometer Suite on ExoMars Trace Gas Orbiter: Calibration Results

I. R. Thomas (1), A.C. Vandaele (1), J.J. Lopez-Moreno (2), M. R. Patel (3), G. Bellucci (4), R. Drummond (1), E. Neefs (1), J. Rodriguez-Gomez (2), C. Depiesse (1), A. Mahieux (1,5), S. Robert (1), F. Daerden (1) and the NOMAD team.
(1) BIRA-IASB, Avenue Circulaire, Uccle, Brussels, Belgium; (2) IAA, Granada, Spain; (3) Open University, Milton Keynes, UK; (4) INAF-IAPS, Rome, Italy; (5) FNRS, Brussels, Belgium (ian.thomas@aeronomie.be)

Abstract

NOMAD (Nadir and Occultation for MArs Discovery) is a suite of three high-resolution spectrometers on-board the ExoMars Trace Gas Orbiter. Observing in the ranges 200-650nm and 2.2-4.3µm, the instrument will be able to detect and map a wide variety of Martian gases in unprecedented detail. The instrument was calibrated during March and April 2015; this presentation will describe the results of the tests performed and the expected performance when the instrument begins observing the planet in late 2017.

1. Introduction

The ExoMars Trace Gas Orbiter is a joint ESA-Roscosmos mission consisting of (1) an orbiter, and (2) an entry, descent and landing demonstrator. The mission is scheduled for launch in January 2016; to begin its nominal science mission around Mars in late 2017. The science mission will continue until 2019, covering an entire Martian year. NOMAD is one of the four instruments on-board the orbiter. The three spectrometers cover the UV-visible and infrared ranges, operating in solar occultation, limb and nadir-viewing modes, generating a huge dataset of Martian atmospheric observations during the mission across a wide spectral range [4].

SO channel. The solar occultation channel operates in the infrared, from 2330 to 4540cm^{-1} (2.2-4.3µm) at a resolution of ~0.15cm^{-1}, and is an improved copy of the SOIR instrument which was operating on Venus Express [3,8]. The channel consists of an echelle grating in combination with an acousto-optic tunable filter (AOTF): the dispersive element provides the spectral discrimination, while the filter selects the diffraction order [4]. A cooled infrared detector array is used to maximise the signal-to-noise ratio (SNR) as much as possible.

LNO Channel: This operates in a similar way to the SO channel, utilising an AOTF, echelle grating and cooled infrared detector also, but with a slightly reduced spectral range (2630 to 4540cm^{-1}; 2.2-3.8µm) and resolution (~0.3cm^{-1}) to increase SNR and reduce thermal noise [4]. This channel primarily points nadir, but is capable of making limb and solar occultation measurements if desired, or should the SO channel fail.

UVIS Channel: UVIS operates from 200-650nm at a resolution of ~1nm. It is a copy of the miniature grating spectrometer originally designed for the ExoMars lander with two added telescopes for measurements from orbit, rather than from the surface. UVIS can operate in solar occultation, limb, and nadir observational modes [5].

2. Scientific Objectives

When operating nominally, NOMAD has the resolving power to identify many trace gases that exhibit absorption features within the spectral range of the three channels. These include: CO_2 (incl. $^{13}CO_2$, ^{17}OCO, ^{18}OCO, $C^{18}O_2$), CO (incl. ^{13}CO, $C^{18}O$), H_2O (incl. HDO), NO_2, N_2O, O_3, CH_4 (incl. $^{13}CH_4$, CH_3D), C_2H_2, C_2H_4, C_2H_6, H_2CO, HCN, OCS, SO_2, HCl, HO_2, and H_2S [1,2,5,6].

The order-of-magnitude increase in spectral resolution over previous instruments will enable spatial and temporal mapping of several isotopologues of potential methane and water will be possible, providing important measurements of the Martian D/H and methane isotope ratios globally. Sensitivity studies [1,6] have shown that in occultation mode, using expected SNR values [4,7], NOMAD should have the ability to measure methane concentrations <25 parts per trillion (ppt) in solar occultation mode, and 11 parts per billion in nadir mode. Occultation detections as low at 10 ppt could be made if spectra are averaged sufficiently [1]. Using SO and LNO in combination with UVIS,

aerosol properties such as optical depth, composition and size distribution can also be derived [10].

In addition to trace gases, NOMAD will also continue to monitor the major seasonal cycles on Mars, extending existing datasets made by successive space missions in the past decade.

3. Current Status

The first stage of calibration was completed on 5th April 2015. Measurements were made in a thermal vacuum chamber at the Centre Spatial de Liege, at five different instrument temperatures (-12, -7, +5, +15 and +20ºC), covering the range of expected temperatures while in orbit around Mars. A limited range of SO measurements were made at a single instrument temperature in air.

During testing, a problem was discovered with the LNO channel detector, which required it to be exchanged for the flight-spare equivalent before delivery to the spacecraft. After a short re-certification and re-calibration campaign (at temperatures of -15 and +10ºC) ending on 28th April, NOMAD was ready for mounting on the spacecraft during the first week of May 2015.

A range of calibration measurements were made:

- Mapping of bad detector pixels (SO/LNO/UVIS)
- Pixel response linearity w.r.t. radiance (SO/LNO/UVIS)
- Detector thermal saturation rate/dark current at different temperatures (SO/LNO/UVIS)
- Detector and AOTF spectral calibration using gas cells (SO/LNO)
- Channel spectral calibration using emission lamps (UVIS)
- Detector temperature-dependent spectral calibration (LNO/UVIS nadir)
- Blackbody measurements at various temperatures to correlate observations with SNR model (LNO)
- Straylight calibration (UVIS nadir)

In this presentation, initial results from this extensive range of tests will be presented, demonstrating the 'as-built' performance of NOMAD in comparison to the expected performance [4,7,9] during the instrument design phase. The results from this work will form the basis of the data pipeline that will be used to generate scientific results from the returning data.

4. Summary and Conclusions

NOMAD, a suite of three spectrometers for detection and mapping of gases in the Martian atmosphere, was successfully built, tested and calibrated by IASB-BIRA and its industrial and academic partners. At the time of writing, the instrument has passed all tests and is ready for mounting onto the ExoMars Trace Gas Orbiter satellite.

In late 2017, NOMAD will enter nominal science orbit and begin transmitting back to Earth a new and exciting range of Martian observations. This presentation will outline the results of the calibration campaign, showing how the instrument is expected to perform when orbiting Mars.

Acknowledgements

We would like to thank the entire NOMAD team for their help, and Belspo, the Belgian Science Policy Office, for funding the work, and the ESA Prodex Office and payload management teams for all their hard work and assistance.

References

[1] Drummond, R. (2011) Planetary and Space Science, 59, pg. 292–298.

[2] Drummond, R. et al. (2013) EPSC Poster 2013-175.

[3] Mahieux, A. et al. (2009) Optics Express, 17, pg. 2005-2014.

[4] Neefs, E. et al. (2015) NOMAD. An Integrated Suite of Three High-Resolution Spectrometers for the Infrared, Visible and Ultraviolet Domain for ESA's ExoMars Mission - Design, Manufacturing and Testing of the Infrared Channels, Applied Optics (submitted).

[5] Patel, M. R. (2014) Fifth international workshop on the Mars atmosphere: Modelling and observations.

[6] Robert, S. et al. (2015) Performances of the NOMAD/ExoMars instrument, (in preparation)

[7] Thomas, I. R. et al. (2015) Optical and radiometric models of the NOMAD instrument – Part II: The IR channels, SO and LNO, (in preparation).

[8] Vandaele, A.C. et al. (2008) J. Geophys. Res., 113.

[9] Vandaele, A.C., et al. (2015) Optical and radiometric models of the NOMAD instrument – Part I: The UVIS channel, (in preparation).

[10] Wilquet, V. et al. (2009) J. Geophys . Res., 114.

EPSC Abstracts
Vol. 10, EPSC2015-471, 2015
European Planetary Science Congress 2015

Investigating the formation of detached layers of dust on Mars with a global climate model

C. Wang (1,2), T. Bertrand (1), F. Forget (1), A. Spiga (1), and E. Millour (1)
(1) LMD, Université Paris 6, Paris, France, (2) East China Normal University, Shanghai, China (chao.wang@lmd.jussieu.fr)

Abstract

The Martian dust cycle is of great importance for the current climate of Mars. Recently, detached layers of dust on Mars have been observed by Mars Climate Sounder (MCS), as well as the Thermal Emission Spectrometer (TES) and Compact Reconnaissance Imaging Spectrometer for Mars (CRISM). The origin of the detached layers is poorly understood. They cannot be reproduced by the traditional Global Climate Model (GCM). In this work, we parameterize strong convective dust storms (called rocket dust storms) in the GCM developed at the Laboratoire de Météorologie Dynamique (LMD). And the model outputs show that the detached layers of dust observed by the MCS are successfully predicted by the GCM with this new parameterization.

1. Introduction

Several atmospheric processes have been proposed for explaining the formation of the observed detached layers of dust, including small-scale dust lifting [1], slope winds [2], scavenging of the dust particles by water ice clouds [3] and rocket dust storm [4].

In LMD GCM, a new water cycle has been parameterized by taking into account the scavenging of water ice clouds [3]. However, this process didn't yield to satisfying results in the GCM. In LMD Martian Mesoscale Model (MMM), a detached layer was successfully reproduced [4]. In the MMM simulation, a rocket dust storm governed by deep convective motions which lead to the lifting and injection of dust at high altitudes in the Martian troposphere (∼30-50 km) was firstly resolved by the MMM. Combined to horizontal transport by large-scale winds, rocket dust storms produce a detached layer at high altitudes. But this process cannot be replicated by the GCM due to the low spatial resolution, which is typically ∼200 km. So for the purpose of reproducing the detached layers of dust in LMD GCM, we parameterize the rocket dust storm in LMD GCM to inject dust at high altitudes and see how this process couples with large-scale circulation to form detached layers.

2. Modeling method

2.1 Model description

The LMD Mars GCM is used with various recent improvements, including dust, carbon dioxide and water cycles. The model is also used with a thermal plume model parameterized in the planetary boundary layer, yielding sub-grid scale convection. A "semi-interactive" scheme is used for guiding the evolution of dust, where the total amount integrated along the vertical axis is rescaled to a prescribed dust map, but the shape of the vertical profile of dust is free to evolve.

2.2 Rocket dust storm parameterization

This is a sub-grid parameterization. For each mesh, two dust trace species were defined, i.e. dust corresponding to environmental dust (background-dust) and dust associated to the rocket dust storm (storm-dust).

1. Dust injection scheme: The storm-dust were injected in a GCM mesh only when strong dust column optical depth gradient $\Delta\tau$ are observed (typically $\Delta\tau > 0.2$, based on specific dust scenario). The spatial and temporal distributions of storms thus obtained in GCM are in line with observations.
2. Definition of the mesh fraction where the dust storm is concentrated, for each GCM level.
3. Calculation of radiative transfer through the mesh (background-dust) and through the storm (storm-dust + background-dust). Heating rates inside and outside the storm are thus obtained.
4. Considering that the increase of radiative energy related to the presence of a storm is entirely converted to adiabatic cooling, the vertical velocity of storm-dust can be directly deduced from the

extra dust radiative heating. This storm-dust is then transported vertically in the GCM.

5. Detrainment within the storm: conversion of storm-dust into background-dust and control of the ascent of the storm.
6. Horizontal transport: the dust injected in the higher layers of the GCM is transported horizontally by large scale GCM winds.

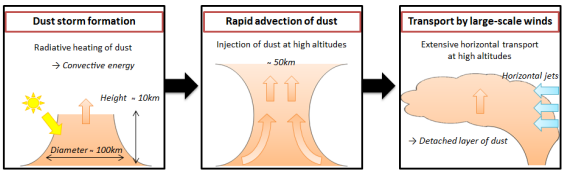

Figure 1: The principle of the parameterization of rocket dust storm

3. Results and conclusions

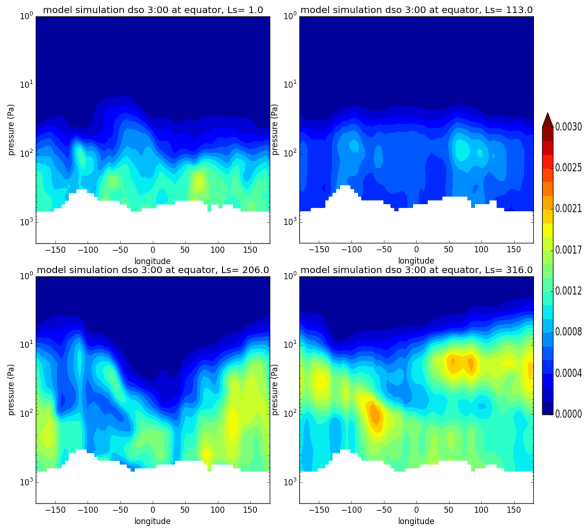

Figure 2: The model derived nightside (3h00) dust vertical distribution at equator at L_s=1.° (upleft), 113.° (upright), 206.° (downleft), and 316.° (downright).

The Figure 2 shows four cross-sections at equator about longitudinal and vertical distribution of model derived dust density scaled opacity (DSO). The detached layers can be easily identified. The altitude of the detached layers in Figure 2 reach a altitude ranging from ∼15 km to ∼ 60 km. Therefore, the rocket dust storm can produce detached layers of dust in the GCM. It should be noticed that not all the rocket dust storm will result in detached layers. The reason is that when the convective energy is not strong enough, the dust cannot be injected at high altitudes. Thus, it will stay below the planetary boundary layer and then mixes with the atmosphere.

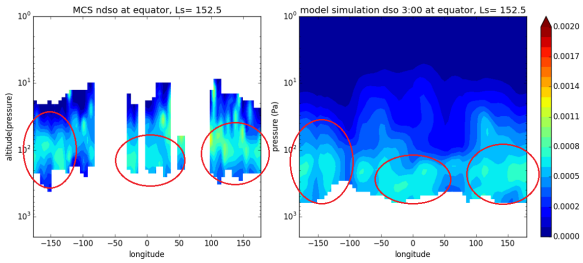

Figure 3: Comparison between MCS observation and Model simulation: nighttime dust DSO (3h00) at equator averaged from L_s=150.∼155.°.

u The comparison between MCS observation and model outputs has also been implemented. The Figure 3 shows the comparison of averaged dust DSO from L_s=150∼155°. The longitudinal distribution are quite matched between observation and simulation. But the altitude of the model derived detached layers are lower than observation. This could be caused by a strong sedimentation and/or insufficient injection of dust in GCM.

References

[1] Heavens N., Richardson M., Kleinböhl A., et al: The vertical distribution of dust in the Martian atmosphere during northern spring and summer: Observations by the Mars Climate Sounder and analysis of zonal average vertical dust profiles, J. Geophys. Res. Planets, Vol. 116(E4), 2011.

[2] Rafkin S.: The potential importance of non-local, deep transport on the energetics, momentum, chemistry, and aerosol distributions in the atmospheres of Earth, Mars, and Titan. Planetary and Space Science, Vol. 60(1), pp.147-154, 2012.

[3] Navarro T., Madeleine J., Forget F., et al: Global climate modeling of the Martian water cycle with improved microphysics and radiatively active water ice clouds, J. Geophys. Res. Planets, Vol. 119, pp. 1479–1495, 2014.

[4] Spiga A., Faure J., Madeleine J., et al: Rocket dust storms and detached dust layers in the Martian atmosphere, J. Geophys. Res. Planets, Vol. 118(4), pp.746-767, 2013.

EPSC Abstracts
Vol. 10, EPSC2015-499, 2015
European Planetary Science Congress 2015

Current thermal state of Mars from scaled models of surface heat flow

Laura M. Parro (1), Alberto Jiménez-Díaz (1, 2) and Javier Ruiz (1)
(1) Departamento de Geodinámica, Universidad Complutense de Madrid, 28040 Madrid, Spain (lmparro@ucm.es),
(2) Instituto de Geociencias, IGEO (CSIC, UCM), 28040 Madrid, Spain.

Abstract

In this work we scale heat flow differences across the martian surface from crustal and topographic differences in the planet, and also taking into account the heat radioactive production provided by the crust and the lithosphere mantle. Our aim is present a preliminary global heat flow model, which will can compared with deductions from InSight in order to gain understanding of the present heat flow pattern of Mars, and their implications for Martian thermal history.

1. Introduction

To understand the current thermal state of the Martian subsurface and interior, must be known values of temperature and heat flow. Until the arrival and InSight mission, which includes the HP^3 heat flow probe, no direct heat flow measurements exist for Mars. A commonly used indirect method is based on the relation between the thermal state of lithospheric rocks and their mechanical strength, which, applied to regions of different ages provides information on the thermal evolution of Mars [1]. In this sense, the finding of a very limited flexure caused by the north polar cap load indicates a very thick (>300 km) present-day effective elastic lithosphere (T_e) on the North Polar Region (NPR) [2], which can be used to obtain very robust estimates of the current heat flow at that region [1]. Here, we perform a global, first-order, scaling of the heat flow deduced for the NPR, in order to present a preliminary global heat flow model, which will can compared with deductions from InSight in order to gain understanding of the present heat flow pattern of Mars, and their implications for Martian thermal history.

2. Lithospheric heat production

The lithosphere is not only heated from below by internal the heat inside the planet, but also by the decay of the radioactive elements it contains. Therefore, we take into account the heat radioactive production provided by both, the crust and the lithosphere mantle. Neglecting lateral heat transfer, the surface heat flow of Mars may be considered the sum of the heat generated in the crust and the heat flow from the mantle. In turn, the heat flow of the mantle is consequence of the heat radioactively produced in the mantle lithosphere (or, more generally, in the stagnant lid), and of the heat coming-up from the deep interior.

The component of the heat flow arising from crustal radioactive heat sources is the sum of the contributions from all the heat-producing radioactive elements (HPE). HPE abundances on the surface of Mars have been estimated from measurements by the GRS instrument aboard 2001 Mars Odyssey spacraft. K and Th abundances were measured directly, whereas a Th/U ratio of 3.8 was assumed [e.g., 3]. The so-obtained average value of the surface heat production of Mars is currently 4.9×10^{-11} W Kg^{-1} [3], or 0.14 mW m^{-2} per each kilometre of crustal column.

On the other hand, HPE abundances in the mantle lithosphere are poorly constrained. Here we use HPE mantle lithosphere abundances 0.1 times the average value for the martian crust [see 1], which translates to ≈0.017 mW m^{-2} per each kilometre of mantle lithosphere column.

3. Scaling of heat flow from variations in crustal thickness

Taking into account average crustal and mantle lithosphere heat production values discussed in the previous section, and assuming a constant heat flow from the deep interior, we can scale heat flow differences across the martian surface from crustal and topographic differences in the planet.

Crustal thickness variations were derived from topography and gravity following the procedure of potential theory [4] by assuming an average thickness of 50 km, This mean crustal thickness is slightly higher than previous models [5], but in line with geophysical and geochemical evidences [6-8], and consistent with average thickness usually used in modeling of lithospheric strength [e.g., 1, 7]. Our crustal thickness model uses densities of 2,900 and 3,500 kg m^{-3}, respectively, for the lithospheric mantle, values widely used for Mars [1, 5, 7].

For anchoring our model, we calculated an upper limit heat flow of 17.0 from T_e = 300 km at the NPR, following the procedure and parameters described in [1] and using a crustal thickness of 35 km in NPR, as derived by our crustal thickness model in this region.

4. Present-day heat flow model

The results are shown in Figure 1. The surface heat flow varies between 14 and 23 mW m^{-2}, with minimum values in regions of crust thinned by giant impact basin, and maximum values corresponding to the thickest crust in the Taumasia, Syria Planum and south Tharsis regions.

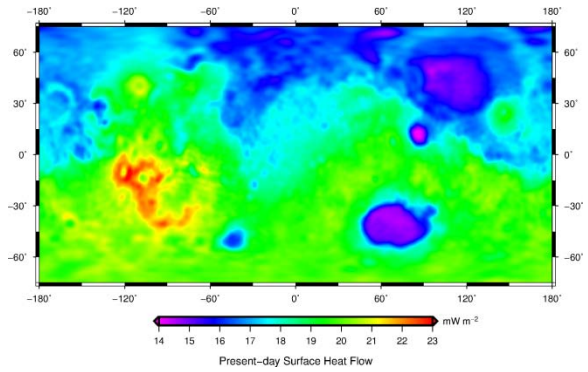

Figure 1: Global model of present-day surface heat flow.

Interestingly, the obtained average surface heat flow is 18.4 mW m^{-2}. If we take into account a present-day radioactive heat production equivalent to a surface heat flow of 14.3, according to the compositional model of [9], then an Urey ratio (defined as the ratio between the total radioactive heat production and the total surface heat loss) of around 0.8 is obtained for the present-day Mars. This value is higher than it (≈0.6) predicted by some thermal evolution models of [10], but consistent with a more limited interior cooling deduced from lithospheric strength analysis [11].

5. Conclusions

Our results of current thermal state of Mars, and the corresponding construction of these models and maps, are preliminary and a first step in our attempt of characterizing the global heat flow, their implications for the thermal history of Mars, and overlooking evaluate specific landing zones upcoming ExoMars missions 2016, 2018 and InSight.

Acknowledgements

This work is conducted as part of the project UPWARDS-633127, funded by the European Union's Horizon 2020 Programme (H2020-Compet-08-2014).

References

[1] J. Ruiz et al., Icarus 215, 508-517, 2011.

[2] R.J. Phillips et al., Science 320, 1182-1185, 2008.

[3] B. C. Hahn, S. M. McLennan and E. C. Klein, Geophys. Res. Lett., Vol. 38, L14203, 2011.

[4] M. A. Wieczorek and R.J. Phillips., J. Geophys. Res. 103, 1715-1724, 1998.

[5] G. A. Neumann et al., J. Geophys. Res. 109, E08002, 2004.

[6] M. A. Wieczorek and M. T. Zuber, J. Geophys. Res. 109, E01009, 2004.

[7] P. J. McGovern et al., J. Geophys. Res. 109, E07007, 2004.

[8] J. Ruiz et al., Icarus 203, 47-57, 2009.

[9] H. Wänke and G. Dreibus, Philos. Trans. R.Soc. London A349, 2134-2137, 1994.

[10] A. C. Plesa et al., J. Geophys. Res., in press, 2015.

[11] J. Ruiz, Sci. Rep. 4, 4338, 1-7, 2014.

EPSC2015

TP5 Abstracts

Part 2 out of 2

EPSC Abstracts
Vol. 10, EPSC2015-502, 2015
European Planetary Science Congress 2015

Data assimilation of temperature and aerosols on Mars

T. Navarro, F. Forget and E. Millour
LMD, Paris, France (navarro@lmd.jussieu.fr)

Abstract

The latest results of data assimilation on Mars using the Laboratoire de Météorologie Dynamique (LMD) Mars Global Climate Model (MGCM) and (Mars Climate Sounder) MCS observations are presented, with the estimation of both temperature and aerosols and an emphasis on the prediction and forecasting of the Martian atmosphere.

1. Introduction

Data assimilation is a technique widely used in geoscience, especially meteorology and weather forecast. It enables to optimally reconstruct a best estimate of the atmospheric state by combining instrumental observations and theoretical information provided by a numerical model.

Data assimilation on Mars has been studied for 20 years [1], using nudging and Kalman Filter techniques by various teams. This work updates the development of a data assimilation chain by coupling the LMD MGCM with the Local Ensemble Transform Kalman Filter (LETKF) [2] assimilation framework [3].

2. Data assimilation description

2.1 Motivation

The reasons to develop such an assimilation are numerous:

- The reconstruction of atmospheric fields is *per se* a strong motivation. It provides a best estimate of the known atmosphere and could be seen as a useful tool for atmospheric science community.

- One of the main objectives of the Trace Gas Orbiter (TGO), that will be launched in 2016, is to detect the presence and origin of trace gas in the Martian atmosphere. A data assimilation chain using data from the Atmospheric Chemistry Suite (ACS) on board TGO can be used to backtrack winds to locate the sources of such trace gases.

- Another asset of data assimilation is the possibility to point out disagreements between model and observations. It is a very powerful tool to estimate MGCM parameters or characterize instrumental errors.

2.2 Atmospheric Model

The model used in this data assimilation scheme is the MGCM developed at LMD [4]. It includes a semi-interactive dust scheme guided by dust scenarios, a water cycle that includes radiatively active water ice clouds with interaction between dust and clouds.

2.3 Data assimilation scheme

The principle of data assimilation is to successively alternate two steps: analysis and forecast (figure 1). In the analysis step, an *a priori* estimate of the system state, called the background, is used to obtain a new estimate, called the analysis, by being combined to observations. The forecast, or propagation step, consists of applying the numerical model to the analysis to get a new background after time integration (of typically 6 hours).

The assimilation scheme used is LETKF, which consists of an approximation of the Kalman Filter. It uses an ensemble, that is to say a set of a large enough number of forecast members that samples the variability of the system. The analysis step then consists of applying the filter to the background ensemble to create a new ensemble, the analysis. Observations are localized, that is to say their influence is limited and weighted in space within an arbitrary range.

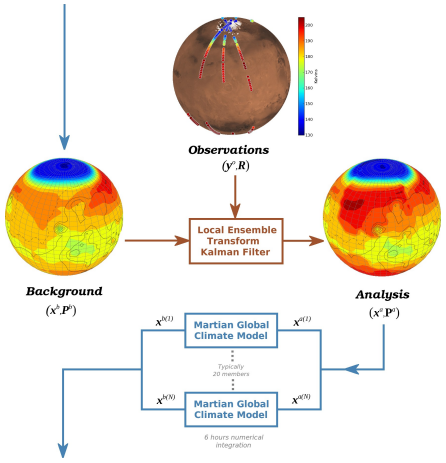

Figure 1: Diagram of the functioning of the LETKF over one cycle

3. Results

The present work shows the assimilation of observations from the Mars Climate Sounder (MCS) on board Mars Reconnaissance orbiter.

When compared to Earth, the specificities of the Martian atmosphere (low atmospheric density, water in trace quantities, absence of oceans) give Mars a very predictable weather. For a large portion of the year, instabilities in the Martian atmosphere do not grow [5]. This makes assimilation on Mars more difficult because the main source of disagreement between model and observations are biases (whether these are model or observational biases), rather than flow instabilities [6]. In order to tackle this issue, the approach in this work is to use observations to get an estimate of the two main aerosols that are strong forcings of the Martian atmosphere, rather than just the atmospheric flow. These aerosols are:

- Dust loading of the atmosphere, which controls most of its thermal structure, through dust radiative effects.

- Water ice clouds, whose radiative effects are known to be possibly as significant as the ones of dust, depending on the time of the year.

The estimation of aerosols in three dimensions in the Martian atmosphere and their evolution in time compensates for a bias that exists for simulations without assimilation, given the fact that it is a challenge to impose a realistic distribution of aerosols in a Martian GCM. It has the potential to greatly improve our capability to predict the future state of the atmosphere on a few days time-scale (figure 2), paving the way to an operational weather forecast on Mars.

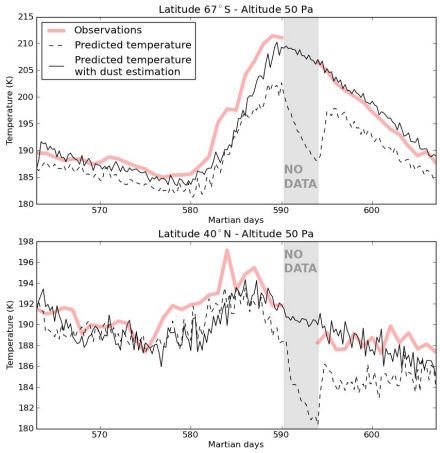

Figure 2: The impact on temperature prediction with and without estimation of dust during a regional dust storm.

References

[1] Lewis, S.R, et al.: Data assimilation with a martian atmospheric gcm: An example using thermal data, ASR, 19(8), pp. 1267-1270, 1995

[2] Hunt, B.R., et al.: Efficient data assimilation for spatiotemporal chaos: A local ensemble transform Kalman filter, Physica D, 230(1), pp. 112–126, 2006

[3] Navarro, T., et al.:Detection of detached dust layers in the Martian atmosphere from their thermal signature using assimilation, GRL, 41, pp. 6620-6626, 2014

[4] Forget, F., et al: Improved general circulation models of the Martian atmosphere from the surface to above 80 km, JGR, 104, 24, pp.155-176, 1999

[5] Newman, C.E., et al: Investigating atmospheric predictability on Mars using breeding vectors in a general-circulation model. QJRMS, 130(603), pp. 2971–2989, 2004

[6] Rogberg, P., et al: Assessing atmospheric predictability on Mars using numerical weather prediction and data assimilation, QJRMS, 136, pp. 1614–1635, 2010

EPSC Abstracts
Vol. 10, EPSC2015-508, 2015
European Planetary Science Congress 2015

Micro-Ares, An electric field sensor for ExoMars 2016

G. Déprez (1), F. Montmessin (1), O. Witasse (2), L. Lapauw (1), F. Vivat (1), S. Abbaki (1), P. Granier (1), D. Moirin (1), R. Trautner (2), R. Hassen-Khodja (1), E. d'Almeida (1), L. Charnenal (1), J-J. Berthelier (1), F. Esposito (3), S. Debei (4), S.Rafkin (5), E.Barth (5)
(1) Laboratoire Atmosphère Terrestre, Millieux et Observations Spatiales (LATMOS), Guyancourt, France, (2) European Space Agency, ESTEC, 2201 AZ Noordwijk, Netherlands, (3) INAF - Osservatorio Astronomico di Capodimonte, Napoli, Italy, (4) CISAS - Università degli Studi di Padova, Padova, Italy, (5) SouthWest Research Institute (SwRI), Boulder (CO), USA

Abstract

For the past few years, LATMOS has been involved in the development of Micro-ARES, an electric field sensor part of the science payload (DREAMS) of the ExoMars 2016 Schiaparelli entry, descent and landing demonstrator module (EDM). It is dedicated to the very first measurement and characterization of the Martian atmospheric electricity.

1. Introduction

The Martian atmospheric electric fields are suspected to be at the very basis of various phenomenon such as dust lifting [1][2][3], formation of oxidizing agents [2][4] or Schumann resonances [5]. Although the data collection by DREAMS will be restricted to a few days of operations, these first results will be of importance to understand the Martian dust cycle, the electrical environment and possibly relevant to atmospheric chemistry. The instrument, a compact version of the ARES instrument for the ExoMars Humboldt payload [6], is composed of an electronic board, with an amplification line and a real-time data processing DSP, which handles the electric signal measured between the spherical electrode (located at the top of a 27-cm high antenna) that adjusts itself to the local atmospheric potential, and the lander structure, connected to the ground.

Figure 1 : Micro-ARES antenna and board

2. Scientific goals

Although the Martian electric activity has never been observed, the interest of the scientific community has been ever growing during the past ten years since they should be responsible for various phenomenon such as:
- The existence of a Martian global electrical circuit where dust-devils and dust storms are the generator and the ionosphere ($\sigma \approx 1$S/m), conductive atmosphere ($\sigma \approx 10^{-11}$ S/m) [7] and ionized ground are the circuit, where significant currents could flow.
- The Martian dust cycle, which most impressive manifestations are the annual global dust storms, is suspected to be intrinsically linked to the electric-field since very simple calculations shows that the aerodynamic and electrostatic forces on dust grains are of the same order of magnitude [1][2][3][6].
- The atmospheric chemistry is also believed to be highly affected by the creation of energized free electrons which lead to the fabrication of oxidizing agents (O^-, OH^- or H_2O_2) [2][4] which could efficiently remove organic materials.
- The same way electromagnetic waves appear in the Earth-ionosphere cavity, those waves, called Schumann resonances, could appear on Mars [5][8], bringing new insights about the peculiar Martian ionosphere.

3. Field test campaign

The field measurement in Martian-like conditions, at least in terms of meteorological events, had to be performed in order to prove the good behaviour of Micro-ARES and it ability to retrieve the necessary scientific data. Those tests have been carried out in July 2014 in Moroccan Sahara desert, in parallel with DREAMS-like instruments (wind speed, pressure, hygrometry, temperature, optical depth at least) and above all, another electric-field measurement device, properly calibrated, which has been used as a reference for comparison. The main difference

between the Earth and Mars surface atmosphere is the atmospheric conductivity, which is about two orders of magnitude higher on Mars. Therefore, the antenna had to be adapted so that the input electronics of Micro-ARES could behave the same way it will on Mars.

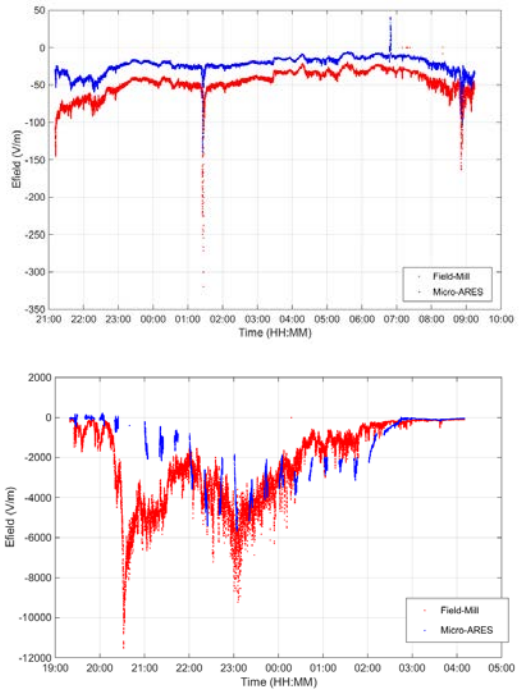

Figure 2 : Calm and Storm wheather comparison between Field mill (red) and Micro-ARES(blue)

This test campaign shew a very high correlation between the data acquired by Micro-ARES and the one harvested by the Field-mill, the main differences being caused by their different installation height (2m vs. 80cm from the ground). The instrument has even been able to measure the Earth Schumann resonances, despite their very low amplitude (100^{th} of µV/m). This campaign has therefore been very conclusive in regards to the ability of the instrument to collect the necessary data in order to answer, at least partially, the questions raised in §2.

4. Martian chamber test campaign

In order to confirm or adjust the antenna-atmosphere coupling model [9], which is capital for the proper data processing, it has to be tested in a Martian atmospheric chamber (CO2 atmosphere, cooled down to temperatures around -100°C) which is available at LATMOS.

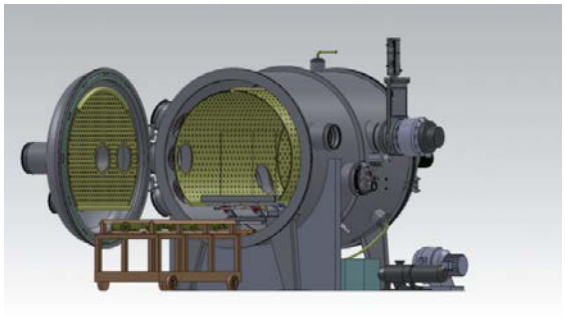

Figure 3 : 60x60x60 climate chamber

The test will be performed in the chamber with the adequate atmosphere and an ionizing device (UV LEDs or Corona effect generator) in order to bring up the conductivity to the ones we expect on Mars [7], and the antenna placed between two metallic plates where the electric field generated can reach up to 24kV/m. In order to make the electric field uniform between the plates, several metallic hoops will be placed around the antenna, between the plates, with their potentials linearly evolving. These tests, combined with a precise electric modelling of the lander, will help to fully understand and quantify the electric field deformation around the lander and properly process the data gathered by Micro-ARES.

References

[1] J.F. Kok & N.O.Renno (2008) PRL 100,014501.

[2] J.F. Kok & N.O.Renno (2009) GRL VOL. 36, L05202

[3] J.F. Kok & N.O.Renno (2009) EGU General Assembly 2009 p.504

[4] W.M. Farrell & G.T. Delory (2006) GRL VOL. 33, L21203

[5] C. Béghin (2009) PSS 57 p.1872–1888

[6] J.J. Berthelier (2000) PSS 48 p. 1193-1200

[7] M. Michael (2008) JGR VOL.113

[8] A. Sukhorukov (1991) PSS 39 p.1673-1676

[9]G. Molina-Cuberos (2012) PSS 58 p. 1945-1952

EPSC Abstracts
Vol. 10, EPSC2015-520, 2015
European Planetary Science Congress 2015

Long-term O_2 nightglow observations in the polar night on Mars by SPICAM/MEx

A. Fedorova (1), S. Guslyakova (1), F. Lefèvre (2), F. Montmessin (2), D. Churbanov (3), O.I. Korablev(1), J-L. Bertaux(2)
(1) Space Research Institute (IKI), Moscow, Russia (fedorova@iki.rssi.ru / Fax: +7-495-333-21-02),
(2) CNRS LATMOS, 11 Bd d'Alembert, 78280 Guyancourt, France
(3) Moscow Institute of Physics and Technology (MIPT), 9 Institutsky dr., 141700 Dolgoprudny, Moscow Region, Russia

1. Introduction

The oxygen nightglow is a sensitive tracer of the thermospheric circulation. In contrast to the $O_2(a^1\Delta_g)$ dayglow that results from the ozone photodissociation on Mars, the $O_2(a^1\Delta_g)$ nightglow is a product of the recombination of O atoms formed by CO_2 photolysis on the dayside at altitudes higher than 80 km and transported downward above the winter pole by the Hadley circulation. The first direct observation of the night-side emission were provided at limb geometry by the OMEGA spectrometer on the Mars-Express orbiter in 2010 (3 vertical profiles have been detected) [1] and confirmed and studied later by CRISM on Mars-Reconnaissance-Orbiter [2] and SPICAM on Mars-Express [3]. The first detections indicate that the emission is about two orders of magnitude less intense than the dayglow. All observations related to Southern and Northern poles at polar night.

2. Observations

The infrared AOTF spectrometer SPICAM IR sounds the Martian atmosphere in the near-IR range (1-1.7 μm) with the spectral resolution of 3.5 cm^{-1} in nadir, limb, solar and star occultation modes since January 2004 [4]. It allows to perform measurements of the O_2 emission with rather high spectral power (~2200) and has obtained the first seasonal map of the oxygen emission on the dayside of Mars [5]. FOV of spectrometer at nadir and limb is 1°. Since 2010 the spectrometer began continuous monitoring of the O_2 nightglow in Mars' polar regions. In 2010-2015 SPICAM IR provided ~260 limb observations on the night side and ~1400 stellar occultations in IR. About 500 resulting vertical profiles of the oxygen nightglow have been obtained in both hemispheres. (fig.1).

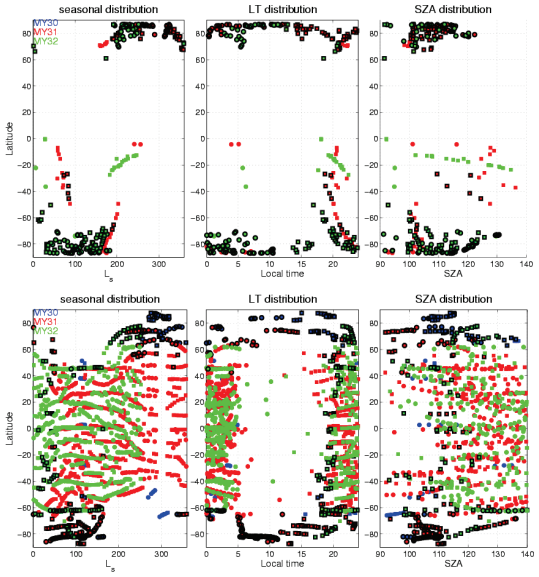

Figure 1. Distribution of limb observations (top) and stellar occultations (bottom) with season, local times and SZA for MY30-32. The black signs mark orbits where the emission has been detected.

3. Results and discussion

We will present preliminary results of the O_2 nightglow observations in Northern and Southern hemispheres at different Martian years. Vertically integrated intensity of the emission varies from 0.15 to 0.5 MR. For the North pole the emission peak locates at 35-42 km that is lower than 40-55 km for the South pole and the emission rate is a more intense for the North compared with the South. As the emission is a result of atomic oxygen recombination in descending branch of the Hadley cell, it should be strongly sensitive to a transport of these atoms to the polar region of Mars. In this connection a comparison of the received profiles with the three-dimensional general circulation model of Mars is important [6]. In this work the seasonal variations of the vertically integrated emission rate and altitude variations of the peak intensity for the slant emission in comparison with the LMD GCM will be presented.

In case of stellar occultation, observations of the atmospheric density by SPICAM UV [7, 8] allow to retrieve temperature profiles in Southern and Northern polar regions. As shown in [3], the simultaneous observations of the nightglow and temperature-density profiles can help to retrieve the atomic oxygen profiles at altitudes from 40 to 70 km.

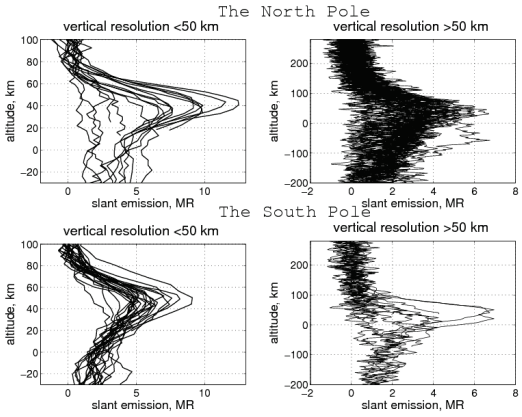

Figure 2. Vertical profiles of the $O_2(a^1\Delta_g)$ nighttime emission rate for several observations at the North and South poles.

Acknowledgements

Authors acknowledge RFBR grant 15-02-07812 a for financial support and the Central office of the European Space Agency (ESA). We thank our collaborators and technical team at the three institutes for the design and the fabrication of the instruments (LATMOS-Service d'Aeronomie/France, BIRA/Belgium and IKI/Russia).

References

[1] Bertaux, J. L., B. Gondet, F. Lefèvre et al. (2012), First detection of O_2 1.27 μm nightglow emission at Mars with OMEGA/MEX and comparison with general circulation model predictions, J. Geophys. Res., 117, E00J04, doi:10.1029/2011JE003890.

[2] Clancy, R. T., et al. (2012), Extensive MRO CRISM observations of 1.27 μm O_2 airglow in Mars polar night and their comparison to MRO MCS temperature profiles and LMD GCM simulations, J. Geophys. Res., 117, E00J10, doi:10.1029/2011JE004018.

[3] Fedorova, A.A., Lefèvre, F., Guslyakova, S. et al., The O_2 nightglow in the martian atmosphere by SPICAM onboard of Mars-Express, Icarus, Volume 219, Issue 2, p. 596-608, 2012.

[4] Korablev, O. and 16 colleagues (2006), SPICAM IR acousto-optic spectrometer experiment on Mars Express, J. Geophys. Res., 111, E09S03, doi:10.1029/2006JE002696, 2006

[5] Fedorova A., Korablev O., Perrier S. et al. Observation of O_2 1.27 μm dayglow by SPICAM IR: seasonal distribution for first Martian year of Mars-Express// J. Geophys. Res., 111, E09S07, doi:10.1029/2006JE002694, 2006.

[6] Lefèvre F., Lebonnois S., Montmessin F., Forget F.. Three-dimensional modeling of ozone on Mars, J. Geophys. Res. 109. E07004. doi:10.1029/2004JE002268, 2004.

[7] Bertaux J.-L., O. Korablev, S. Perrier et al., SPICAM on Mars Express: Observing modes and overview of UV Spectrometer data and scientific results, J. Geophys. Res., 111, E10S90, doi:10.1029/2006JE002690, 2006.

[8] Forget, F., F. Montmessin, J.-L. Bertaux et al. (2009), Density and temperatures of the upper Martian atmosphere measured by stellar occultations with Mars Express SPICAM, J. Geophys. Res., 114, E01004, doi:10.1029/2008JE003086.

EPSC Abstracts
Vol. 10, EPSC2015-528, 2015
European Planetary Science Congress 2015

Martian ionospheric response to low solar activity as observed by multiple datasets

B. Sánchez-Cano (1), **O. Witasse** (2), M. Lester (1), S.E. Milan (1), B.E.S. Hall (1), P.-L. Blelly (3), K. Peter (4), M. Grandin (5), M. Cartacci (6) and M. Pätzold (4)

(1) Radio and Space Plasma Physics Group, Department of Physics and Astronomy, University of Leicester, University Road, Leicester LE1 7RH, United Kingdom, (2) European Space Agency, ESTEC – Scientific Support Office, Keplerlaan 1, Noordwijk 2200 AG, The Netherlands, (3) Institut de Recherche en Astrophysique et Planétologie, F-31028 Toulouse, CEDEX4, France, (4) Rheinisches Institut für Umweltforschung an der Universität zu Köln, Abt. Planetenforschung, Köln, Germany, (5) Sodankyllä Geophysical Observatory, University of Oulu, Sodankylä, Finland, (6) Istituto di Astrofisica e Planetologia Spaziali, Istituto Nazionale di Astrofisica, Rome, Italy

Abstract

Solar cycle variations in solar radiation create density changes in the Martian ionosphere. This work shows the solar cycle impact on the ionosphere of Mars, with particular attention to the different ionospheric response observed during the period of extreme low solar activity in 2008 and 2009. This unique behaviour is analysed on the basis of multiple instrument observations of the Mars Express spacecraft and with empirical and numerical models.

1. Introduction

Since the ionosphere is strongly dependent on the solar activity, a good knowledge of the behaviour of the ionospheric variability for a whole solar period is something essential. Using Mars Express data from the period 2005–2012, differences in the electron density structure of the Martian ionosphere have been observed, and seem to be linked to changes in the ionospheric temperature due to the solar cycle variation [1]. Plasma parameters such as the scale height as a function of altitude, the peak characteristics, the total electron content (TEC), the temperatures, and the ionospheric pressures are seen to have characteristic signatures during specific periods of the solar cycle. The largest variations are seen during the period of very low solar minimum, when a reduction in ionization occurs, resulting in a topside scale height decrease not predicted by modelling.

2. Ionospheric response

Mars' ionospheric response to the extreme solar minimum between end-2007 and end-2009 followed a similar pattern to the response observed in the Earth's ionosphere, despite the large differences related to internal origin of the magnetic field between both planets.

In the particular case of the topside, the ionospheric temperature was cooler, and therefore a reduction in the scale height is found on the observations. Two different scale heights were observed. From the peak altitude at about 130 km to nearby 180 km, the profile is well defined with a constant neutral scale height like the one defined by Chapman's theory. However, from this transition point, the topside behaviour is better reproduced with a neutral scale height with a linear variation in altitude, although with rate slower than the reference scale height. The solar wind-ionosphere pressure balance might be the cause since the ratio between these two pressures could be smaller than in other phases of the solar cycle, and therefore an induced magnetic field could be found at deeper/lower ionospheric altitudes than in other phases of the solar cycle [1].

Regarding the behaviour of the whole atmospheric TEC [2], an extreme reduction not predicted before is observed for that period. On average, the TEC shows a very compressed ionosphere with 30-40% less of free electrons in the atmosphere than in the preceding and the following periods. This decrease could be caused by the prolonged minimum of solar X-ray

radiation measured during that period on Earth. This radiation is the cause of the formation of the Martian ionospheric bottomside. To test this hypothesis, radio science data from Mars Express and modelling studies are presented and compared with other datasets.

6. Summary and Conclusions

Plasma parameters such as the scale height as a function of altitude, the main peak characteristics (altitude, density), the TEC, the temperatures, and the ionospheric thermal pressures show variations related to the solar cycle. Major deviations are detected during the period of very low solar minimum, when ionospheric cooling occurs.

This study is based on the comparison of multiple instrument dataset from the Mars Express Spacecraft. Empirical and numerical modelling is done to understand the peculiar behaviour of the Martian ionosphere during the latest solar minimum.

Acknowledgements

BS-C, ML and SEM acknowledge support through STFC grant ST/K001000/1. BESH acknowledges support from the STFC Ph.D. studentship ST/K502121/1. Authors acknowledge Mars Express MARSIS PIs and Mars Express MaRS PI M. Pätzold for making data accessible.

References

[1] Sánchez – Cano, B., D.D. Morgan, O. Witasse, S.M. Radicella, M. Herraiz, R. Orosei, M. Cartacci, A. Cicchetti, R. Noschese, W. Kofman, C. Grima, J. Mouginot, D.A. Gurnett, M. Lester, P.-L. Blelly, H. Opgenoorth and G. Quinsac.: Total Electron Content in the martian atmosphere: a critical assessment of the Mars Express MARSIS datasets, J. Geophys. Res. Space Physics, 120, 2166–2182, 2015, doi:10.1002/2014JA020630.

[2] Sánchez – Cano, B., M. Lester, O. Witasse, S.E. Milan, B.E.S. Hall, P.-L. Blelly, S.M. Radicella, D.D. Morgan.: Evidence of scale height variations in the Martian ionosphere over the solar cycle, *submitted to GRL*.

EPSC Abstracts
Vol. 10, EPSC2015-533, 2015
European Planetary Science Congress 2015

Defrosting processes on the Russell crater megadune of Mars: quantitative analysis and interpretation

S. Douté (1), Chen Wu (2), Xian Guo (2) and Bin Luo (2)
(1) Institut de Planétologie et d'Astrophysique de Grenoble (IPAG), UJF-CNRS, UMR 5274, 38041 Grenoble. (e-mail: sylvain.doute@obs. ujf-grenoble.fr), (2) The State Key Laboratory of Information Engineering in Surveying, Mapping and Remote Sensing (LIESMARS), Wuhan University, Wuhan, Hubei 430079, PR China

Introduction and summary

The megadune located in the Russell Crater of Mars is the siege of a complex defrosting sequence implying seasonal CO2 and a small amount of water ice in each spring [3]. Besides on its pole facing slope, the dune displays gullies thought to have been carved by liquid water although they could also be related to dry avalanches triggered by the defrosting activity. In order to improve our understanding of seasonal versus secular phenomena, we conducted a quantitative analysis of a time series of joint image pairs : hyperspectral (CRISM) and high-resolution panchromatic (HiRISE), both sensors operating on board MRO. Automatic extraction and characterization of sublimation structures (e.g. dark spots) in the HiRISE images is performed on the basis of their geometry or their texture with image processing methods. The different conditions of CO2 ice are mapped by applying unsupervised linear spectral unmixing methods on the CRISM images. Modeling the spectral signatures with a radiative transfer model reveals the structural organization of the ice and its level of dust contamination. Finally we propose a joint interpretation of all the resulting products for understanding the defrosting processes and their role in shaping the dune.

1. Methods

A key preliminary step to achieve is the fine co-registration of both type of imagery. The processing of one given HiRISE image is performed with a multi-scale method in several stages : Pixel Shape Index classification [4], geometric filtering and regularization. The extraction of the endmembers - spectra deconvolved of effects related to the limited spatial resolution of the CRISM sensor and interpreted as different physical conditions of CO2 - is achieved using unsupervised linear spectral unmixing methods VCA and MVC-NMF [2]. The spatial distribution of the endmembers is computed in the form of maps giving their respective surface fraction in each pixel. Modeling of the spectra is performed with a semi-analytical model aimed at simulating the reflectance of a rough slab layer containing impurities [1]. The temporal dimension of observations allows us to locate and quantify the changes.

2. Interpretation

We perform the joint interpretation of the different products derived from the analysis of the CRISM and HiRISE data : (i) the dark spot distribution maps derived from the morphological analysis (ii) the corresponding estimation of the growth (shrinking) rate of the spots as a function of the position on the dune (iii) the distribution of the surface fractions occupied by the different physical conditions recognized by spectral unmixing.

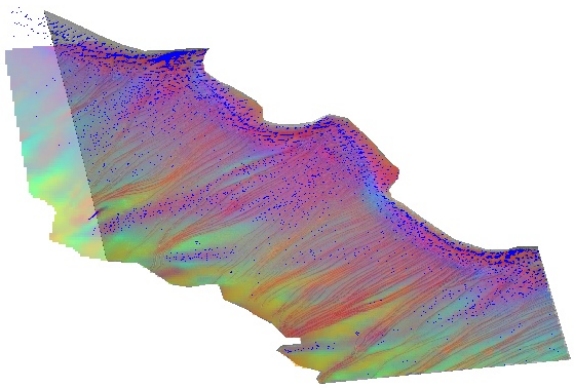

Figure 1: stacking of two products characterizing the Russell dune at a given date: (i) detection mask of the active areas in blue (ii) color composite showing the spatial distribution of the different CO2 ice conditions (structure and dust contamination).

At Ls=158° we note a very intense activity close to the crest of the dune with the growing of numerous individual spots. Conjointly the abundance maps show a high superficial contamination of the ice by the dust. On the main slope numerous small spots are appearing where granular ice is abundant. At the contrary, area dominated by a slab of compact ice on top of granular ice are devoid of spots. In a time span of 14°Ls the superficial contamination shows a dramatic spatial expansion on the slope of the dune. The spot growth rate is substantial in 4 topographical controlled regions located on the dune slope and separated by gaps of no activity. We also note flow like features associated with the deepest gullies with very high level of dust contamination. However they do not show substantial spot growth except in their upper part. Consequently we can infer that the dust contamination on the slope of the dune has two distinct origins: the activity of the neighboring spots (local source) one the one hand and the avalanches of dust coming from the crest ("distant" source) on the other hand. At Ls=172° limited area of granular weakly contaminated CO2 ice appear on the crest. We interpret the latter phenomena as re-condensing CO2 gas. Between Ls=172° and Ls=179° a slab of compact ice on top of granular ice is detected in some area. We observe the migration of this physical condition from the bottom part of the dune to the upper part. At Ls=179° we note the appearance of a new spectral endmember interpreted as the complete metamorphosis of the CO2 ice into a compact slab directly in contact with the sandy substratum of the dune. Between Ls=179° and Ls=181° the abundance of granular weakly contaminated CO2 ice builds up in some places along with an increased apparent reflectance factor. Once again we interpret the latter phenomena as freshly condensed CO2 gas in the granular form. During the same period the upward migration on the slope of the dune of the slab of compact ice on top of granular ice also continues. At Ls=181° the activity of the spots is much reduced compared to earlier times both in the slope and along the crest of the dune. The completely metamorphosed ice is mostly abundant in discontinuous area along the crest of the dune where are situated the most extended, sometimes coalescent spots. In addition this condition is also widespread in the western part of the slope. At contrary it has been replaced by an optically thick layer of dust - likely the completely defrosted sandy substratum- in the flow like features and in the large dark area all in the lower half part of the slope.

3. Conclusions

Our study documents in great details the evolution of the CO2 ice physical condition and degree of contamination by dust as well as the associated phenomena prior to the complete sublimation of these seasonal deposits. The main conclusion of our study is that intense ejection of dust occurs in multiple places on the crest of the dune Russell because of the CO2 sublimation. This phenomenon leads to the accumulation of a thick dust layer on the ice that causes dust avalanches channeled in the gullies. Thus it is now established that the gullies are currently not active by the flow of water but by the flow of dust. In addition we note two remarkable observations: (i) the evolutionary path of CO2 ice implies a top-down metamorphosis associated to sublimation leading to a slab of decreasing thickness (iii) the condensation of CO2 gas back to the ground in the form of granular weakly contaminated CO2 ice occurs in some places.

Acknowledgements

This research was carried out under the project " I2-Mars" conjointly funded by the Agence Nationale de la Recherche (ANR) and the National Science Fundation of China (NSFC).

References

[1] F. Andrieu, F. Schmidt, S. Douté, B. Schmitt and O. Brissau.d Radiative transfer model for Solar System ices, this conference.

[2] Ceamanos, X.; Douté, S.; Luo, B.; Schmidt, F.; Jouannic, G. and Chanussot, J. Intercomparison and validation of techniques for spectral unmixing of hyperspectrak images: a planetary case study. IEEE Transactions on Geoscience and Remote Sensing, 2011, 49, 4341 - 4358.

[3] Gardin, E.; Allemand, P.; Quantin, C. and Thollot, P. Defrosting, dark flow features, and dune activity on Mars: Example in Russell crater J. Geophys. Res., AGU, 2010, 115, E06016.

[4] X. Huang and L. Zhang, "Morphological Building/Shadow Index for Building Extraction From High-Resolution Imagery Over Urban Areas," IEEE Journal of Selected Topics in Earth Observations and Remote Sensing 2011.

EPSC Abstracts
Vol. 10, EPSC2015-541, 2015
European Planetary Science Congress 2015

Towards real-time Martian external magnetic field proxies

B. Langlais and F. Civet
Laboratoire de Planétologie et Géodynamique, CNRS UMR 6112, Université de Nantes, France

Abstract

Mars possesses no dynamic magnetic field of internal origin as it is the case for the Earth or for Mercury. Instead Mars is characterized by an intense and localized magnetic field of crustal origin. This field is the result of past magnetization and demagnetization processes, and reflects its evolution. The Interplanetary Magnetic Field (IMF) interacts with Mars' ionized environment to create an external magnetic field. This external field is weak compared to lithospheric one but very dynamic, and may hamper the detailed analysis of the internal magnetic field at some places or times. Because there are currently no magnetic field measurements made at Mars' surface, it is not possible to directly monitor the external field temporal variability as it is done in Earth's ground magnetic observatories. In this study we examine two indirect ways of quantifying this external field. First we use the Advanced Composition Explorer (ACE) mission which measures the solar wind about one hour upstream of the bow-shock resulting from the interaction between the solar wind and the Earth's internal magnetic field and extrapolate these measurements to Mars. Second we directly use Mars Global Surveyor magnetic field measurements to quantify the level of variability of the external field on a daily basis. We present a comparison of these two proxies and demonstrate their complementarity. These proxies will especially be useful for upcoming magnetic field measurements made around or at the surface of Mars.

1. Introduction

The external magnetic field on Mars is very dynamic, as it can be seen on Fig 1. We show night side measurements acquired above an area devoid of crustal field during different orbits separated by about 1°. The very disturbed one (more than twice the mean field) happens close to well documented 2003 Halloween magnetic super-storm [1].

On Earth, surface (observatory) measurements at constant locations routinely allow to separate daily (periodic) variations from rapid changes (magnetic storms). External field geometry is sufficiently constrained to define dedicated indices, e.g., Dst for the ring current, or AE for the ionospheric auroral electrojet. It is also possible to use the interplanetary magnetic field – IMF [2].

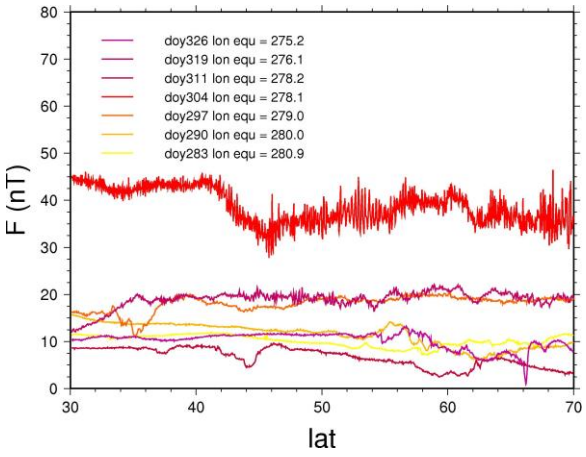

Figure 1: MGS total field measurements at the end of 2003 along seven orbits above the same location.

No such measurements exist on Mars. In this study we describe two approaches. The first one resembles to a virtual observatory approach, in which measurements are corrected from static internal magnetic fields and then stacked on a daily basis to compute a daily index. The second one is based on measurements acquired at the L1 Earth-Sun Lagrange point and extrapolated at Mars' position.

2. A local proxy

Mars Global Surveyor flew around Mars during 7 years on nearly circular and sun-synchronous orbit, with a fixed periapsis close to the South Pole. At a given location/altitude, there are many measurements (~once a week), that may be seen in a virtual observatory scheme. Over 6,000,000 magnetic field measurements at 400-km altitude. The median value for each 0.5x0.5°cell is found; individual difference to median value is computed for all data; and daily rms differences are computed from individual differences.

The median value at a given location may be seen as the static field at a given location, regardless of its origin (internal or external) or of the a priori model used to remove the crustal field. We show on Fig. 2 this proxy at the end of 2003. The signature of the Halloween magnetic storm is visible near doy 300.

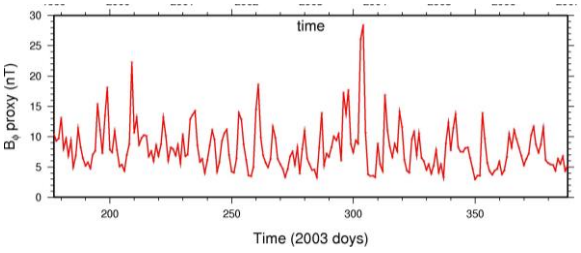

Figure 2: Daily magnetic local proxies on Mars, based on MGS measurements at the end of 2003.

3. An extrapolated proxy

No direct measurement of the solar wind pressure or interplanetary magnetic field exist at Mars. But such measurements exist between the Earth and the Sun, at L1 Lagrange point, by Advanced Composition Explorer (ACE) since 1997. These measurements may be extrapolated to Mars' position [3, 4]. IMF is propagated along Parker's spiral arms, only when the Earth and Mars are close to the same arm, time shift is computed to take into account both spiro-radial and along-orbit displacement. The three components of the IMF are L2-averaged on a daily basis. We compare them to MGS measurements (after crustal field correction) in a planet centered, sunstate reference frame (Fig. 3).

There is a 0.8 correlation between time-shifted ACE and MGS-based time series, each lasting about 200 days. This correlation proves that the external magnetic field around Mars can be relied to the IMF, and that both the local and the extrapolated proxies are representative of the external magnetic field variability at Mars.

4. Conclusion

The local proxy can be used to sub-select magnetic field measurements associated with a low external field variability, and therefore to reduce the temporal variations of the magnetic field above a given location. This would improve the characterization of static fields of internal origin [5].

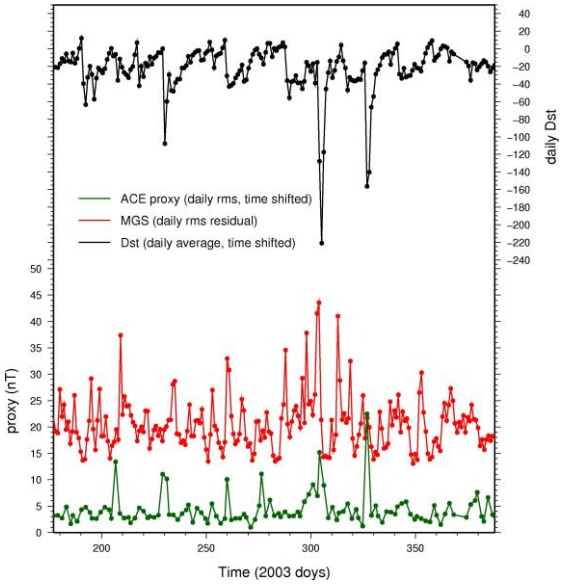

Figure 3: Dst (terrestrial index, time-shifted to Mars), ACE extrapolated and MGS daily residuals during 200 days at the end of 2003.

The extrapolated proxy confirms the validity of the local proxy approach (when measurements are available), and can be used to identify magnetic quiet periods on Mars without local measurements when the Earth and Mars are close to the same Parker's spiral. Thanks to these complementary proxies, it will be possible to provide a near real-time prediction of the external magnetic field variability during the forthcoming InSight mission.

Acknowledgements

Financial Support provided by CNES and CNRS.

References

[1] Crider, D. et al.: MGS observations of the Halloween 2003 solar superstorm's encounter with Mars, J. Geophys. Res., 110, 2005. [2] Lesur, V., et al. : GRIMM, the GFZ reference internal magnetic field model based on satellite and observatory data, Geophys. J; Int., 173, 2008. [3] Vennerstrom, S., et al., The magnetic field is the pile-up region at Mars and its variation with the solar wind, Geophys. Res. Lett., 30, 2003. [4] Civet, F. and P. Tarits, Electrical conductivity of the mantle of Mars from MGS magnetic observations, Earth Plan. Spa., 66, 2014. [5] Langlais B., and M. Purucker, A polar magnetic paleopole associated with Apollinaris Patera, Planet. Spa. Sci., 55, 2007.

EPSC Abstracts
Vol. 10, EPSC2015-542, 2015
European Planetary Science Congress 2015

OMEGA/MARS EXPRESS SURVEY OF SOUTH POLAR CAP DURING SOUTH SUMMER (MY 33).

Gondet[1], Y. Langevin, J.-P. Bbring[1],[1]IAS, batiment 121, 91405 Orsay Campus, France, gondet@ias.u-psud.fr

Introduction: The South Polar cap of Mars as been observed by a lot of instruments (Themis, TES, MOC, HRSC, CRISM, HIRISE), on board of different missions (from Viking to MRO). OMEGA [1], the hyper spectral VIS/NIR imager on board Mars Express, observations during recession in 2004-2006 as been published by Langevin at al [2] in 2007.

We will present here recent observations obtained by OMEGA in 2015 during south summer.

MEX orbit is elliptical nearly polar (inclination ~86.6°). Observational conditions (illumination, altitude, season) at the same area are never the same as well as the main mission parameters (occultation, eclipses and datarate). In 2015, for the first time, OMEGA had the possibility to observe the South Polar cap during summer at global scale (Fig 1). For this campaign only the visible channel was use (from .4 to .9 µm).

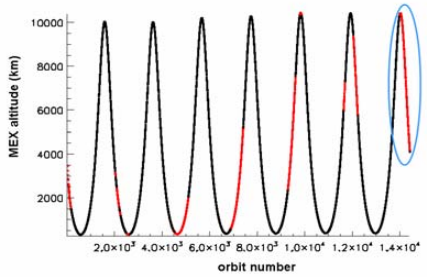

Fig 1.: Evolution of the altitude of the South Pole observation. In red: favorable conditions. In blue, area used.

Data sets: Table 1 summarizes the list observations made by OMEGA over the South Pole in nadir mode during the recession period (fig 2). At the same time 22 limb observations, cross correleted with SPICAM, over the South Pole were acquired. Some dust detached layer were observed (fig 3)

orbit	Ls	SEA	MEX alt (km)
13960	263.6	24.8	10400
13982	267.6	24.9	10350
14025	275.5	24.8	10100
14061	282.	24.4	9800
14120	292.6	22.9	9000
14163	300.1	21.4	8000
14177	302.6	20.8	7700
14219	309.8	19.	6800
14257	316.2	17.	6000
14275	319.2	16.	5700
14300	323.3	14.6	5300
14353	331.9	11.5	4300
14383	336.7	10.	3900
14408	340.5	8.	3500
14443	345.9	6.	3000

Table 1: Omega observations in nadir mode

Fig 2.: Exemple of 3 different observations in nadir mode

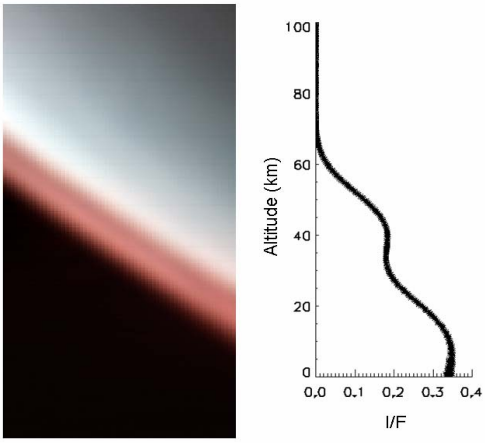

Fig 3.: Limb observation with detached layer at 45 km.

Thanks to this new database we will try to put new constrains in the relationship between seasonal cap characteristics and atmospheric circulation models, in particular in the role of dust whose composition and grain size are deductible from OMEGA spectra.

Reference: [1] Bibring, J.P. et al., OMEGA: Ob servatoire pour la Minéralogie, l'Eau, les Glaces et l'Activité, ESA SP 1240, 2004a
[2] Langevin et al. JGR 2007

EPSC Abstracts
Vol. 10, EPSC2015-574, 2015
European Planetary Science Congress 2015

Modelling the performances of the WISDOM radar on the Oxia Planum potential landing site for ExoMars

V. Ciarletti (1), Y. Hervé (1), S. Dorizon (1), A. Le Gall (1), C. Quantin (2), J. Broyer (2), J. Davis (3) and P. Grindrod (3)

(1) UVSQ (UPSay); CNRS/INSU; LATMOS-IPSL, 11 bd d'Alembert, 78280 Guyancourt, France

(2) Laboratoire de Géologie de Lyon: Terre, Planètes, Environnements, Université Lyon 1, ENS Lyon, CNRS UMR 5271, Villeurbanne, 2, rue Raphaël Dubois, 69622 Villeurbanne cedex, France

(3) Department of Earth and Planetary Sciences, Birkbeck, University of London, London, UK

Abstract

The search for evidence of past or present life is the main objective of the ESA-Roscosmos ExoMars rover mission [1]. The rover will be equipped with a suite of instruments dedicated to the investigation and characterization of the surface and shallow subsurface of Mars. In particular, a drill will provide, for the first time, ground samples from a depth of approximately 2 meters and a Ground Penetrating Radar named WISDOM (Water Ice Subsurface Deposit Observations on Mars) will map the shallow subsurface down to a depth of a few meters revealing its stratigraphy and structure, and thus providing invaluable insights into its origin and geological history.

A review of the candidate sites for the ExoMars rover mission has been conducted and four landing sites have been preselected [2] among which the Oxia Planum site (Fig. 1).

In this paper, we use all available information on Oxia Planum to build plausible geological models of the near-surface and translate them into geoelectrical models based on the expected dielectric constant and conductivity values published in the literature. Electromagnetic simulations are then run to assess the performances of the WISDOM radar at Oxia Planum.

1. The Oxia Planum potential landing site

Oxia Planum, a proposed landing site for ExoMars 2018, is located between 16° and 19° of latitude north and -23° to -28° of eastern longitude. This region exhibits one of the widest Mg/Fe phyllosilicate unit as mapped globally with OMEGA and with CRISM multispectral data [3]. The entire region corresponds to light toned and finely layered units. Thanks to HiRISE image stereo-couples acquired over the landing ellipse, we did a systematic investigation of the layers exposed in the upper part of the ramparts of small impact craters from 300 m to 1 km in diameter. The exposed layers were systematically mapped and their thicknesses were measured under Geographic Information System (GIS) software. The goal was to retrieve the stratigraphy solved by HiRISE data of the ten first meters of Oxia Planum subsurface as 10 m is the maximum depth of penetration of WISDOM. The results show that these ten first meters are composed of 4 to 9 well-identified layers on HiRISE images. The thicknesses of these layers range from 0.4 m to 5 m with an average thickness of 1.2 m.

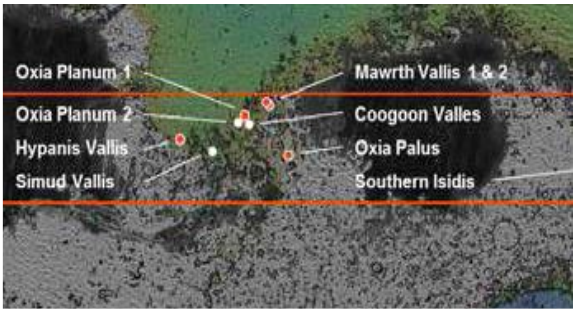

Fig. 1: The landing sites candidate for the ExoMars rover mission

2. The instrument

The WISDOM GPR [4] will be accommodated the mission Rover and operated from the surface. WISDOM has been designed to meet the scientific requirements of the ExoMars mission, which is to investigate the shallow subsurface down to a depth of ~3 m with a vertical resolution of a few centimeters. The data provided by WISDOM will be critical to understanding the local geologic context and to identifying and prioritizing the most promising targets for investigation by the drill. It will also aid in the identification of potential hazards, such as the presence of buried rocks, which could damage the drill and jeopardize the mission.

The stratigraphic profiles of shallow subsurface provided by WISDOM will allow the analysis of superpositional and cross-cutting relationships of the detected geological units and will give access to their relative timing, erosional history, deformational and structural development

Earlier field tests performed with a mock-up representative of the instrument, allowed us to verify the instrument performances and anticipate the fact that the penetration depth will be larger than 5 m in favorable environments. The purpose of the present study is to simulate the behavior of the instrument on Mars.

3. Simulations tool and results

Electromagnetic simulations that take into account the characteristics of the WISDOM radar (namely its distance to the surface, center frequency, frequency bandwidth, and antenna radiation pattern) have been performed. They were conducted using the OPEN TEMSI-FD software, which is based on the Finite Difference Time Domain method (FDTD). This non-commercial software was developed by C. Guiffaut [5] from the XLIM lab.

Simulation have been run for a variety of subsurfaces including layers with varying thickness, slope and geoelectrical nature, different degrees of roughness at the interfaces, and the presence of embedded blocks and random inhomogeneities within the geological units.

The results of the simulations will be presented for the retrieved stratigraphy of Oxia Planum. The obtained simulated data will be, when possible, compared to actual radar data acquired with WISDOM.

Acknowledgment

The WISDOM project is supported by CNES and DLR.

C. Quantin-Nataf and Jordan Broyer are supported by the European Research Council under the European Union's Seventh Framework Program (FP7/2007-2013)/ERC Grant agreement n° 280168.

References

[1] ESA, 2013. ExoMars Science Management Plan, Doc. No: EXM-MS-PL-ESA-00002, Issue: 6, Rev. 0, 20 September 2013, 66 p.

[2]http://www.esa.int/Our_Activities/Space_Science/Four_candidate_landing_sites_for_ExoMars_2018

[3] Quantin et al., EPSC 2015

[4] Ciarletti V et al., 2011, WISDOM a GPR designed for shallow and high resolution sounding of the Martian subsurface, Proceedings of the IEEE, 99, 5,pp 824-836

[5] Guiffaut, C., TEMSI-FD, Solver based on the finite difference in the time domain method," XLIM Laboratory, 2001-2007.

EPSC Abstracts
Vol. 10, EPSC2015-580, 2015
European Planetary Science Congress 2015

Tests of GCM pressure predictions for water ice stability using Mars Odyssey Neutron Spectrometer data

J. T. Wilson (1), V. R. Eke (1), R. J. Massey (1), R. C. Elphic (2), W. C. Feldman (3), S. Maurice (4), L. F. A. Teodoro (5).
(1) Institute for Computational Cosmology, Durham University, UK, (2) Planetary Systems Branch, NASA Ames Research Center, USA, (3) Planetary Science Institute, USA, (4) IRAP-OMP, France, (5) BAER, NASA Ames Research Center, USA . (j.t.wilson@durham.ac.uk)

Abstract

We have used the pixon image reconstruction technique on the Mars Odyssey Neutron Spectrometer epithermal neutron data to produce an improved global map of the hydrogen abundance on Mars. We will compare this to the predictions for surface hydration from the martian general circulation models, in order to provide both new constraints on, and tests of, the models.

1. Introduction

Much of our knowledge of the martian atmosphere is encapsulated in the General Circulation Models (GCMs): numerical simulations based on those developed for weather and climate forecasting on Earth. These models are constrained using the in-situ measurements of the martian atmosphere made by the various landers and rovers from the Viking missions to the present MSL Curiosity rover. However these measurements lack the spatial and temporal resolution to fully characterize the martian atmosphere.

The predictions of the GCMs have been compared with remotely sensed global data including that from the Thermal Emission Spectrometer (TES) [4] and the Mars Climate Sounder. The GCMs are found to be in agreement with most available observations and have been used to predict previously unobserved phenomena.

We propose another test of and constraint on the GCMs using the water equivalent hydrogen (WEH) distribution derived from the observations made by the Mars Odyssey Neutron Spectrometer (MONS). The stability of water ice on the surface of Mars is strongly dependent on atmospheric pressure and temperature. We will examine how the pressure variations predicted by the GCMs correlate with changing hydration as revealed in the MONS neutron data, noting that the form of the hydration (i.e. water ice or hydrated minerals) will affect the stability of the deposits and that this varies across the surface.

Previously, the utility of the MONS data in constraining the distribution of water, on scales similar to the GCM resolution (typically ~300 km), has been limited by its poor spatial resolution due to the large footprint of the MONS (its point spread function (PSF) has a full width at half maximum of

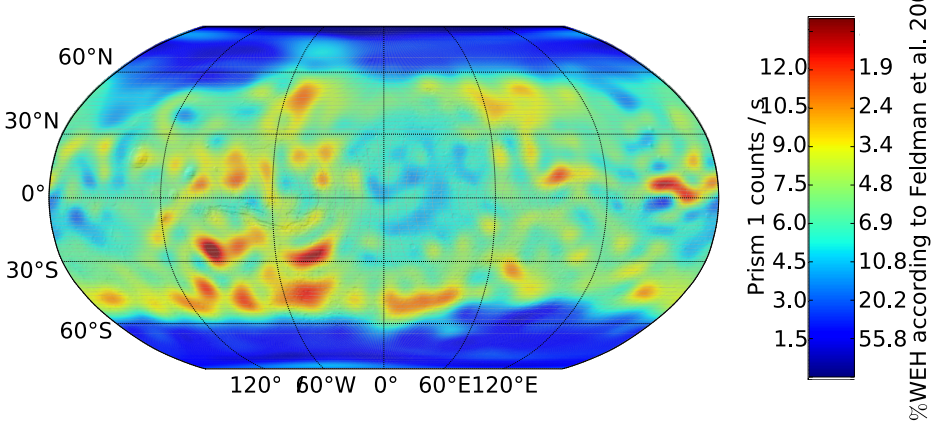

Figure 1: Robinson projection showing a pixon reconstruction of the MONS prism-1 data. Underlayed is a MOLA shaded relief map. The colour bar also shows the conversion to wt. % water equivalent hydrogen from Feldman et al. (2004) [2].

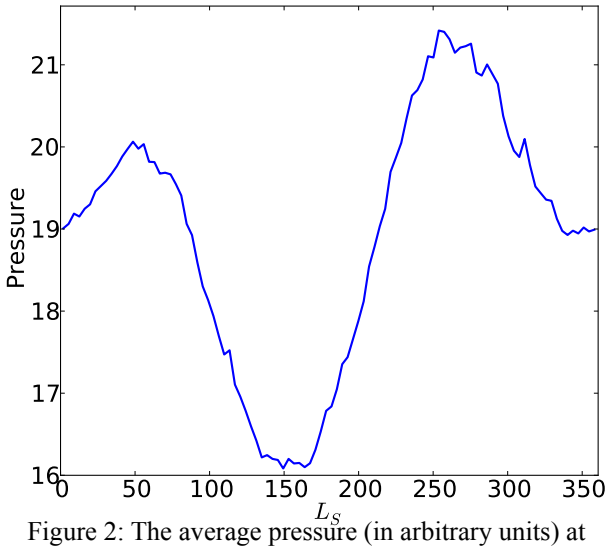

Figure 2: The average pressure (in arbitrary units) at 50°N in the LMD GCM against solar longitude, L_S.

~550km). Here we have used the pixon image reconstruction technique to improve the spatial resolution of this data set by suppressing noise and removing the effect of blurring with the PSF. At the poles this technique has been shown to give a spatial resolution of between 45-100 km [5]. Our reconstructed data set is available for the entire surface of Mars and will be compared to the predictions of the GCMs globally.

1.1 Image Reconstruction

The pixon method is a spatially-adaptive image reconstruction process that aims to deconvolve observed data from the PSF, to infer the simplest image consistent with the data [1]. Using this technique we have carried out the first global Bayesian reconstruction of a remotely sensed planetary data set, the result of which is shown in Figure 1.

The pixon method's adaptive smoothing algorithm works such that regions of the image with a higher signal to noise ratio are given the freedom to vary on small scales and those with low signal to noise ratio vary only on larger scales. This is done to create an image that has a spatially constant information content, which has the effect of precisely maximizing the entropy of the reconstructed image.

We use the frost-free prism-1 data (a measure of epithermal neutrons) from the MONS instrument of the three martian years from 2001, which has been corrected for altitude and look direction of the spacecraft and variation in environmental conditions [3]. We take only the data from where CO_2 frost is not present as it inhibits atmospheric exchange with the soil.

The conversion from epithermal neutron count rate to WEH is done using the relation in Feldman et al. (2004) [2].

2. Constraining the GCMs

GCMs depend on several important parameters associated with atmospheric and surface properties. One key property is the thermal inertia, which depends on the presence of water ice near the pole. Replicating the Viking and later missions atmospheric pressure histories requires taking into account near-surface water ice content and spatial distribution at high latitudes. In particular ice content is directly related to thermal conductivity and thermal inertia, and spatial variations of these govern the input and release of energy (and water vapour) seasonally. Therefore, the pixon reconstruction in the polar regions can be used to outline deviations from a uniform ice distribution poleward of 80°N which will influence local circulation and precipitation.

At all latitudes the pressures and temperatures predicted by the GCMs can be used to infer water concentrations in near-surface soil, which are measured globally in the MONS data. We will compare both the NASA Ames and Laboratoire de Météorologie Dynamique (LMD) models to our reconstructed data set. The variation in pressure with time in the LMD model is shown in Figure 2, this information can be used to predict surface water abundances globally, which we will then compared to the measured water abundances derived using the pixon reconstruction technique on the MONS data.

References

[1] Eke, V. (2001), A speedy pixon image reconstruction algorithm, Mon. Not. R. Astron. Soc., 324, 108–118.

[2] Feldman, W. C., et al. (2004), Global distribution of near-surface hydrogen on Mars, J. Geophys. Res., 109, E09006.

[3] Maurice, S., et al. (2011), Mars Odyssey neutron data: 1. Data processing and models of water-equivalent-hydrogen distribution, J. Geophys. Res., 116, E11008.

[4] Navarro, T., et al. (2014), Global climate modeling of the Martian water cycle with improved microphysics and radiatively active water ice clouds, J. Geophys. Res. Planets, 119, 1479–1495.

[5] Teodoro L. F. A. et al. LPC XLIV, Abstract #2623.

EPSC Abstracts
Vol. 10, EPSC2015-597, 2015
European Planetary Science Congress 2015

Cold Ion Escape from the Martian Ionosphere

M. Fränz (1), E. Dubinin (1), D. Andrews(2), H. Nilsson (2), S. Barabash (2), and A. Fedorov (3)
(1) MPI for Solar System Research, Katlenburg-Lindau, Germany (fraenz@mps.mpg.de / Fax: +49-551-384979-240), (2) Institute for Space Physics, Kiruna & Uppsala, Sweden, (3) Institut de Recherche en Astrophysique et Planetologie, Toulouse, France

Abstract

We here report on new measurements of the escape flux of oxygen ions from Mars by combining the observations of the ASPERA-3 and MARSIS experiments on board the European Mars Express spacecraft. We show that in previous estimates of the total heavy ion escape flow the contribution of the cold ionospheric outflow with energies below 10 eV has been underestimated. Both case studies and the derived flow pattern indicate that the cold plasma observed by MARSIS and the superthermal plasma observed by ASPERA-3 move with the same bulk speed in most regions of the Martian tail. We determine maps of the tailside heavy ion flux distribution derived from mean ion velocity distributions sampled over 7 years. If we assume that the superthermal bulk speed derived from these long time averages of the ion distribution function represent the total plasma bulk speed we derive the total tailside plasma flux. Assuming cylindrical symmetry we determine the mean total escape rate for the years 2007 to 2014 at $2.9 \pm 0.2 \times 10^{25}$ atoms/s which is in good agreement with model estimates. In this talk we will also try to compare these results with more recent observations by the MAVEN spacecraft. Possible mechanism to generate this flux can be the ionospheric pressure gradient between dayside and nightside or momentum transfer from the solar wind via the induced magnetic field since the flow velocity is in the Alfvénic regime.

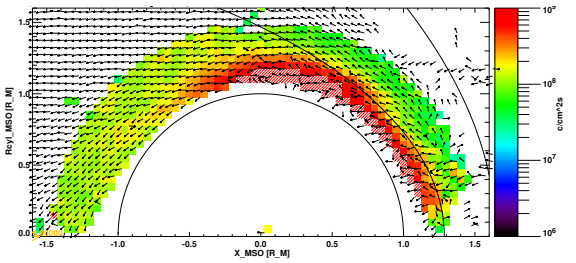

Figure 1: Total flux calculated from total velocity derived from the mean MEX Aspera IMAEXTRA VD with spacecraft velocity and potential correction observed between 1 May 2007 and 1 June 2014 multiplied by the mean MARSIS local density observed over the same period in the same spatial bins, scaled in /cm^{2}s. The vertical component of vectors shows the deviation from the cylindrical symmetry axis.

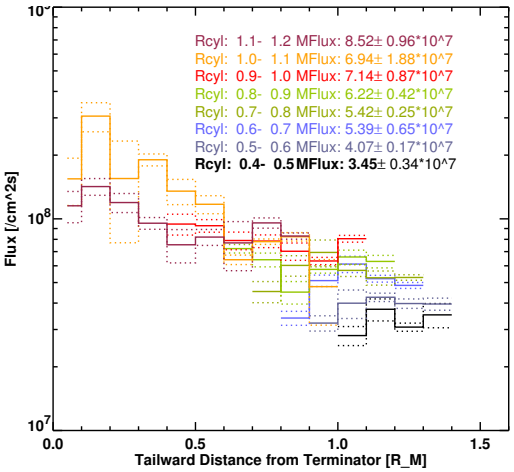

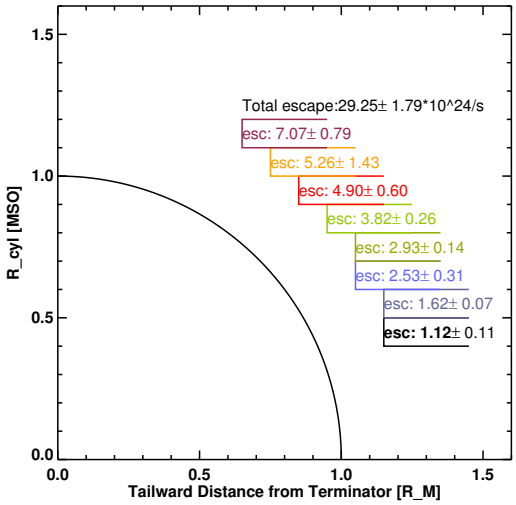

Figure 2: Top: Total mean flux as in Fig.1 in cylindrical bins with respect to the MSO_X axis as a function of tailward distance from the terminator plane. Numbers in the upper right corner give the mean flux over the last 0.3 R_M of each cylindrical shell, where combined observations of MARSIS and Aspera-3 were obtained. Bottom: Position of the cylindrical shells used for the mean flux calculation and escape (ions/s) calculated from the cross section of the cylindrical shells multiplied by the mean flux for each cylindrical shell. Standard deviations are from the flux variation over this distance.

EPSC Abstracts
Vol. 10, EPSC2015-602, 2015
European Planetary Science Congress 2015

Surface release of methane on Mars: A model study in the framework of the future NOMAD mission

S. Viscardy (1), F. Daerden (1), L. Neary (1), A. García Muñoz (2), A. C. Vandaele (1) and the NOMAD team

(1) Belgian Institute for Space Aeronomy (BIRA-IASB), Brussels, Belgium, (2) ESA/RSSD, ESTEC, 2200 AG Noordwijk, The Netherlands (sebastien.viscardy@aeronomie.be)

Abstract

Two connected tasks are tackled in this work in order to provide useful information for the highly sensitive NOMAD solar occultation channel [1] on the future ExoMars Trace Gas Orbiter mission. Firstly, an analysis of potential chemical by-products of methane is carried out using a 1D model for atmospheric chemistry. Secondly, we aim to investigate the time and space evolution of methane after different surface release scenarios using a 3D Global Circulation Model (GCM) for the atmosphere of Mars (GEM-Mars), focusing specifically on the vertical distribution of methane.

1. Introduction

In the past decade, the detection of methane (CH_4) in the atmosphere of Mars has been reported several times [2, 3, 5, 8, 9]. These observations have strongly drawn the attention of the scientific community and triggered a renewed interest in Mars as their implications for the geochemical or biological activities are remarkable. However, given that methane is expected to have a photochemical lifetime of several centuries, the relatively fast loss rates of methane estimated from Earth-based measurements remain unexplained [6]. Although this gave rise to objections against the validity of those observations [11], recent in situ measurements [9] confirmed that methane is being occasionally released into the atmosphere from an unknown source (possibly from the ground). This is in this context that we present a model study of the behaviour of methane plumes and some preliminary results on the chemistry of methane in the atmosphere of Mars.

2. Chemistry of methane

Ten years ago, a chemical scheme involving methane and related compounds was proposed [10]. Photolysis and oxidation of methane (see Figure 1) leads to the production of several organic species of which the most important ones are formaldehyde (CH_2O), methanol (CH_3OH), and ethane (C_2H_6). In this work, all those reactions were implemented in a 1D model for atmospheric chemistry initially developed by A. García Muñoz [4]. A discussion will be held about the CH_4 loss reactions and the production of related species in the framework of the future NOMAD mission.

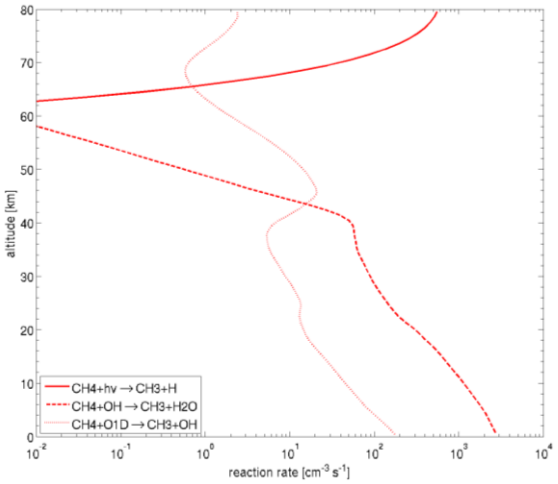

Figure 1. Rates of methane loss reactions as function of the altitude.

3. Surface release of methane

Mischna *et al.* (2011) investigated the behaviour of methane plumes formed in the Martian atmosphere [7]. Following on from that work, a 3D General Circulation Model for the atmosphere of Mars (called GEM-Mars) is used, paying specific attention to the evolution of the vertical distribution of methane after different surface release scenarios.

A few days after its release from the ground, methane is not uniformly dispersed into this atmosphere but can rather form layers at altitudes as high as 25-30 km (see Figure 2).

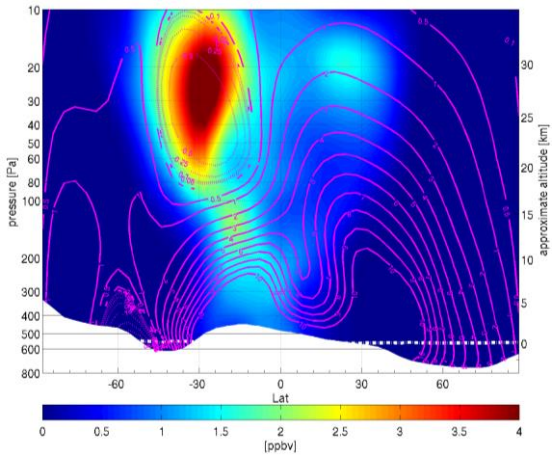

Figure 2. Zonal mean of methane mixing ratio 13.5 days after an instantaneous release at the equator. Contours in magenta represents the uniform values of the mass stream function.

4. Summary and Conclusions

This work in progress aims to develop a GCM (GEM-Mars) in order to support the future NOMAD mission. Two linked aspects are addressed: i) the chemistry of methane on Mars; ii) the evolution of methane in the atmosphere after surface release. We specifically put in evidence the remarkable formation of layers. This is relevant for the highly sensitive IR solar occultation of NOMAD with high vertical resolution.

References

[1] Drummond, R., Vandaele, A.-C., Daerden, F. Fussen, D., Mahieux, A., Neary, L., Neefs, E., Robert S., Willame, Y., and Wilquet, V., Studying methane and other trace species in the Mars atmosphere using a SOIR instrument, Planetary and Space Science, Vol. 59, pp. 292-298 (2011).

[2] Fonti, S. and Marzo, G. A., Mapping the methane on Mars. Astronomy and Astrophysics, Vol. 512, A51 (6 p.) (2010).

[3] Formisano, V., Atreya, S., Encrenaz, T., Ignatiev, N., and Giuranna, M., Detection of methane in the atmosphere of Mars, Science, Vol. 306, pp. 1758-1761 (2004).

[4] García Muñoz, A., McDonnell, J. C., McDade, I. C., and Melo, S. M. L., Airglow on Mars: Some model expectations for the OH Meinel bands and the O_2 IR atmospheric band, Icarus, Vol. 176, 75-95 (2005).

[5] Krasnopolsky, V. A., Maillard, J. P., and Owen, T. C., Detection of methane in the Martian atmosphere: Evidence for life? Icarus, Vol. 172, pp. 537-547 (2004).

[6] Lefèvre, F. and Forget, F., Observed variations of methane on Mars unexplained by known atmospheric chemistry and physics, Nature, Vol. 460, pp. 720-723 (2009).

[7] Mischna, M. A., Allen, M., Richardson, M. I., Newman, C. E., and Toigo, A. D., Atmospheric modeling of Mars methane surface releases, Planetary and Space Science, Vol. 59, pp. 227-237 (2011).

[8] Mumma, M. J., Villanueva, G. L., Novak, R. E., Hewagama, T., Bonev, B. P., Disanti, M. A., Mandell, A. M., and Smith, M. D., Strong release of methane on Mars in northern summer 2003, Science, Vol. 323, pp. 1041-1045 (2009).

[9] Webster, C. R. *et al.*, Mars methane detection and variability at Gale crater. Science, Vol. 347, pp. 415-417 (2014).

[10] Wong, A.-S., Atreya, S., and Encrenaz, T., Chemical markers of possible hot spots on Mars, Journal of Geophysical Research , Vol. 108, 5026 (7 p.) (2003).

[11] Zahnle, K., Freedman, R. S., and Catling, D. C., Is there methane on Mars?, Icarus, Vol. 212, pp. 493-503 (2011).

EPSC Abstracts
Vol. 10, EPSC2015-607, 2015
European Planetary Science Congress 2015

Forecasting atmospheric dust loading on Mars using statistics of past observations

L. Montabone (1, 2), F. Forget (2) and E. Millour (2)
(1) Space Science Institute, Boulder, CO, USA, (2) CNRS – Laboratoire de Météorologie Dynamique, Paris, France (lmontabone@spacescience.org)

1. Introduction

The onset of local dust storms on Mars can happen very suddenly, and the development into large regional or even planetary-encircling storms can be rapid and rather unpredictable, taken into account the current knowledge of dust lifting mechanisms and meteorological feedback.

Forecasting at least the dust optical depth of the atmospheric column (if not the dust opacity profile and the size of the dust particles) expected at a particular location and season is a key issue for safe spacecraft landing on Mars. Next spacecraft to land on the martian surface will be ESA's Exomars 2016 'Schiaparelli' module in Meridiani Planum (-6.1° lon, -1.9° lat) during the so-called 'dust storm season' (northern hemisphere winter, around L_s~245°). It will be followed by ESA's Exomars 2018 Rover and NASA's 2020 Rover, whose landing sites have yet to be confirmed, as of May 2015.

Although operative dust storm forecast currently presents significant challenges, a forecast based on the statistics of past information is more readily achievable, thanks to the plethora of dust optical depth observations available since the Mariner era. In particular, Montabone et al. [3] have reconstructed the atmospheric dust climatology at all locations on the planet from MY 24 through MY 31 using observations from the Mars Global Surveyor/TES, the Mars Odyssey/THEMIS, and the Mars Reconnaissance Orbiter/MCS. The multiannual dataset of daily gridded maps of retrieved IR column dust optical depth (CDOD) they have produced can serve the purpose of statistically forecasting the dust loading at selected seasons and locations on the planet. Specifically to Meridiani Planum and Gusev Crater, moreover, the Mars Exploration Rovers (MER) 'Opportunity' and 'Spirit' have continuously collected near-IR CDOD observations (as retrieved by Lemmon et al. [1]), from L_s~330°, MY 26, to date for Opportunity, and until L_s~67°, MY 29, for Spirit.

2. Statistical dust loading forecast

In this study, as a test-case of statistical dust loading forecast, we use the MER 'Opportunity' dataset [1] and the multiannual dust climatology dataset [3] to estimate the CDOD expected in Meridiani at the season of Schiaparelli's landing, and to examine how much the atmospheric dust loading can change (in statistical terms) over a given time period. In other words, we want to estimate the probability Y % that the CDOD changes by X % after n sols, for each sol within Schiaparelli's extended landing window (L_s=[220°, 270°]) in the Meridiani Planum area.

The lower panel of Fig. 1 shows that, in this particular case, the dust loading decreases with time after sol-of-year 475 (see the sol-based Mars calendar in [3]), L_s~245°. The histogram of the CDOD relative difference for "10-sol ahead of time" conditions in Meridiani clearly shows the signature of this decrease – a significant negative bias in the mean value (Fig. 2, including all years). This happens despite regional dust storms occurring in MY 27 and 29, and a planet-encircling dust storm occurring in MY 28, within the considered time range (Fig. 1). The cumulative histogram in Fig. 3 allows us to estimate the probability of dust loading change (independently of increase or decrease) in Meridiani for "10-sol ahead of time" conditions.

When looking at the specificity of Meridiani Planum during the considered season, Fig. 4 illustrates that it is rather representative of the global situation. The histograms are obviously smoother (more grid points are taken into account), but the negative bias in the mean value due to the general decrease of the dust loading after sol-of-year 475 is still present.

The global decrease in dust loading after L_s~245° can be linked to the solsticial pause in baroclinic wave activity [2], which considerably reduces dust lifting in the northern plains. This phenomenon has the consequence of reducing the probability of large regional cross-equatorial storms, which are one of the main sources of dust loading increase in the northern hemisphere autumn and winter seasons.

3. Figures

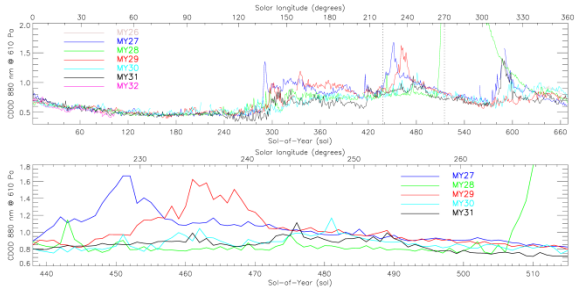

Figure 1: Time series of near-IR (880 nm) CDOD as retrieved by [1] from MER 'Opportunity' at Meridiani Planum over 7 Mars years (data are plotted until L_s~50° in MY 32, although Opportunity is still collecting observations as of May 2015). The dashed vertical lines in the upper panel indicate the time range considered in the lower panel and in the subsequent analysis. The CDOD values are normalised to the 610 Pa reference pressure.

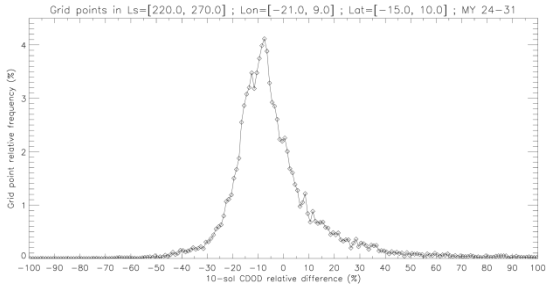

Figure 2: Using the Montabone et al. [3] multiannual dust climatology dataset, we have calculated the CDOD relative difference between each sol in the solar longitude range L_s=[220°, 270°] and 10 sols ahead in time, within a grid box centred on Meridiani Planum ([-21°, 9°] lon, [-15°, 10°] lat), for Martian years 24 through 31. This figure shows the histogram of this relative difference.

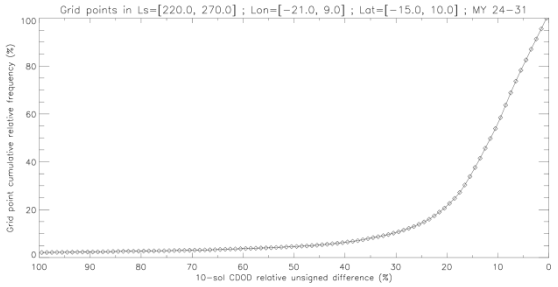

Figure 3: Cumulative histogram for the absolute value of the same variable as in Fig. 2.

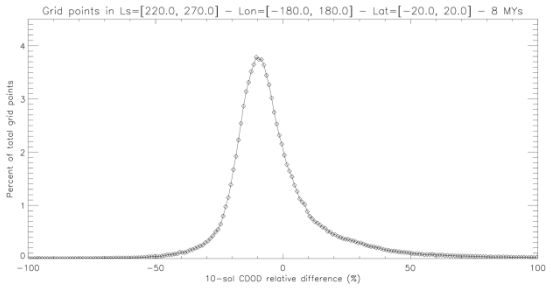

Figure 4: Same as in Fig. 2 for a latitude band [-20°, 20°] and all longitudes.

Acknowledgements

The authors acknowledge the use of retrievals of CDOD for MER 'Opportunity' provided by M. Lemmon. This work is part of a study for the environmental characterization of the entry, descending and landing of Exomars 2016 'Schiaparelli' module (ESA-Thales Alenia Space).

References

[1] Lemmon, M.T., M.J. Wolff, J.F. Bell III, M.D. Smith, B.A. Cantor, P.H. Smith: Dust aerosol, clouds, and the atmospheric optical depth record over 5 Mars years of the Mars Exploration Rover mission. Icarus 251, 96-111, 2015.

[2] Lewis, S.R. D. P. Mulholland, P. L. Read, L. Montabone, R. J. Wilson, and M. D. Smith: The solsticial pause on Mars: 1 A planetary wave reanalysis; preprint submitted to Icarus, 2015.

[3] Montabone, L., F. Forget, E. Millour, R.J. Wilson, S.R. Lewis, B. Cantor, D. Kass, A. Kleinboehl, M.T. Lemmon, M.D. Smith, M.J. Wolff: Eight-year climatology of dust optical depth on Mars. Icarus 251, 65-95, 2015.

EPSC Abstracts
Vol. 10, EPSC2015-610, 2015
European Planetary Science Congress 2015

Impact of Radiatively Active Water Ice Clouds in the GEM-Mars GCM

L. Neary and F. Daerden
Belgian Institute for Space Aeronomy, Brussels, Belgium (lori.neary@aeronomie.be)

Abstract

Water ice clouds have proven to be an important driver in the temperature distribution and overall climate of the Martian atmosphere. Clouds have both a direct and indirect radiative effect on temperature and circulation, which in turn can modify the water vapour distribution and that of other trace gases.

We have included the radiative effect of water ice clouds (RAC) in the GEM-Mars GCM model, using Mie code and optical indices to compute the scattering properties of ice particles.

We present preliminary results from simulations with and without RAC, and compare these initial tests with Mars Climate Sounder (MCS), Thermal Emission Spectrometer (TES) and Mars Color Imager (MARCI).

The GEM-Mars model

GEM-Mars is a three-dimensional general circulation model (GCM) of the Mars atmosphere extending from the surface to approximately 150 km based on the GEM (Global Environmental Multiscale) model, the operational data assimilation and weather forecasting system for Canada (Côté et al., 1998). The dynamical core is an implicit two-time-level semi-Lagrangian scheme on an Arakawa C-grid with a log-hydrostatic-pressure terrain-following vertical coordinate discretized on a Charney-Phillips grid (Girard et al., 2014). The model has both a hydrostatic and non-hydrostatic formulation, providing a single platform for simulations on a variety of horizontal scales. The model code is fully parallelized using OMP and MPI.

The GCM includes the relevant physical processes such as CO_2 condensation, planetary boundary layer mixing, gravity wave drag and surface parameterisations. A simple water cycle, gas-phase chemistry and passive tracers are also included. Because of the vertical extent of the model, UV heating, non-LTE effects and molecular diffusion are also included.

The scattering and absorption effects of dust are taken into account and the model includes interactive dust lifting by saltation and dust devils, based on the work of Kahre et al. (2006) and Newman et al. (2002). Three particle sizes of dust are transported using the dynamical core and optical properties are those given by Wolff et al. (2006, 2009). The active dust scheme has been successfully utilized to examine dust layering as seen by the Phoenix lander (Daerden et al. 2015, submitted).

For water ice clouds, a uniform radius of 2 μm is used as a starting point, with optical properties calculated using the indices of Warren and Brandt (2008). A simple bulk condensation scheme is used at present. The modularity of the model permits the inclusion of a more sophisticated microphysical parameterisation such as that used by Daerden et al. (2010) at a later date.

Simulations performed

For these initial tests, the GEM-Mars model was run for one Martian year with and without the impact of radiatively active water ice clouds. Both runs kept the same settings for dust devil and wind lifting rates, and the opacities were not scaled to observed values (i.e. free-running advected dust tracers).

The horizontal resolution of the model is $4^\circ \times 4^\circ$ with 103 log-hydrostatic-pressure levels up to $\sim$150 km.

In the following sections, we discuss the impact of RAC on temperature, circulation, dust lifting, water vapour and ice, and ozone.

Temperature

Figure 1 shows the difference in zonal mean temperature profiles for 4 seasons for the simulations with and without RAC. There is a general equatorial warming around 10 Pa of 10-15° K, but greater for the L_s 90 season where clouds are more dominant. There is also

warming in the winter polar regions at the equinoxes. The RAC have a infrared cooling effect in the lower levels, which can be seen more clearly when the zonal means for day and night are separated (not shown here).

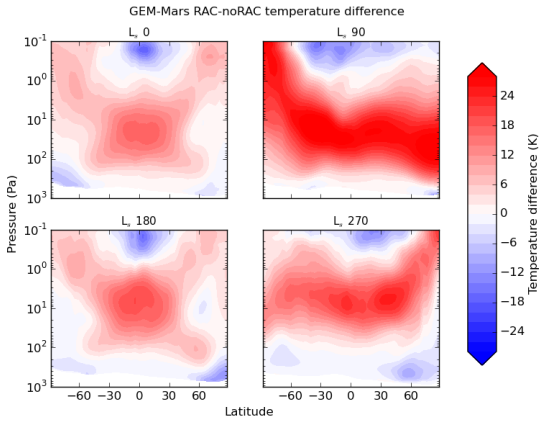

Figure 1: Temperature difference between the simulations with and without RAC. Red scale shows warming, blue shows a cooling effect.

We also compare the zonal mean temperature profiles with those from MCS (Kleinbohl et al., 2009) averaged over several years. Figure 2 shows the difference between the averaged MCS seasonal profiles and those of GEM-Mars. Before the introduction of RAC, the temperatures around 10 Pa region were too cold in the model (not shown), where now they are improved, with difference of less than 10 K depending on the season and location. The largest improvement was seen in the L_s 90 season, where water ice clouds form in the equatorial region. There are still some biases as the inclusion of RAC has indirect effects as well, such as influencing the amount of dust lifted off the surface and an increase in the strength of the Hadley cell circulation.

Impact on dust

An indirect effect of RAC is on the rate of dust lifting, which depends on the surface wind stress. A small decrease in wind stress due to RAC causes a decrease of nearly half in the optical depth due to lifted dust. The rate of dust lifted due to dust devils does not change as significantly. Figure 3 shows the zonal mean optical depth for the two simulations, separated into optical depth from dust devils and wind lifting.

Figure 4 shows the dust optical depth at the equator compared with TES (Smith et al., 2002). The dust in the model is not scaled to observations or tuned to any specific year, which can be done by adjusting an efficiency parameter or threshold. The timing of the dust storm compares well with TES in both cases but the values are too low, especially with the addition of RAC. Sensitivity tests are ongoing. Another factor in the dust optical depth is the change in circulation as discussed in the following section.

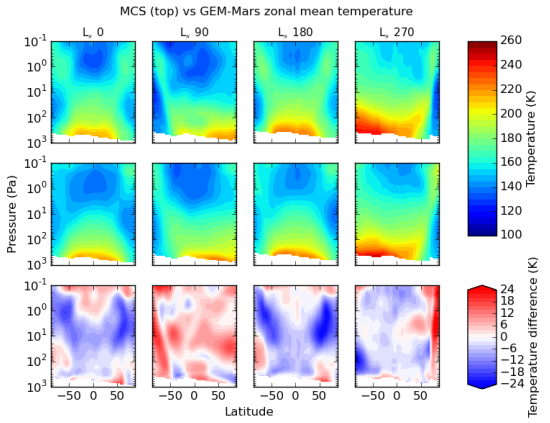

Figure 2: Averaged zonal mean temperature profiles from MCS (top), GEM-Mars with RAC (middle) and the difference (GEM-MCS) of the 2 fields (bottom). In the difference plots, blue indicates a cool bias in the model, red means the model is warmer than MCS.

Change in circulation

The inclusion of RAC increases the height of the Hadley circulation as suggested in Navarro et al. (2014). Figure 5 shows the change in zonal average mass stream function with the implementation of RAC. The circulation reaches higher in the atmosphere, which has a consequence of transporting the dust and water vapour to higher levels. For dust, there is a combination of reduced lifting as well as more transport, reducing the optical depth, although the reduced lifting is the dominant factor.

Impact on water vapour and ice

Due to the enhanced Hadley circulation, we see a decrease in the amount of total column water vapour, because it is transported higher in the atmosphere, reducing the column amount. The mean vertical profiles of ice extinction compare better with MCS with the inclusion of RAC (not shown here).

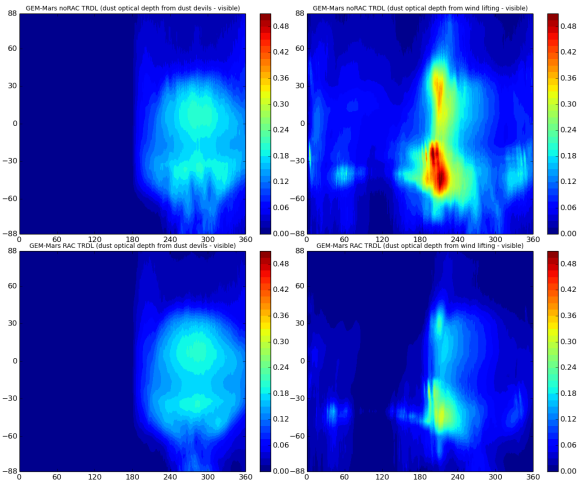

Figure 3: Dust optical depth for RAC and noRAC simulations. Top row is the RAC simulation, left: dust optical depth from dust devils, right: from wind lifting. Bottom row is the noRAC run, left: dust optical depth from dust devils, right: from wind lifting.

The complex interaction between dust, water vapour, ice and temperature make it difficult to quantify the direct effects of RAC. As these tests are preliminary, we have not tried to separate the direct and indirect effects and allowed the model to run without constraints. Sensitivity tests are necessary to understand more about these complexities.

The change in vertical distribution of water also impacts ozone as seen in the following section.

Ozone

Ozone reacts with the products of H_2O photolysis, leading to an anti-correlation between ozone and water vapour in the daytime. With the transport of water vapour to higher altitudes in the RAC simulation, we see a decrease in the the total column amount of ozone. Figure 6 shows a comparison of mean vertical profiles of ozone and water vapour for the two simulations. In the equinox seasons, especially in L_s 90, the layer of ozone at 10 Pa seen in the noRAC simulation is affected by the increased transport of water vapour in the RAC run.

Figure 7 shows this effect as compared with preliminary retrievals from the MARCI instrument (Malin et al., 2001). The inclusion of RAC reduces the column amount most significantly in the first half of the year, leading to better agreement with MARCI, notably at high latitudes in the northern summer, when the north

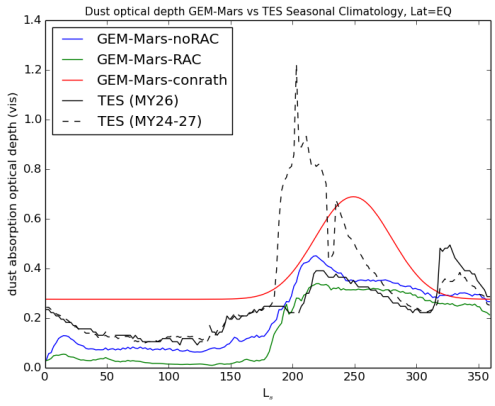

Figure 4: Dust optical depth compared with TES. The black solid line is TES, MY26 (a lower dust year) and the dashed line is the average from MY24-27. The RAC run is in green, without RAC is in blue and the climatological dust values previously used is given as a reference in red.

polar permanent water ice cap is sublimating.

Summary and Conclusions

Overall, with the addition of RAC, temperatures in the 10 Pa region increased by 10-20 K, depending on season and location. The largest impact is during aphelion, where an equatorial cloud belt is formed. An indirect effect of RAC is on the amount of dust lifted which depends on the surface wind stress.

The increase in strength of the Hadley circulation has a significant impact on the vertical distribution of trace gases in the atmosphere.

It should be stressed that these are very initial tests, with no tuning of the dust or water cycle, but the results are very promising.

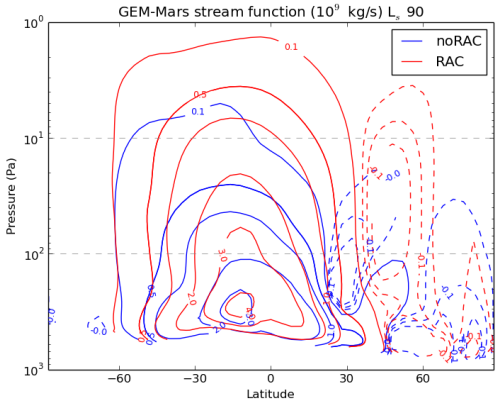

Figure 5: Zonal mean mass stream function in 10^9 kg/s for L_s 90, with (red contours) and without (blue) RAC. Positive solid lines indicate counter-clockwise flow.

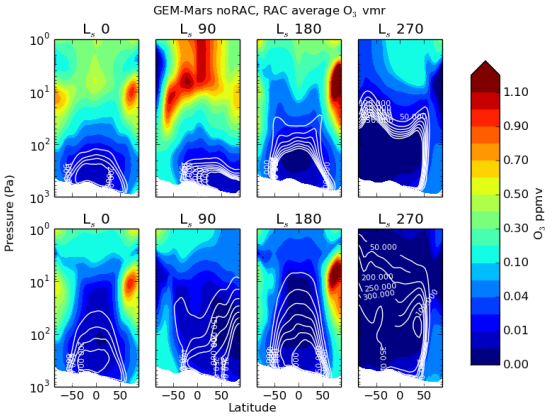

Figure 6: Top row is the noRAC simulation for 4 seasons and the bottom is with RAC. The colour contours are ozone mixing ratio and the white contours represent water vapour mixing ratios.

Acknowledgements

The research presented here has received support from the European Union Seventh Framework Program (FP7/2007-2013) under grant agreement no 607177, the CROSS DRIVE project. Thank you to R.T. Clancy for providing MARCI ozone data.

References

[1] Côté J., Gravel S., Méthot A., Patoine A., Roch M. and Staniforth, A., 1998. The operational CMC–MRB Global Environmental Multiscale (GEM) Model. Part I: Design considerations and formulation, *Mon. Wea. Rev.*, *126*(6), 1373–1395.

[2] Daerden, F., Whiteway, J.A., Davy, R., Verhoeven, C., Komguem, L., Dickinson, C., Taylor, P.A., Larsen, N., 2010. Simulating observed boundary layer clouds on Mars. *Geophys. Res. Let. 37*, L04203. doi:10.1029/2009GL041523

[3] Girard, C., Plante, A., Desgagné, M., McTaggart-Cowan, R., Côté, J., Charron, M., Gravel, S., Lee, V., Patoine, A., Qaddouri, A., Roch, M., Spacek, L., Tanguay, M., Vaillancourt, P.A., Zadra, A., 2014. Staggered Vertical Discretization of the Canadian Environmental Multiscale (GEM) Model Using a Coordinate of the Log-Hydrostatic-Pressure Type, *Mon. Wea. Rev.*, *142*, 1183–1196.

[4] Kahre M.A., Murphy, J.R., and Haberle, R.M., 2006. Modeling the Martian dust cycle and surface dust reservoirs with the NASA Ames general circulation model, *J. Geophys. Res.*, *111*, E06008.

[5] Kleinböhl, A., Schofield, J.T., Kass, D.M., Abdou, W.A., Backus, C.R., Sen, B., Shirley, J.H., Lawson, W.G., Richardson, M.I., Taylor, F.W., Teanby, N.A., McCleese, D.J., 2009. Mars Climate Sounder limb profile retrieval of atmospheric temperature, pressure, and dust and water ice opacity. *Journal of Geophysical Research* 114. doi:10.1029/2009JE003358

[6] Malin, M.C., Bell, J.F., Calvin, W., Clancy, R.T., Haberle, R.M., James, P.B., Lee, S.W., Thomas, P.C., and Caplinger, M.A., 2001. Mars Color Imager (MARCI) on the Mars Climate Orbiter. *J.Geophys. Res.*, *106*E8, 17651–17672.

[7] Newman C.E., Lewis, S.R., Read, P.L., Forget, F., 2002. Modeling the Martian dust cycle, 1. Representations of dust transport processes, *J. Geophys. Res.*, *107*(E12), 5123. doi:10.1029/2002JE001910

[8] Smith, M.D., Pearl, J. C., Conrath, B., Christensen, P.R., Thermal Emission Spectrometer results: Mars atmospheric thermal structure and aerosol distribution.*J. Geophys. Res.*, *106*, E10, 2156–2202. doi:10.1029/2000JE001321

[9] Warren, S.G., and Brandt, S.G., 2008. Optical constants of ice from the ultraviolet to the microwave: A revised compilation. *J. Geophys. Res.*, 113, D14220. doi:10.1029/2007JD009744

[10] Wolff, M.J., Smith, M.D., Clancy, R.T., Spanovich, N., Whitney, B.A., Lemmon, M.T., Bandfield, J.L., Banfield, D., Ghosh, A., Landis, G., Christensen, P.R., Bell III, J.F. and Squyres, S.W. (2006), Constraints on dust aerosols

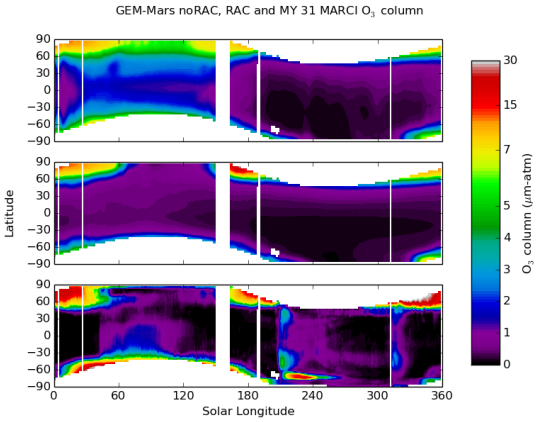

Figure 7: Column ozone compared with MARCI in μm-atm. Top: GEM-Mars noRAC, middle: GEM-Mars RAC, bottom: MARCI.

from the Mars Exploration Rovers using MGS overflights and Mini–TES, *J. Geophys.Res.*, *111*, E12S17. doi:10.1029/2006JE002786

[11] Wolff, M.J., Smith, M.D., Clancy, R.T., Arvidson, R., Kahre, M., Seelos, F., Murchie, S., and Savijärvi, H. 2009. Wavelength dependence of dust aerosol single scattering albedo as observed by the Compact Reconnaissance Imaging Spectrometer, *J. Geophys. Res.*, *114*, E00D04. doi:10.1029/2009JE003350

EPSC Abstracts
Vol. 10, EPSC2015-620, 2015
European Planetary Science Congress 2015

Climatology of Martian water ice clouds from Mars Express/OMEGA observations: derivations of the diurnal cycle

A. Szantai (1), J. Audouard (2), J.-B. Madeleine (1), F. Forget (1), A. Pottier (1), B. Gondet (2), Y. Langevin (2), J.-P. Bibring (2),

(1) Laboratoire de Météorologie Dynamique/IPSL, Université P. et M. Curie, Paris, France,

(2) Institut d'Astrophysique Spatiale, Université Paris-Sud, Orsay, France

(szantai@lmd.polytechnique.fr / Fax: +33-1.69.33.51.08)

Abstract

Images derived from the slope of the water ice absorption band between 3.4 and 3.525 μ m from the OMEGA spectrometer onboard Mars Express have been used to detect clouds. From a series of OMEGA images covering 4 Martian years (between 2004 and 2011), the pixels are used to construct a cloud coverage database over a regular 4D grid in longitude, latitude, solar longitude and Martian local time. It can be used to observe the evolution of clouds over specific regions, and their diurnal and annual cycle. As an example, the diurnal cloud life cycle in the tropics (-25°S to 25°N) during the Northern summer shows the presence of thick clouds in the early morning (possibly haze), which dissipate before noon (local time). In the afternoon, the cloud cover grows again, possibly due to convection generated by the increased solar heating.

1. Introduction

Water ice clouds have been first observed from space in the 1970's (by Mariner and Viking spacecrafts), and more intensively in the 1990's, starting with the MGS mission. But due to their heliosynchronous orbits, most past and current Martian satellites have observed the planet only at a specific local time (LT) during the day (for example at 2pm and 2am LT for MGS) , and therefore cannot provide information about the daily cloud life cycle. In this study, we use OMEGA nadir data at different local times. This is possible due to the unusual Mars Express satellite orbit phasing, which induces a slow drift of the local time between consecutive orbits.

2. Methodology

Following preliminary work by Gondet et al. (e.g. [1]) using the 1.5 μm ice band, a study by Madeleine et al., (2012) [2] has shown the feasibility of extracting (water) ice clouds with an ice clouds index, a parameter derived from the depth of a water ice absorption band around 3.4 μm. After comparison with a threshold value, this IceCloudsIndex indicates if the pixel is cloudy or not (figure 1).

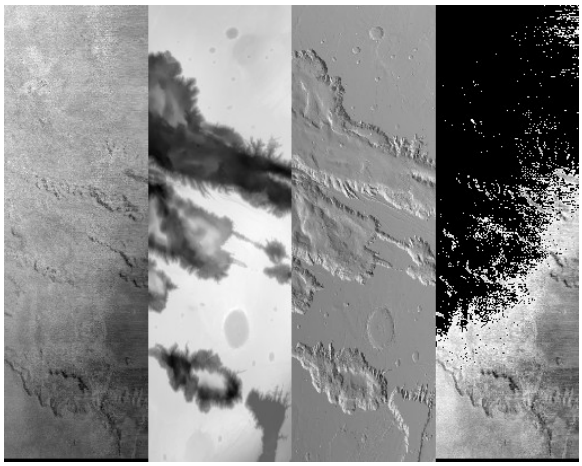

Figure 1 : OMEGA-derived images along a portion of an orbit. From left to right : IceCloudsIndex, MOLA elevation, incidence wrt. local normal, cloudy IceCloudsIndex (from dark gray : thick clouds, to white : thinnest clouds ; black : no cloud).

In a first step, the IceCloudsIndex is calculated and quality-checked for each pixel of all the nadir observing orbits, over a period covering four Martian years (MY 26 to 30).

In a second step a cloud climatology is constructed. The pixels are binned into two 4-dimensional arrays (cloudy and cloudy+non-cloudy) according to their longitude, latitude, solar longitude (Ls) and local time (LT). The bins have sizes of 1° in latitude and longitude, 5° in Ls and 1 (Martian) hour in LT. These arrays are sparsely populated (pixels come from 0 to 3 orbits per bin).

The cloud coverage of each bin is obtained by dividing the number of cloudy pixels in the first array by the number of all pixels in the corresponding bin in the second array.

In a third step, several 4D bins covering larger spatial areas and longer time periods are assembled in order to form 2D our 1D subsets showing temporal evolutions of clouds.

3. Observations and interpretation of results

In the preliminary global part of this study, the percentage of cloud coverage has been averaged temporally over all solar longitudes and local times (figure 2). It shows the almost complete spatial coverage of the planet by the OMEGA instrument, and the main areas where clouds form during the Martian year : the tropical area around Tharsis (in summer), the temperate regions at the edge of the polar hood in both hemispheres, the Hellas basin…

In the second part of this study, cloud percentages have been averaged over several geographic areas. On figure 3, all the percentages of cloudy pixels have been averaged over an area covering all longitudes, tropical latitudes between -25°S and 25°N, and over the Northern summer for Ls between 60 and 120°. This figure shows an important cloud coverage early in the morning (around 6am LT), possibly due to haze formed in the (late) night, a decrease of the cloud coverage resulting from solar heating in the late morning, and an increase again in the afternoon, possibly following the onset of convection.

4. Conclusion

OMEGA data, available at different local times of the Martian day can be used to investigate the diurnal cloud life cycle, over sufficiently large regions. The 4D cloud climatology will also constitute a data product for the validation of outputs from Martian climate models, such as the Martian Global Climate Model developed at LMD.

References

[1] Gondet, B., Bibring, J.-P., Langevin, Y., Poulet, F., Montmessin, F., Forget, F. (2006). One martian year observation of H_2O ice clouds By OMEGA/Mars Express. Mars Atmosphere Modelling and Observations, *http://www-mars.lmd.jussieu.fr/granada2006/abstracts/Gondet_Granada2006.pdf*

[2]. J.-B. Madeleine, F. Forget, A. Spiga, M. J. Wolff, F. Montmessin, M. Vincendon, D. Jouglet, B. Gondet, J.-P. Bibring, Y. Langevin, and B. Schmitt, 2012. Aphelion water-ice cloud mapping and property retrieval using the OMEGA imaging spectrometer onboard Mars Espress. Jnl. Geophys. Res., 117, E00J07.

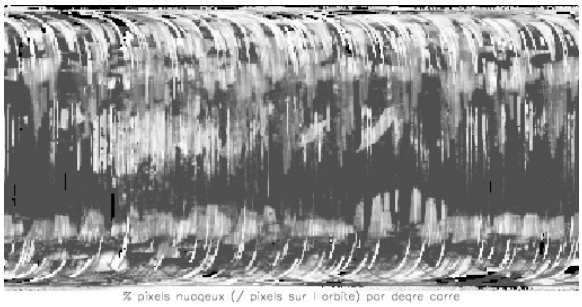

Figure 2 : global map of cloud cover percentage (black : absence of data ; dark grey : no cloud ; bright white : full (100 %) cloud cover) for all solar longitudes and local times, -180°W to 180°E longitude.

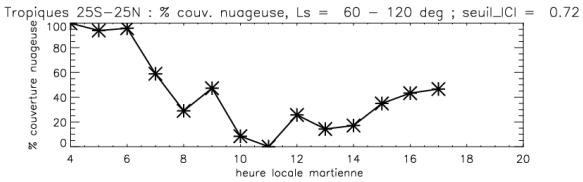

Figure 3 : percentage of cloud cover in the tropics [-25°S ; 25°N] for different local times, during Northern summer (Ls = [60°; 120°]), all longitudes.

EPSC Abstracts
Vol. 10, EPSC2015-636, 2015
European Planetary Science Congress 2015

Braided alluvial fan in the Terra Sirenum region, Mars

S. Adeli (1), E. Hauber (1), L. Le Deit (2), M.G. Kleinhans (3), T. Platz (4), P. Fawdon (5) and R. Jaumann (1)

(1) Institute of Planetary Research, German Aerospace Center, DLR, Berlin, Germany (Solmaz.Adeli@dlr.de). (2) Laboratoire de Planétologie et Géodynamique, Université de Nantes, France. (3) Faculty of Geosciences, Universiteit Utrecht, Netherlands. (4) Max Planck Institut für Sonnensystemforschung, Göttingen, Germany. (5) Department of Physical Sciences, The Open University, UK.

1. Introduction

Amazonian-aged outflow channels on Mars have been recently identified using high resolution orbital data [e.g. 1, 2]. They display morphological evidence of fluvial erosion, including streamlined forms, scour marks, and erosional islands. In most cases, the source of water is interpreted as either a groundwater aquifer, melting of glacial deposits or ground ice (e.g., by impacts), or lake overflow. Irrelevant of the source, the presence of liquid water during the Amazonian has significantly increased our knowledge about the recent history of the Martian climate.

Here we report the presence of an Amazonian-aged outflow channel located on the rim of the Ariadnes Colles basin (37°S/178°E) that has an alluvial fan on its downstream part. The study area is located in the Noachian highlands of Terra Sirenum, the site of a large hypothesized paleolake [3]. This so-called Eridania lake existed during the Late Noachian-Early Hesperian and drained into Ma'adim Vallis, one of the largest valleys on Mars. The Ariadnes Colles basin was part of the Eridania paleolake and hosted later a closed lake.

2. Data and methods

We used HRSC and CTX images as well as CTX and MOLA topographic data (DTM) to analyze the morphological and hydrological characteristics of the Ariadnes outflow channel. We performed crater size frequency distribution (CSFD) analysis on CTX images to determine the absolute model ages of the fluvial events using CraterTools [4] and CraterStat 2 software [5], based on the chronology function of [6] and the production function of [7].

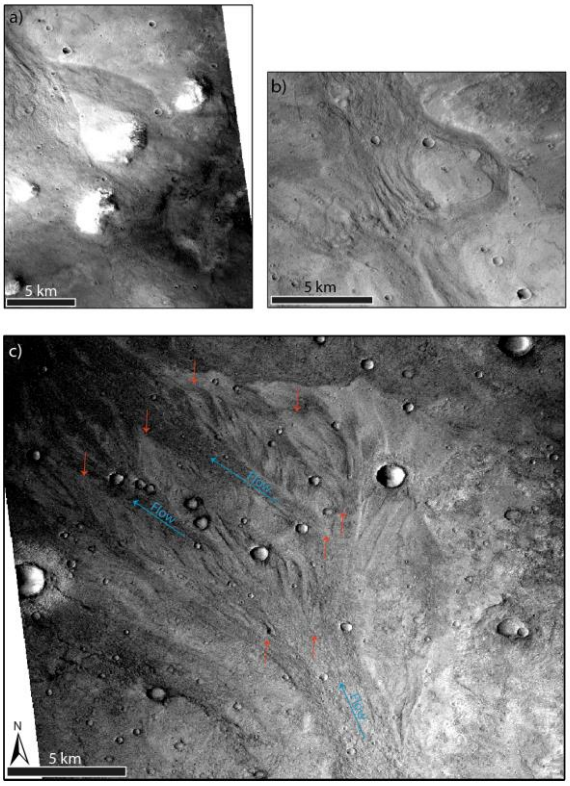

Fig.1: Morphological details of the Ariadnes outflow channel. a) Channel head. The water flowed through the gaps between the bright mounds, but the source of the water is unclear. b) Deep scour marks and erosional islands on the upstream section of the channel bed. c) Braided alluvial fan. The main channels are marked by blue arrows, and the beginning and ending of the major bar systems by red arrows.

3. Geomorphological investigation

The Ariadnes outflow channel is about 50 km long. It is incised into the ejecta blanket of a relatively fresh impact crater, and partly removed the ejected material. Besides the Ariadnes channel, the ejecta blanket has not been visibly modified by another erosional process and the crater has a sharp and steep

rim. Crater counting of the ejecta suggests an absolute model age of around 1.7 Ga (Early Amazonian) for the impact event. We assume the crater age as the maximum age of the fluvial activity that formed the Ariadnes outflow channel.

The channel head is located at NE and SW sides of a 500 m height mound (Fig.1-a). The SW channel cuts the NE one, and therefore it formed later than the NE channel. Alternatively, both channel heads may have been active earlier but the last or few last outflow events occurred only through the left channel, which may as well reveal a change in the morphology of the source of water.

The channel has an average width of about 3 km and its depth varies between 30 m at its maximum and 10 m at its minimum. On the channel bed, we can observe deep grooves that are indicative of scouring of bedrock by catastrophic and high pressure flood flows [8] (Fig.1-b). Remnants of the ejecta blanket are visible as erosional islands (Fig.1-b). Whether the channel was carved by one continuous event or multiple events is unclear.

The downstream part of the channel is marked by a wide braided alluvial fan (Fig.1-c). An alluvial fan, by definition, forms when a confined feeder channel deposits most of its sediments load in an unconfined area [9]. This is the case for the Ariadnes outflow channel, as the feeder channel incised the ejecta blanket and, as soon as it reached the unconfined area downslope of the ejecta blanket, the deposition started. The absolute model age of the alluvial fan suggests an age of 470 Ma for the last fluvial event.

The alluvial fan, at its widest place, is about 15 km wide, and is composed of bars that are partly separated by multiple channels. These bars, deposited in the direction of the water flow, represent ever-changing patterns of migration and collision into each other (Fig. 1-c).

There is no clear morphological evidence of the source of the water. However, at the head of the channel, there is a closed depression that fits to the 400 m contour line (MOLA DTM). It may have hosted a lake, the overflow of which possibly carved the outflow channel.

4. Hydrological modelling

In order to better understand the formation mechanism of the Ariadnes outflow channel, we analyzed the channel hydrological parameter using the methods described in [10]. The alluvial fan volume of 2.4 km^3 is comparable with the volume of the eroded ejecta (2.52 km^3) on the upstream part of the channel. This suggests that no or very few sediments had been added to the system from the source area of water.

The discharge rate (Qw) has been estimated as 34 km^3/day for 30 m of channel depth and 6.9 km^3/day for 10 m. The volumetric sediment transport rate (Qs) is ~0.3 km^3/day and ~0.02 km^3/day respectively. We chose a grain size of 2 mm for the above calculation, which is the mean value measured by [11] using in-situ data of the MSL rover. The water to sediment ratio would be 130 to 370, which is a relatively high value compared to terrestrial examples of catastrophic flows. We have to note that due to the data resolution constraint and lack of some basic information e.g. precise grain size, these values may be overestimated.

5. Conclusions

The Ariadnes outflow channel represents clear evidence of one or several fluvial events in Terra Sirenum during the Amazonian. Based on the analysis of CSFD, we were able to narrow the channel formation time window from 1.7 Ga to 470 Ma.

The hydrologic modeling would provide important insights, e.g. the amount of water, flow duration, and source of water, into the understanding of the formation mechanism of this channel, as well as the climatic evolution of Mars.

References

[1] Mangold N. and Howard A.D., (2013), *Icarus 226, 385-401*. [2] Erkeling G., et al., (2011), *Icarus 215, 128-152.* [3] Irwin R.P., et al., (2002) *Science 296,2209*. [4] Kneissel T., et al., (2011), *PSS 59, 1243-1254.* [5] Michael G.G. and Neukum G., (2010), *Earth & Planetary Sci. Let 294, 223-229.* [6] Hartmann W.K. & Neukum G. (2001), *Space Sci Rev., 96, 165-194.* [7] Ivanov B.A. (2001), *Space Sci. Rev. 96, 87-104.* [8] Baker V.R. & Kochel R.C. (1979) *JGR 84, 7961-7983.* [9] Blair T. & McPherson J. (1994), *J. Sedimentary Res.64, 451-490.* [10] Kleinhans et al., (2010), *Earth & Planetary Sci. Let. 294, 378-392.* [11] Miller L. et al., (2014), *Geophysical Res. Let. 10.1002/2014GL060991*.

EPSC Abstracts
Vol. 10, EPSC2015-649, 2015
European Planetary Science Congress 2015

Towards identifying mass wasting by change detection in HiRISE images of the north pole of Mars

L. Fanara (1,2), K. Gwinner (1), E. Hauber (1) and J. Oberst (1,2)
(1) Institute of Planetary Research, DLR, Berlin, Germany, (2) Technical University of Berlin, Germany
(Lida.Fanara@dlr.de / Fax: +49-30-67055402)

Abstract

We are investigating change detection tools for detecting and quantifying changes caused by mass wasting on Mars. The increasing amount of High Resolution Imaging Science Experiment (HiRISE) images has made the detection of fine-scale changes possible, but manual change detection is very time-consuming. Our goal is to support the analysis of surface changes in the north polar region, where mass wasting is very common [1], with automated change detection tools, in order to improve our understanding of dynamic geological processes and related climatic parameters of the planet.

1. Mass Wasting

Since the first time HiRISE captured an avalanche at the north polar steep slopes of Mars in 2008 [2], a much improved temporal coverage of it has been achieved by the HiRISE experiment. This allows for a thorough investigation into change detection which will in turn support the analysis of active geological processes from different perspectives. Russell et al. [3] have demonstrated the occurrence of numerous mass wasting events at one particular scarp over 5 Mars years through image to image comparison. We investigate how this can be achieved over larger areas and in a more automated way.

In one case (Fig. 1) we observed that a "rock" fall seems to have created a relief change along the way carving a linear furrow into the talus deposits at the base of the steep North Polar Layered Deposit (NPLD) scarp and scattering some smaller boulders on the way. The largest boulder involved travelled the longest down-slope and is roughly 4m long × 2m wide × 2m high (through shadow measurements). The coarse fraction of the "rock" fall deposit and the linear furrow show a distinct topographic relief in the image. From the shading pattern of the furrow, the steepness of its inward dipping flanks can be roughly estimated as 10°, which leads to an estimate of about 1m for its depth. Interestingly, the images of the surrounding area seem to show a change at the foot of the NPLD as well.

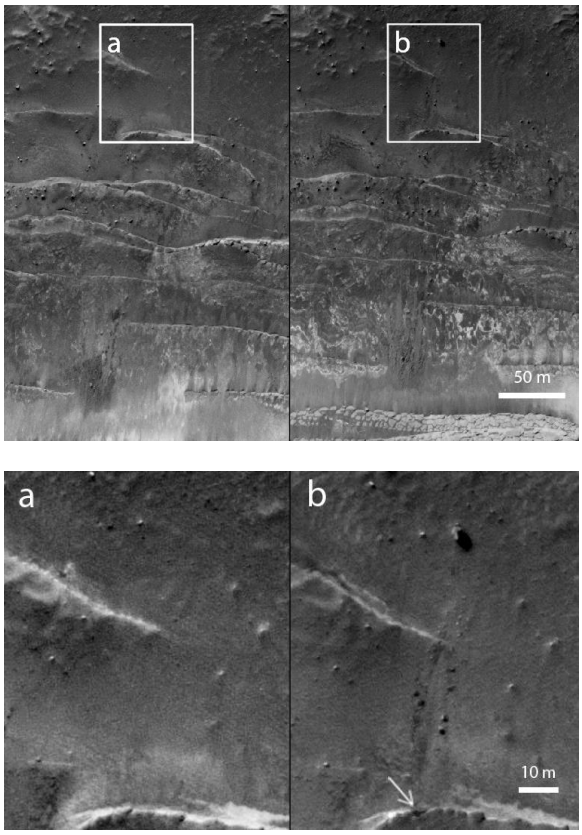

Figure 1: Example of change within 10 days; a boulder has fallen between HiRISE images ESP_016292_2640_RED (left) and ESP_016423_2640_COLOR (right). The boulder is roughly 4m long × 2m wide × 2m high and has fallen from the upslope step coming to rest around 70 m away from its source, which can be seen as a dark gap at the bottom of (b).

This is the most impressive example of mass wasting among many others that were observed between those two images, or between two other images of the same month and area. The effort of detecting such changes could be significantly reduced if a more automated way were to be developed.

2. Change Detection

Wagstaff et al. [4] and Di et al. [5], dealt with this issue, focusing on larger-scale changes, induced by other phenomena (e.g. impact craters, dark slope streaks). Sidiropoulos and Muller [6] attempt a more generalized approach for all kinds of change based on multiple types of images. Observed mass wasting events, such as "rock" falls, however result in very small changes only visible in HiRISE images, and therefore require a process-specific approach with high geometric accuracy.

The fundamental steps of image-based change detection are image selection, accurate image registration, radiometric corrections and the method of change detection itself. A common problem that arises during this process is the detection of trivial changes, such as shadows. In order to avoid this, we are developing a sophisticated system that will reject these and only select the ones which reflect change on the surface of Mars. The image features that can potentially be exploited are various and include modification of scarp edges, new boulders, albedo changes due to new deposits or erosion, and active avalanches.

A further development would be to recognize such changes, which actually occur in three-dimensional space, on HiRISE Digital Terrain Models (DTMs). Detectable height changes are likely associated with new scars in the source area of "rock" falls, new talus deposits, and erosion, as in the example of Fig. 1. Due to the high rate of imaging at the north pole, there are multiple images which comprise stereo pairs and can be used to create 'before' and 'after' DTMs in order to detect differences in 3D. In the particular case of Fig. 1 for example, there are 25 candidate stereo partners for the first image and 9 candidate stereo partners for the second image. DTM-based mapping of height changes, however, is an extremely challenging task due to the requirements on the resolution and accuracy of co-registration in an area characterised by steep slopes.

3. Summary and Conclusions

Active mass wasting at the north pole of Mars can be studied based on numerous available HiRISE images. This activity is normally associated to many small surface changes. Our goal is to create an automated change detection system for HiRISE images and if possible HiRISE DTMs, to allow for a more rigorous approach to mapping regional changes and quantifying related volumes and erosion rates.

Acknowledgements

This work is co-funded by the European Union's Seventh Framework Programme under iMars grant agreement n° 607379.

References

[5] Di, K., Liu, Y., Hu, W., Yue, Z., and Liu, Z.: Mars surface change detection from multi-temporal orbital images, 35th International Symposium on Remote Sensing of Environment, 22-26 April 2013, Beijin, China, 2013.

[1] Russell, P. S., Byrne, S., Hansen, C. J.: Active mass wasting of ice layers and seasonal CO_2 frost in the north polar region of Mars, 41th Lunar and Planetary Science Conference, 1-5 March 2010, The Woodlands, Texas, USA.

[3] Russell, P. S., Feleke, S., and Byrne, S.: Landslide erosion rates of north polar layered deposit cliffs and the underlying basal unit, Eighth International Conference on Mars, 14-18 July 2014, Pasadena, California, USA, 2014.

[2] Russell, P., Thomas, N, Byrne, S., Herkenhoff, K., Fishbaugh, K., Bridges, N., Okubo, D., Milazzo, M., Daubar, I., Hansen, C., and McEwen, A.: Seasonally active frost-dust avalanches on a north polar scarp of Mars captured by HiRISE, Geophysical Research Letters, Vol. 35, L23204, 2008.

[6] Sidiropoulos, P. and Muller J.-P.: Identifying candidate temporal changes on Mars through image matching, European Planetary Science Congress, 7–12 September 2014, Cascais, Portugal, 2014.

[4] Wagstaff, K. L., Panetta, J., Ansar, A., Greeley, R., Pendleton Hoffer, M., Bunte, M., and Schörghofer, N.: Dynamic landmarking for surface feature identification and change detection, ACM Transactions on Intelligent Systems and Technology, Vol. 3, pp. 49:1-49:22, 2012.

EPSC Abstracts
Vol. 10, EPSC2015-663, 2015
European Planetary Science Congress 2015

The challenge and scientific application of the CO2 4.3 μm atmospheric limb emission of Mars

M. A. López-Valverde (1), A. Piccialli (2), M. Giuranna (3), B. Funke (1), M. López-Puertas (1), A. A. Jurado-Navarro (1), M. García-Comas (1), F. González-Galindo (1), J. J. López-Moreno (1) and S. Jiménez-Monferrer (1)
(1) Instituto de Astrofísica de Andalucía/CSIC, Granada, Spain. (valverde@iaa.es / Fax: +34-958-814530)
(2) LESIA, Observatoire de Paris, Meudon, France
(3) Istituto di Astrofisica e Planetologia Spaziali/INAF, Rome, Italy

Abstract

The atmospheric fluorescent emissions of CO2 at 4.3-um have been observed in the daytime upper atmosphere of Mars from a limb geometry by the instruments OMEGA and PFS on board Mars Express [1, 8]. Initial analysis using non-local thermodynamic equilibrium (NLTE) models show that the emissions are well understood [7, 3, 6]. Yet they have not been exploited to derive important thermospheric parameters, like CO2 densities and temperatures. Our major goals are to improve current NLTE models with a joint study of OMEGA and PFS data, and to build an ambitious state-of-the-art NLTE retreival scheme for Mars. Recent progress has been made in these directions on Mars, Venus and Earth. We will present a summary of these efforts and the difficulties and expectatives for its application to the Mars Express data.

1. Introduction

Infrared NLTE emissions by atmospheric molecules, specially under fluorescent or solar-pumping situations, are powerful tools to sound the upper layers of a planetary atmosphere [5]. Limb observations, in addition, are specially suited for a proper vertical sounding. The particular emissions by the ro-vibrational bands of CO_2 around 4.3 μm share these two advantages and are among the strongest molecular emissions in the infrared in the three terrestrial planets [6]. The instruments OMEGA and PFS have been performing systematic observations of these emissions on board Mars Express since 2003 and form a dataset which needs to be properly exploited. However, their scientific exploitation has a couple of difficulties, inherent to the NLTE nature of the emissions. One of them is the need to develop a suitable NLTE forward model (based on the theoretical NLTE population models) which produce simulated radiances in sufficiently good agreement with the observations. Another difficulty is linked to the inherent uncertainties in the microscopic description of the NLTE populations involved in a CO2 atmosphere like that of Mars. Specifically, the lack of laboratory information on collisional energy exchanges between CO2 states at high vibrational states and with isotopes. Actually, when spectral resolution and sensitivity are good enough, insight into and retrieval of some collisional rate coefficients are possible from remote souding [4]. A third difficulty is the large optical thickness of these emissions in a limb geometry, which may produce variations in the actual location of the "emitting region" along the line-of-sight. Retrievals under optically thin conditions, free from this last difficulty because the emitting region is at the tangent point, have recently been carried out for CO at 4.7 μm in the upper atmosphere of Venus [2]. A careful evaluation of all these conditions and difficulties, and a proper fit of the OMEGA and PFS data with a NLTE forward model are needed in order to evaluate the ability to investigate the upper Martian atmosphere using these datasets, and are the focus of an ongoing effort in our teams.

2. Recent NLTE results

2.1. Mars upper atmosphere

The OMEGA and PFS datasets seem to obey the expected NLTE behaviour of the emissions regarding the two most important aspects: spectral shape and absolute magnitude of the emitted radiance. Also the variation of these with altitude and solar illumination seem to be understood, at least in a global or averaged sense [7, 3]. In order to explain the spectral shape measured by OMEGA, however, changes in vibrational-vibrational exchanges between $CO_2(\nu_3)$ states was needed; a solution which also improved similar measurements by VIRTIS/Vex in the Venus thermosphere

[6]. An extended study using both OMEGA and PFS is needed, in particular the PFS higher spectral resolution, can be very useful to settle this question.

2.2. Venus upper atmosphere

In the Venus upper atmosphere, the 4.3 μm emissions by CO_2 present similar difficulties. A simpler retrieval (optically thin situation) was applied to the limb fluorescent emissions by CO at 4.7 μ from VIRTIS/Venus Express, obtaining both CO abundance and temperatures simultaneously [2]. CO observations in Mars, at least available from PFS, should also be exploited, and a joint retrieval with CO_2 at 4.3 μm shall be particularly useful to obtain the total carbon content in the Martian thermosphere.

2.3. Earth upper atmosphere

An interesting study in the Earth's upper atmosphere using MIPAS/Envisat observations has been recently conducted in the Granada group [4]. Jurado-Navarro and colleagues not only derived CO_2 but also rate coefficientes of a few vibrational-to-vibrational and vibrational-to-translation energy transfer routes involving CO_2 states. Unfortunately the OMEGA and PFS spectral resolutions are not as good as those of MIPAS, but the NLTE retrieval scheme used by these authors should be applied to the Martian case to examin the possibility of similar derivations. In the case of Mars, or Venus, the collisional exchanges driving the populations are slighlty different, and offer new insight into the governing NLTE mechanisms in a CO_2 atmosphere.

3. Summary and Conclusions

The NLTE limb emissions of CO2 at 4.3 um observed by Mars Express are a unique dataset to extend our description of the upper mesosphere and the thermosphere of Mars. The understanding of the emissions, their correct simulation and the NLTE retrieval of densities and temperatures are our major objectives. A further strategy behind this work is the preparation of suitable retrieval tools for the analysis of the upcoming ExoMars Trace Gas Orbiter (EMTGO), specifically to exploit infrared measurements of the upper atmosphere subject to NLTE features in a completely different observing mode (atmospheric absorption) from two of the EMTGO instruments: NOMAD and ACS.

Acknowledgements

This work has received funding from the European Union's Horizon 2020 Programme (H2020-Compet-08-2014) under grant agreement UPWARDS-633127

References

[1] V. Formisano, A. Maturilli, M. Giuranna, E. D'Aversa, and M. A. López-Valverde. Observations of non-lte emission at 4 5 microns with the planetary fourier spectrometer abord the mars express mission. *Icarus*, 182:51–67, May 2006.

[2] G. Gilli, M. López-Valverde, J. Peralta, S. Bougher, A. Brecht, P. Drossart, and G. Piccioni. Carbon monoxide and temperature in the upper atmosphere of venus from virtis/venus express non-lte limb measurements. *Icarus*, 248(0):478 – 498, 2015.

[3] M. Giuranna, A. Kutepov, L. Rezac, A. Feofilov, and V. Formisano. Analysis and modelling of PFS/MEx limb observations of 4.3-μm CO2 non-LTE emission. In *European Planetary Science Congress 2012*, page 682, Sept. 2012.

[4] A. A. Jurado-Navarro, M. Lopez-Puertas, B. Funke, M. García-Comas, A. Gardini, G. P. Stiller, and T. von Clarmann. Vibration-vibration and vibration-thermal energy transfers of co2 with n2 from mipas high resolution limb spectra. *J. Geophys. Res*, submitted, 2015.

[5] M. López-Puertas and F. W. Taylor. *Non-LTE radiative transfer in the Atmosphere*. World Scientific Pub., Singapore, 2001.

[6] M. A. López-Valverde, M. López-Puertas, B. Funke, G. Gilli, M. García-Comas, P. Drossart, G. Piccioni, and V. Formisano. Modelling the Atmospheric Limb Emission of CO_2 at 4.3 μm in the Terrestrial Planets. *Planet. Space Sci.*, 59:988–998, 2011.

[7] A. Piccialli, P. Drossart, M. A. Lopez-Valverde, F. Altieri, A. Määttänen, B. Gondet, O. Witasse, and J. P. Bibring. Characterization of OMEGA/MEx CO2 non-LTE limb observations on the dayside of Mars. In *European Planetary Science Congress 2012*, page 504, Sept. 2012.

[8] A. Piccialli, E. Palomba, M. A. López Valverde, G. Gilli, D. Grassi, M. D'Amore, and V. Formisano. Pfs-mex nadir observations at 4.3 um in the mars atmosphere with account for non-lte emissions. In *European Planetary Science Congress 2006*, pages 257–+, 2006.

EPSC Abstracts
Vol. 10, EPSC2015-684, 2015
European Planetary Science Congress 2015

ExoMars 2018 Rover Candidate Landing Sites: Aram Dorsum and the Hypanis Vallis Delta

E. Sefton-Nash (1), S. Gupta (2), M. Balme (3), P. Grindrod (1), P. Fawdon (3), J. Davis (4), P. Sidiropoulos (5), V. Yershov (5) & J-P. Muller (5)
(1) Dept. of Earth and Planetary Sciences, Birkbeck, University of London, UK, (2) Dept. of Earth Science & Engineering, Imperial College, London, UK, (3) Dept. of Physical Sciences, The Open University, Milton Keynes, UK, (4) Dept. of Earth Sciences, University College London, UK. (5) Mullard Space Science Laboratory, University College London, UK.

1. Introduction

The search for life on Mars is a cornerstone of international solar system exploration. In 2018, the European Space Agency will launch the ExoMars Rover to further this goal. The ExoMars Rover's key science objectives are to: 1) search for signs of past and present life on Mars; 2) investigate the water/geochemical environment as a function of depth in the subsurface; and 3) characterize the surface environment. ExoMars will drill into the sub-surface to look for indicators of past life using a variety of techniques, including assessment of morphology (potential fossil organisms), mineralogy (past environments) and a search for organic molecules and their chirality (biomarkers).

The choice of landing site is vital if the objectives are to be met. The landing site must: (i) be ancient (≥3.6 Ga); (ii) show abundant morphological and mineral evidence for long-term, or frequently recurring, aqueous activity; (iii) include numerous sedimentary outcrops that (iv) are distributed over the landing region (the typical Rover traverse range is a few km, but ellipse size is ~104 by 19 km). Various engineering constraints also apply, including: (i) latitude limited to 5º S to 25º N; (ii) maximum altitude of the landing site 2 km below Mars's datum; and (iii) few steep slopes within the ellipse.

In 2014, two international workshops were held to discuss potential landing sites. The outcome of these workshops was a shortlist of four possible sites: Aram Dorsum, Hypanis Delta, Mawrth Vallis, and Oxia Planum. We proposed the Hypanis and Aram Dorsum sites and led the scientific presentations for these sites at the Workshops. Here, we present the science cases for Aram Dorsum and Hypanis Vallis.

2. Aram Dorsum

The Aram Dorsum site in western Arabia Terra (Fig. 1) is situated about half way between Meridiani Planum and the dichotomy boundary, where Arabia Terra meets the northern lowlands. Aram Dorsum itself is a flat-topped, branching, sinuous ridge-like feature that is surrounded by smoother marginal materials. We interpret Aram Dorsum to be a former fluvial channel system that has been preserved in positive relief by differential erosion. Such features are fairly common on Mars [1], and are also well-studied on Earth [2]. Aram Dorsum is interesting in that it is overlain by overburden materials including both ejecta from nearby 10-50 km diameter craters, and regionally-extensive, sedimentary layers [3]. These materials are Noachian, so Aram Dorsum itself must be at least this old.

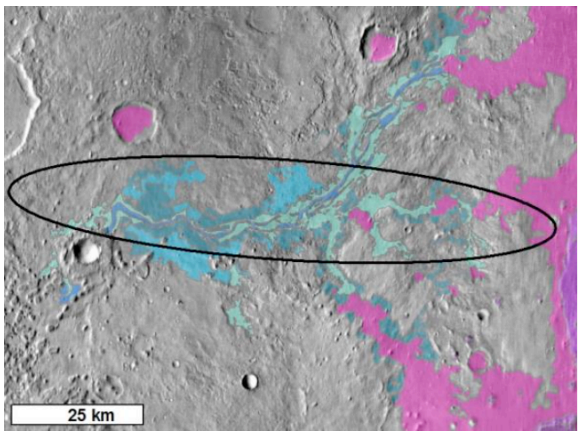

Figure 1: Aram Dorsum site and 2018 landing ellipse. Blue/green areas are Aram Dorsum or its marginal units. Flow is inferred to be East-to-West. Purple areas are regionally extensive, Noachian-aged superposing sedimentary units.

The presence of channels at different stratigraphic positions indicates long-lived fluvial activity, not catastrophic flow. This is reinforced by the overall sinuous, branching morphology of the channel, consistent with a river-like fluvial system. Aram Dorsum is a Noachian-era, aggradational, multithread/sinuous river-system, including small tributaries and extensive flood plain-like marginal deposits. It displays clear evidence for the long-lived

action of water in the Noachian. Although the inverted channel likely contains mainly coarse-grained sedimentary outcrops, the channel marginal unit is probably fined-grained sediments, or could contain lenses and/or 'islands' of fine-grained material suitable for preserving biosignatures. Importantly, the system has been exposed from beneath >100s of metres of overburden materials; outliers of such overburden are still present. Such burial/exhumation greatly benefits preservation of biosignatures. Science targets comprising channel marginal units and inliers within the overburden cover a significant proportion of study area and are distributed throughout the ellipse.

3. Hypanis Vallis

The Hypanis landing site in northern Xanthe Terra is situated on the dichotomy boundary. Our study area includes fluvio-deltaic deposits at the termini of Sabrina Vallis and Hypanis Vallis (Fig. 2). Mapped Sabrina terminal deposits are constrained to within the buried crater, Magong. The Hypanis deltaic system is more extensive, with multiple depositional lobes extending to the north and east.

Significant aeolian modification has occurred since delta formation, with crater counts on both Sabrina [6] and Hypanis [8] delta units revealing crater-retention ages of < 100 Ma, supported by the presence of ubiquitous aeolian features and suggesting recent exhumation from overburden. The large crater population classifies the study area as mid to late Noachian terrain [6, 8].

CRISM observation FRS0003157E ('Y' in Fig. 2) shows a 1.9 μm hydration signature that spatially aligns with exposed strata in eroded deltaic sediments, indicating putative hydrated minerals in discrete layers. A spectral unit in FRS0003134F ('X' in Fig. 2) is defined by the combined presence of the 1.9 μm absorption plus a strong 2.3 μm dropoff in reflectance, indicative of the presence of Fe/Mg-phyllosilicates [4,5]. Both spectral signatures are located between, but not immediately adjacent to, the Sabrina or Hypanis deltas, perhaps indicating that extensive ancient fluvial activity has influenced mineralogy throughout the landing ellipse. The Sabrina Vallis delta deposits in Magong crater also indicate a weak Fe/Mg-phyllosilicate signature that is consistent with the presence of nontronite, verminculite or saponite in delta sediments [6].

The Hypanis site displays clear evidence for the long-lived action of water in the Noachian. The total northward flow, including that through a now degraded channel connecting Nanedi Vallis to Hypanis Vallis, removed and deposited ~850 km^3 of material, of which the Hypanis deposits are estimated to comprise ~150 km^3 [7]. The most rewarding science target may lie in the Sm, Em and Le units, which are pervasive throughout the ellipse. Sm and Le exhibit fine-scale layering and the presence of phyllosilicates. Low-energy depositional environments that formed or influenced delta-proximal exposures of these units may have concentrated any potential biosignatures transported from the upstream Hypanis-Nanedi fluvial system.

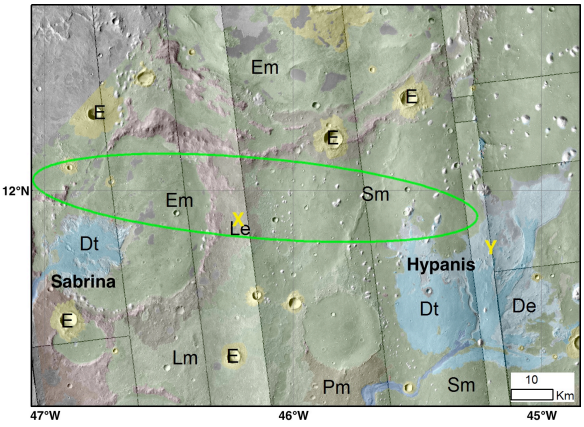

Figure 2: Geologic map of Hypanis study area overlaid on CTX. Deltaic units are blue. The nominal 104 x 19 km 2018 landing ellipse is bright green. CRISM observations are the yellow 'X' and 'Y'.

Recent exhumation of this formation could imply its protection from the surface environment for much of Mars' history, resulting in a high preservation potential for any biomarkers emplaced in the Hypanis-Sabrina delta system.

References

[1] Pain et al. (2007) Icarus 190, 478-491.
[2] Williams, R.M.E., et al. (2009) Geomorphology, 107, 300-315.
[3] Hynek, B.M., et al. (2002), J. Geophys. Res.,107, E10:5088.
[4] Pelkey, S. M. et al. (2007), J. Geophys. Res., 112, E08S14.
[5] Viviano-Beck, C. E. et al. (2014), J. Geophys. Res. Plan. 119, p. 1403-1431.
[6] Platz, T. et al., (2014) First Mars 2020 Landing Site Workshop, Crystal City, VA, USA.
[7] Hauber, E. et al., (2009), Plan. Space Sci. 57, p. 944-957.
[8] Werner, S. (2014) Pers. Comm.

EPSC Abstracts
Vol. 10, EPSC2015-697, 2015
European Planetary Science Congress 2015

ExoMars 2018: the candidate landing sites

D. Loizeau (1), J. C. Bridges (2), J. L. Vago (3), E. Hauber (4), J. Flahaut (5), F. Westall (6), A. G. Fairen (7), the ExoMars LSSWG (8) and the ExoMars team
(1) Université de Lyon, France, (2) University of Leicester, UK, (3) ESA-ESTEC, The Netherlands, (4) DLR-Berlin, Germany, (5) VU Amsterdam, The Netherlands, (6) Centre de biologie moléculaire, Orléans, France, (7) Centro de Astrobiología, Spain (8) ExoMars 2018 Landing Site Selection Working Group: F. Westall, H. G. Edwards, L. Whyte, A. Fairén, J.-P. Bibring, J. Bridges, E. Hauber, G. G. Ori, S. Werner, D. Loizeau, R. Kuzmin, R. Williams, J. Flahaut, F. Forget, J. L. Vago, D. Rodionov, O. Korablev, O. Witasse, G. Kminek, L. Lorenzoni, O. Bayle, L. Joudrier, V. Mikhailov, A. Zashirinsky, S. Alexashkin, F. Calant-ropio, and A. Merlo. (damien.loizeau@univ-lyon1.fr; jcb36@leicester.ac.uk)

Abstract

The ExoMars 2018 rover and platform will land on Mars with a suite of instruments to search for past and present life. After a call for landing sites in 2013, the selection process is considering 4 potential sites at the moment. The next step should select 2 final candidates during the fall 2015.

1. Introduction

The ExoMars 2018 mission will land a rover on Mars with the scientific objectives to search for signs of past and present life on Mars and to investigate the water/geochemical environment as a function of depth in the shallow subsurface. To this purpose, the rover will carry a comprehensive suite of instruments (the Pasteur payload) dedicated to geology and exobiology research [1]. The rover will be able to travel several kilometres and analyse surface and subsurface samples down to a 2 meter depth. The very powerful combination of mobility with the ability to access in-depth locations, where organic molecules can be well preserved, is unique to this mission [1].

1.1 Landing site constraints

On December 2013, an invitation was sent to the scientific community to propose scientifically compelling landing sites (LS) [2], which comply to the main engineering constraints for landing and operation. These include a landing ellipse of 19 km × 104 km, an altitude < -2 km, a latitude between 5°S and 25°N.
Scientifically interesting LS include locations with evidence for long duration or frequently recurring aqueous activity, low energy transport and deposition, fined-grained, recently exposed sediments, and/or hydrated minerals such as clays or evaporites. The outcrops of interest must be distributed over the landing ellipse to ensure their accessibility. LS must also comply with planetary protection requirements: They must not contain features currently considered as Mars Special Regions [2].

1.2. Eight proposed sites

Initially, eight LS were found to be compliant with the science, engineering, and planetary protection requirements by the Landing Site Selection Working Group (LSSWG) [3]. These sites were presented by their proposers and discussed at the first LS workshop: http://exploration.esa.int/mars/53944-proposed-landing-sites-for-exomars-2018-mission/.

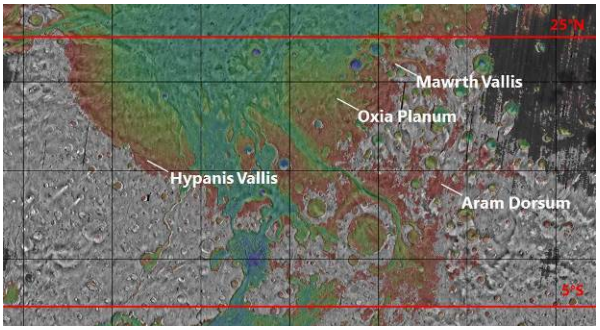

Figure 1: Location of the final candidate landing sites.

2. Landing site selection

Following the first LS workshop, four sites were selected for further investigation (figure 1) on the basis of their higher potential for long lived water activity, the presence of fine-grained sediments, and the higher concentration of potential targets over the whole landing ellipse [3]. The study of these sites,

both in terms of scientific interest and engineering safety, is still on-going, and a second workshop took place at the ALTEC facility, in Torino (Italy, December 2014).

2.1. Landing sites overview

We describe hereafter the geology of these four LS as they have been presented at the workshops.

Aram Dorsum (7.9°N, 348.8°E). The proposed ellipse lies in a local topographic low, ~100 km north of Crommelin crater in the large Oxia Palus region [4]. The site comprises layered sedimentary rocks and a distinct inverted channel system. The overlying unit would be late Noachian/early Hesperian, indicating an ancient age for the channel.

Hypanis Valles (11.8°N, 314.96°E). The proposed ellipse is located at the margin of the fluvial fan/deltaic systems at the termination of Hypanis Valles, just below the transition between the highlands and the plains around Chryse [5]. Another deltaic deposit is in Magong crater at the terminus of Sabrina Vallis, just SW of the proposed LS. This LS targets fan-like deposits that were interpreted to be the remnants of a prograding delta. The lower strata of the Hypanis delta appear to be enriched in Fe/Mg-rich phyllosilicates as suggested by CRISM observations, as well as the Sabrina delta.

Mawrth Vallis (22.16°N, 342.05°E). The proposed LS is in middle to late-Noachian terrains south-west of the Mawrth Vallis channel [6,7]. The region surrounding Mawrth Vallis contains one of the largest exposures of phyllosilicates detected on the Martian surface [8], associated to light-toned layered deposits [9-11]. Outcrops at the proposed landing site show a general sequence of Al-phyllosilicates on top of Fe-smectites, indicating a long wet history. The rocks show the highest degree of alteration identified on Mars. The deposition and alteration are ancient (mostly > 3.8 Ga), and the rocks are well preserved.

Oxia Planum (24,55°E ; 18,2°N). The ellipse covers large exposures of Fe/Mg-phyllosilicates rich rocks detected on both OMEGA and CRISM multispectral data [12]. These detections are associated with layered rocks in a topographic low and may represent the south-western extension of the Mawrth Vallis clay-rich deposits, pointing to an extended alteration process. The crust there is ancient (> 4 Ga) and has undergone intense erosion > 3.6 Ga ago, although the phyllosilicate bearing rocks have been exposed only recently (< 100 Ma ago).

2.2. Astrobiological interest

Of interest in all the chosen sites is the evidence for varying amounts of liquid water in contact with volcanic materials, during different time spans. The volcanic substrates could have supported chemolithotrophic life, and even possibly organitrophic life living off the dead lithotrophs [13].

2.3. Further characterisation and down-selection

New data are being actively acquired by the HRSC, HiRISE and CRISM teams to support the ExoMars 2018 landing site selection process. The ellipses are large and new data are important for characterizing the potential science targets and evaluating the safety of the sites. The proposing teams, the ExoMars project team and the LSSWG will continue their analysis and comparison of the sites, aiming to select two final candidate sites by the fall 2015 —in time for the start of the mission's Critical Design Review (CDR). The final selection of the landing site is expected within 2017.

Acknowledgements

The LSSWG wishes to thank all the proposers and workshop participants for their insightful contribution to the landing site selection process of the ExoMars 2018 mission.

References

[1] http://exploration.esa.int/mars/48088-mission-overview/ [2] http://exploration.esa.int/mars/53462-call-for-exomars-2018-landing-site-selection/ [3] ExoMars 2018 LSSWG recommendation: http://exploration.esa.int/mars/54707-recommendation-for-the-narrowing-of-exomars-2018-landing-sites/ [4] Balme M. et al., 1st first ExoMars 2018 LSS SW. [5] Gupta S. et al., 1st first ExoMars 2018 LSS SW. [6] Gomez F. et al., 1st first ExoMars 2018 LSS SW. [7] Poulet F. et al., 1st ExoMars 2018 LSS SW. [8] Poulet, F., et al. (2005), Nature 438(7068), 623-627. [9] Loizeau, D., et al. (2007), JGR 112,E8. [10] Loizeau, D., et al. (2010), Icarus 205(2), 396-418. [11] Michalski, J. R., and E.Z. Noe Dobrea (2007), Geology 35(10), 951-954. [12] Quantin C. et al., 1st ExoMars 2018 LSS SW. [13] Westall et al., (2013), Astrobiology, 13, 887-897.

EPSC Abstracts
Vol. 10, EPSC2015-699, 2015
European Planetary Science Congress 2015

Hints at diapirism in Arabia Terra bulged craters (Mars)

R. Pozzobon (1), M. Massironi (2) A. P. Rossi (3) F. Sauro (4) C. Carli (5) L. Marinangeli (6) G. Cremonese (1)

(1) INAF - Oapd, (2) Department of Geosciences, Università degli Studi di Padova, (3) Jacobs University Bremen, (4) Università degli Studi di Bologna, (5) INAF - IAPS, (6) IRSPS DiSPUTer, Università D'Annunzio

Abstract

Impact craters within Arabia Terra region, on Mars, display a large central bulge, sometimes showing a well-preserved stratification (light albedo layered deposits). In craters like Crommelin or an unnamed crater (that is numbered 12000088**)** located a few hundreds kilometers on the East some unusual landforms and structures among the layered deposits were observed. In particular, on Crommelin's bulge and its surroundings we found fold systems with axis parallel to the bulge perimeter. The fold sets are typical compressional structure often associated to diapiric rise on Earth [1]. In addition on top of 12000088 crater's bulge the evidence of sulfate signatures was detected as well as the presence of small bowl-shaped depressions. Several fluid-carved channels that depart radially from the bulge are cut by a ring of normal faults, thus suggesting a collapse of the bulge summit. Thus, on the basis of the previous observations it is possible to hypothesize that diapiric rise could have been responsible for central bulging both on Crommelin and 12000088 craters and likely on other bulged craters on Arabia Terra.

1. Methods

A high-resolution image dataset as well as DTMs were required to perform structural analyses on both craters to verify strata dips and dip directions within the Crommelin crater floor and evaluate the presence of faulting in the 12000088 Crater central bulge. In order to have an overall detailed view as well as good coverage of the study areas overlapping CTX images (6 m/px) were selected as pairs to produce stereo DTMs. In addition, where available, HiRISE stereo images (0.25 m/px) were used. The DTMs were produced with Ames Stereo Pipeline and validated with the alignment on HRSC DTM (from DLR 100 m/px) and calibrating the heights according to MOLA topography (460 m/px) [2]. Moreover, the Compact Reconnaissance Imaging Spectrometer for Mars (CRISM) onboard Mars Reconnaissance Orbiter (MRO) was used to study the spectral signatures on the crater 12000088 bulge's summit.

2. Crommelin Crater's Folds

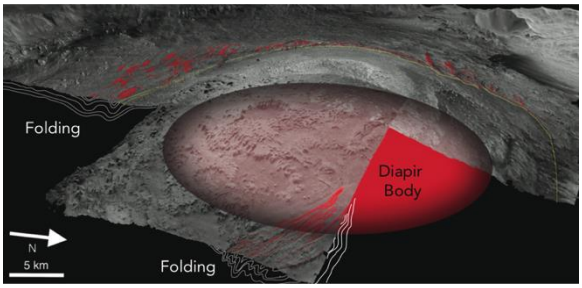

Figure 1: Perspective view and conceptual sketch of the diapiric body emplacement that likely caused bulging and folding. The diapir stays under the sedimentary layering coverage

Several areas around Crommelin Craters bulge display clear stratification identified as ELD (Equatorial Layered Deposits, [3]) suitable for analysis of strata dips and dip directions on DTMs. Four different areas with folded stratigraphy were identified all around the central bulge displaying concentric axial planes. On the western sector of the bulge a sequence of symmetric folds was identified, bearing two anticlines and a syncline inbetween. The approximate wavelength is ~2.5-3 km and the amplitude is ~4-6 km. On the NW sector of Crommelin Crater a sequence of 3 synclines and anticlines was measured and identified as asymmetric folds. The average amplitude is ~2.5-3 km and the wavelength ~2 km. A similar case can be found in the NE sector of the crater on the bulge slope where we identified another set of kilometric scale strongly asymmetric synclines and anticlines. In all these cases the axial planes are concentric to the central bulge and the folds vergence is radial pointing outwards. In the southern sector several basin-like structures are present displaying a clear inward-dipping stratification with the dip angle progressively increasing towards the center of the basin. The major folding phase presents the axial plane concentric to the bulge and a second one more gentle orthogonal

3. Crater 12000088 structures and terrains composition

Crater 12000088 is located ~650 km eastern to Crommelin and is slightly smaller in size being ~50 km in diameter. This crater is actually composed of two intersecting craters, with the younger crater (~20 km in diameter) superimposed to the larger one. The inner bulge's height is less pronounced and follows an inner average slope that is in accordance with the regional slope. The bulge is surrounded by a change in slope in correspondence to several radial channels that appear to be water-carved (fig. 2). On the eastern part some furrows and channels seem to flow preferentially in direction of the deeper smaller crater. A ring of normal faults all around the central bulge were identified on images and verified with DTM topographic profiles. Most of the channels are cut by the ring of faults as well as the ejecta blanket of a ~7 km crater (fig. 2) supporting the hypothesis of tectonic summit collapse of the bulge (clearly visible also in fig. 2). Spectra analyzed from CRISM show clearly overtone absorption bands compatible with hydrated mineralogy. In particular the presence of absorption around 1.2, 1.5, 2.0, and 2.4um are indicative of hydrated sulfate (e.g., Mg-sulfates).

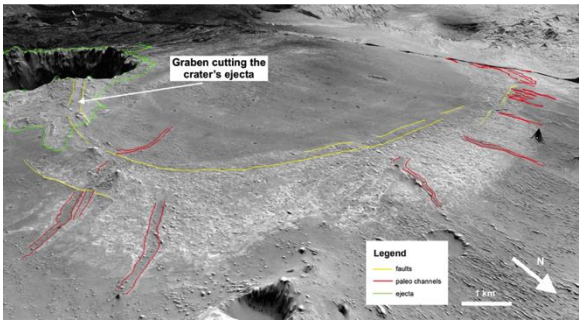

Figure 2: Perspective view of 12000088 crater interior. The crosscutting relationship between radial channels, faults system and inner crater's ejecta is clearly recognizable. To emphasize the morphologies a 5x vertical exaggeration was applied on the CTX stereo DTM

3.1 Karst Morphologies

On the top of 12000088 crater's bulge from HiRISE images and stereo DTMs we recognized some peculiar circular features that cannot be associated to impact craters, since they completely lack rims and ejecta, although being in some cases ~100 m in diameter. Doline-like depressions on the bulge were analysed with photoclinometric method based on sun incidence to infer the topography and slopes. The measurements showed several similarities with collapse dolines commonly found in gypsum terrains on Earth presenting a high circularity index, steep walls and debris at their bottom. Similar features developed in gypsum, with minor axes ranging from 10 to 150 meters comparable to those on 12000088 cratere can be found in New Mexico [4] and Turkey [5] confirming the karst sinkholes genesis hypothesis.

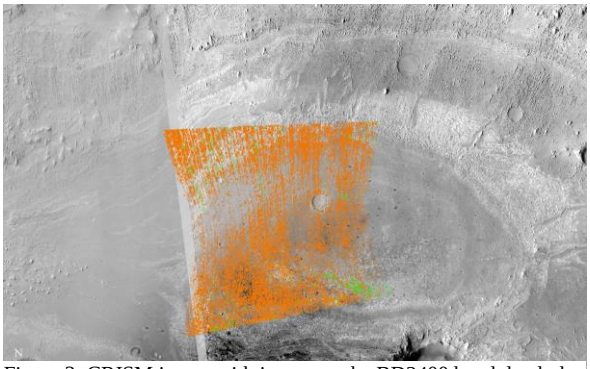

Figure 3: CRISM image with in orange the BD2400 band depth that emphasizes the presence of sulphates. In green the BD1900FRT that highlights the presence of a small amount of hydrated minerals.

4. Implications

All these evidences suggest that crater bulges may be hint for diapiric phenomenon at different stages of evolution, either being a subsurface or an exhumed diapir body. This led to deformation of the surrounding rocks giving origin to fold sets (Crommelin Crater) and to normal faulting and bulge's dissolution caused by the encounter with a subsurface fluid table (Crater 12000088). The trigger for the phenomenon could have been the impact cratering itself, having removed a rock mass volume that generated a differential lithostatic load favoring low density buried salt bodies to uprise.

References

[1] Dooley, T. P., *et al.*, Inflation and deflation of deeply buried salt stocks during lateral shortening. *J. Struct. Geol.* 31, 582–600 (2009). [2] Moratto, Z.M., *et al*., 2010. Ames Stereo Pipeline, NASA's Open Source Automated Stereogrammetry Software. In: Proceedings of the 41st Lunar and Planetary Institute Science Conference. Houston, Texas, [2364]. [3] Hynek, B. Met *al.*, 2002, Geologic setting and origin of Terra Meridiani hematite deposit on Mars: *JGR: Planets*, v. 107, no. E10, p. 18-11-18-14. [4] Stafford KW *et al.*, 2008a. Epigene and hypogene karst manifestations of the Castile Formation: Eddy County, New Mexico and Culberson County, Texas, USA. *International Journal of Speleology 37* (2): 83-98. [5] Karacan E., Yilmaz I., Collapse dolines in miocene gypsum: an example from SW Sivas (Turkey). *Environmental Geology* 29(3/4), 263- 266.

EPSC Abstracts
Vol. 10, EPSC2015-722-1, 2015
European Planetary Science Congress 2015

Can terrestrial impact craters cause changes in the geoid undulation? A case study

T. Statella (1), S.M. Figueiredo (1), P. Pina (2)
(1) Instituto Federal de Educação, Ciência e Tecnologia de MT, Brazil (thiago.statella@cba.ifmt.edu.br, stheemelo@hotmail.com) (2) Instituto Superior Técnico, Lisboa, Portugal (ppina@tecnico.ulisboa.pt)

Abstract

In this abstract the hypothesis that impact craters may cause changes in the geoid undulation on Earth is tested. The Vargeão Dome crater in Brazil has been chosen as the case study. The geoid undulation *N* has been calculated in 315 points spread over the region and no variation due to the presence of the crater has been noted.

1. Introduction

On solid planetary bodies, impact cratering is currently being referred as the most important resurfacing and land forming process. In planets such as Mars, craters can be easily identified by visual analysis performed on remotely sensed data. On Earth, a number of resurfacing processes take part. Hence, the impact craters can be erased or masked by erosional and depositional processes or land cover. Much effort has been done to detect impact craters on Earth. There is a broad field of research on the subject comprising, among others, the analysis of optical [1] and microwave [2] remote sensing data, digital elevation models [3] and global gravitational models [4]. Despite that, only a few 188 (http://passc.net/EarthImpactDatabase) confirmed impact craters on our planet have been reported. In this abstract, we investigate if an impact crater can cause changes in the geoid undulation. If that hypothesis is confirmed, then geoid undulation models can be an alternative method for searching for candidates of impact craters on Earth.

2. Setting

Up to date, seven impact craters have been confirmed [5] in Brazil, which are Araguainha Dome, Serra da Cangalha, Riachão, Vargeão Dome, Vista Alegre, Cerro Jarau and Santa Marta. In this abstract, we have chosen to study the geoid undulation in Vargeão Dome crater. Vargeão Dome is a circular feature located in the Santa Catarina state, Southern Brazil, formed in Cretaceous volcanic rocks of the Serra Geral Formation. This unit comprises mainly continental flood basalts and subsidiary intermediate and acidic volcanic rocks whose emplacement are related to the rifting of Gondwana and the formation of the South Atlantic Ocean [6]. The crater has the center coordinates 26°47'S and 52°10'W (SIRGAS2000 reference frame), its diameter is ~12 km and its age is ~123 Ma.

3. The geoid undulation

The geoid is the equipotential surface of the Earth's gravity field, which best fits, in a least square sense, the global mean sea level. It is a surface that defines zero elevation for orthometric heights measurements. The orthometric height H is the distance along the plumb line between the geoid and the point on the Earth's surface. The distance between the geoid and the reference ellipsoid is the geoid undulation N. N can be obtained by field gravity measurements or, as an alternative, by the difference between ellipsoidal heights h and orthometric heights: $N = h - H$. The ellipsoidal height h is the distance measured from the reference ellipsoid to the point on the surface of the Earth. The geoid is a smooth but highly irregular surface whose shape results from the uneven distribution of mass within and on the surface of the Earth. Consequently, the geoid undulation also varies according to the mass distribution inside the Earth's crust.

3.1 Brazilian undulation model

The Brazilian undulation model is named MAPGEO2010 and has a grid resolution of 5' in latitude and longitude. It was estimated by using

more than 928,000 terrestrial gravimetric points for the South America. The procedures for the determination of the model can be found on http://www.ibge.gov.br/english/geociencias/geodesia/calculo_do_modelo.shtm. The mean accuracy of the model is ± 0.32 m. The lowest accuracy occurs in the North and Northwest regions of the country where it can reach up to ± 0.50 m.

4. Results

Our assumption is that the impact crater produced by a planetary body may alter the mass distribution immediately below Earths' surface and force the geoid undulation to change. We have used MAPGEO2010 to calculate the geoid undulation in 315 points spread over the Vargeão Dome crater. The points were placed in a grid with 30" of resolution in latitude and longitude. The adopted reference frame was the Brazilian SIRGAS2000. Fig. 1 shows a map of the region. The background image is a Landsat-7 scene, composite bands 3 (B), 4 (G) and 5 (R). From the points with *N* values, we have calculated contour lines with a vertical distance of 0.05 m. In Fig. 1, the *N* values are positive over the region meaning that the geoid lies above the ellipsoid surface there. By analyzing the contour lines, one can see that there is a Southeast trend of increasing values and no changes in the geoid undulation due to the presence of the crater are noted.

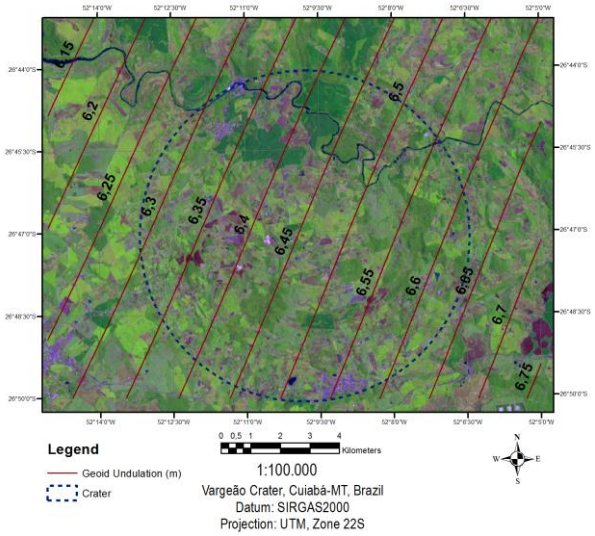

Figure 1: Geoid undulation in Vargeão crater.

5. Conclusion

After analyzing the contour lines made up of 315 points of geoid undulation values in the region of Vargeão crater, as shown in Fig. 1, the hypothesis that an impact crater may change the geoid undulation could not be confirmed. In the data shown in Fig. 1 the geoid undulation has not been affected by the presence of the impact feature. On the other hand, the hypothesis cannot be discarded yet. The Brazilian model has a poor 5' by 5' resolution in latitude and longitude, which roughly corresponds to an area of ~9.25 km by 9.25 km. As the crater has a diameter of ~12 km, most of the *N* values were obtained by interpolation (carried out by the MAPGEO2010 itself). Thus, we are going to perform another test with a much larger structure, the Araguainha impact crater, whose diameter is ~40 km. In addition, we are going to test the EGM2008 global gravity field model.

References

[1] Zumpreskel, H. and Bischoff, L.: Remote sensing and GIS analysis of the Strangways impact structure, Northern territory, Australian Journal of Earth Sciences, Vol. 52, pp. 621-630, 2005.

[2] Chiarro, A. et al.: ERS Synthetic Aperture Radar imaging of impact craters, ERSA Publication Division, 2003.

[3] Krogli, S.O., et al.: Automatic detection of circular depressions in digital elevation data in the search for potential Norwegian impact structures, Norwegian Journal of Geology, Vol. 87, pp. 157-166, 2007.

[4] Kalvoda, J. et al.: Mass distribution of Earth landforms determined by aspects of the geopotential as computed from the global gravity field model EGM2008, AUC Geographica, Vol. 48, pp. 17-25, 2013.

[5] Crósta, A.P. and Vasconcelos, M.A.R.: Update on the current knowledge of the Brazilian impact craters, Lunar and Planetary Science Conference, March 2013, The Woodlands, USA, 2013.

[6] Crósta, A.P. et al.: Geology and impact features of Vargeão dome, southern Brazil, Meteoritics and Planetary Science, Vol. 47, pp. 51-71, 2012.

EPSC Abstracts
Vol. 10, EPSC2015-731, 2015
European Planetary Science Congress 2015

Early MAVEN results on the Mars upper atmosphere and atmospheric loss to space

B. M. Jakosky (1), J. G. Grebowsky (2), J. G. Luhmann (3), and the MAVEN Science Team
(1) LASP, Univ. of Colorado, Boulder, USA, (2) NASA/GSFC, Greenbelt, USA, (3) SSL, Univ. of California, Berkeley, USA (bruce.jakosky@lasp.colorado.edu)

Abstract

The Mars Atmosphere and Volatile Evolution (MAVEN) spacecraft went into orbit around Mars on 21 September 2014. After a commissioning phase that included science observations of Mars and of Comet Siding Spring during its close approach, its primary science phase began on 16 November 2014 and will run for a full Earth year, until November 2015. Early results on structure, composition and dynamics of the upper atmosphere and on escape to space will be presented.

1. Introduction

MAVEN has been collecting data since prior to the formal start of the primary science mission in November 2014. The spacecraft and all science instruments are functioning well, and science data is being collected utilizing our planned observing scenarios. The first two deep-dip campaigns have been carried out successfully (February and April, 2015), and the next two are scheduled (July and September).

By the time of EPSC, we expect to have a preliminary understanding of the instrument behavior, operations, and calibrations. We also expect to have sufficient data collected to allow us to reach preliminary conclusions about the state of the upper atmosphere, interactions with the solar wind, escape of atmospheric gas to space at the present epoch, and integrated escape to space over time. These results will be presented at the meeting.

2. Mission objectives

The science objectives of the MAVEN mission are to characterize the upper atmosphere and ionospheric structure and composition, the interactions of the sun and the solar wind with the planet, and the processes driving loss of gas from the atmosphere to space. Our goal is to understand the chain of processes leading to escape today, learn how to extrapolate back in time, and determine the integrated escape of atmosphere over Martian history.

These goals follow on previous observations that suggest that the early Mars atmosphere was very different from today's, and that it was thick enough to allow liquid water to be present and more stable. MAVEN is addressing the questions of where did the water go and where did the CO_2 go? Loss to space is indicated as being important based on observations of escaping atoms at present, fractionated light stable isotopes most consistent with loss having been important, and the apparent absence of a sufficiently large surface/subsurface reservoir for CO_2.

3. Mission Description

The MAVEN spacecraft is in an elliptical orbit whose altitude ranges from about 150 km to 6200 km above the surface. This orbit allows the spacecraft to pass through the upper atmosphere on each orbit to allow *in situ* observations, and also to make global-scale remote-sensing observations near apoapsis. In addition, we are lowering periapsis to ~125 km for up to four five-day periods during the mission. At the higher densities observed during these "deep-dip" campaigns, we make observations down to the altitudes at which the upper atmosphere transitions to the lower atmosphere. Thus, we sample the entire upper-atmospheric column, all the way out to altitudes at which the solar wind interacts with the planet and its magnetosphere.

The orbit precesses with time, with periapsis moving through local time (sampling the entire range of 0-24H) and latitude (between $\pm 75^{o}$, given its orbital inclination). With this variation, the spacecraft is able to obtain good three-dimensional coverage around Mars and to sample all regions of near-Mars space.

Having had a successful orbit insertion, fuel that had been reserved for a recovery from a problem MOI is now available for an extended mission. With appropriate planning, MAVEN may be able to continue to make science observations for up to a full solar cycle. Of course, the actual longevity will be determined by the fuel usage required for orbit adjustments to ensure that we stay within our periapsis "density corridor" that maximizes the science return.

4. Science instruments

MAVEN has nine instrument sensors collected into eight separate instruments. The sensors can be thought of as being grouped into instruments measuring different aspects pertaining to the goals of MAVEN.

The first group of instruments measures the properties of the solar wind and of the sun that drive the processes in the upper atmosphere:

Solar Wind Ion Analyzer, SWIA (Instrument lead is Jasper Halekas, U. Iowa).

Solar Wind Electron Analyzer, SWEA (David L. Mitchell, U. California Berkeley).

Extreme Ultraviolet Monitor, EUV (Frank Eparvier, U. Colorado Boulder).

Solar Energetic Particle, SEP (Davin Larson, U. California Berkeley).

The second group measures the structure and composition of the upper atmosphere and of the ions in the ionosphere, and also measures isotope ratios that can tell us about the integrated escape to space. In this group, NGIMS measures properties *in situ* at the location of the spacecraft, and IUVS measures them remotely, providing a powerful combination of local and global measurements:

Imaging Ultraviolet Spectrograph, IUVS (Nick Schneider, U. Colorado Boulder).

Neutral Gas and Ion Mass Spectrometer, NGIMS (Paul Mahaffy, NASA/GSFC).

The third group measures the properties of the ionosphere that both drive escape and determine the composition and properties of the escaping ions:

Magnetometer, MAG (Jack Connerney, NASA/GSFC).

Langmuir Probe and Waves, LPW (Bob Ergun, U. Colorado Boulder).

Suprathermal and Thermal Ion Composition, STATIC (Jim McFadden, U. California Berkeley).

With this combination of measurements, we are able to observe the entire chain from solar energy input that drives the processes controlling the upper atmosphere and ionosphere, to the upper-atmosphere response, to the loss of neutrals and ions to space.

6. Summary and Conclusions

The MAVEN spacecraft and instruments are doing well. The data are of high-quality, and all indications as of this writing are that we will be able to address the science questions and achieve the science goals that were the original drivers for the mission. Results will be presented at the meeting.

In addition, MAVEN is on track to being able to carry out an extended mission that would allow us to observe throughout the remainder of a Mars year (including the high-water-abundance northern-hemisphere-summer season) and through different phases of the solar cycle. Observing at these times will have high science value for understanding the Mars environment.

EPSC Abstracts
Vol. 10, EPSC2015-735, 2015
European Planetary Science Congress 2015

Reconstructing the infilling history within Robert Sharp Crater, Mars: Insights from morphology and stratigraphy

J. Brossier (1), L. Le Deit (2), E. Hauber (1), N. Mangold (2), J. Carter (3) and R. Jaumann (1)
(1) Institut für Planetenforschung, DLR, Berlin, Germany (Jeremy.Brossier@dlr.de), (2) Laboratoire de Planétologie et Géodynamique, LPG-Nantes, Université de Nantes, France, (3) Institut d'Astrophysique Spatiale, IAS, Université Paris-Sud, France.

1. Introduction

Robert Sharp (133.59°E, -4.12°N) is a 150 km diameter impact crater, located in the equatorial region of Mars, near Gale Crater, where the MSL rover Curiosity landed in August 2012. Using orbital data, an iron chlorine hydroxide named akaganéite that typically forms in highly saline and chlorinated aqueous environments on Earth has been detected in Robert Sharp crater [1]. Interestingly, akaganéite has also been detected in Gale Crater from the ground [2,3]. In order to reconstruct the paleo-environments in the region, we produce a geological map of Robert Sharp (Fig. 1). Crater counts provide time constraints on its infilling history.

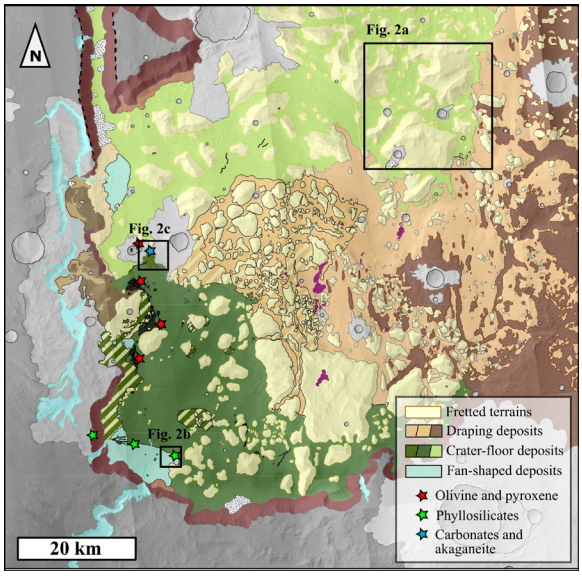

Figure 1. Geological map of Robert Sharp crater, displayed on a mosaic of CTX images. Locations of figures 2a-2c are indicated.

2. Physiography

Robert Sharp crater displays a varied and complex physiography. It is an open basin towards the northern plains (Fig. 1); its northern rim being entirely degraded. Its eastern rim is not exposed at the surface and appears to be buried under deposits. No central peak is visible in Robert Sharp. Instead, numerous knobs and mesas of varied sizes and shapes, that are representative of the fretted terrains [4,5] crop out in the crater (Fig. 2a) and display a rather heterogeneous distribution. Overall, the eastern part of Robert Sharp raises 1.5 km higher than its western part that results into a west-east asymmetry. Nevertheless, the western rim is higher than the eastern one, with about 500 m and -1000 m of elevation respectively. As a result, Robert Sharp shows a physiography significantly different from its neighbors, Gale crater and Knobel crater, suggesting a different geological history.

3. Geologic Mapping Results

The geological units of the Robert Sharp crater are defined according to their localization, physical characteristics (e.g. thermal inertia), morphology, geometry, and mineralogical composition.

Valleys are incised in the western and southwestern crater rim of Robert Sharp, i.e. the lower rims. They are several tens of kilometers long, mostly linear and do not show any hierarchization. Fan-shaped deposits with flat-topped surfaces are located at the outlet of these valleys and may be interpreted as fan deltas. Detection of phyllosilicates at the foot of these fan deltas (Fig. 2b) as well as on the surrounding plateaus suggest that clay was transported from the plateaus and deposited within the crater, or just formed in situ during an episode of aqueous activity [6].

Draping deposits partly fill the crater in the eastern part and cover the fretted terrains, as well as the surrounding plateaus at the east. These draping deposits are subdivided into 3 units based on their surface texture (rough, smooth and hummocky embaying fretted terrains).

In the western part of Robert Sharp crater, the floor is covered by deposits which are posterior to draping deposits and fretted terrains. These crater-floor deposits consist of alluvial deposits, and fluvio-lacustrine deposits, which expose dune-fields of dark-mafic materials (olivine and pyroxene) in some locations. Additionally, significant signatures of Fe-rich carbonates and traces of akaganéite have been detected on these crater-floor deposits [1], as shown in Fig. 2c.

4. Age Determination Results

The estimated ages of the southwestern and western fan-shaped deposits are ~ 1.30 ± 0.37 Ga and 501 ± 69 Ma, respectively, which corresponds to Amazonian ages. The crater-floor units have been formed at ~ 3.5 Ga, during the early Hesperian epoch. Additionally, we perform crater counts on chloride-rich deposits [7-9] (Fig. 2d), located in a basin on the surrounding plateaus at the south of Robert Sharp (131.94°E, -6.4°N). This basin shows an Amazonian age, about 1.12 ± 0.33 Ga, which is similar to the southwestern fan-shaped deposits. It suggests a synchronous formation of these chloride-rich deposits and the fan-shaped deposit. Moreover, our measurements are consistent with those of recent studies [6,10].

5. Timing of events and Conclusion

Our work shows that the Robert Sharp crater underwent a variety of geological events. We suggest the following timing of events: After the impact that formed the crater in the late Noachian epoch [11], Robert Sharp crater experienced the deposition and erosion of the fretted terrains, followed by the aeolian/aerial deposition of the draping deposits during the Hesperian epoch [4,5]. The presence of valleys and possible fan deltas as well as hydrous minerals in the region (i.e. chlorides [7-9], phyllosilicates [6], carbonates, and akaganéite [1]), suggests the occurrence of fluvio-lacustrine episodes. Akaganéite precipitates from acidic, highly saline, iron and chlorine rich fluids. Detection of akaganéite suggests that Robert Sharp has experienced an acidic and oxidizing environment during the last alteration phase of a drying lake within the crater. The lacustrine phase is likely related to the aqueous activity that formed the chloride-rich deposits on the plateaus [7-9]. The last episodes of aqueous activity may be as recent as the early-middle Amazonian period. As shown in the Robert Sharp crater, Mars has known aqueous phase activities well after the late Noachian/ early Hesperian boundary.

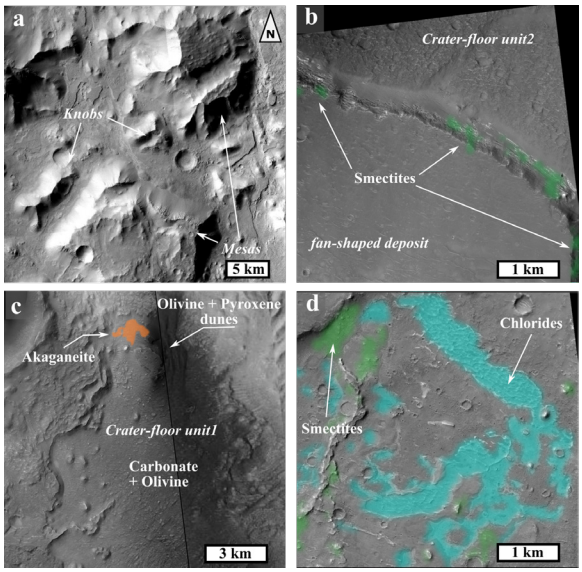

Figure 2. a/ Fretted terrains (i.e. mesas and knobs). b/ Phyllosilicates detected at the foot of the southwestern fan delta [6]. c/ Akaganeite and carbonates detected on crater-floor units within the crater [1]. d/ Chloride-rich deposits detected on the surrounding plateaus [7-9].

References

[1] Carter, J. et al. (2014) *Icarus*. [2] Ming, D. W. et al. (2014) *Science*. [3] Vaniman, D. T. et al. (2014) *Science*. [4] Irwin, R. P. and Watters, T. R. (2010) *JGR*, 115 (E11). [5] Irwin, R. P. et al. (2004) *JGR*, 109 (E9). [6] Ehlmann, B. L. and Buz, J. (2014) *LPSC*. [7] Osterloo, M. et al. (2008) *Sciences*, 319 (5870), 1651-1654. [8] Osterloo, M. et al. (2010) *JGR*, 115 (E10). [9] Ruesch, O. et al. (2012) *JGR*, 117 (E11). [10] Hauber, E. et al.(2013) *JGR*. [11] Tanaka, K. L. (1986) *JGR*, 91 (B13).

EPSC Abstracts
Vol. 10, EPSC2015-751, 2015
European Planetary Science Congress 2015

Initial Results from the MAVEN IUVS Echelle

J.T. Clarke (1), M. Matta (1), W. McClintock (2), N. Schneider (2), J. Deighan (2), I. Stewart (2), G. Holsclaw (2), and B. Jakosky (2)
(1) Center for Space Physics, Boston University, USA, (2) LASP, University of Colorado, USA (jclarke@bu.edu / Fax: +01-617-353-6463)

Abstract

This presentation will give the present status and early results of the echelle channel in the IUVS instrument on the MAVEN spacecraft at Mars. The channel studies H, D, and O in the upper atmosphere of Mars at high spectral resolution (0.008 nm). One primary goal is to study the ratio of D/H in the martian upper atmosphere, and determine the underlying principles that control the escape of H and D into space, with relevance to the historic escape of water from Mars. Initial data indicate that the echelle channel is working well, and we detected the D emission in the first observation of the sunlit disc of Mars.

1. Introduction

The IUVS instrument on MAVEN contains the first echelle spectrograph to be sent to another planet. The system has a novel optical design to enable long-aperture measurements of emission lines in the absence of continuum emission, intended primarily to measure the H and D Ly α emission lines and thereby the D/H ratio from the martian upper atmosphere [1]. The design provides for higher photon counting rates by observing through the long aperture, while maintaining the high spectral resolution in the narrow direction of the aperture. The system also detects the OI 1304 triplet emission with the three component lines well resolved. The echelle system obtains altitude profiles of these emissions every fourth MAVEN orbit, with data both outbound and inbound looking at a constant look direction that scans the atmosphere in altitude. The echelle spectrum is recorded using the same FUV microchannel plate detector as the low resolution IUVS system, and emission lines appear diffusely filling a 1.6 x 0.1 degree aperture (Figure 1) with a spectral resolution of 0.008 nm.

2. Scientific Goals

The main scientific goal of the echelle channel is to measure H and D Ly α emissions from resonantly scattered solar emission, and from these data derive the D/H ratio of the martian upper atmosphere. The ratio HDO / H_2O is roughly 5-10 times higher than in the terrestrial atmosphere. This has been interpreted as being due to the escape of a large volume of water into space, likely early in the history of Mars [2,3]. Since H atoms escape faster than D atoms, the D/H ratio increases with time as more water is lost [4]. There are a number of caveats to this interpretation, including uncertainties in the diffusion of H and D atoms to the upper atmosphere, and different condensation and photodissociation rates of H_2O compared with HDO. MAVEN measurements are intended to determine the average ratio, and any changes with location or season on Mars, to provide a detailed understanding of the physical principles of the escape of both species. This study has gained new importance with the detection of an apparently changing ratio of HDO / H_2O in the lower atmosphere with latitude and season on Mars [5], which implies that the isotopic ratios of different reservoirs of water differ from location to location, perhaps from the poles to the equator.

The derivation of the D/H ratio from brightness measurements requires the use of a radiative transfer model, since the H line is optically thick while the D line is optically thin. The D line exhibits limb brightening, and the effective altitude of the peak can also in principle be used to determine the altitude of the homopause. The OI 1304 triplet line ratio will provide information about both the optical depth of the O line of sight column, and also the contribution of photoelectron excitation to the total emission. Early results from the echelle channel will be presented.

3. Figures

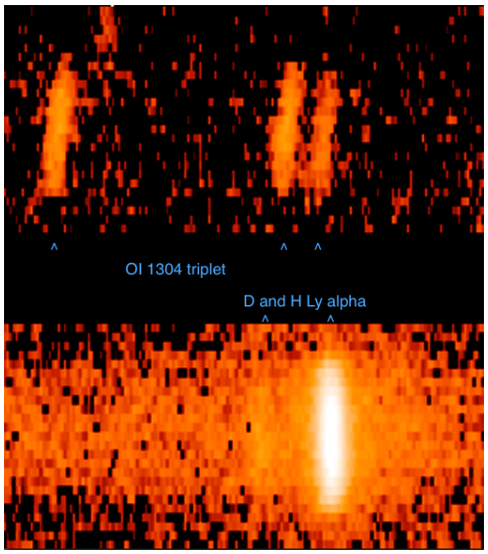

Figure 1: Detector image of the H and D lines (below) and the OI triplet (above) resolved into images of the aperture. The H and D lines (separation 0.033 nm) are well separated by the 0.008 nm resolution of the instrument, however the D line is much fainter and requires a longer integration time to detect.

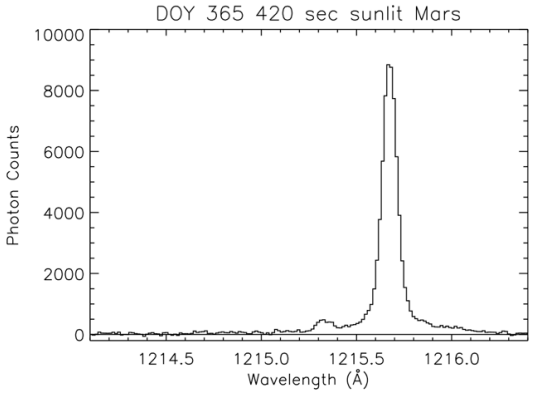

Figure 2: Reduced spectrum of the H (121.567 nm) and D (121.533 nm) lines from the observation in Figure 1, with a 420 sec exposure looking down on the sunlit martian disc. The extended wings on the H line are due to grating scatter.

Acknowledgements

We acknowledge the contributions of the whole MAVEN IUVS team, including the science team, the engineering support staff, and all the people who worked on the MAVEN mission. This research has been supported by NASA sub-contract 1543375 from LASP to Boston University.

References

[1] McClintock, W.E. et al. (2014) *Sp. Sci. Rev*. doi:10.1007/s11214-014-0098-7.

[2] Owen, T., in *Mars,* ed. H. Keiffer *et al.,* Univ. of Arizona Press, 818-833

[3] Krasnopolsky, V., M. Mumma, and R. Gladstone [1998], *Science, 280*, 1576-1580

[4] Yung, Y.L. and D. Kass, (1999) *Science, 280,* 1545-1546.

[5] Villanueva, G. *et al.* [2015], *Science*, 10.1126/science.aaa3630.

EPSC Abstracts
Vol. 10, EPSC2015-779, 2015
European Planetary Science Congress 2015

Analysis of continuous multi-seasonal in-situ subsurface temperature measurements on Mars

M. D. Paton (1), A. –M. Harri (1), T. Mäkinen (1), H. Savijärvi (2) O. Kemppinen (1) and A. Hagermann (3)

(1) Finnish Meteorological Institute, PO Box 503, FIN-00101 Helsinki, Finland (2) Department of Physics, University of Helsinki, PO Box 503, Finland (3) Department of Physical Sciences, the Open University, Milton Keynes, UK

Abstract

Our investigations reveal the local thermal properties on the Martian surface at the Viking Lander 1 (VL-1) site. We achieved this by using the VL-1 footpad temperature sensor which was buried, and due to its location, was under shadow for extensive periods of time during each sol. Reconstruction of the surface and subsurface temperature history of the regolith in the vicinity of the temperature sensor was made using a 1-D atmospheric column model (UH-FMI) together with a thermal model of the lander. The results have implications for the interpretation of subsurface thermal measurements made close to a spacecraft or rock, interpretation of remote sensing measurements of thermal inertia and understanding the micro-scale behavior of the Martian atmosphere.

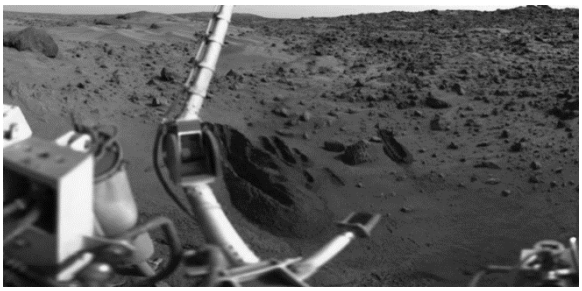

Figure 1: A view of the terrain at the Viking lander site.

1. Introduction

In situ thermal measurements of the regolith are required on Mars as they can complement thermal inertia measurements made remotely from orbit, provide a ground truth, characterise the thermal properties with depth to investigate the regolith structure, study the evolution of the thermal properties with time to investigate the exchange of volatiles with the atmosphere. Thermal probes have been included on spacecraft landers to investigate the surface energy balance, evolution of volatiles and key thermal properties, e.g. most recently Phoenix on Mars and the Philae lander on P67/Churyumov–Gerasimenko, and in the future the InSight mission will deploy a mole into the Martian regolith to measure the thermal and environmental properties.

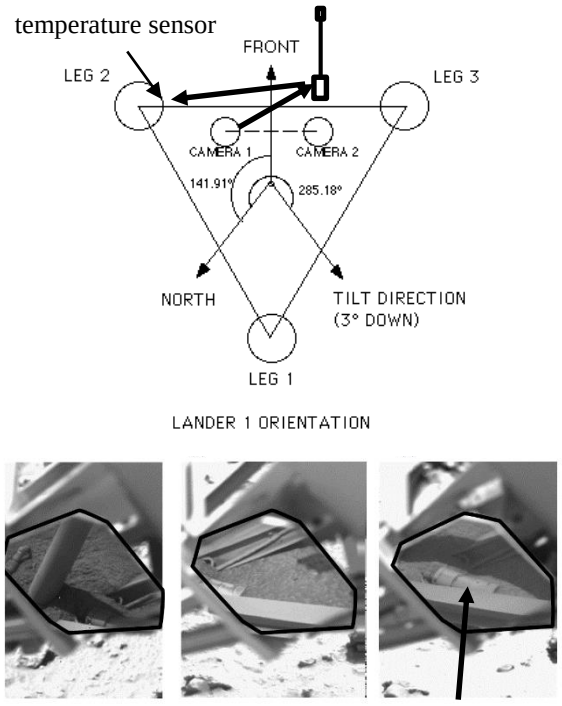

Figure 2: Images of the footpad temperature sensor (bottom) reflected in the sampler boom mirror at different times. Bold arrows in the above schematic show viewing orientation. Modified top image from reference [3].

2. Viking lander 1

The landing of Viking Lander 1 (VL-1) took place in June 1976 during the Martian northern hemisphere summer at a solar longitude of Ls 97 at 22.697 N 48.222 W. The spacecraft landed on mixed terrain with areas of fine grained material and areas of coarser grained material. As VL-1 touched down on the Martian surface its footpad #2 penetrated loose fine grained material burying the footpad and temperature sensor. The sensor survived and continued to make measurements for the duration of the mission (> 3 Martian years). The footpad temperature sensor was buried between 1.2 and 2.4 cm [2].

3. Results

A 3D spacecraft model was used to determine the timings of the shadows cast by the lander. A thermal model of the spacecraft together with a 1-D column model of the atmosphere and regolith [1] was used to predict the subsurface temperatures of the regolith around the footpad temperature sensor (see fig. 2).

Figure 3 shows the sensitivity of the predicted temperatures on the uncertainties of the input parameters. Measurement from the footpad temperature sensor is also shown for comparison. The uncertainty of the spacecraft model input parameters, e.g. reflected and emitted radiation from the regolith.

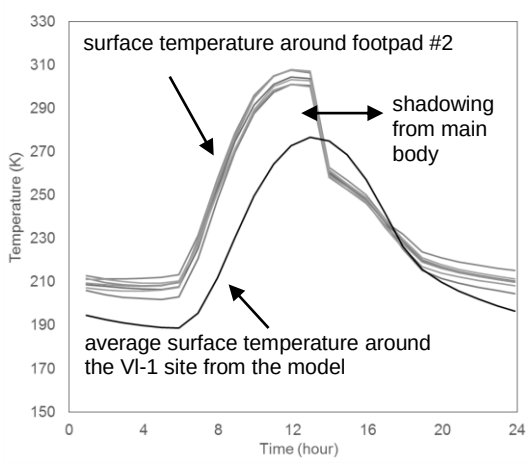

Figure 3: Thermal modelling results showing the sensitivity of the surface temperature on the uncertainty of the spacecraft model inputs. The season is Ls 180º (autumn equinox).

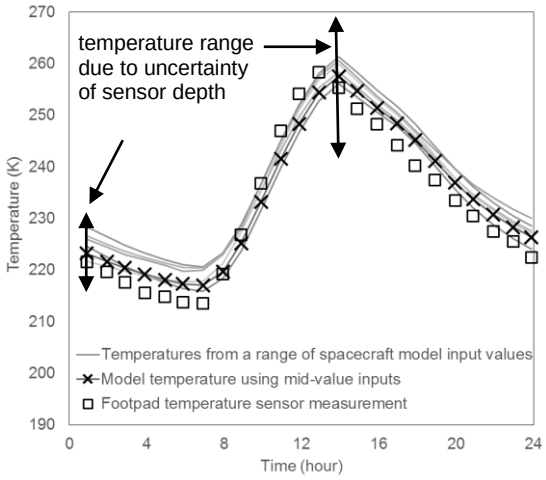

Figure 4: Model results compared to measurements for Ls 180º. Depth is 1.8 cm and thermal inertia is 98 tiu (Thermal Inertia Units). Reasonable fits also obtained for other combinations of depths and thermal inertias. Temperature range due to depth uncertainty - arrow.

4. Concluding remarks

We unravel the thermal influences of the VL-1 on a patch of regolith around its footpad. Even though there is extensive shadowing from the spacecraft it appears thermal radiation emitted from the lander raises the regolith temperature above the surrounding regolith.

A thermal inertia, around the VL-1 footpad #2, of 98 tiu +/- 20 tiu is consistent with our modelling approach given the uncertainty in knowing the depth of the sensor. This is likely much lower than the thermal inertia of the adjacent area of coarser grained material. A consequence is that adjacent areas will have divergent surface temperatures that then could influence the local climate at the VL-1 site.

References

[1] M. D. Paton, A. -M. Harri, T. Makinen and H. Savijärvi.: Martian atmospheric column model with high-fidelity subsurface thermal scheme, Geoscientific Instrumentation, Methods and Data Systems, Vol. 2, pp. 17-27, 2013.

[2] H. J. Moore, R. E. Hutton, G. D. Clow, and C. R. Spitzer, Physical Properties of the Surface Materials at the Viking Landing Sites on Mars, U.S. Geological Survey Professional Paper 1389, 1987.

[3] R. B. Tucker, Viking Lander imaging investigation: Picture catalog of primary mission experiment data record, NASA Reference Publication 1007, 1978.

EPSC Abstracts
Vol. 10, EPSC2015-786-1, 2015
European Planetary Science Congress 2015

Recurring Slope Lineae on Mars: Atmospheric Origin?

A. McEwen (1), M. Chojnacki (1), C. Dundas (2), L. Ojha (3), M. Masse (4), E. Schaefer (1), C. Leung (1)
(1) University of Arizona, Tucson, USA. (2) USGS, Flagstaff, USA. (3) Georgia Tech, Atlanta, USA. (4) Université Paris Sud, France.

Abstract

Recurring Slope Lineae (RSL) are seasonal flows or seeps on warm Martian slopes. Observed gradual or incremental growth, fading, and yearly recurrence can be explained by seasonal seeps of water, which is probably salty. The origin of the water is not understood, but several observations indicate a key role for atmospheric processes. If sufficient deliquescent salts are present at these locations, the water could be entirely of atmospheric origin.

1. Introduction

Recurring Slope Lineae (RSL) on Mars may be produced by the seasonal flow or seepage of water on relatively warm slopes. They are narrow (<5 m), relatively dark markings on steep (25°–40°), low-albedo slopes, which appear and incrementally extend during warm seasons, then fade and recur in the same approximate location over multiple Mars years [1]. RSL lack clear water absorption spectral bands, but the fans on which they terminate have distinctive color and spectral properties [2]. The lineae commonly follow small gullies, but few topographic changes have been detected via 30 cm/pixel images from the Mars Reconnaissance Orbiter (MRO) High Resolution Imaging Science Experiment (HiRISE). The first documented group of RSL occur between ~48–32°S latitude and develop primarily in late southern spring and summer, favoring equator-facing slopes—times and places where peak surface temperatures exceed 250 K [1]. Active RSL also occur in equatorial regions of Mars (0–15°S), most commonly in the Valles Marineris troughs [3]. Like the first group, these equatorial RSL are especially active on sun-facing slopes, moving from north- to south-facing slopes and back to track the peak insolation. We have also confirmed RSL in low-albedo Acidalia Planitia (35°N), active in northern spring and summer with the most vigorous extension in early spring [4]. RSL advance rates are highest at the beginning of each season, followed by much slower lengthening [5].

There are several key gaps in our understanding of RSL. Most importantly, the origin of water to drive RSL flow is unknown. The time of day of active flow is also unknown. Most RSL locations are steep, rocky, low-albedo slopes, with daily peak surface temperatures typically >250 K, and commonly >273 K, in the active season, but there must be additional factors, because many times and places with these properties lack detectable RSL [6]. Water has not been confirmed to be present, but laboratory experiments show that even minor amounts of water (5 wt. % and no liquid film on surface) can darken basaltic soils while producing only weak spectral features [7, 8]. These spectral features may be undetectable in CRISM spectra obtained from MRO's midafternoon orbit, due to partial dehydration and evaporation.

2. Evidence for Atmospheric Effects

The behavior of RSL strongly suggests fluid flow, and we are not aware of any entirely dry process known to create seasonal flows that progressively grow over weeks and months. Seasonal melting of shallow ice would explain the RSL observations, but it would be difficult to replenish such ice annually, and ice inherited from an earlier climate would be quickly depleted. Deeper groundwater may exist and could reach the surface at springs or seeps, but this cannot explain the wide distribution of RSL, extending to the tops of ridges and peaks [1, 9]. Also, there are apparent RSL on equatorial dunes composed of permeable sand, unlikely to be a groundwater source. This leaves an atmospheric origin, but the dryness of the Martian air (~10 pr. microns average column abundance [10]) is a challenge.

Several observations show that atmospheric dust opacity has a significant effect on RSL activity,

whether or not RSL water comes from the atmosphere [1, 3, 11]. The evidence for the source of water being atmospheric includes the following:

1. RSL extend to tops of ridges and peaks in many locations.
2. RSL originate over many spots, up to thousands, within a single HiRISE image, rather than being concentrated at a few key locations like springs.
3. Perchlorates and other hygroscopic salts are common on Mars.
4. Complex RSL flow boundaries may be exactly repeated from year to year [4], perhaps explained by deliquescence of salt deposited by past RSL flow.
5. RSL fans in Valles Marineris transiently darken during or just after periods of high dust opacity [3], perhaps due to stability of deliquesced liquids into the afternoons when MRO observes.

Deliquescence provides a mechanism for trapping water from the atmosphere [12-14]. Condensation of frost is also possible at these sites but direct melting of such frost is unlikely to produce RSL [4].

Seasonal variation in the atmospheric column abundance of water vapor does not match the RSL activity over active locations [3, 15]. Although subsurface exchange during the early stages of the MY28 global dust storm has been suggested to affect column abundances [16], the progressive obscuration of water vapor as dust rises is an alternate explanation [10]. However, near-surface water vapor exchange with the shallow subsurface has been reported by MSL [17].

Can deliquescence trap sufficient water to explain RSL? RSL are highly concentrated in Coprates Chasma, with RSL and their fans covering a total area of ~6 x 10^7 m^2. Assuming 10% water by volume (5% by wt.) a 10 mm flow depth gives 6 x 10^4 m^3 of water [18]. The atmosphere over the full area of Coprates Chasm at ~10 pr. microns contains ~20× more water. Thus, sufficient water may be present in the atmosphere, but must be efficiently trapped over small areas. The principal difficulty is that evaporation during the warm part of the day may exceed deliquescence during cooler times, in spite of efflorescence relative humidities as low as 5% [13, 14], but the cooler days under dusty air may enable liquid to acumulate. HiRISE shows that there are often bright deposits after RSL have faded (possible salt deposits), but they are generally too small to be resolved by MRO/CRISM spectral imaging and may usually be anhydrous. Recent detection of hydrated deliquescent salts at RSL sites in some seasons [19] supports this hypothesis.

3. Summary and Conclusions

The potential for water activity creates new exploration opportunities, to search for extant life or resources, as well as challenges such as the definition of special regions for planetary protection. If RSL form via atmospheric deliquescence, then they are likely eutectic brines with temperatures and water activities too low to support terrestrial life [20].

References

[1] McEwen A. S. et al. (2011) *Science*, 333, 740-744.

[2] Ojha, L. et al. (2013) GRL 40, 5621-5646.

[3] McEwen A. S. et al. (2014) *Nat. Geosci.*, 7, 53-58.

[4] Dundas, C.M. et al. (2015) LPSC 46, 2327.

[5] Schaefer, E. et al. (2015) LPSC 46, 2930.

[6] Ojha L. et al. (2014) *Icarus*, 231, 365-376.

[7] Masse, M. et al. (2014) PSS 92, 136-149.

[8] Pommerol, A. et al. (2013) JGR Planets 118, 2045-2072.

[9] Chojnacki, M. et al. (2014) LPSC 45, 2701.

[10] Smith M. (2008) *AREPS 36*, 191–219.

[11] Stillman D. E. et al. (2014) *Icarus*, 233, 328-341.

[12] Gough, R. et al. (2011) EPSL 312, 371.

[13] Gough, R. et al. (2014) EPSL 393, 73.

[14] Nuding, D.L. et al. (2014) Icarus 243, 420-428.

[15] Toigo, A. et al. (2013) JGR 118, 89-104.

[16] Trokhimovskiy et al. (2015) Icarus 251, 50-64.

[17] Martin-Torres, F. J. et al. (2015) Nature Geos. 8, 357-361.

[18] Chojnacki, M. et al. (2015) LPSC 46, 2537.

[19] Ojha, L. et al., this conference.

[20] Rummel, J.D. et al. (2014) Astrobiology 14, 887-968.

EPSC Abstracts
Vol. 10, EPSC2015-788-2, 2015
European Planetary Science Congress 2015

Daily Variation of Heavy Carbon Dioxide in Mars Atmosphere

T. A. Livengood (1,2), Th. Kostiuk (2), J. Kolasinski (2), T. Hewagama (3), W. G. Henning (1,2), M. Sornig (4), T. Stangier (5), P. Krause (5), G. Sonnabend (6)
(1) CRESST, University of Maryland, USA, (2) NASA Goddard Space Flight Center, USA, (3) University of Maryland, USA, (4) Rhenish Institute for Environmental Research, Cologne, Germany, (5) University of Cologne, Germany, (6) Radiometer Physics GmbH, Meckenheim, Germany (timothy.a.livengood@nasa.gov)

Abstract

The atmosphere of Mars is significantly enriched in C and O heavy isotopes, detected by ground based high-resolution infrared spectroscopy as well as *in situ* measurements by the *Phoenix* lander and Mars Science Laboratory *Curiosity* rover. Heavy isotope enrichment is consistent with the preferential loss of light isotopes in eroding Mars' primordial atmosphere. Infrared spectroscopy of Mars collected in May 2012 as well as in March and May of 2014 from the NASA IRTF resolves rovibrational transitions of normal-isotope carbon dioxide as well as singly-substituted minor isotopologues, enabling remote measurements of carbon and oxygen isotope ratios as a function of latitude and local time of day. Earlier measurements obtained in October 2007 demonstrated that the relative abundance of O-18 increased linearly with increasing surface temperature over a relatively warm early-afternoon temperature range, but did not extend far enough to inspect the effect of late-afternoon cooling. These results imply that isotopically enriched gas is sequestered overnight when surface temperature is minimum and desorbs through the course of the day as temperature increases. Current spectroscopic constants indicate that the peak isotopic enrichment could be significantly greater than what has been measured *in situ*, apparently due to sampling the atmosphere at different time of day and surface temperature. The observing runs in 2012 and 2014 measured O-18 enrichment at several local times in both morning and afternoon sectors as well as at the subsolar, equatorial, and anti-subsolar latitudes. The two runs in 2014 have additionally observed O-17 and C-13 transitions in the morning sector, from local dawn to noon. These observations include a limited sampling of measurements over Gale Crater, which can be compared with contemporary *in situ* measurements by the *Curiosity* rover to investigate the degree of agreement between *in situ* and remote methods and potentially to calibrate the spectroscopic constants required to accurately evaluate isotope ratios all over Mars.

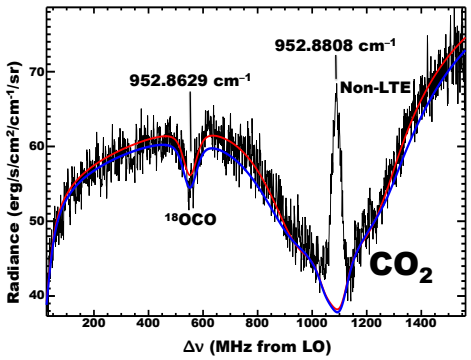

Figure 1: High-resolution infrared spectrum of CO_2 in Mars atmosphere at 952.8808±0.0534 cm^{-1} (bandwidth, not uncertainty). The measured spectrum is dominated by wings of the telluric CO_2 transition at the rest frequency, spanning the Doppler-shifted CO_2 transition formed in Mars troposphere with a non-local thermodynamic equilibrium (non-LTE) core emission formed in the mesosphere, and the ^{18}OCO absorption formed in the Mars troposphere. The blue curve models the emergent spectrum for standard temperature profile and surface temperature. The red curve arises from an iteratively improved lower-atmosphere temperature profile and surface temperature. Both models use the telluric isotope ratio, resulting in a poor fit to the ^{18}OCO feature, demonstrating the opportunity to constrain fitting the isotope ratio.

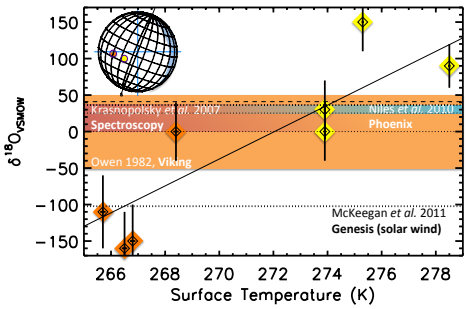

Figure 2: Spectroscopically measured deviation of Mars carbon dioxide ^{18}O from terrestrial VSMOW standard, permille (‰). Measurements on the subsolar point are orange (~0.8" FWHM field of view on map). Measurements at subsolar latitude, but offset 20° longitude toward planetary east (1.33 hours of local time) are in yellow. The light orange band indicates mass spectrometry by *Viking* landers (0±50‰) [4,5]; the red band indicates remote spectroscopy by Krasnopolsky *et al.* [1], 18±18‰; and the blue band indicates *in situ* mass spectrometry from the *Phoenix* lander, 31.0±5.7‰ [3]. Webster *et al.* [6] report 48±5‰ enhancement of ^{18}O from *Mars Science Laboratory*, somewhat greater than *Phoenix* and at the upper limit of the *Viking* range. A dotted line indicates the unenriched solar wind measured by the *Genesis* mission, -102.3±3.3‰ [2].

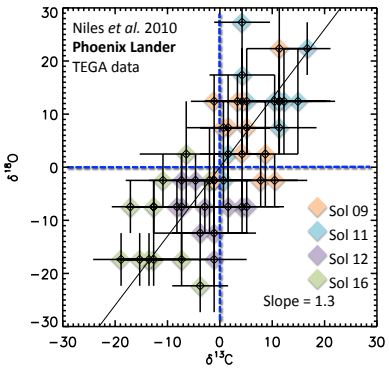

Figure 3: Corroboration from Phoenix lander measurements (data re-plotted from [3]), which show evidence for mass-dependent fractionation of isotopes, consistent with sequestration processes that significantly modify the isotopic enrichment of atmospheric CO_2.

Acknowledgements

This research was supported by the NASA Planetary Astronomy Program. The authors were visiting astronomers at the NASA Infrared Telescope Facility, operated by the University of Hawaii under Cooperative Agreement no. NCC 5-538 with the National Aeronautics and Space Administration.

References

[1] Krasnopolsky, V. A., J. P. Maillard, T. C. Owen, R. A. Toth, and M. D. Smith: Oxygen and carbon isotope ratios in the Martian atmosphere. *Icarus* **192**, 396–403, doi: 310.1016/j.icarus.2007.1008.1013, 2007.

[2] McKeegan, K. D., A. P. A. Kallio, V. S. Heber, G. Jarzebinski, P. H. Mao, C. D. Coath, T. Kunihiro, R. C. Wiens, J. E. Nordholt, R. W. Moses, D. B. Reisenfeld, A. J. G. Jurewicz, and D. S. Burnett: The Oxygen Isotopic Composition of the Sun Inferred from Captured Solar Wind. *Science* **332**, 1528–1531, doi: 10.1126/science.1204636, 2011.

[3] Niles, P. B., W. V. Boynton, J. H. Hoffman, D. W. Ming, and D. Hamara: Stable Isotope Measurements of Martian Atmospheric CO_2 at the Phoenix Landing Site. *Science* **329**, 1334–1337, doi: 10.1126/science.1192863, 2010.

[4] Owen, T.: The composition of the Martian atmosphere. *Adv. Sp. Res.* **2**, 75–80, doi: 10.1016/0273-1177(82)90107-7, 1982.

[5] Owen, T.: The composition and early history of the atmosphere of Mars, in *Mars*, edited by H. H. Kieffer, B. M. Jakosky, C. W. Snyder and M. S. Matthews, pp. 818–834, University of Arizona Press, Tucson, 1992.

[6] Webster, C. R., P. R. Mahaffy, G. J. Flesch, P. B. Niles, J. H. Jones, L. A. Leshin, S. K. Atreya, J. C. Stern, L. E. Christensen, T. Owen, H. Franz, R. O. Pepin, A. Steele, and M. S. Team: Isotope Ratios of H, C, and O in CO_2 and H_2O of the Martian Atmosphere. *Science* **341**, 260–263, doi: 10.1126/science.1237961, 2013.

EPSC Abstracts
Vol. 10, EPSC2015-795, 2015
European Planetary Science Congress 2015

Automatic slope streak detection in MOC, CTX and HiRISE images

F. Puga (1), P. Pina (2) and E.A. Silva (1)
(1)FCT-UNESP, Presidente Prudente, Brazil, (2) CERENA-IST, University of Lisboa, Portugal
(ferpuga@gmail.com)

Abstract

We present an algorithm to detect slope streaks on Mars. It is mainly based on morphological operators and it is successfully tested on images of MOC, CTX and HiRISE cameras on different locations of Mars.

1. Introduction

Slope streaks are features typically dark, narrow and fan-shaped which are seen on downslope reliefs [6]. Studies of these features are important because they may provide a clue for understanding the basic properties of Martian surface layer, dust and water cycles and also some of the most recent climate changes [3]. Many surveys on Mars are being developed with remotely sensed imagery in order to understand the physical processes triggering of these patterns. All the studies that quantify some characteristics of the streaks, are based on manual interactive procedures to delineate only a small portion of the available slope streaks and to measure their morphometric characteristics as area, length or thickness [2][1]. The availability of a methodology to segment the streaks and to extract meaningful information would naturally increase the regional knowledge and the statistical significance, as a much larger amount of images from different locations could be fully analyzed. Since there is no approach in the literature to deal with this problem in an automated manner, we propose an algorithm to deal with the segmentation of dark slope streaks on Mars.

2. Method

The algorithm developed is constituted by a sequence built in three main steps: 1- pre-processing, 2- detection and 3- post-processing. The procedure is based on Mathematical Morphology operators, Otsu method and a shape-based post-processing filtering. The pre-processing of the images consists in attenuating small bright/dark objects. Thus, a filtering operation based on surface area opening and surface area closing [5] is used. In the detection step, the dark streaks are first enhanced through a top-hat transform by closing [5]. The next stage of the detection step consists of the thresholding with Otsu method [4] that permits binarizing the images in an automatic way. Also in the detection step we use a thinning/pruning-reconstruction procedure, so in this way we are able to keep the thin structures, which would be suppressed by the erosion. The post-processing is based on the morphology of the streaks. Thus, to filter out false positive detections, those structures that have an individual low value ratio 'length/width' are excluded from the image. We are able to use this filter since slope streaks are always long elongated features.

3. Image Datasets and Results

In order to include the diversity of dark slope streaks and different illumination conditions, the dataset was built containing images from different locations of Mars captured along different daily periods and solar longitudes. Currently, our dataset is constituted by 190 images: 90 MOC narrow-angle (resolutions in the range 1.4-6.5 m/pixel), 90 CTX (5-6 m/pixel) and 10 HiRISE (0.25-0.50 m/pixel), that is, those from which we have already performed ground-truth images manually. Therefore, the algorithm developed is applied to each individual image of the dataset mentioned. Examples of the results obtained with the algorithm application for each camera (MOC, CTX and HiRISE) are shown in Figure 1. The performance of the algorithm is evaluated through the computation of the following quantities: *true detection percentage* $D = TP/(TP+FP)*100$, *branching factor* $B=FP/TP$, and *quality percentage* $Q = TP/(TP+FP+FN)*100$. Here, *TP* denotes true positive detections, *FP* false positive detections and *FN* false negative detections. *TP*, *FP* and *FN* were obtained through comparisons with ground-truth images of the dark slope streaks. The application of the algorithm in each one of the

190 images of the dataset led to an overall quality performance of about 80% (Table 1).

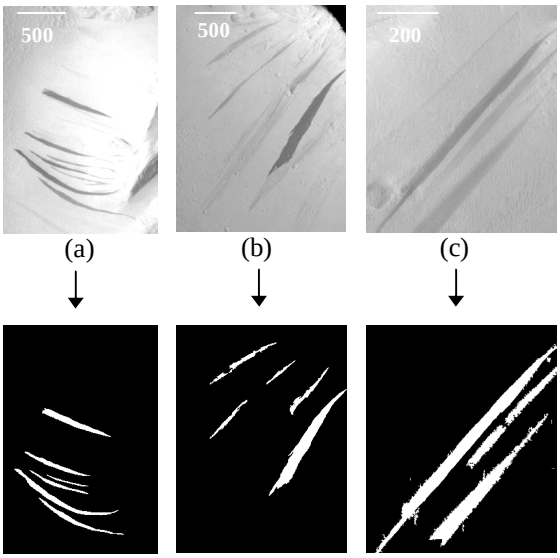

Figure 1: Examples of algorithm performance in images (a) CTX D01_027725_2078 (b) MOC M0307769 (c) HiRISE ESP_011730_2105

In what concerns the sensor, the quality is higher with HiRISE images than with MOC and CTX ones. This seems to be due to the fact that HiRISE images only survey smaller regions on the Martian surface (a consequence of its very high resolution) and normally the scenes under analysis contain mainly slope streaks and very few of other type of surface features.

Table 1: Average Performances (by Camera and Global)

Sensor	**Nb. of Images**	**D %**	**B**	**Q %**
MOC	90	87.93	0.14	77.97
CTX	90	93.67	0.20	78.52
HiRISE	10	84.50	0.03	82.09
MOC + HiRISE + CTX	190	89.70	0.18	80.03

4. Conclusions

The algorithm presented is still an ongoing process. Currently, the algorithm identifies slope streaks in high resolution images from Mars (0.25-6.5 m/pixel) with a quality detection of about 80%. The result can be considered very good as the dataset built is representative of a very large diversity of terrains where these features occur. Although there is still room for improvement, namely to detect the more faint streaks, we consider that this segmentation algorithm is already very useful for start mapping slope streaks on Mars at large scale.

References

[1] Bergonio, J., Rottas, K., Schorghofer, N.: Properties of martian slope streak populations. Icarus, Vol 225, pp. 194-199, 2013.

[2] Chilton, H., Phillips, C.: Temporal Contrast Changes in Dark Slope Streak on Mars. Lunar and Planetary Science Conference XXXXIV, Abs. #3109, Houston TX, 2013.

[3] Kreslavsky, M. A. and Head J. W.: Slope streaks on Mars: A new "wet" mechanism. Icarus, Vol. 201, pp. 517-527, 2007.

[4] Otsu N.: A threshold selection method from gray-level histograms. IEEE Transactions on Systems, Man, and Cybernetics 9: 62–66, 1979

[5] Soille, P.: Morphological Image Analysis. Springer-Verlag, Berlin, 2004.

[6] Sullivan, R.., Thomas, P., Veverka, J., Malin, M., Edgett, K. S.: Mass movement slope streaks imaged by the Mars Orbiter Camera, Journal of Geophysical Research, Vol. 106(E10), pp. 23607-23633, 2001.

EPSC Abstracts
Vol. 10, EPSC2015-844, 2015
European Planetary Science Congress 2015

From MGS to MAVEN: Analysis of electron plasma voids through statistical and case study

M. Steckiewicz (1), C. Mazelle (1), N. André (1), P. Garnier (1), D.L. Mitchell (2), R. Lillis (2), J. McFadden (2), J. Connerney (3), L. Andersson (4), J. Luhmann (2), B. Jakosky (4), E. Penou (1), V. Génot (1), M. Bouchemit (1), E. Budnik (1), A. Biegun (1) A. Beth (1), A. Fedorov (1)

(1) CNRS, IRAP, Toulouse, France (2) Space Science Laboratory, Berkeley, USA (3) Goddart Space Flight Center, Washington DC, USA (4) Laboratory for Atmospheric and Space Physics, Boulder, USA

Contact: msteckiewicz@irap.omp.eu

Abstract

The Mars Atmosphere and Volatile Evolution spacecraft (MAVEN) entered in orbit around Mars on September 21st, 2014 and began its scientific phase two months later. Compared to its predecessors, i.e. Mars Global Surveyor which orbited around Mars at 400 km from 1999 to 2006, and Mars Express which has been around Mars since 2003 with a periapsis at 270 km, MAVEN will provide unprecedented observations of the neutral and plasma environment of the planet thanks to its unique orbital coverage and its sophisticated instrument suite. Its precessing orbit is highly elliptical with a 4.5h period and a nominal periapsis at 150 km with "deep-dip campaigns" down to 125 km. While MGS did not carry any ion spectrometer and MEX does not carry any magnetometer, MAVEN has a complete set of plasma instruments including the Solar Wind Electron Analyzer (SWEA) measuring the energy and angular distributions of electrons of energetic range from 3eV to 4.6 keV with a 2 seconds rate.

From November 2014 to February 2015 MAVEN's periapsis sampled northern latitudes from 30 to 70 degrees from the dawn to the dusk terminator in the night-side above regions with and without significant crustal magnetic sources. On nearly each periapsis a drop of more than two orders of magnitude of suprathermal electrons with energies above 3 eV can be observed. Electron plasma voids have already been reported from MGS and MEX observations and their location suggested a strong link with crustal magnetic sources on the surface of the planet that can generate magnetic loops excluding electrons. We will first revisit the properties of electron plasma voids from MGS and MEX observations and compare/contrast them with the new MAVEN multi-instrumental observations that reveal with unprecedented details the highly variable structure of these voids. Their numerous observations above the Northern hemisphere where crustal magnetic sources are much weaker than in the southern hemisphere reveal that additional generation mechanisms must be taken into account. We will then discuss the various possible origins of these electron plasma voids in relation to the variability of the nightside ionosphere of Mars.

References

[1] D.L. Mitchell, R.P. Lin, C. Mazelle, H; Rème, P.A. Cloutier, J.E.P. Connerney, M.H. Acuña, and N.F. Ness, Probing Mars' crustal magnetic field and ionosphere with the MGS Electron Reflectometer, JGR, vol. 106, NO. E10, Pages 23,419-23,427, 2001.

EPSC Abstracts
Vol. 10, EPSC2015-848, 2015
European Planetary Science Congress 2015

Probability of solar panel clearing events at the Insight landing sites (Mars) from a dust devil track survey

D. Reiss (1) and R. D. Lorenz (2)
(1) Institut für Planetologie, Westfälische Wilhelms-Universität, Wilhelm-Klemm-Str. 10, 48149 Münster, Germany,
(2) Johns Hopkins University Applied Physics Laboratory, 11100 Johns Hopkins Road, Laurel, MD 20723, USA.

1. Introduction

The InSight robotic lander is scheduled to land on Mars in September 2016. InSight was designed to perform the first comprehensive surface-based geophysical investigation of Mars [1]. Passage of vortices may have a number of influences on the geophysical measurements to be made by InSight. Seismic data could be influenced by dust devils and vortices via several mechanisms such as loading of the elastic ground by a surface pressure field which causes a local tilt [e.g. 2]. In addition, the power supply of the InSight instruments is provided by solar arrays. Solar-powered missions on Mars like the Sojourner rover in 1997 were affected by a decline in electrical power output by 0.2-0.3 % per day caused by steadily dust deposition on its horizontal solar panel [3]. The solar-powered Mars Exploration Rovers (MERs) Spirit and Opportunity experienced similar dust deposition rates [4] which led to steady power decrease over time endangering longer rover operation times. The much longer operation times of the rovers were made possible by unanticipated 'dust clearing events' of the solar arrays by wind gust or dust devils [5]. Recent studies imply that dust devils are primarily responsible for those recurrent 'dust clearing events' [6]. In this study we investigate the potential frequency of intense dust devil occurrences at the InSight landing site regions, which are able to remove dust from its solar panels. We analyzed newly formed dust devil tracks within a given time span using multi-temporal HiRISE image data covering the same surface area. Based on these measurements we will give encounter rate predictions of intense (high tangential speed and high pressure drop) dust devils with the InSight lander.

2. InSight landing site region

In 2013, four final landing site ellipses in Elysium Planitia located between 133.8°-139.5°E and 2.8-5°N (Fig. 1) were selected [7]. Within this region we analyzed multi-temporal HiRISE images covering the same surface area within a relatively short time period. In total, 8 image pairs were available at the start of the analysis (Fig. 1; Ids 1-8). Newly formed dust devil tracks were identified and mapped, and the width, length, and azimuth of each dust devil track was measured.

3. Results

In total, 557 dust devil tracks were identified in 8 image pairs acquired between March 2010 and February 2014. No active dust devils in these image pairs were observed.

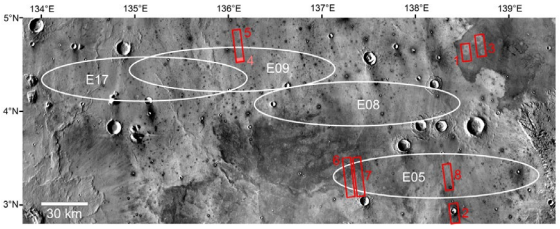

Fig. 1. The final four InSight landing ellipses (white color; E05, E08, E09, and E17) in Elysium Planitia (based on [7]). Frames and identitiy numbers (Ids 1-8) show areas of HiRISE stereo pairs (red) and overlapping surface area of two HiRISE images (pink).

Morphology. Fig. 2 shows an example of a typical newly formed DDT. The DDTs in the study region are relatively straight which is also expressed in their low mean sinuosity of 1.03 (standard deviation = 0.004). The sinuosity is lower compared to mean values of ~1.3 and ~1.08 measured by [8] in Russell and Gusev crater, respectively.

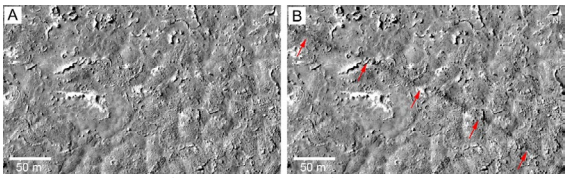

Fig. 2. Example of observed track formation between HiRISE images. A: HiRISE image ESP_016942_1845 at LS=61.30°. No tracks visible. B: HiRISE image ESP_018010_1845 at LS=97.83°. The new NW-SE oriented dust devil track has a width of 5 m. Images were acquired 81 sols (martian days) apart.

Track widths. Measured DDT widths vary from 1 – 30 m with a mean and median width for all measured DDT of 3.99 m and 3.08 m (standard deviation = 3.13), respectively. In general, narrower DDTs occur much more frequently as broader ones, i.e. the size distribution is strongly skewed. This can simply be explained by size-frequency distributions of dust devils: On Earth and Mars, smaller dust devils occur more frequently than larger ones [e.g., 9, 10], hence narrower DDTs should be expected to occur more frequently as larger ones. [11] suggested the size distribution of Martian dust devils may be described by a power law with a differential exponent of -2: fuller discussion of this question is found in [12] and [13]. As discussed in these papers, the break in frequencies occurring at DDT widths that we observe here between 1 – 2 m and 2 – 3 m can be explained by limitations of DDT identification due to the spatial image resolution of around 30 cm/pixel (i.e. poor detection efficiency at small sizes, rather than a low abundance).

Track lengths. Many DDT run out of the HiRISE image, hence the complete length of the DDT cannot be measured. Although there is a broad scattering in the results, a trend for increasing DDT lengths versus DDT widths can be seen. Such a relationship of increasing lengths with increasing widths (likely comparable to dust devil diameters) would be expected due to the fact that larger dust devils have longer durations [14] who suggested an empirical correlation for both Earth and Mars data of t=40d0.66, where t is the longevity in seconds and d the diameter in meters. The exponent allowed by the data may be between about 0.5 and 0.75, with 0.66 as a best guess round number (there exists large scatter in the data). The track length data where the full tracks were observed, are described by the least-squares fit $L=181d^{0.71}$. The exponent here is reassuringly consistent with the longevity exponent of 0.66 in the expression by [14].

Frequency and seasonal variations. Seasonally most image pairs cover solar longitudes (L_S) between 51° and 93° (northern spring), except for one covering L_S=215°-250° (northern autumn). The frequency of newly formed DDTs per square kilometer per sol (ddt km^{-2} sol^{-1}) varies between 0.002 and 0.08 (Fig. 3). However, within the last three acquired image pairs with a frequency of 0.002–0.005 ddt km^{-2} sol^{-1} a strong fading of already existing DDTs occurred, indicating suppressed dust devil activity probably caused by increased dust deposition. We compared the seasonal DDT formation rate to the Dust Devil Activity (DDA) index (Fig. 3), which is defined as the flux of energy available to drive dust devils [15]. It is related to the surface sensible heat flux and thermodynamic efficiency and generally increases with the depth of the convective planetary boundary layer, the difference between air and surface temperatures and the surface wind stress. Input parameters for the calculation of the DDA index were derived from the Mars Climate Database (MCD version 5.1) [16]. The seasonal DDA index was calculated in LS=10° steps and averaged from 5 daily calculations between 9-17 local time. Although the available mul-titemporal HiRISE data is so far limited to certain seasons, the DDA index indicates an average seasonal DDT formation rate around 0.04 ddt/km^2/sol.

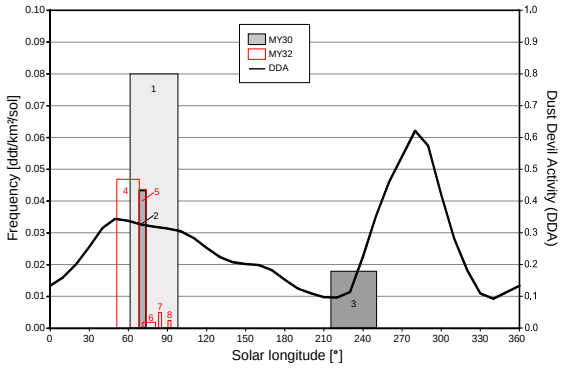

Fig. 3. Seasonal DDT frequency of the analyzed image pairs in comparision to the Dust Devil Activity (DDA) index of [15].

4. Solar panel clearing predictions

The formation of DDTs is of operational interest, in that InSight is solar-powered, and the accumulation of dust on its solar panels may influence the amount of data the lander can send back, and ultimately the operational lifetime of the lander itself. By multiplying the track widths by the track lengths, we obtain a DDT area formation rate (e.g. for the Id1 data, we find a total of 1.6 km^2 of DDTs formed by 396 DDTs in a 61km^2 survey area over 81 sols) of about 0.0003 km^2/km^2/sol. Inverting this implies that a given spot on the surface may be cleared of dust once in 3000 sols (i.e. every ~5 Mars years). Based on the measurements of Ids 1-5 (Ids 6-8 show fading of tracks) and the seasonal DDA index (Fig. 3), the average seasonal DDT formation rate is around 0.04 ddt/km^2/sol. After normalization of track widths, lengths, and using the average DDT formation rate of 0.04 ddt/km^2/sol we calculated an average DDT area formation rate of about 0.00007 km^2/km^2/sol for the InSight landing site regions, which implies that InSight's solar panels may be cleared of dust in average once in ~15000 sols (i.e. every ~22 Mars years). In so far as clearing dust from a solar panel is in principle the same process as the formation of a DDT (i.e. the removal of a layer of dust [17, 18]), then the DDT formation rate we have observed is not favorable for expecting any reversal of dust accumulation on InSight's solar panels since the recurrence interval of ~22 martian years is much longer than the expected mission duration. The main reason for this very long recurrence interval is the small dust devil size population observed from DDTs. On the other hand, we have not yet had the opportunity to observe the DDT formation rate at the season at which dust devil activity would be expected to be highest based on the DDA index from L_S ~250°-320° (Fig.3). Finally, the total encounter rate of the InSight lander with less intense dust devils (not able to remove significant amounts of dust) and dustless vortices will be much higher. Orbital obervations showed that only 14% of active dust devils leave tracks [19]. Measurements of DDT formation rates with HiRISE [8] and the comparison to observed active dust devils by Spirit rover [10, 20] in Gusev crater implies a ratio between 1/500 and 1/110 [8]. This ratio even does not include dustless vortices, which indicates that the total encounter rate of vortices with the InSight lander might be several 100 factors higher than our predictions for intense dust devils.

References [1] Banerdt W. B. et al. (2012) LPS XLIII, Abstract #2838. [2] Sorrells G. G. (1971) Geophys. J. R. Astron. Soc. 71–82. [3] Golombek M. P. (1999) JGR 104, 8523-8553. [4] Kinch K. M. et al. (2007) JGR 112, E06S03. [5] Vaughan A. F. et al. (2010) Mars 5, 129-145. [6] Lorenz R. D. and Reiss D. (2015) Icarus 248, 162-164. [7] Golombek M. P. et al. (2014) LPS XLV, Abstract #1499. [8] Verba C. A. et al. (2010) JGR 115, E09002. [9] Sinclair P. C. (1969) J. Appl. Met. 8, 32–45. [10] Greeley R. et al. (2010) JGR 115, E00F02. [11] Lorenz R. D. (2009) Icarus 203, 683-684. [12] Kurgansky M. V. (2012) Icarus 219, 556-560. [13] Lorenz R. D. (2011) Icarus 215, 381-390. [14] Lorenz R. D. (2013) Icarus 226, 694-970. [15] Rennó N. O. et al. (1998) JAS 55, 3244-3252. [16] Millour E. et al. (2014) 8th Inter. Conf. on Mars, Abstract #1184. [17] Greeley R. et al. (2005) JGR 110, E06002. [18] Reiss D. et al. (2010) GRL 37, L14203. [19] Cantor B. A. et al. (2006) JGR 111, E12002. [20] Greeley R. et al. (2006) JGR 111, E12S09.

EPSC Abstracts
Vol. 10, EPSC2015-859, 2015
European Planetary Science Congress 2015

Teleconnection event during a martian regional dust storm

L. Montabone (1, 2), T. Kuroda (3) and S. I. Thomson (4)
(1) Space Science Institute, Boulder, CO, USA, (2) CNRS – Laboratoire de Météorologie Dynamique, Paris, France, (3) Department of Geophysics, Tohoku University, Japan, (4) Department of Applied Mathematics and Theoretical Physics, University of Cambridge, UK (lmontabone@spacescience.org)

1. Introduction

In contrast with teleconnection patterns, which can be thought as vast atmospheric regions dynamically coupled over long time scales, a transient teleconnection event couples distant regions over much shorter time scales, through the propagation of some kind of mediating signal.

The signature of a transient teleconnection event, for instance, has been identified in a reanalysis of the martian atmosphere (which includes observations from the Mars Global Surveyor/TES instrument) during the onset of the 2001 (Martian Year -MY- 25) planet-encircling dust storm. Montabone et al. [3] and Martinez-Alvarado et al. [2] have identified a long-range radiative-dynamical coupling between the site where a regional dust storm (about a thousand kilometres across) had its explosive growth, near the Hellas Planitia basin, and the area where subsequent storms appeared in the Tharsis region, on the opposite side of the planet. In this specific case, the mediating signal that allowed the teleconnection has been identified in the interference of the diurnal and "Kelvin" components of the thermal tides.

In this study, we describe another possible transient teleconnection event, coupling the northern (NH) and southern (SH) hemispheres rather than the eastern and western ones. This event analogously originates from the development of a large regional dust storm, which seems to induce a radiative-dynamical coupling between the two hemispheres.

We use the publicly available MGS/TES Mars Analysis Correction Data Assimilation (MACDA) dataset v1.0 ([3]) to identify and analyse the event.

2. Teleconnection event in MY 26

In late MY 26 winter (L_s~310°), a dust storm originated in the North-East corner of the Tharsis Plateau, crossed the equator and expanded in the SH (L_s~320°). See the evolution of the atmospheric column dust optical depth (CDOD) in Fig. 1. This late winter storm had a strong effect in the NH, via the transient modification of the global circulation. The increase of air downwelling and consequent adiabatic compression at high northern latitudes produced an episode of enhanced polar warming at several altitudes (see Fig. 2), severely affecting also the shape and strength of the northern polar vortex. We are interested in understanding the mechanisms underlying the transient teleconnection event that connected the SH, where the dust storm and related direct atmospheric heating were mostly located, and the NH, where the effects on the polar warming and the circulation were observed.

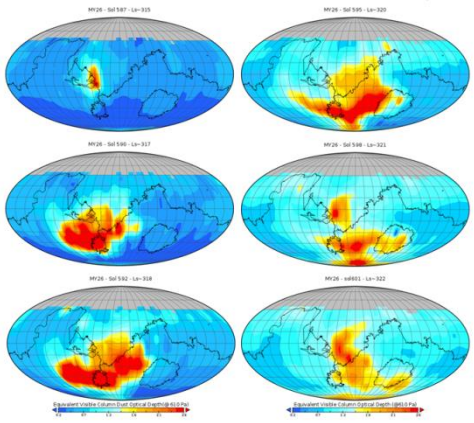

Figure 1: Maps of gridded equivalent-visible CDOD observations normalized to 610 Pa ([5]) from L_s~315° through L_s~322° (~3 sols apart) in MY 26, showing the development of the cross-equatorial storm.

In order to understand which mediating signal allowed the teleconnection in this specific case, we investigate several individual atmospheric wave components, including migrating tides, non-migrating tides, planetary waves, and gravity waves.

Figs. 3 and 4 show the individual components before and during the polar warming enhancement, 16 sols apart. The analysis reveals strong differences in the migrating tide and planetary wave components, which induce the strengthening and displacement of both the peak of the westerly polar jet and the peak of the easterly equatorial jet. It is likely that the modification of the migrating tides (with largest amplitudes between 30°S and the equator, see Fig. 4) is directly produced by the localised atmospheric heating due to the presence of dust. The understanding of the origin of the dynamical coupling between the displacement of the migrating tides and the enhancement of the northern high-latitude planetary waves, though, requires further detailed analysis.

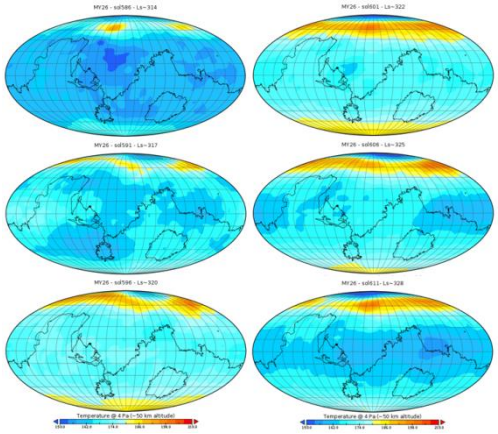

Figure 2: Maps of temperature at about 4 Pa level (~50 km altitude) from L_s~314° through L_s~328° (5 sols apart) in MY 26, extracted from MACDA ([4]).

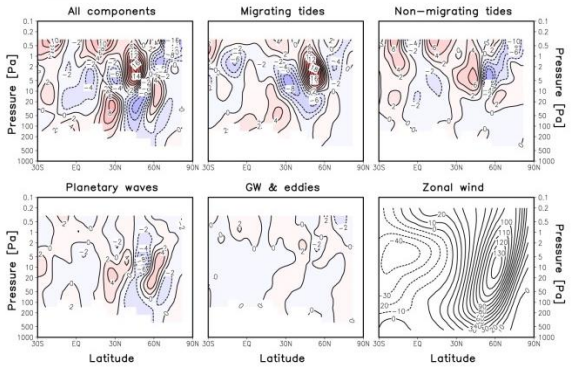

Figure 3: Analysis of the atmospheric wave components and zonal wind for sols 584-586, L_s~315°, MY 26, extracted from MACDA ([4]). The analysis is carried out as detailed in [1].

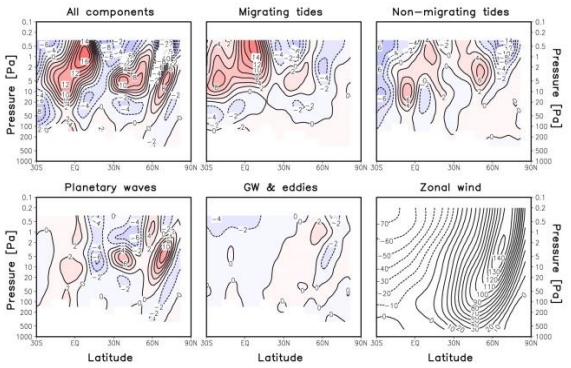

Figure 4: Same as in Fig. 3 for sols 600-602, L_s~322°, MY 26. These plots show the atmospheric wave components corresponding to the peak of the polar warming enhancement, as represented in the top right panel of Fig. 2.

Acknowledgements

LM acknowledges support by the US National Aeronautics and Space Administration under Grant No. NNX13AK02G issued through the Mars Data Analysis Program 2012.

References

[1] Kuroda, T., A.S. Medvedev, P. Hartogh, M. Takahashi: On Forcing the Winter Polar Warmings in the Martian Middle Atmosphere during Dust Storms. J. Meteor. Soc. Japan, 87, 913–921, 2009.

[2] Martinez-Alvarado, O., L. Montabone, S.R. Lewis, I.M. Moroz, and P.L. Read: Transient teleconnection event at the onset of a planet-encircling dust storm on Mars. Ann. Geophys. 27, 3663-3676, 2009.

[3] Montabone, L., O. Martinez-Alvarado, S. R. Lewis, P. L. Read, and R. J. Wilson: Teleconnection in the Martian Atmosphere During the 2001 Planet-encircling Dust Storm. 3rd International Workshop on the Mars Atmosphere: Modeling and Observations, Williamsburg, VA (USA). LPI Contribution No. 1447, p. 9077, November 2008.

[4] Montabone, L., K. Marsh, S.R. Lewis, P.L. Read, M.D. Smith, J. Holmes, A. Spiga, D. Lowe and A. Pamment: The Mars Analysis Correction Data Assimilation (MACDA) Dataset V1.0, Geoscience Data Journal, doi: 10.1002/gdj3.13, 2014.

[5] Montabone, L., F. Forget, E. Millour, R.J. Wilson, S.R. Lewis, B. Cantor, D. Kass, A. Kleinboehl, M.T. Lemmon, M.D. Smith, M.J. Wolff: Eight-year climatology of dust optical depth on Mars. Icarus 251, 65-95, 2015.

EPSC Abstracts
Vol. 10, EPSC2015-862, 2015
European Planetary Science Congress 2015

A potential Mars 2020 rover landing site at a delta in Magong Crater, Mars

E. Hauber (1), T. Platz (2,3), L. Le Deit (4), S. van Gasselt (5), K. Kinch (6), M.B. Madsen (6), H. Rosenberg (5)
(1) Institute of Planetary Research, German Aerospace Center, Berlin, Germany (Ernst Hauber@dlr.de); (2) Max Planck Institute for Solar System Research, Göttingen, Germany; (3) Planetary Science Institute, Tucson, Arizona, USA; (4) Laboratoire de Planétologie et Géodynamique, University of Nantes, Nantes, France; (3) Freie Universität Berlin, Planetary Sciences & Remote Sensing, Berlin, Germany; (6) Niels Bohr Institute, University of Copenhagen, Copenhagen, Denmark.

Abstract

For the upcoming NASA 2020 Mars rover mission we identified a potential landing site that meets all geological criteria including the presence of Noachian/Early Hesperian aqueous sediments and mineral phases and access to unaltered igneous rocks. Our proposed landing site is located at the terminus of Sabrina Vallis in Magong crater. The 25 km × 20 km landing ellipse is centred at 11.990°N, 313.425°E. This site features deltaic sediments and distal lacustrine sediments. Weak signatures of Fe/Mg-bearing phyllosilicates were detected at central delta cliff sections. Lacustrine sediments are cut by a partially exhumed igneous dyke. On the crater floor of Magong crater remnants of an approximately 1 m thick dark deposit are observed, which is interpreted to be a tephra layer sourced from an adjacent volcanic field within Lederberg crater. Detailed terrain analysis of the landing site shows that engineering constraints are met with respect to slope and relief.

1. Introduction

Our proposed 2020 Mars rover landing site is located in Magong crater at the highland/lowland transition zone in northern Xanthe Terra. The landing ellipse is placed at the distal end of the Sabrina Vallis delta. Sabrina Vallis extends for about 250 km in W-E direction, cutting into Middle Noachian highland material (unit mNh; [1]).

2. Data and methods

For morphological investigations we used HRSC nadir (12.5 m/px), CTX (5-6 m/px), and HiRISE (0.25 m/px) images. Terrain analysis was performed on HRSC (75 m/px) and CTX-derived (15 m/px) digital elevation models (DEM). Albedo and thermal inertia values are derived from TES data. Spectral signatures are based on CRISM images.

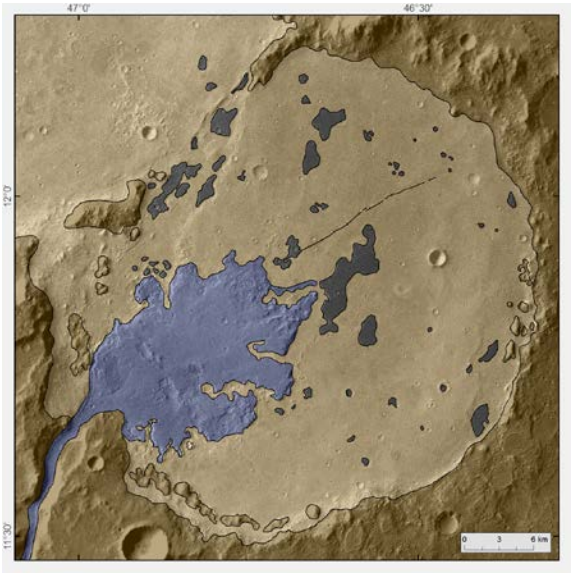

Fig. 1: Simplified geological map of Magong crater hosting the Sabrina Vallis delta. Blue: deltaic deposits, pale brown: crater floor unit, dark grey: tephra deposit, brown: highland material. The narrow line feature in the centre represents a dyke.

3. Geology

In our initial survey we prepared a basic geological map (Fig. 1), where four units are distinguished: 1) crater floor unit, 2) dark deposit, 3) deltaic deposits, and 4) highland material. Deltaic deposits are layered subhorizontally as exposed in distal cliff sections (Fig. 2a). The delta is covered by fine-grained sediments obscuring any potentially coarse-grained components and surficial proximal to distal facies changes. Due to the mantling, CRISM data only show weak signatures of Fe/Mg phyllosilicates (person. comm. J. Carter) exposed in central delta

cliffs. The crater floor unit appears dust-free and exhibits a rough texture peppered with eroded impact craters (Fig. 2c). Small aeolian bedforms are only observed in some larger craters. The crater floor unit represents aqueous and subaqueous sediments. Fresh craters exposed dark-toned underlying strata. The dark deposit overlies the crater floor unit and is approximately 1 m thick (Fig. 2b). It occurs in isolated patches throughout the crater floor. A narrow ridge runs across the crater floor in NE-SW direction, which is interpreted to be the top portion of a partially exhumed dyke (Fig. 2d).

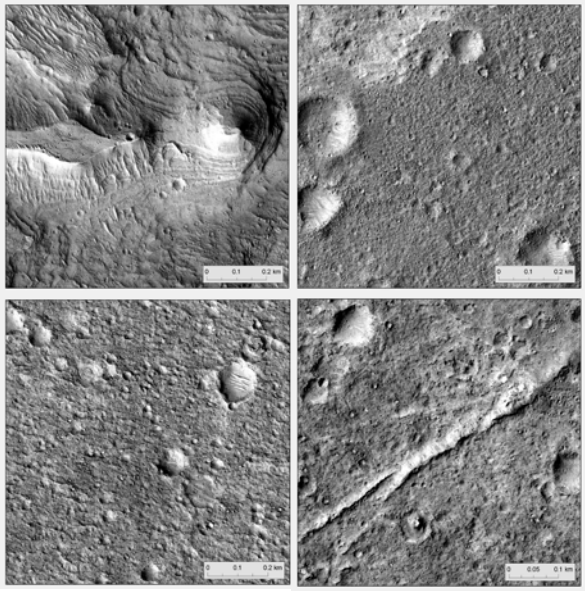

Fig. 2: Close-up HiRISE views of the deltaic sediments (a), hypothesized tephra deposit (b), crater floor material (c), and the linear ridge (an exhumed dyke?) (d).

3. Terrain analysis

The mean elevation within the landing area based on the HRSC-DEM is -2681m ± 48 m (1σ). Slope values range between 0-18.1° with an average of 2.4° ± 1.8° (1σ). The expected slopes at a 2 m baseline length are expected to be about 2.9° based on CTX and MOLA DEMs. The relief over a 1000 m baseline length is for most areas within the landing ellipse less than 75 m with a few patches exceeding 100 m (Fig. 3).

Fig. 3: Relief/slope map of Magong crater for a 1 km baseline length. Red areas exceed the 100 m relief threshold value. Yellow and orange colours mark relief values of 50-75 m and 75-100 m, respectively. Greenish colours mark the relief of <50 m within a 500 m radius. The 25 km × 20 km landing ellipse is shown in yellow. →

4. Discussion

Sabrina Vallis and the surrounding terrain are characterised by periods of extensive fluvial activity. The Sabrina valley system was formed at about 3.8 Ga with its delta representing the last stage of activity at about 3.4 Ga [2]. The crater floor material was deposited at 3.7 Ga with a major erosive event taken place at about 2.2 Ga. This event eroded most of the tephra leaving only isolated patches behind. The tephra was likely emplaced through explosive eruptions at hypothesized volcanic tuff rings within the adjacent Lederberg crater [3]. At the landing site there is access to fluvial and lacustrine sediments where signatures of life may be found. Sampling igneous rocks from the dyke will advance our understanding of the Martian magmatic evolution. The widespread tephra deposit would give insights into eruption dynamics and will also serve as a regional time-stratigraphic marker horizon.

References

[1] Tanaka, K.L., et al.: USGS Scientific Investigation Map, SIM 3292, 2014. [2] Hauber, E., et al.: JGR, 2013, pp. 1-16. [3] Brož, P. & Hauber, E.: JGR, 2013, pp. 1656-167.

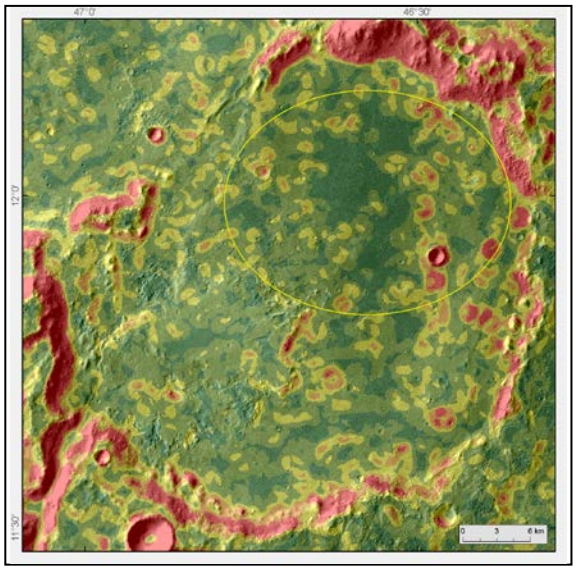

EPSC Abstracts
Vol. 10, EPSC2015-876-1, 2015
European Planetary Science Congress 2015

The Present Near-Surface Inventory of Water on Mars: How Well Does it Constrain the Past Inventory and the Existence of a Former Ocean?

S. M. Clifford (1) and F. McCubbin (2),
(1) Lunar and Planetary Institute, Houston, TX, USA (clifford@lpi.usra.edu), (2) University of New Mexico Albuquerque, NM, USA.

Abstract

Over the past 40 years, estimates of the total outgassed inventory of water on Mars have ranged from a global equivalent layer (GEL) ~7-1000 m deep [1, 2]. However, Carr and Head [3] have recently argued that it is not the total inventory of outgassed water that is important, but the amount that exists in climatically exchangeable surface and near-surface reservoirs – suggesting that any exchange with water in the deep subsurface is precluded by the existence of a thick cryosphere, at least during the Amazonian and Hesperian. Based on this assumption, and their estimate of the present day near-surface inventory of H_2O (~34 m GEL, stored as ice in the polar layered deposits (PLD), lobate debris aprons, ice-rich latitude dependent mantles, and as shallow ground ice), they then extrapolate the evolution of this inventory backward in time, taking into account the introduction of new water by volcanism and outflow channel activity and the loss of water by exospheric escape. They conclude that, at the end of the Noachian, Mars had a near-surface water inventory of ~24 m and ~62 m by the end of the Hesperian – inventories that Carr and Head [3] argue were incompatible with the existence of a former ocean.

Yet, estimates of the amount of water lost or gained, over Martian geologic history, have large uncertainties. Further, the freezing and subsequent burial of a Noachian or Hesperian ocean (by volcanic ash, lavas, and eolian and fluvial sediments) provides a plausible and effective means of sequestering many hundreds of meters of H_2O (GEL) well below the ~60-80 m depths sampled by the MARSIS surface permittivity investigations [4]. The potential survival of a buried remnant of a former ocean, outflow channel discharge, and past climatically emplaced ice-rich latitude dependent mantles, is consistent with theoretical expectations of the hydrologic and climatic evolution of Mars, the abundant geologic evidence for km-thick accumulations of volcanic and sedimentary deposits, and the observed distribution and morphologic characteristics of fluidized ejecta craters, as well as other geomorphic indicators of subsurface volatiles, throughout the northern plains [5-7]. This suggests that the present near-surface inventory of H_2O places no constraint on either the past near-surface inventory, or the former existence of a northern ocean.

Near-Surface Inventory of H_2O and Resurfacing History of the Northern Plains

Current research suggests that Mars accreted from a population of planetesimals that were more volatile rich than those that formed the Earth [8, 9], yielding an initial Martian planetary inventory of (bound) water ~600-4000 m deep (GEL). A potentially large, but unknown, fraction of this inventory was released from the interior by the formation of an early magma ocean, as well as by subsequent impact and volcanic degassing. It is not known how much of the initial outgassed inventory survived the early period of atmospheric escape – nor how much more was added by volcanic outgassing during the Noachian. However, there is persuasive evidence that Mars experienced intense volcanic activity throughout its first billion years of geologic evolution. This evidence is apparent at the eastern end of Valles Marineris, where ~4-5 km of layered stratigraphy is exposed in the canyon walls, capped by a plateau unit that dates from the Late Noachian [10, 11]. Additional evidence is provided by the regional flow directions of Late Noachian/Early Hesperian valley networks, which indicate that the vast bulk of Tharsis volcanic province was in place prior to the last episode of valley network formation [12].

This inability to quantify the inventory of water on Mars during the Noachian motivated Carr and Head [3] to try a different approach, based on three key assumptions: (1) that the inventory of water present in climatically exchangeable near-surface reservoirs can be considered in isolation from the planet's total outgassed inventory of water, (2) that the present near-surface inventory of water is reasonably well-known, and (3) that we can accurately estimate the amount of water added and removed from the near-surface inventory during the Amazonian and Hesperian. In this way, Carr and Head [3] attempt to

deduce the Late Noachian near-surface inventory of water by extrapolating the present inventory backward in time. While the validity of all three assumptions can be debated, it is the first that represents the most serious weakness of the Carr and Head [3] approach, as extensive resurfacing has heavily modified the nature of the near-surface environment over time.

For example, early Mars global climate models [13, 14] suggest that, if the Noachian inventory of water was large enough to form a northern ocean, it would have rapidly frozen – creating a northern ice sheet. While sublimation may have redistributed some of this ice to high elevations (forming snowpacks and glaciers) [15], Noachian Mars was the most geologically active period in the planet's history [11]. Higher atmospheric pressures would have resulted in enhanced eolian erosion, with global dust storms redistributing dust across the planet. Fluvial discharges, associated with the formation of the valley networks and earliest outflow channels, would have caused extensive erosion and carried substantial volumes of water and sediment to low elevations – especially in the northern plains. Finally, the intense volcanic activity that characterized this era could have readily blanketed any frozen remnant of an early ocean, outflow channel discharge, or ice-rich latitude dependent mantles, with volcanic ash and lavas – 10's to 100's of meters deep.

This episodic resurfacing would have had a profound effect on the stability and preservation of ice at depth [7, 16]. For example, at mid-latitudes, a mantle of regolith <10 cm deep is sufficient to thermally isolate near-surface ice from daily temperature extremes, greatly reducing its sublimative loss. Mantles >1-2 m, provide enough insulation to protect ice from annual temperature extremes, allowing buried ice to survive for billions of years. Present-day Martian examples of this effect include the defrosted regions of the south polar layered deposits and the ice-rich latitude dependent mantles. Numerous examples of the preservation of glacial ice, by its burial beneath mantles of sediment, volcanic ash and lava, can also be found on Earth (Fig. 1a).

Conclusions

If early Mars possessed an inventory of outgassed water sufficient to form an early ocean, then a frozen relic of that body may survive at depth to the present day. While sublimation undoubtedly depleted some fraction of the initial inventory of ice, later episodes of outflow channel activity and obliquity-driven polar ice redistribution, combined with the concurrent accumulation of ~0.5 - 1.5 km of sediments and volcanics, since the Noachian [17], would have led to the development of a complex volatile stratigraphy throughout the northern plains [7] – at depths well below those associated with the present near-surface inventory of ice (Fig 1b). Thus, even if we could assess the present near-surface inventory of ice with high precision, it would place no constraint on either the past near-surface inventory of H_2O or the former presence of a northern ocean. Finally, because the burial of ice significantly inhibits its diffusive communication with the atmosphere [16], any estimate of the original outgassed inventory or water, inferred from the present atmospheric D/H ratio [18], must be considered a minimum.

References: [1] Anders, E. and T. Owen (1977) Science 198.4316: 453-465; [2] Carr, M. H (1986) Icarus 68, 187–216; [3] Carr, M. H., and J. W. Head III (2015) GRL, DOI:10.1002/2014GL062464; [4] Mouginot et al. (2012), GRL, 39, L02202; [5] Lucchitta et al. (1986) JGR. 91, E166-E174. [6] Costard, F. and Kargel J. (1995). Icarus. 114, 93-112; [7] Clifford, S. M., and T. J. Parker (2001), Icarus, 154, 40–79; [8] Walsh et al. (2011) Nature, 475(7355), 206-209; [9] Brasser, R. (2013) Space Science Reviews 174.1-4 (2013): 11-25; [10] Mangold et al. (2004) Science, 305, 78–81, doi:10.1126/science.1097549; [11] Tanaka et al. (2014) Geologic map of Mars: U.S. Geological Survey Scientific Investigations Map 3292, scale 1:20,000,000, pamphlet 43 p., http://dx.doi.org/10.3133/sim3292; [12] Phillips et al. (2001) Science 291.5513 (2001): 2587-2591; [13] Forget et al. (2013) Icarus, 222, 81–99. [14] Wordsworth et al. (2013) Icarus 222, 1–19; [15] Head, J. W., and D. R. Marchant (2014) Antarctic Science 26.06 (2014): 774-800; [16] Carr, M. H. (1990) Icarus 87, 210–227; [17] Head, J. W., Kreslavsky, M. A., & Pratt, S. (2002). JGR-Planets, 107(E1), 3-1. [18] Villanueva et al. (2015) Science 348.6231 (2015): 218-221.

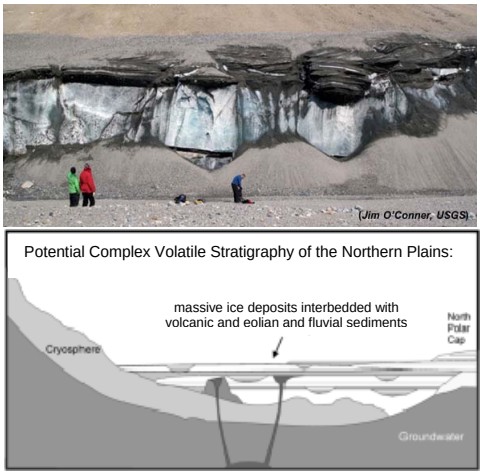

Fig. 1. (a) Several meter-thick sedimentary layer preserving remnant ice from the last glacial maximum in Garwood Valley, Antarctica. (b) Potential complex volatile stratigraphy of the Martian northern plains.

EPSC Abstracts
Vol. 10, EPSC2015-892, 2015
European Planetary Science Congress 2015

Data-Model Comparisons of Planetary Ions at Mars

S. M. Curry[1] J. G. Luhmann[1], C. F. Dong[2], T. Hara[1], Y. Harada[1], F. Leblanc[3], R. Modolo[3], Y. Ma[4], D. Brain[7], R.Lillis[1], R. Livi[1], J. McFadden[1], J. Halekas[5], J. Espley[6], D. Mitchell[1], D. Larson[1], J. Connerny[6], B. M. Jakosky[7], [1]Space Sciences Laboratory, Univ. of California at Berkeley, Berkeley, CA, 94720 (smcurry@ssl.berkeley.edu), [2]Atmospheric Oceanic and Space Sciences, University of Michigan, Ann Arbor, MI 48109 [3]LATMOS-IPSL/CNRS, Guyancourt F-78280, France, [4]Earth, Planetary, and Space Sciences, University of California Los Angeles, Los Angeles, CA 90095, [5]Department of Physics and Astronomy, University of Iowa, Iowa City, IA 52242, [6]NASA Goddard Space Flight Center, Greenbelt, MD 20771, [7]Laboratory for Atmospheric and Space Physics, University of Colorado, Boulder CO 803033

1. Abstract

We present a Mars Atmospheric and Volatile EvolutioN (MAVEN) data-model comparison to better constrain the response of Mars' atmosphere to changes in the interplanetary magnetic field (IMF) configuration, specifically with how the IMF influences the escape of the atmosphere. Because Mars lacks a dipole magnetic field, the solar wind directly interacts with the upper neutral atmosphere to create 'pick-up' ions. The pick up ions can subsequently escape to space, with a spatial dependence on the IMF configuration. We will present global maps of escaping O^+ during different solar cycle phases for multiple IMF conditions using a magnetohydrodynamic and test particle simulation. We will compare these to the relevant MAVEN datasets and examine how the different IMF configurations could influence the escape rate from Mars' atmosphere. Using the models, we will also address the role of the solar cycle and crustal field orientation.

2. Introduction

Diagenetic and isotopic evidence suggests that Mars hosted large inventories of water (e.g. [1,2]), much of which may have escaped to space [3]. When water in the atmosphere is photodissociated, the resulting hydrogen can be removed via hydrodynamic escape [4] while the resulting oxygen is 16 times heavier and requires ~2 eV at Mars to escape, which is more than most photochemical processes provide. Thus other mechanisms are necessary to explain the removal of oxygen from these atmospheres.

One of the non-thermal mechanisms for removing oxygen is through the interaction with the solar wind. Mars lacks an intrinsic dipole magnetic field, which creates a scenario where neutral oxygen can be ionized and 'picked up' and accelerated by the background convective electric field. Pick-up ions can affect two significant processes for atmospheric escape: 1) sputtering via pick-up ion precipitation as well as 2) escape through pick-up ion acceleration [5]. In the first process, pick-up ion precipitation drives atmospheric escape through sputtering when an energetic ion re-impacts the atmosphere and collides with neutral oxygen, exchanging momentum and causing the neutral oxygen to have enough energy to escape the atmosphere. In the second process, oxygen can escape when it is ionized and swept away by the solar wind.

2. Approach

Simultaneous measurements of plasma and magnetic fields are critical for assessing how much of the ionized gases in Mars' atmosphere escape; MAVEN is the first spacecraft since Phobos in 1988 to carry both plasma instruments and a magnetometer. Using the available observations, we present comparisons of simulated heavy planetary ions with MAVEN plasma data to better constrain atmospheric loss rates at Mars. Specifically, questions remain about the effect of the interplanetary magnetic field (IMF) on atmospheric erosion due to the lack of a dipole magnetic field. Past data observations have indicated that most of the pick-up ion escape is behind the planet through the tail, but numerous simulations have predicted a high-energy plume driven the convective electric field generated by the IMF. The MAVEN data will be compared to model results from the Mars Test Particle (MTP) simulation and the BATS-R-US magnetohydrodynamic (MHD) simulation in order to capture both the fluid and kinetic behavior of the upper atmosphere. Both simulations use a 3-D neutral atmosphere, and the

MHD simulation is a single fluid, multi-species realization [6,7].

3. Preliminary results

The most observed IMF configurations at Mars have been a Parker spiral in the towards and away sector [8]. Using the suite of models mentioned above, we present maps of escaping O^+ on a spherical shell around Mars at 3 R_M. We will compare the high altitude plasma observations of O^+ using the particle and field instruments on MAVEN, including STATIC, SWIA, SWEA and MAG. Specifically, we will present magnetic field observations of a reversal in the IMF from a towards to an away sector, highlighting the response of the observed behaviour of the heavy ions seen by SWIA and STATIC.

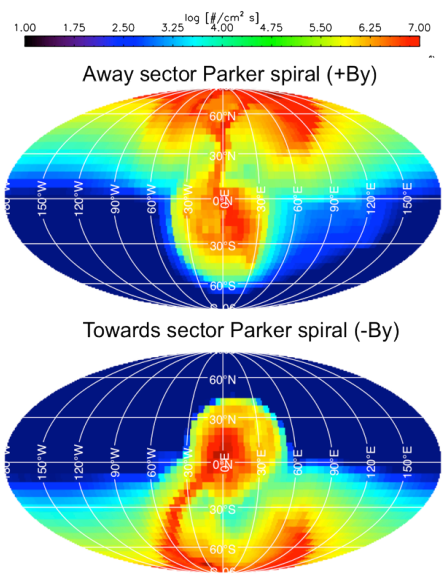

Figure 1: The Molleweide projection of escaping O^+ from 3 R_M is looking directly downtail of the planet. The flux is on a log scale in units of cm^{-2} s^{-1}. The top panel illustrates the escape pattern for an away sector IMF while the bottom panel illustrates the escape pattern for a towards sector IMF.

Acknowledgements

I would like to acknowledge the invaluable input and advice from Janet Luhmann, as well as Andrew Poppe and Christina Lee. I would also like to acknowledge the entirety of the MAVEN team.

References

[1] McElroy et al. (1982) *Science* 251, 1614

[2] Squyres et al., (2004) *Science*, 306(5702), 1709-14

[3] Jakosky et al. (2002) *Nature* 412, 237-244

[4] Kasting et al. (1983) *Icarus* 53(3), 479-508

[5] Luhmann et al. (1991), *JGR, 96, 5457*.

[6] Bougher et al. (2007), *GRL, 33,* 2

[7] Dong et al. (2014) *GRL*, 41, 2709-2715

[8] Brain et al. (2006) *Icarus*, 2, 464-473

EPSC Abstracts
Vol. 10, EPSC2015-898, 2015
European Planetary Science Congress 2015

MAVEN measurements of photochemical escape of oxygen from the Martian atmosphere

R. J. Lillis [1] J. Deighan[2], J. L. Fox[3], S. W. Bougher[4], T. Cravens[5], Y. Lee[4], P. R. Mahaffy[6], M. Benna[6], M. K. Elrod[6], L. Andersson[2], J. McFadden[1] ,[1]Space Sciences Laboratory, Univ. of California at Berkeley, Berkeley, CA, 94720 (rlillis@ssl.berkeley.edu), [2]Laboratory for Atmospheric and Space Physics, University of Colorado, Boulder CO 80303, [3]Wright State University Department of Physics, Dayton, OH 45435, [4]Atmospheric Oceanic and Space Sciences, University of Michigan, Ann Arbor, MI 48109, [5]Department of Physics and Astronomy, University of Kansas, Lawrence, KS 66045, [6]NASA Goddard Space Flight Center, Greenbelt, MD 20771.

1. Introduction

One of the primary goals of the Mars Atmosphere and Volatile Evolution Mission (MAVEN) mission is to characterize rates of atmospheric escape at the present epoch and relate those escape rates to solar drivers [1]. One of the major escape processes is known as photochemical escape, which is broadly defined as a process by which a) an exothermic reaction in the atmosphere/ionosphere results in an upward-traveling neutral particle whose velocity exceeds planetary escape velocity and b) the particle is not prevented from escaping through any subsequent collisions [2]. At Mars, photochemical escape of oxygen is expected to be a significant channel for atmospheric escape, particularly in the early solar system when extreme ultraviolet (EUV) fluxes were much higher [3]. Thus characterizing this escape process is central to understanding the role escape to space has played in Mars' climate evolution.

2. Approach

Because escaping hot atoms cannot easily be directly measured, models of production and transport (through the atmosphere) of such atoms must be used to constrain escape rates. These models require altitude profiles of neutral densities and electron and ion densities and temperatures, as well as compositional information.
All the relevant quantities upon which photochemical escape depends are measured by MAVEN at the relevant altitudes (130-300 km). The Langmuir Probe and Waves (LPW) instrument measures electron density and temperature [4], the Neutral Gas and Ion Mass Spectrometer (NGIMS) measures neutral and ion density [5]and the SupraThermal And Thermal Ion Composition (STATIC) instrument [6] measures ion density and temperature. Four separate calculations must be made for every inbound and outbound altitude profile [7]:

1. Profiles of O_2^+ dissociative recombination (DR) rates are calculated straightforwardly from electron temperature, electron density and O_2^+ density.
2. Profiles of rotational and vibrational distributions of O_2^+ ions are calculated from profiles of CO_2, O, O_2, O^+, CO_2^+ and CO^+ via a lookup table from an empirical model.
3. Profiles of energy distributions of hot O atoms are calculated from the results of step 2 and from profiles of electron and ion temperatures.
4. Profiles of all neutral densities are input into models of hot O transport in order to calculate photochemical escape fluxes from DR of O_2^+.

3. Preliminary results

We present photochemical escape fluxes as a function of all relevant factors, in particular solar zenith angle and EUV flux. The latter will change with solar activity, solar rotation and Mars heliocentric distance, while MAVEN will sample the former from ~10° to 150° as the periapsis location precesses over the first 5 months of the primary mission. Figure 1 shows an example of aphotochemical escape rate calculation from December 2014 at a solar zenith angle of 75°. Figure 2 shows calculated photochemical escape rates as a function of solar zenith angle for ~100 periapsis passes. At 60° solar zenith angle the calculated escape fluxes range from 0.1 to 5 x 10^7 cm^{-2} s^{-1} compared with modeled escape fluxes ranging from 1 to 40 x 10^7 cm^{-2} s^{-1}.
These results are still very preliminary and subject to change as calibrations evolve. Validated photochemical escape fluxes from the MAVEN primary mission, combined with further simulations with progressively higher EUV fluxes, will eventually enable a total integrated loss estimate over

the course of Martian history and hence a determination of the impact of this loss process on the evolution of the Martian climate.

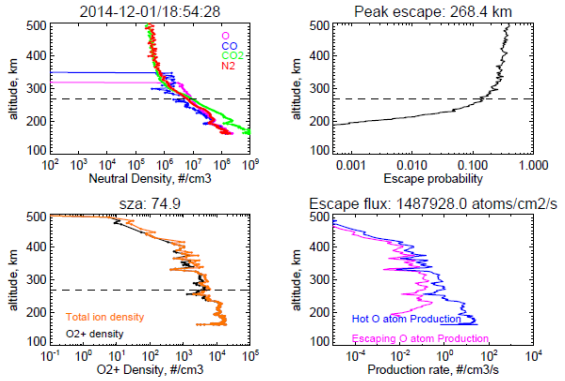

Figure 1: Example of photochemical escape rate calculation. Top left panel shows measured neutral densities. Top right panel shows average escape probability as a function of the altitude at which hot O atoms are produced via dissociative recombination. Bottom left panel shows measured ion densities. Bottom right panel shows of production rates of total and escaping hot O atoms.

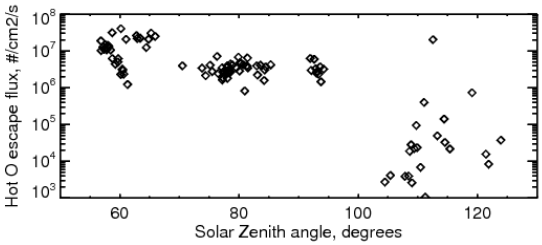

Figure 2: Hot oxygen escape fluxes calculated from periapsis passes in November and December 2014, shown as a function of solar Zenith angle.

References

[1] Jakosky et al. (2014), *Space Sciences Reviews*, DOI 10.1007/s11214-015-0139-x

[2] Fox and Hac (2009), Icarus 204, 527-544

[3] Zahnle and Walker, *Reviews of Geophysics and Space Physics*, 20, 2, 280-292.

[4] Andersson et al. (2015), *Space Sciences Reviews*, in review.

[5] Mahaffy et al. (2014), Space Sciences Reviews doi: 10.1007/s11214-014-0091-1

[6] McFadden et al. (2015), *Space Sciences Reviews*, in review.

[7] Lillis et al. (2015), *Space Sciences Reviews*, in review.

EPSC Abstracts
Vol. 10, EPSC2015-921, 2015
European Planetary Science Congress 2015

Fluvio-lacustrine Landforms and Associated Phyllosilicates of a Paleolake at Libya Montes, Mars: Evidence of Complex Hydrologic activity

G. Erkeling (1), M. A. Ivanov (2), D. Reiss (1), H. Hiesinger (1), J. L. Bishop (3,4), D. Tirsch (4), L. L. Tornabene (5), R. Jaumann (4)
(1) Institut für Planetologie (IfP), WWU Münster, Wilhelm-Klemm-Straße 10, 48149 Münster, Germany. (2) Vernadsky Inst. RAS, Moscow, Russia. (3) Carl Sagan Center, The SETI Institute, Mountain View, California, USA. (4) Institute of Planetary Research, German Aerospace Center (DLR), Berlin, Germany. (5) University of Western Ontario, London, ON, Canada. (gino.erkeling@uni-muenster.de / Fon: +49-251-8336376)

Introduction

The last decades of Mars research have revealed numerous observations of past flowing and ponding of water on the surface of Mars, including channels, valleys, paleolakes, seas and oceans. A region on Mars with the highest density of fluvial and lacustrine landforms is the Noachian-aged Libya Montes highland at the southern rim of Isidis Planitia [e.g., 1-5]. In particular, a 60-km diameter crater paleolake site located at 85.8°E/2.7°N reveals a diverse and complex setting of fluvial and lacustrine landforms [4]. The dense appearance of valleys, fan-shaped deposits and associated mineral assemblages record the repeated occurrence of liquid, flowing and standing water and provide significant insights into the aqueous geologic record of Libya Montes. The complex hydrologic activity proposed for this crater lake site indicates a great potential for discovery of past environmental conditions that may have been favorable for life [4].

The complex geologic and geochemical nature of this site encouraged multiple proposals for candidate landing sites for future rover missions to Mars [e.g., 4,6,7]. Although this site has not yet been selected as a landing site due to difficulties meeting the engineering requirements of near-future missions to Mars, it has been monitored with high priority by recent Mars orbiter missions. New HiRISE images provide, together with the HRSC DEM for the geologic context (Fig.1), a terrific view into the paleolake site and, in particular, of the fan-shaped deposits. Here we present the morphologic maps of the deposits at HiRISE scale (Fig. 2-4) and added hyperspectral CRISM data to investigate the mineralogy in greater detail.

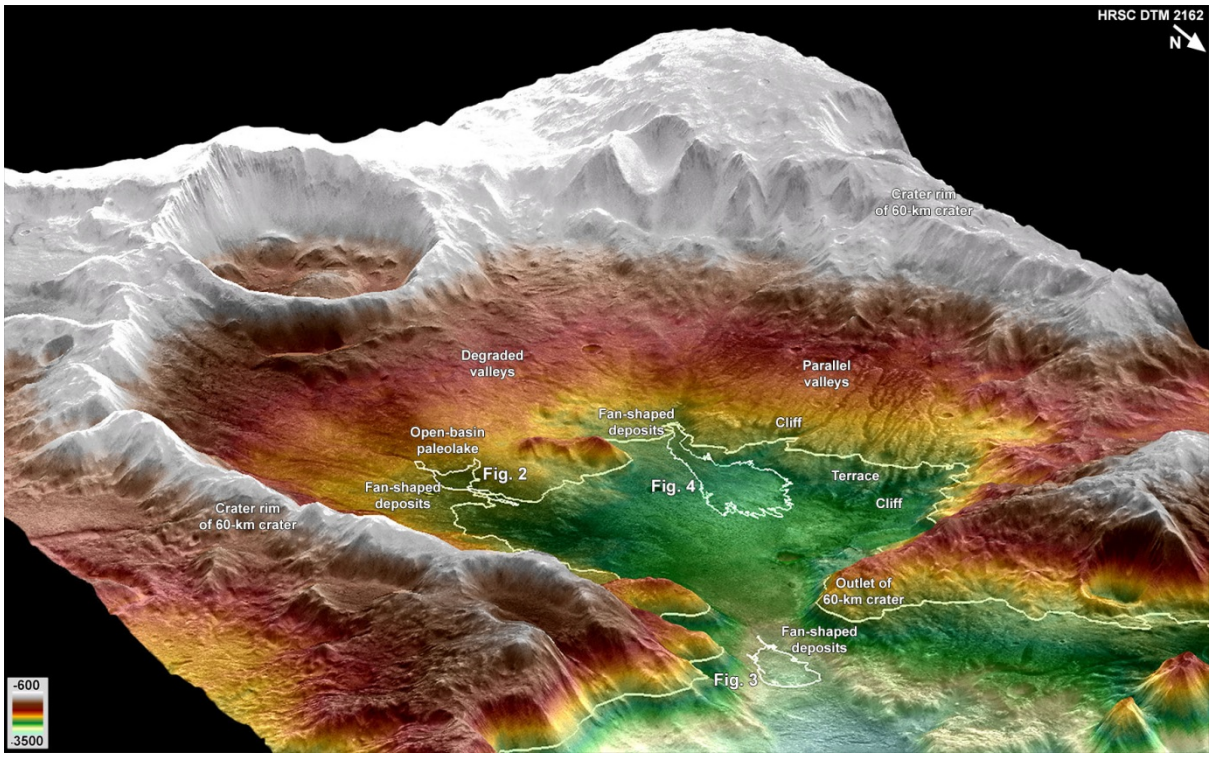

Fig. 1: Perspective view of the 60-km diameter crater at the boundary between the Libya Montes and Isidis Planitia. The crater-lake site hosts a complex diversity of fluvial, lacustrine and possible fluvio-glacial landforms, in particular degraded valleys, parallel (tunnel) valleys, two cliffs and a terrace, an outlet cut into the northern rim of the 60-km crater, a delta with associated Al-rich phyllosilicates, a small-scale open-basin paleolake with another delta, widespread bright, polygonally-fractured Fe/Mg phyllosilicates, and an alluvial fan. Color-coded HRSC h_2162 DTM on CTX mosaic.

Proposed formation history

The stratigraphically oldest units in the 60-km crater are heavily degraded valleys that are partly dendritic and are present only on some sections of the eastern and southeastern walls. They are comparable to the dendritic valley networks observed elsewhere in Libya Montes and represent earliest phases of fluvial activity characterized by precipitation-induced surface runoff [e.g., 1-4]. At that time (~3.8 Ga, [4]), water was possibly also initially ponding in the 60-km crater. As the terrain declines toward the north, water may have spilled over the northern rim of the crater and resulted in an initial breach in the wall. The crater rim should have been initially intact to an elevation above -2500 meters. This is supported by the elevation of fluvial and lacustrine landforms in the 60-km crater, which suggest later and repeated ponding events.

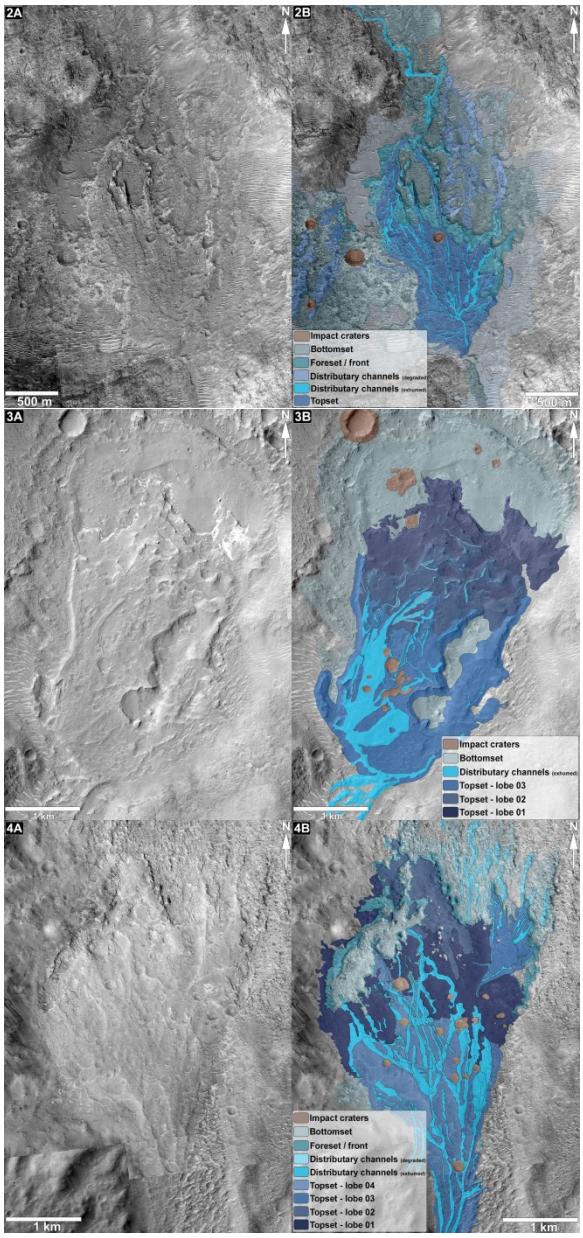

Fig. 2: HiRISE-based morphologic maps of (2AB) a small-scale open-basin paleolake with fan-shaped deposits, (3AB) deltaic deposits at the outlet of the 60-km crater, and (4AB) an alluvial fan.

We proposed that a second lake-size standing body of water is associated with cliffs near -2500 and -2800 meters elevation along which the majority of valleys terminate. A terrace between the cliffs may also be related to a lake-size standing body of water and suggests, together with the cliffs, variations of the lake-level and distinct still-stands. Further evidence for fluvio-lacustrine processes that occurred later and were different from those that formed the degraded valleys and the initial breach are the parallel valleys and a few individual valleys that appear stratigraphically higher than the degraded valleys. One of the individual valleys drains as the inlet channel into a small open-basin paleolake (Fig. 2). Our HiRISE based morphologic map shows the fan-shaped deposits, including typical morphologies such as a topset lobe with numerous exhumed distributary channels, a heavily degraded foreset and the degraded and buried remnants of the bottomset. The latest fluvio-lacustrine activity at this site appeared likely along a distributary channel along the western edge of the fan-shaped deposits. The distributary channel follows the channel through the outlet breach. The topographic setting in an open-basin crater-lake site, the lobe morphologies and strong evidence for hydrous alteration supports the interpretation of this feature as a delta.

Overspill events of the second lacustrine phase had eroded the breach in the northern rim of the 60-km crater to its present state at -3100 meters elevation. In a depression immediately north of the outlet, another fan-shaped deposit indicates a third phase of lake formation (Fig. 3). The deposits consist of three individual topset lobes with decreasing extent from oldest to youngest, suggesting that the amount of water was also decreasing during formation. The stratigraphically oldest lobe (Topset-lobe 01, Figure 3) is heavily degraded and does not show many distributary channels. Abundant bright polygonally-fractured materials along the front of lobe 01 are rare in Libya Montes and have been interpreted as Al-rich phyllosilicates, particularly montmorillonite [4] and/or beidellite [5,8]. The topographic setting in a closed basin, the lobe morphologies and strong evidence for hydrous alteration supports the interpretation of this feature as a delta.

The fan-shaped deposit located in the center of the 60-km crater (Figure 4) very likely shows a late-stage depositional event in the 60-km crater and also indicates that a possible lake did not exist during the crater formation. The orientation of the lobes perpendicular to the parallel valleys suggests that the materials have been deposited significantly later. Also the rim of the 60-km crater was already breached at -3100 meters elevation and did not allow ponding up to -2500 meters, the level of the alluvial fan. However, four distinct lobes of the fan-shaped deposit and Fe/Mg phyllosilicates present in the stratigraphically oldest lobes are possibly the result of repeated events of erosion, transport and deposition, and suggest a complex formation history. The general morphologic setting of the fan on a steep slope and not in a basin is more comparable to an alluvial fan. Finally, fluvial activity responsible for the formation of the alluvial fan was still active (~<3.6 Ga, [4]) but waning and insufficient to form a lake.

Conclusion

We interpret the morphologic–geologic setting and associated mineral assemblages of the 60-km crater-lake site as resulting from repeated fluvial activity, multiple lake-size standing bodies of water and an environmental change over time toward decreasing water availability.

References: [1] Crumpler and Tanaka, 2003, JGR, 108, ROV 21-1. [2] Erkeling, et al., 2010, EPSL, 294, 291-305. [3] Jaumann et al., 2010, EPSL, 294, 272-290 [4] Erkeling, et al., 2012, Icarus, 219. [5] Bishop et al., 2013, JGR, 118, 487–513 [6] Erkeling et al., 2011 MEPAG, RFP round VI; NKB-269-122010 CDP [7] Erkeling et al., 2014, 1st ExoMars 2018/2020 LSSW, Madrid [8] Tirsch et al., 2015, 46th LPSC,#1738.